Structure and Collectivity of Highly Deformed Nuclei Along the N=Z Line

Ryan David Owen Llewellyn

Doctor of Philosophy
University of York
Physics

June 2020

Abstract

The lifetimes of the first excited 2^+ states in the $N = Z$ nuclei ^{80}Zr, ^{78}Y and ^{76}Sr have been measured using the γ-ray lineshape method following population via nucleon-knockout reactions from intermediate-energy rare-isotope beams. ^{80}Zr, ^{78}Y and ^{76}Sr are the heaviest $N = Z$ nuclei where such measurements have been made to date. The extracted reduced electromagnetic transition strengths yield new information on where the collectivity is maximised and provide evidence for a significant, and as yet unexplained, odd-odd vs. even-even staggering in the observed values. The experimental results are analysed in the context of state-of-the-art large-scale shell model and nuclear density-functional theory (DFT) model calculations. DFT calculations incorporating $T = 1$ np pairing reproduce the measured $B(\mathrm{E2}\downarrow)$ values of the even-even nuclei but fail to replicate the extent of the reduction in $B(\mathrm{E2}\downarrow)$ seen with the odd-odd ^{78}Y.

The mirror energy differences (MED) of the ^{79}Zr/^{79}Y mirror pair have also been measured, again the heaviest nuclei where such measurements have been taken. This is the first observation of the excited yrast states of ^{79}Zr. No-core configuration-interaction (NCCI) model calculations show good agreement with the remarkably small experimental MED up to $J = (\frac{9}{2}^+)$, with a deviation at higher spin. The success of the NCCI model provides a stepping-stone to using the same approach for future MED analysis.

Contents

List of Tables

List of Figures

Acknowledgements

First and foremost I'd like to thank my supervisors Prof. Mike Bentley and Prof. Bob Wadsworth for their continual guidance and support over the last four years. Without them this thesis would not have been possible.

I would like to thank the members of the nuclear physics group at York, in particular Chris, Luke M, Ben, Antonio, Gustavo, Soham, Paolo and Luke T for the laughs and great stories and Scott, Thoryn, Sivi and Rehab for their help with any analysis. I would also like to thank my collaborators Prof. Jacek Dobaczewski, Dr. Hiro Iwasaki, Prof. Wojciech Satuła and Dr. Dirk Weisshaar for answering my questions and providing the calculations for this thesis.

Finally I'd like to thank my family and Kellie for their support and keeping me motivated as well as the Costa at the Roger Kirk Centre for their medium Americanos and the Co-op meal deal section for providing me with the fuel to complete this work.

Declaration

I declare that this thesis is a presentation of original work and I am the sole author. This work has not previously been presented for an award at this, or any other, University. All sources are acknowledged as References. Some parts of this thesis have however been previously published in journals:

1. R. D. O. Llewellyn, M. A. Bentley, R. Wadsworth, H. Iwasaki, J. Dobaczewski *et. al*, "Establishing the Maximum Collectivity in Highly Deformed $N = Z$ Nuclei", Phys. Rev. Lett., **124**, 152501 (2020)

2. R. D. O. Llewellyn, M. A. Bentley, R. Wadsworth, J. Dobaczewski, W. Satuła, H. Iwasaki *et. al*, "Spectroscopy of Proton-Rich ^{79}Zr: Mirror Energy Differences in the Highly Deformed *fpg* Shell", Submitted to Phys. Lett. B

Chapter 1

Introduction

Nuclei, and more specifically their constituent neutrons and protons, are the building blocks of all known matter. The fundamental interaction that binds these together governs everything from the microscopic scale to the behaviour of supernovae. An understanding as to why nuclei exhibit different shapes and its relation to nucleon collectivity is one of the key components of our knowledge of the intricacies of the nuclear force. Our ability to replicate the evolution of collectivity and low-spin state energies at the extremes of the nuclear chart is one of the best benchmarks of our fundamental understanding of nuclear theory.

Features of nuclear structure can be categorised into either single-particle or collective effects - where both neutrons and protons interact coherently. In terms of collective effects, nuclei with equal numbers of neutrons and protons ($N = Z$) are of particular interest given that they are predicted to be prime candidates of possessing deuteron-like isoscalar $T = 0$ neutron-proton (np) pairs [1] i.e. np pairs coupled with a total spin $J > 0$ [2, 3] as a consequence of their wave function overlap, a concept first hypothesised in 1958 [4]. $N = Z$ nuclei in the mass (A) 80 region have been predicted to exhibit some of the most deformed nuclear shapes in the whole of the nuclear chart [5, 6, 7, 8] (see Fig. 1.1). Indeed, the measured 2^+ state energies of nuclei in this region, e.g. ^{76}Sr [9], ^{78}Y [10] and ^{80}Zr [11], of < 300 keV are lower than one would expect. This provides a further indication of this region containing highly-deformed nuclei with enhanced collectivity. Calculations in the neutron-deficient $N = Z$ region around $A = 80$ have predicted $T = 0$ np pairing to increase in dominance in $A > 76$, $N = Z$ nuclei [12], growing at higher spin in the case of ^{80}Zr [13]. The issue of whether these $N = Z$ nuclei exhibit these isoscalar np pairing correlations is a topic of

great debate in nuclear physics [14] and there is as of yet no conclusive experimental evidence of this phenomenon. Therefore, nuclei in this neutron-deficient region of the nuclear chart and the question as to the role of $T = 0$ np pairing in these nuclei is particularly intriguing for nuclear physicists.

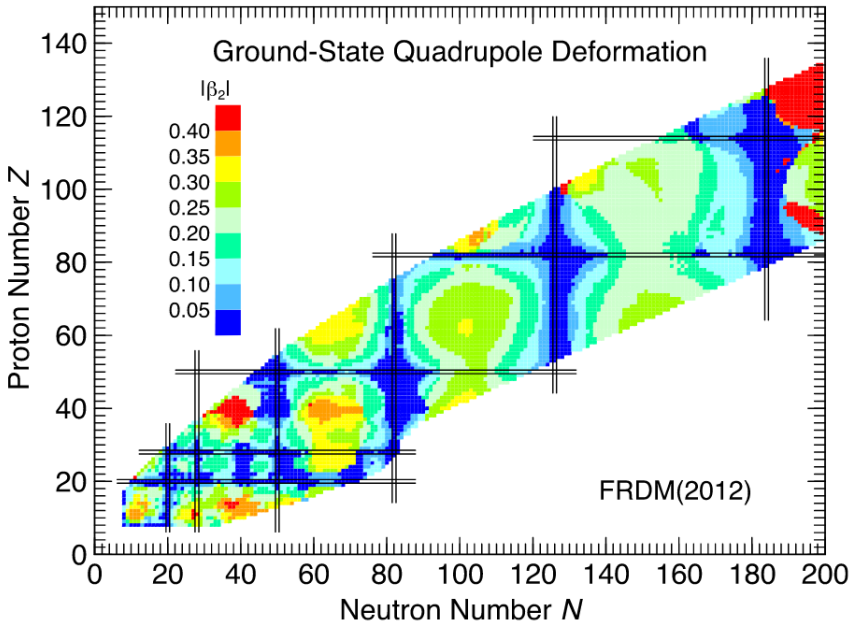

Figure 1.1: The quadrupole ground-state deformation across the Segré chart. The $N = Z \approx 40$ region is predicted to exhibit some of the largest deformations of the whole nuclear chart. Taken from [5].

The degree of nucleon collectivity can be probed through measurements of the reduced transition rates of the 2^+ to ground-state decays, or $B(\mathrm{E2}; 2^+ \rightarrow 0^+)$ [denoted $B(\mathrm{E2}\downarrow)$] values, which can be derived from the lifetime of the 2^+ state. $B(\mathrm{E2}\downarrow)$ values of the $N = Z$ ^{64}Ge [15], ^{68}Se [16, 17], ^{70}Br [17], ^{72}Kr [18, 19], ^{74}Rb [20] and ^{76}Sr [21] have previously been measured, with the end goal of eventually extending the picture of the evolution of collectivity to ^{100}Sn, the heaviest known $N = Z$ nucleus. These measurements demonstrated a clear, rapid increase in collectivity above ^{70}Br, where the heaviest $N = Z$ nucleus measured to date, ^{76}Sr, was deduced to exhibit a large quadrupole deformation of $\beta_2 = 0.45(3)$. This sudden increase in collectivity, which can be attributed to the intrusion into the $g_{9/2}$ orbital [22, 23], is also accompanied by the fact that nuclei in this region have been found to possess intrinsic coexisting nuclear shapes [24, 25, 26, 27] making this an attractive region of the nuclear chart to test the limits of nuclear models. Moreover, the question still remains as to the exact

location of the maximum collectivity along the $N = Z$ line. This is particularly interesting when approaching the mid-fp shell at $N = Z = 39$ between the spherical, doubly-magic ^{56}Ni and ^{100}Sn, where naturally the maximum deformation would be expected. Establishing the evolution of collectivity and where the maximum collectivity is found along the $N = Z$ line and assessing the current state-of-the-art theoretical nuclear calculations' ability to reproduce the trends in collectivity will provide a stringent test of our understanding of nuclear structure and the effects of different orbitals.

Modern developments of radioactive beams, high-precision, position-sensitive detectors accompanied by advances in experimental techniques have opened a gateway to new research into neutron-deficient nuclei further along the $N = Z$ line [14]. The primary aim of this investigation was to measure the lifetimes of the first excited 2^+ states of the $N = Z$ ^{78}Y and ^{80}Zr, the two heaviest $N = Z$ systems where such measurements have been made to date, along with a repeat measurement of ^{76}Sr. ^{78}Y and ^{80}Zr represent the $28 < N = Z < 50$ mid-shell point and the first $N = Z$ nucleus beyond the mid shell, respectively. The ^{92}Mo primary beam at the National Superconducting Cyclotron Laboratory (NSCL) at Michigan State University (MSU) in 2016 was developed specifically for this experiment. This has provided, for the first time, the opportunity to populate the low-lying states of these $A > 76$, $N = Z$ nuclei through nucleon-knockout reactions. $B(\mathrm{E2}\downarrow)$ measurements in this region will provide invaluable insight into the evolution of collectivity at the previously inaccessible extremes of the nuclear chart.

Although ^{80}Zr was initially predicted to be spherical [28], it was found to produce a yrast decay scheme consistent with a deformed, rotational structure [11]. Beyond mean-field method calculations predict ^{80}Zr to be highly deformed, with five almost degenerate shapes being predicted all with 0^+ ground states below an excitation energy of 2.5 MeV [29]. The lowest energy of these is predicted to exhibit a near-axial deformation of $\beta_2 = 0.55$ (see Fig. 1.2), corresponding to a $B(\mathrm{E2}\downarrow)$ ∼80% larger than that measured for ^{76}Sr [21], suggesting a significant increase in collectivity beyond the mid shell. ^{80}Zr also plays a key role in astrophysical processes, where it is an rp-process waiting point [30], meaning an understanding of its low-lying structure is vital.

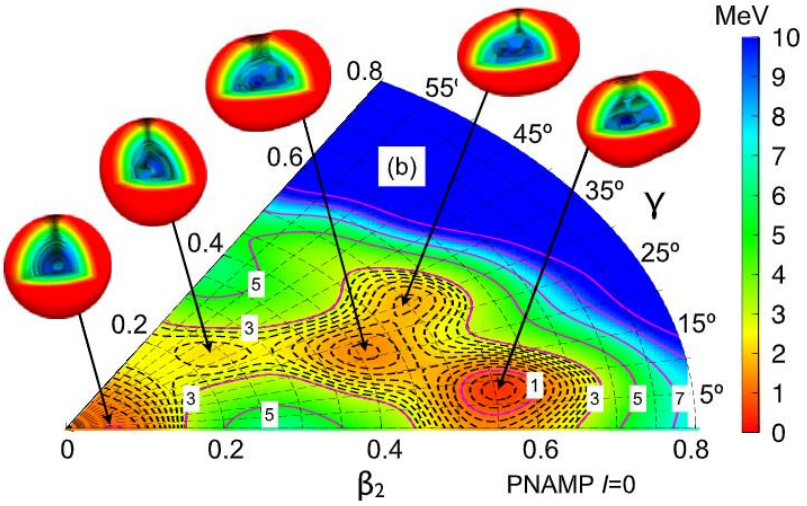

Figure 1.2: Potential energy surface plot calculated for ^{80}Zr through beyond mean-field methods. ^{80}Zr is predicted to exhibit five different shapes, all below an excitation energy of 2.5 MeV, with ground state deformations as large as $\beta_2 = 0.55$ being predicted. Calculations are taken from [29].

The development of the ^{92}Mo primary beam at NSCL also provided the opportunity to explore the ^{79}Zr/^{79}Y mirror pair through nucleon-knockout reactions for the first time. Mirror nuclei are particularly fascinating as these provide a means to test the fundamental symmetry of the nuclear force and the principle of isospin symmetry [31]. The observed energy differences between isobaric analogue states and their spin and orbital dependence provide insight into the breaking of this fundamental symmetry and its evolution in different mass regions. There have been extensive studies into these mirror energy differences in the upper-*sd* and lower-*fp* shells (see for example Refs. [32, 33, 34, 35, 36]). The investigation of the ^{79}Zr/^{79}Y mirror pair are the heaviest and most deformed nuclei where such a study has been performed to date. This is the first instance of probing these energy differences in the upper-*fpg* region, as well as the first observation of the excited yrast states of ^{79}Zr.

Chapter 2

Theory

The work presented in this thesis will comprise of $B(\mathrm{E2}\downarrow)$ measurements of the $N = Z$ ^{76}Sr, ^{78}Y and ^{80}Zr and mirror energy difference measurements of the ^{79}Zr/^{79}Y mirror pair. This chapter will discuss the background physics which motivated this experiment, including nucleon pairing and its relation to collectivity, the fundamental symmetries that can be probed through mirror energy differences and the experimental methods used to populate states of the nuclei of interest. The experimental results are later compared to theoretical calculations performed through shell-model and mean-field approaches. The principles and limitations of each method will be discussed in this chapter.

2.1 Nucleon Pairing

In nuclei where $N > Z$ traditional isovector ($T = 1$) neutron-neutron (nn) and/or proton-proton (pp) pairing modes coupled to total angular momentum $J = 0$ are prevalent [14], as shown in Fig. 2.1(a). In most $N > Z$ nuclei the effects of neutron-proton (np) pairing are usually negligible given the separation between the neutron and proton levels. However, in nuclei with equal numbers of protons ($N = Z$) the spatial overlap of the neutron and proton wave functions at the Fermi surface allows them to act coherently, meaning a correct treatment of np pairing is essential. Neutrons and protons are capable of pairing in the $T = 1$ configuration [see Fig. 2.1(a)] and since neutrons and protons are distinguishable particles, and therefore do not abide by the rules of the Pauli Exclusion Principle, they are also permitted to couple to isoscalar $T = 0$ pairing modes with $J > 0$ [14] [see Fig. 2.1(b)].

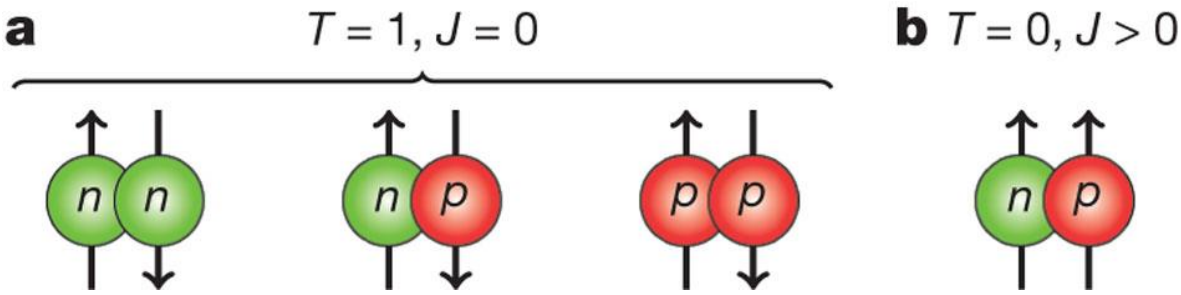

Figure 2.1: Isovector $T = 1$ (a) and isoscalar $T = 0$ (b) neutron-proton pairing modes. Taken from [2].

Previous spectroscopy of $A < 80$, $N = Z$ nuclei has suggested that at low excitation energies $T = 1$ np pairing modes are dominant [14]. Isoscalar $T = 0$ pairing has been predicted to become of increasing dominance in $A \gtrsim 76$, $N = Z$ nuclei [1, 12] with a nuclear superfluid [37, 38, 39], analogous to *'Cooper pairs'* [40] in superconductors, with an admixture of competing $T = 1$ and $T = 0$ pairing modes being hypothesised. Neutron-proton pairing correlations have been found to have a significant impact on Gamow-Teller transitions [41] and neutrinoless double-β decay [42]. The charge-symmetric nature of the nuclear force implies that in $N = Z$ nuclei $T = 1$ $J = 0$ np pairing should exist in equal amounts as $T = 1$ nn and pp pairing [14].

The effects of $T = 0$ np pairing behaviour as a part of a collective condensate still eludes experimental verification [14]. Through analysis of shell-model wave functions the experimentally deduced energy levels of ^{92}Pd [2] were suggested to contain an np-paired phase consisting of four $J = 9$ anti-aligned np pairs in the ground state which gradually align their spins with increasing angular momentum. Energy levels up to $J = 14$ deduced from recently obtained γ-ray energy spectra for the $N = Z$ ^{88}Ru [43] found a delay in the alignment of the $g_{9/2}$ neutrons and protons, that is expected in moderately deformed rotating nuclei, when compared to $N > Z$ nuclei with the standard $T = 1$ pairing field. Spectroscopy of the $N = Z$ ^{96}Cd [44] suggested that the 9^+ state could be explained in terms of the coupling of $T = 0$ and $T = 1$ np pairs [44]. Although the conclusions from these results are postulated in regards to shell-model calculations (see e.g. Ref. [45]), these calculations are limited as they do not incorporate mixed quasiparticle wave functions which embody the effects of a correlated neutron-neutron, proton-proton and neutron-proton condensate [14, 46].

Large scale shell-model (LSSM) calculations are derived from effective nucleon-nucleon

interactions (see Chapter 2.3.1.1). Therefore, accounting for the ramifications of an np-pairing condensate through this method is no trivial matter. As discussed in Ref. [14], the most feasible method of integrating np-pairing correlations into theoretical calculations is likely to be through a mean-field approach. The inclusion of mixed neutron-proton wave functions encompassing np-pairing correlations in density-functional theory is an area of ongoing work [3, 47]. The current status of np pairing in mean-field calculations, and its implications to the work presented in this thesis, are discussed in further detail in Chapter 2.3.4,

2.2 Isospin

The nuclear force can be considered to be both charge independent and charge symmetric [48]. The charge-independent nature of the nuclear force dictates that the strength of the force between a neutron and a proton (V_{np}) will be equal to the average of the nuclear force between proton-proton (V_{pp}) and neutron-neutron (V_{nn}) pairs:

$$V_{np} = \frac{V_{pp} + V_{nn}}{2}, \tag{2.1}$$

whilst charge symmetric means that neutron-neutron forces are equal to proton-proton forces:

$$V_{nn} = V_{pp}. \tag{2.2}$$

Although these principles are simplified, they reflect the underlying symmetry between neutrons and protons. The powerful concept of isospin [49] states that both protons and neutrons can be considered as manifestations of the same particle, called the *'nucleon'*. Each can be distinguished by assigning them with different projections of the isospin quantum number, denoted by t_z, with the neutron and the proton having values of $+\frac{1}{2}$ and $-\frac{1}{2}$, respectively [31]. The total isospin projection T_z of a nucleus with mass A consisting of N neutrons and Z protons is therefore given by:

$$T_z = \sum^{A} t_z = \frac{N - Z}{2}. \tag{2.3}$$

A nucleus can occupy states with a total isospin T which can assume values given by:

$$\frac{\mid N - Z \mid}{2} \leq T \leq \frac{\mid N + Z \mid}{2}, \tag{2.4}$$

in increments of one. The allowed T states for a nucleus with a given T_z are illustrated in the schematic created by M. A. Bentley in Fig. 2.2, satisfying the isospin rules in Eq. 2.4. Neutron-proton pairs coupled in a $T = 0$ configuration are in general found to increase the binding energy of the system. Therefore in most nuclei the ground states have an isospin of $T =\mid T_z \mid$ since higher T states tend to possess a much greater energy. It can also been seen in Fig. 2.2 that $T = 0$ states are only permitted in $N = Z$ ($T_z = 0$) nuclei. However, it must be noted that this schematic does not necessarily apply to odd-odd $N = Z$ nuclei. It has been observed in some odd-odd $N = Z$ nuclei, particularly in the mid-fpg shell ($A \sim 46$), that the first $T = 1$ states are actually lower in energy than the $T = 0$ states [50].

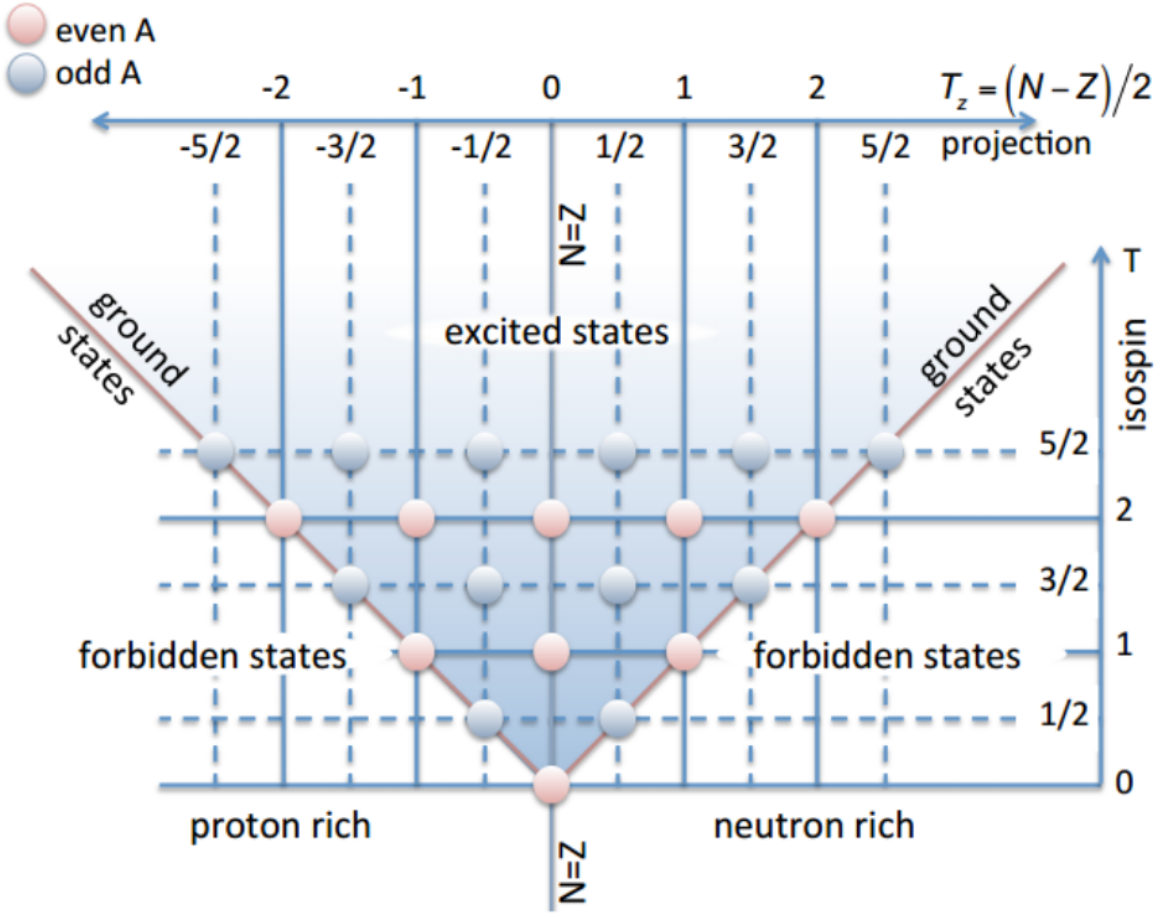

Figure 2.2: The 'Bentley Isospin Triangle' displaying the possible excited isospin T states for a nucleus with T_z. The lowest permitted T states for a nucleus are equal to $\mid T_z \mid$. It must be noted that this does not apply to all odd-odd $N = Z$ nuclei where in the mid fpg shell $T = 1$ states have been found to be lower in energy than their $T = 0$ counterpart.

2.3 Nuclear Models

2.3.1 Single-Particle Shell Model

Atomic theories based on a shell-model approach have shown excellent agreement with experimental data; impressive given the complicated nature of atomic structure. The nuclear shell model was developed as a method of explaining the properties of nuclear structure using a similar approach. However, there are some distinct differences between the atomic and nuclear cases, the first being that the atomic potential is produced by the Coulomb field of the nucleus (i.e. an external source) whilst in the nuclear case the potential is created by the nucleons themselves. Another major difference is the fact that electrons occupying atomic levels move within orbits which are free from collisions with other electrons. The same can not be said for nucleons, which have diameters which are large in comparison with the nucleus meaning that the effects of collisions of defined orbits cannot be neglected.

Key experimental evidence that provides an indication of a nuclear shell model are the magic numbers. The magic numbers of 2, 8, 20, 28, 50, 82 and 126 are numbers of neutron/protons that exhibit binding energies considerably larger than expected. By only considering two-body interactions, the nuclear Hamiltonian, H, can be described in terms of the the sum of kinetic energy, T, and potential energy, V:

$$H = T + V = \sum_{i=1}^{A} \frac{p_i^2}{2m_i} + \sum_{j>i}^{A} V_{i,j}(r_i, r_j). \tag{2.5}$$

The final V term needs to be approximated with an average potential. An infinite square well has a increase in potential that is too sharp and would imply that an infinite amount of energy would be required to separate a neutron or proton. A central potential in the form of a Harmonic Oscillator (HO) defined as:

$$V_{HO}(r) = \frac{1}{2} m\omega^2 r^2, \tag{2.6}$$

where m is the the mass of the nucleon, ω is the angular frequency of the oscillator and $\hat{\mathbf{r}}$ is the radial distance of the nucleon, proves to be too diffuse with respect to the radius. To correct for this, the central nuclear potential is often parametrised with a Fermi function known as the Woods-Saxon potential [51] in the following manner:

$$V_0(r) = \frac{-V_0}{1 + e^{\frac{r-R_0}{\alpha}}}, \tag{2.7}$$

Here the radius of a spherical nucleus is given by $R_0 = 1.25\ \mathrm{A}^{\frac{1}{3}}$ fm and the values V_0 and α are empirically derived, typically with values of ∼57 MeV and ∼0.65 fm, respectively. A slight modification is applied to the V_0 parameter separately for neutrons and protons to account for when a nucleus exhibits neutron excess:

$$V_{0p} = V_0 + \frac{(N-Z)}{A} V_I \text{ for protons,} \tag{2.8}$$

$$V_{0n} = V_0 - \frac{(N-Z)}{A} V_I \text{ for neutrons.} \tag{2.9}$$

This is a consequence of the average proton-neutron potential being slightly stronger than the average neutron-neutron/proton-proton potential [52]. V_I has typical values of -30 MeV, but this and other parameters can be prescribed different values depending upon the mass region and nucleus [52]. In many cases the HO potential is used given its simplicity when solving the Schrödinger Equation.

Since both neutrons and protons are fermions they therefore obey the Pauli Exclusion Principle - where like-fermions are forbidden to occupy the same quantum state. The quantum states that these nucleons occupy are specified by the radial quantum number, n, which takes integer values and the nucleon's angular orbital momentum, ℓ, which is represented by $s, p, d, f, g, h...$ for $\ell = 0, 1, 2, 3, 4, 5...$, respectively. Each ℓ value consists of $2\ell + 1$ m states where each m state can contain a neutron/proton aligned with either spin up ($s_z = +1/2$) or spin down ($s_z = -1/2$). Therefore, the degeneracy of the principal quantum number, n, is given by $2(2\ell + 1)$.

The central potential successfully reproduces the magic numbers of 2, 8 and 20 but fails to reproduce the magic numbers > 20. The inclusion of a spin-orbit potential, representing the coupling of ℓ and s to a total angular momentum $\vec{j} = \vec{\ell} + \vec{s}$, to the central potential was the major breakthrough in splitting the degeneracy of ℓ states and reproducing the higher magic numbers. This potential, which is proportional to the derivative of the central potential $\frac{dV_0(r)}{dr}$, takes the form of:

$$V_{so}(r) = -V_{ls}(\vec{\ell} \cdot \vec{s})\ R_0^2\ \frac{1}{r}\frac{dV_0(r)}{dr}, \tag{2.10}$$

where V_{ls} dictates the strength of the interaction (typically 22 MeV [52]) and R_0 and $\hat{\mathbf{r}}$ are the same as in Eq. 2.7. Furthermore, a centrifugal term (denoted V_{cent}) is included to account for the centrifugal force exerted on nucleons moving within given orbitals:

$$V_{cent}(r) = \frac{\ell(\ell+1)\hbar}{2mr^2}. \tag{2.11}$$

The elementary charge, e, of the proton introduces an additional potential, V_C, a consequence of the Coulomb potential created from the electric field of the protons within a nucleus. This potential takes the form of:

$$V_C(r) = \begin{cases} \frac{Ze^2}{r}\left[\frac{3}{2} - \frac{r^2}{2R_o^2}\right] & \text{for } r < R_0 \\ \frac{Ze^2}{r} & \text{for } r > R_0 \end{cases}$$

where Z is the atomic number of the nucleus. The inclusion of the spin-orbit, centrifugal and Coulomb terms to the central potential culminate to produce the total nuclear potential, $V(r)$, which is defined as:

$$V(r) = \begin{cases} V_0(r) + V_{so}(r) + V_{cent}(r) + V_C(r) & \text{for protons,} \\ V_0(r) + V_{so}(r) + V_{cent}(r) & \text{for neutrons.} \end{cases}$$

Fig. 2.3 demonstrates the importance of the inclusion of the spin-orbit coupling term. The addition of this term allows the magic numbers above 20 to be reproduced.

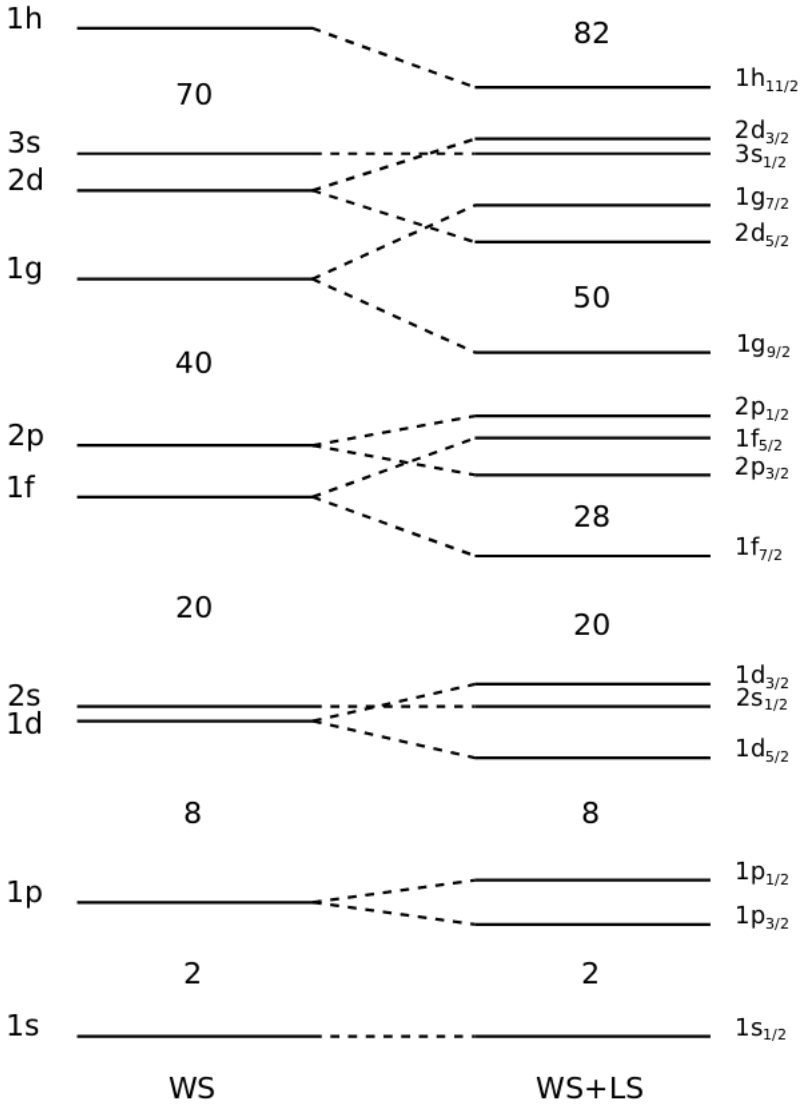

Figure 2.3: The shell model levels derived from the Woods-Saxon central potential without (left) and with (right) the inclusion of the spin-orbit interaction. The labels on the left-hand side indicate the ℓ of the orbital whilst the right-hand side includes the orbital and spin of the state (ℓ_j). The inclusion of the spin-orbit interaction allows the magic numbers above 20 to be reproduced. Adapted from [53].

2.3.1.1 Shell-Model Calculations

Calculations based on a many-particle shell-model approach can be used to predict nuclear structures and derive theoretical values such as energy levels of states and transition probabilities. In shell-model calculations basis states are constructed by considering all available configurations of nucleons with a specific spin, parity and isospin in the single-particle lev-

els. After the prescription of the nuclear Hamiltonian (Eq. 2.5), additional residual nucleon-nucleon interactions must be considered, which are denoted as V_{ij}. The Hamiltonian in this case can therefore be represented as the sum of all possible configurations from single-particle levels [54]:

$$H = \begin{pmatrix} \epsilon_1 & 0 \\ 0 & \epsilon_2 \end{pmatrix} + \begin{pmatrix} \langle\phi_1| V_{11} |\phi_1\rangle & \langle\phi_1| V_{12} |\phi_2\rangle \\ \langle\phi_2| V_{21} |\phi_1\rangle & \langle\phi_2| V_{22} |\phi_2\rangle \end{pmatrix}, \tag{2.12}$$

where $|\phi_1\rangle$ and $|\phi_2\rangle$ are the basis vectors. The first matrix containing ϵ_1 and ϵ_2 represent the single-particle energies, which are usually taken from experimental data. The diagonal elements of the second matrix are the expectation values of V_{11} and V_{22} of $|\phi_1\rangle$ and $|\phi_2\rangle$ whilst the non-diagonal elements dictate the configuration mixing. The matrix is then diagonalised to yield eigenvalues α and β and corresponding eigenvectors $|\psi_1\rangle$ and $|\psi_2\rangle$:

$$|\psi_1\rangle = \alpha \cdot |\phi_1\rangle + \beta \cdot |\phi_2\rangle \text{ and} \tag{2.13}$$

$$|\psi_2\rangle = -\beta \cdot |\phi_1\rangle + \alpha \cdot |\phi_2\rangle, \tag{2.14}$$

where the eigenvalues are normalised such that $\alpha^2 + \beta^2 = 1$.

Considering the effects of excitations of every particle in all but very light systems is far too computationally intensive through this approach. To compensate for this an inert core is created within the calculation whereby the nucleons within the core are forbidden to excite to different orbitals and are therefore excluded from the calculation, drastically decreasing the number of free parameters. This inert core is traditionally assumed to be a doubly-magic nucleus. The shell-model orbitals included within the calculation are known as the *'model space'*, where constituent nucleons within these orbitals are allowed to freely move. Some higher energy orbitals are truncated from the calculation and not included. As a consequence of the assumption of an inert core an *'effective interaction'* must be utilised, which is dependent upon the core, model space and truncation. Examples of these interactions commonly used near the $A = 80$ region are the JUN45 [55] and the PMMU interaction [56], for use in the $p_{\frac{3}{2}} f_{\frac{5}{2}} p_{\frac{1}{2}} g_{\frac{9}{2}}$ and $p_{\frac{3}{2}} f_{\frac{5}{2}} p_{\frac{1}{2}} g_{\frac{9}{2}} d_{\frac{5}{2}}$ model spaces, respectively. Due to these imposed restrictions of model spaces and truncations, the effectiveness of these types of calculation diminishes with nuclei far from a closed shell.

The results presented in this thesis are later compared to shell-model calculations for $N = Z$ nuclei $A \approx 80$ from Ref. [57] in Chapter 7.2. Nuclei in this mass region prove to be particularly challenging to model through a shell-model approach. The closed $N = Z = 28$ core is far from the $N = Z \approx 40$ region, therefore requiring the inclusion a large model space to accommodate the large number of valence particles. Moreover, the large quadrupole deformations of $\beta_2 \sim 0.4$ observed near this mid-shell region and the resulting intruder orbits (see Chapter 2.3.3), such as the $d_{5/2}$ orbital, mean that a large model space is paramount in this case. Likewise, further complications arising from the mixing of nuclear shapes and their triaxiality create more obstacles in performing calculations across this mass region with a consistent treatment.

2.3.2 Rotational Nuclear Excitation

The kinetic energy of a rotating object is given by $\frac{1}{2}I\omega^2$, where I is the moment of inertia of the object and ω is the angular frequency. In the case of a rotating nucleus, this energy is quantised and can be represented in terms of spin J as [58]:

$$E(J) = \frac{\hbar^2}{2I}J(J+1). \tag{2.15}$$

Increasing J results in a rotational band structure with an increasing energy separation: $E(0^+) = 0$, $E(2^+) = 6(\hbar/2I)$, $E(4^+) = 20(\hbar/2I)$ etc. Therefore, a perfectly rigid nucleus would possess an $E(4^+)/E(2^+)$ ratio of 3.33. This is indeed true for most $150 < A < 190$ and $A > 230$ even-even nuclei, but given that nuclei are not strictly a rigid body and possess more of an intermediate stage between a rigid body and a fluid of nucleons there can be deviations in the moment of inertia of a nucleus [58].

2.3.3 Deformed Nilsson Model

The shell model proves to be very successful in describing the behaviour of spherical nuclei. However, in nature nuclei can exhibit a variety of highly deformed nuclear shapes. When a nucleus exhibits a non-spherical potential we can no longer label states with the traditional s, p, d, f, etc. notation as ℓ is not a *'good'* quantum number in this case. Therefore, a modification of the shell model is required to account for deformation of nuclei.

The Nilsson model is a theoretical approach to this problem whereby the nucleus is assumed to be non-spherical. This is achieved through assuming an asymmetric harmonic oscillator potential, resulting in a breaking of the degeneracy of states with different projections of angular momentum, with each spherical orbital giving rise to $(2j + 1)/2$ orbitals. Given this new separation of orbitals these are labelled as such: $\Omega[Nn_z\Lambda]$, where Ω is the projection of a particle's total angular momentum, j, onto the potential's symmetry axis, N is the principal number of the harmonic oscillator, n_z is the number of nodes in the wave function along the symmetry axis and Λ is the component of the orbital angular momentum, ℓ, onto the symmetry axis.

The magnitude and direction of the splitting of the spherical levels are dependent upon the nature and extent of the deformation of the nucleus, in particular the particle's orbit relative to the deformed core. Particles with an orbit with significant overlap with the deformed core will experience a stronger nuclear force, resulting in a lowering of its energy and vice versa. A particle with a large Ω value will have a larger overlap with an oblate nucleus whilst a particle with a small Ω will have a larger overlap with a prolate nucleus. Therefore, for an oblate nucleus orbitals with a large Ω value are lowered in energy whilst for a prolate nucleus orbitals with a smaller Ω value are lowered (see Fig. 2.4).

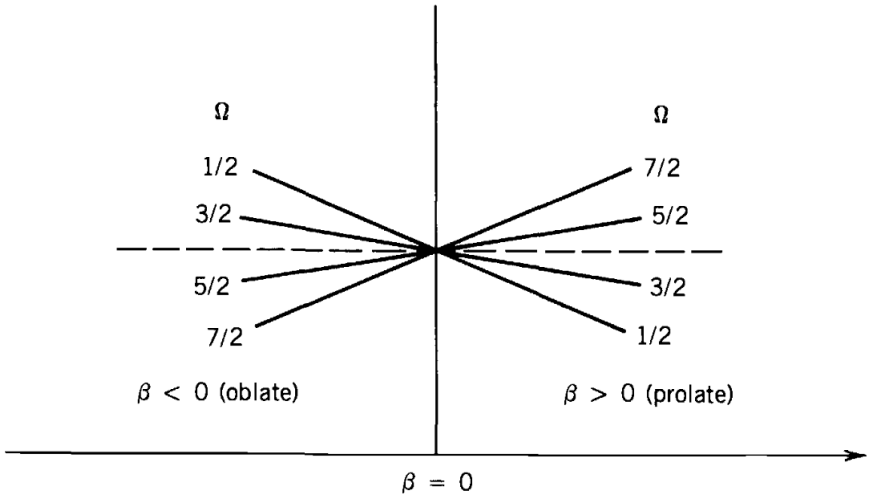

Figure 2.4: The splitting of the degeneracy of the $f_{7/2}$ orbit in a Nilsson model approach. With an oblate deformation the orbit with the highest Ω component is the lowest in regards to energy, and vice versa for a prolate deformation. Taken from [58].

The breaking of the degeneracy of orbitals can result in a complete restructuring of orbitals

in terms of single-particle energies at larger deformations. Higher energy orbitals that become lower in energy with increasing deformations than orbitals that are traditionally considered lower in a spherical model are termed *'intruder orbits'*. These can manifest interesting effects such as providing more stability to deformed nuclear shapes due to a deformation-driving intruder orbit. Fig. 2.5 displays the splitting of the orbitals as a function of deformation up to the $g_{9/2}$ orbital, corresponding to N or $Z < 50$.

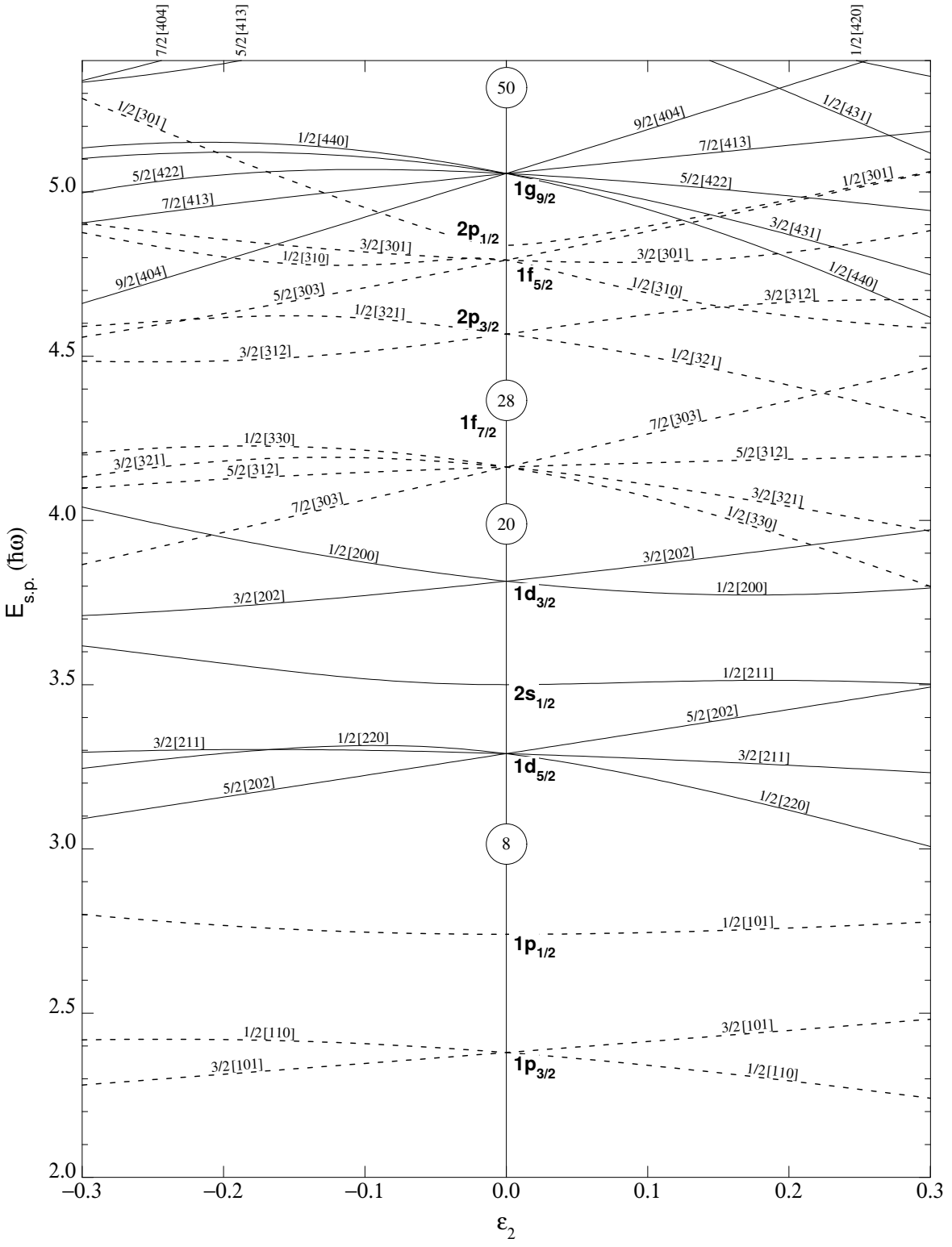

Figure 2.5: The Nilsson diagram for neutrons or protons in the region of N or $Z \leq 50$. The x axis is the deformation parameter ϵ_2, which is almost equal to β_2 at all but very low deformations. The y axis is the single-particle energy levels. From [59].

2.3.4 Density-Functional Theory

The are several different approaches to performing nuclear structure calculations, with each having its own limitations and mass regions where they are most viable. In the lighter mass region *ab-initio* calculations are possible, whereby solutions are based on first principles i.e. from the bare effective interaction [60]. This becomes incredibly challenging as the number of nucleons increases and is only a viable method at the present time for $A \leq 50$. As previously discussed, a shell-model approach to nuclear structure calculations is a more feasible method in the mid-heavy mass region, but again the effectiveness of this method is limited by the computational challenges of a growing configuration space and capability of effective interactions in different mass regions. These type of calculations become impossible with nuclei far from a closed shell, becoming exponentially more complex with a growing number of valence particles. Furthermore, explaining certain phenomena through a shell-model approach has the additional complication of whether the effect can be attributed to a limited model space and/or effective interaction.

Mean-field methods are an approach to nuclear structure calculations whereby an average potential is deduced in which all nucleons move independently of one another [61]. This results in a compound wave function of the nucleus itself, whereby the energy of the nucleus is dependent upon a functional of the density of the nucleus, hence why this method is commonly referred to as Density-Functional Theory (DFT). The energy-density functional depends upon the densities and currents which are used to represent distributions of nucleonic spin, momentum and kinetic energy. These lead to highly nonlinear systems of Hartree-Fock-Bogoliubov (HFB) equations which have to be solved [62]. One of the main advantages of DFT calculations is that due to the mean-field approach calculations are not limited by the number of nucleons or the size of the valence space, making DFT a reliable technique of nuclear structure calculations across the whole nuclear chart, as illustrated in Fig. 2.6.

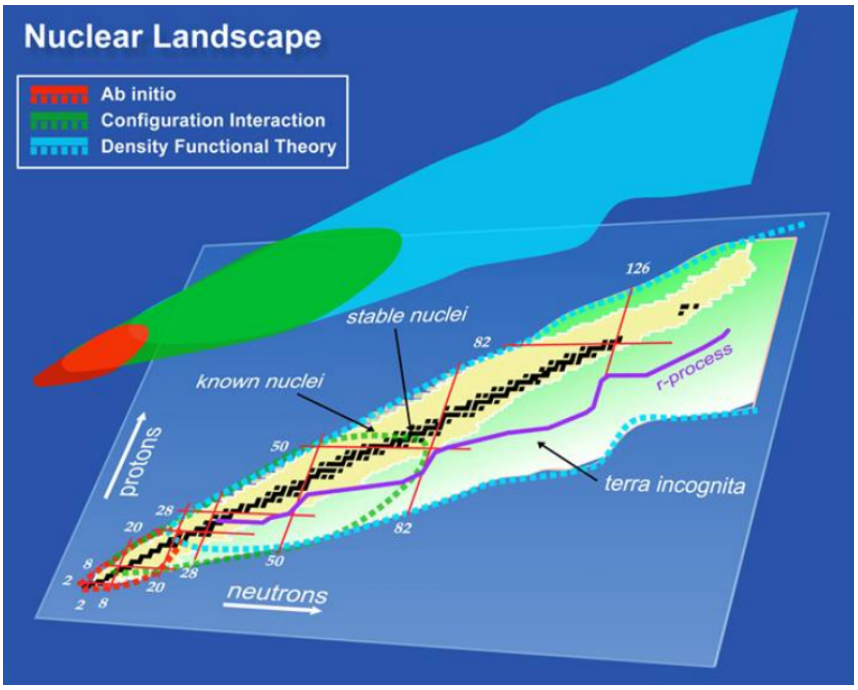

Figure 2.6: The viability of different methods of nuclear structure calculations across the nuclear chart. Taken from [63].

In regards to nucleon-pairing modes, early DFT calculations assumed that $T = 1$ and $T = 0$ pairing modes were mutually exclusive - either only isovector or isoscalar pairing fields were present (see Ref. [64] for a review). These calculations were later extended to incorporate isoscalar pairs of neutrons and protons in identical orbitals. Although this and other calculations include $T = 0$ np pairing, the particle-hole and neutron/proton mean fields are separate. A true self-consistent approach accounting for pairing correlations would assimilate mixed quasiparticle wave functions [65, 66, 67]. The inclusion of this in HFB DFT calculations is currently ongoing [3, 47].

The DFT calculations performed in regards to the results discussed later in Chapter 6 incorporate a condensate of either $T = 1$ nn or pp pairs for the even-even nuclei. When approaching odd-odd nuclei (such as ^{78}Y), pair blocking [68] can be used to mimic $T = 1$ np pairing through forcing the formation of a $T = 1$ $J = 0$ np pair above an even-even core. Through this procedure pair blocking is enforced to forbid the formation of a $T = 1$ neutron or proton pair in a specified orbital, therefore forcing the presence of an unpaired neutron and proton above an even-even core consisting of a $T = 1$ np condensate. The effect of these unpaired nucleons being coupled to $J = 0$ can then be replicated by taking their coupled

$J = 0$ projection [47].

2.4 γ-ray Decay

A nucleus in an excited state can deexcite to a lesser excited state via the emission of a γ ray. This type of decay is typically of energies ranging from ~ 50 keV to as high as several MeV. A nucleus deexciting from a initial state with energy E_i to a final state with energy E_f will emit a γ ray with energy E_γ:

$$E_\gamma = E_i - E_f - T, \tag{2.16}$$

where T denotes the kinetic energy transferred to the nucleus in order to conserve momentum, given by $T = (\Delta E)^2/(2m_f c^2)$. Rest mass energies of nuclei are many orders of magnitude greater than typical γ-ray energies, meaning that T is usually excluded from γ-ray energy calculations.

Deexcitation γ rays can be characterised as either electric (E) or magnetic (M) transitions, with a multiplicity given by 2^L, where L is the angular momentum removed from the nucleus by the γ ray:

$$|J_i - J_f| \leq L \leq |J_i + J_f| \qquad (L \neq 0) \tag{2.17}$$

Furthermore, the parity conservation rules apply:

$$\pi(\mathrm{M}L) = (-1)^{L+1} \tag{2.18}$$

and

$$\pi(\mathrm{E}L) = (-1)^{L}. \tag{2.19}$$

2.4.1 Reduced Transition Strengths

The reduced transition strength of a particular γ-ray transition in a nucleus can reveal information on several properties such as the nucleon configuration before and after the decay, nuclear deformation and the degree of collectivity. Starting from Fermi's Golden rule [69] an expression for the transition probability $\lambda(\sigma L)$ of an electromagnetic transition with character σ (electric or magnetic, denoted by E and M, respectively) and multipolarity, L, from an initial state, J_i, to a final state, J_f, can be expressed as [52]:

$$\lambda(\sigma L) = \frac{8\pi(L+1)}{L[(2L+1)!!]^2}\left(\frac{k^{2L+1}}{\hbar}\right)\frac{|\langle J_f|\,\mathcal{O}(L)\,|J_i\rangle|^2}{(2J_i+1)}, \tag{2.20}$$

where k is the wave number for an electromagnetic transition with an energy, E_γ, defined as:

$$k = \frac{E_\gamma}{\hbar c} \approx \frac{E_\gamma}{197 \text{ MeV fm}}. \tag{2.21}$$

$\mathcal{O}(L)$ is the electromagnetic transition operator, which for an electric transition is defined as [58]:

$$\mathcal{O}(\mathrm{E}L) = \sum_j e_j r_j^L Y_{L\mu}, \tag{2.22}$$

where e_j and r_j^L are the charge and radial distrance of the j^{th} nucleon. The final term of Eq. 2.20 is known as the reduced transition probability, commonly denoted as $B(\sigma L)$, which typically has units of $\mathrm{e}^2\mathrm{fm}^{2L}$ or $\mu_N^2\mathrm{fm}^{2L-2}$ for an electric or magnetic transition, respectively. The $B(\sigma L)$ depends on the overlap between the wave functions of the initial and final states, providing information about the nucleon configuration of the given states at the time of decay. By combining Eq. 2.20 and Eq. 2.21, $\lambda(\sigma L)$ can be expressed as [70]:

$$\lambda(\sigma L) = \frac{2(L+1)}{\hbar\epsilon_0 L[(2L+1)!!]^2}\left(\frac{E_\gamma}{\hbar c}\right)^{2L+1} B(\sigma L), \tag{2.23}$$

where ϵ_0 is the permittivity of free space (8.854×10^{-12} Fm^{-1}). Given the direct relation of the transition probability to the mean lifetime of state, τ_γ, through $\lambda = 1/\tau_\gamma$, the $B(\sigma L)$ of an E2 decay can be expressed in terms of τ_γ as:

$$B(\mathrm{E2}, J_i \to J_f) = \frac{1}{1.226\times10^9 E_\gamma^5\ [\mathrm{MeV}]\times\tau_\gamma\ [\mathrm{s}]} = \frac{815.6}{E_\gamma^5\ [\mathrm{MeV}]\times\tau_\gamma\ [\mathrm{ps}]}\ [e^2\mathrm{fm}^4]. \tag{2.24}$$

Furthermore, the reduced transition strength can be related to the transition matrix element, m_{if}, which corresponds to the square root of the numerator of the final term of Eq. 2.20. This value holds valuable information about the wave function overlap of the initial and final states. Here i and f denote the initial and final states of the transition, respectively. The transition matrix element can be further decomposed into its isoscalar (M_0) and isovector (M_1) components. This can therefore be defined by Eq. 2.25 [58, 71]:

$$m_{if}(\sigma L) = |\langle J_f|\,\mathcal{O}(L)\,|J_i\rangle| = \frac{1}{2}(M_0 - T_z M_1) = [(2J_i+1)\times B(\sigma L; J_i \to J_f)]^{1/2}. \tag{2.25}$$

Reduced transition strengths can provide an indication of the degree of collectivity and shape of a nucleus during a given decay. Compared to single-particle estimates, collective transitions where the nucleus acts coherently exhibit enhanced transition strengths. These single-particle estimates, known as Weisskopf estimates [72], for an electric or magnetic transition are defined as:

$$B(\mathrm{E}L) = \frac{1}{4\pi}\left(\frac{3}{L+3}\right)^2 (1.2A^{1/3})^{2L} e^2 \mathrm{fm}^{2L}, \tag{2.26}$$

$$B(\mathrm{M}L) = \frac{10}{\pi}\left(\frac{3}{L+3}\right)^2 (1.2A^{1/3})^{2L-2} \mu_N^2 \mathrm{fm}^{2L-2}, \tag{2.27}$$

where these values correspond to the expected reduced transition rate if the decay was due to the deexcitation of a single proton, or a Weisskopf unit (W. u.). In particular, reduced transition rates of electric quadrupole transitions [B(E2) values] can provide information about the collectivity of a nucleus given that in even-even nuclei the first excited state is frequently a 2^+ state, which will decay to the ground state with an E2 transition. Therefore, a B(E2) that is orders of magnitude larger than these estimates can indicate a more collective nuclear structure i.e. one that involves the contribution of many nucleons. These estimates can be converted into mean lifetimes (τ, where $\tau = \frac{t_{1/2}}{\ln 2}$) for both electric and magnetic transitions, which are summarised in Table 2.1.

Furthermore, the reduced transition strength of an E2 excitation [denoted B(E2↑)] is related to the reduced transition strength of an E2 deexcitation [denoted B(E2↓)] through:

$$B(\mathrm{E2}\uparrow) = \frac{2J_f + 1}{2J_i + 1} B(\mathrm{E2}\downarrow) \tag{2.28}$$

In the case of this experiment, given that all the measured B(E2↓) are from $2^+ \rightarrow 0^+$ decays, this corresponds to B(E2↑) = 5B($E2\downarrow$). Reduced transition strengths can provide an indication of the quadrupole deformation parameter of a nucleus, β_2, and can be related to the B(E2↑) of a transition through the equation [73]:

$$\beta_2 = \frac{4\pi}{3ZR_0^2}\left[\frac{B(\mathrm{E2}\uparrow)}{e^2}\right]^{1/2} = \frac{4\pi}{3ZR_0^2}\left[\frac{5B(\mathrm{E2}\downarrow)}{e^2}\right]^{1/2}, \tag{2.29}$$

when assuming an axial deformation. Given the strong B(E2↓) dependence of the β_2 of a nucleus, measuring B(E2↓) values can be used as a method of the extracting the deformation of excited states, with a large deformation being an indicative of a enhanced level of nuclear

collectivity. Therefore a measurement of the lifetime and energy of a $2^+ \rightarrow 0^+$ decay provides invaluable information about the degree of a collectivity and deformation of a nucleus.

Table 2.1: Weisskopf estimates of mean lifetime τ (in seconds, where $\tau = \frac{t_{1/2}}{\ln 2}$) for electric and magnetic transitions. E_γ is in units of MeV. Values are converted from [59].

Δ**L**	τ**(E)[s]**	τ**(M)[s]**
1	$\frac{9.75 \times 10^{-15}}{E_\gamma^3 \ A^{2/3}}$	$\frac{3.17 \times 10^{-14}}{E_\gamma^3}$
2	$\frac{1.37 \times 10^{-3}}{E_\gamma^5 \ A^{4/3}}$	$\frac{4.47 \times 10^{-2}}{E_\gamma^5 \ A^{2/3}}$
3	$\frac{2.94 \times 10^{10}}{E_\gamma^7 \ A^2}$	$\frac{9.61 \times 10^{10}}{E_\gamma^7 \ A^{4/3}}$
4	$\frac{9.38 \times 10^{22}}{E_\gamma^9 \ A^{8/3}}$	$\frac{3.06 \times 10^{23}}{E_\gamma^9 \ A^2}$
5	$\frac{4.17 \times 10^{35}}{E_\gamma^{11} \ A^{10/3}}$	$\frac{1.36 \times 10^{36}}{E_\gamma^{11} \ A^{8/3}}$

2.5 Mirror Energy Differences

Building upon the concept of isospin and the symmetry of neutron and protons given in Eqs. 2.1 and 2.2, this implies that in the absence of electromagnetic effects neutron-neutron and proton-proton interactions should be identical. One would therefore expect nuclei with the number of neutrons and protons interchanged (known as mirror nuclei, with $\pm T_z$) to exhibit identical nuclear structures. However, experimentally this is found to not be the case. After normalising to the ground state there are often energy differences observed between excited isobaric analogue states which are known as mirror energy differences (MED). These are therefore defined as:

$$\mathrm{MED}_J = E^*_{J,T,-T_z} - E^*_{J,T,T_z}, \tag{2.30}$$

where E^* is the excitation energy of a state with spin J, T is the total isospin of the nucleus with T_z being the corresponding projection. Examining these energy differences can provide insight into the possible breakdown of the charge symmetry of the nuclear force and have been shown to show a strong J and orbital dependence [74].

In the absence of Coulomb and magnetic effects, MED can be attributed to Isospin Non-Conserving (INC) effects. Theoretical modelling of MED has conventionally taken place within a shell-model framework where these INC effects are a repercussion of '*missing*' physics

of the effective interaction used in shell-model calculations. Throughout the last two decades a shell-model prescription with the inclusion of these effected has been developed to model mirror energy differences and has overall been very successful. These inclusion of INC effects in this approach can be categorised into four separate terms. The first of these is the radial monopole term which accounts for the Coulomb energy linked to nuclear deformation as a function of spin. This therefore is an orbital-dependent term due to the deformation-driving/hindering factors of different orbitals. The second term is the Coulomb multipole term which takes into account the spatial separation of protons depending upon their total coupled spin. For example, when two $f_{7/2}$ protons are coupled to $J = 0$ their spatial separation is at its lowest, therefore corresponding to an increase of the Coulomb energy [32]. Likewise, the Coulomb energy decreases when the two protons recouple to a high angular momentum as their spatial separation increases. A third single-particle monopole term is introduced to account for centrifugal and spin-orbit coupling effects.

The fourth and final term is a nuclear charge-symmetry breaking term. This term emerged as it was found to be a necessary addition to $f_{7/2}$ protons coupled to $J = 2$ in reproducing the experimental MED data in that region [75], where a value of +100 keV was added to the $J = 2$ matrix elements. The same result could be replicated when using -100 keV for $J = 0$, meaning that this contribution is relative to $J = 0/2$. MED of the ^{67}Se/^{67}Ar mirror pair were found to show good agreement with the JUN45 interaction [55] in the fpg space without the need for this term, whilst a value of +300 keV at $J = 0$ showed improved MED agreement in $A = 66$ [76]. The origin of this phenomenon is still not entirely understood and the question still remains as to this effect persists in the higher mass regions. The magnitude and sign of this term and whether it is simply a repercussion of a limited model space remains a topic of debate.

2.6 Nucleon-Knockout Reactions

Nucleon-knockout reactions are direct reactions, meaning that there is no intermediate stage between the initial and final products, which cannot be said for other reaction mechanisms such as fusion-evaporation reactions. Knockout reactions are achieved through medium-heavy beams typically at energies ranging from 40 MeV$-$1 GeV/nucleon [77] on a light target, most commonly ^{9}Be or ^{12}C. Single-nucleon knockout reactions typically have large cross sections

and are favourable in studies of low-spin states given the limited number of states that can be populated [78]. The cross section, σ, of a one-nucleon removal is defined as [77]:

$$\sigma = \sum_{nlj} \left[\frac{A}{A-1}\right]^N C^2S(J^\pi, nlj)\sigma_{sp}(nlj, S_N^{eff}). \tag{2.31}$$

Here A is the mass of the unreacted nucleus, with $\left[\frac{A}{A-1}\right]^N$ representing an A-dependent centre of mass correction term. The C^2S term represents the spectroscopic factor, whist σ_{sp} represents the single-particle cross section and n, ℓ and j correspond to the quantum state of the removed nucleon. The S_N^{eff} dependence of the single-particle cross section denotes the effective separation energy of a nucleon. The spectroscopic factor quantifies the nature and occupancy of the single-particle orbits of a nucleus. Therefore C^2S contains the information beyond the knockout reaction mechanism. In the case of this study, a one-neutron knockout cross section of $\sim$ 10 mb was measured for the ^{81}Zr - 1n reaction to populate bound states in ^{80}Zr.

Two-nucleon removal reactions in contrast are less understood. In comparison to one-nucleon knockout reactions, the cross sections are significantly smaller ($\sim$0.1 mb for $-$2n from ^{80}Y). Since the configurations the two removed nucleons both contribute to the final populated states, this yields a less clear association between experimental data and the underlying nuclear structure. Since the angular momentum generated is generated from the vector coupling of the holes created in the single-particle levels, two-nucleon knockout reactions therefore have a tendency to populate higher spin states than single-nucleon removal reactions.

Given that lifetime measurements performed in this investigation require sufficient statistics of $2^+ \rightarrow 0^+$ decays to resolve the γ-ray lineshape, the low number of states that can be populated and the high cross sections make these types of reactions favourable. These large reaction cross sections are essential when producing neutron-deficient $N \approx Z$ nuclei close to the proton dripline. An example of the possible state population of ^{80}Zr from the one-neutron knockout from the $(\frac{3}{2}^-)$ ground state of ^{81}Zr [79] is shown in Table 2.2. There are three possible orbitals from which a neutron can be removed from to directly populate the 2^+ state of ^{80}Zr. In contrast, there are no possible one-neutron knockout reactions to directly populate the 6^+ state. Given the predicted large deformations in this mass region

it is probable that the $d_{5/2}$ orbital will also play a role, providing direct access to additional negative parity states. The other one-neutron knockout reaction investigated, being ^{79}Sr to ^{78}Sr (where ^{78}Sr was used to confirm the validity of the other measurements), will also have the same possible populated states listed in Table 2.2 given that ^{79}Sr also possesses a $\frac{3}{2}^{(-)}$ ground state [80].

Table 2.2: The possible state population for ^{80}Zr from one-neutron knockout from the $(\frac{3}{2}^{-})$ ground-state of ^{81}Zr. Note that this is also identical for ^{78}Sr (one-neutron knockout from ^{79}Sr) since ^{79}Sr also possesses a $\frac{3}{2}^{(-)}$ ground state.

Populated States	**1n Knockout from Orbital(s)**
0^+	$p_{3/2}$
1^+, 2^+	$f_{5/2}$, $p_{3/2}$, $p_{1/2}$
3^+	$f_{5/2}$, $p_{3/2}$
4^+	$f_{5/2}$
5^+, 6^+	None
3^-, 4^-, 5^-, 6^-	$g_{9/2}$
1^-, 2^-, 3^-, 4^-	$d_{5/2}$

Chapter 3

Experimental Details

3.1 Overview

The primary aim of this experiment was to measure the lifetimes of the $N = Z$ ^{76}Sr, ^{78}Y and ^{80}Zr, the latter two being the heaviest $N = Z$ systems where such measurements have been made to date. ^{78}Y and ^{80}Zr represent the $28 < N = Z < 50$ mid-shell point and the first $N = Z$ nucleus beyond the mid shell, respectively. The secondary aim was to was to measure the MED of the ^{79}Zr/^{79}Y mirror pair, the heaviest nuclei where such measurements have been taken.

The experiment to investigate these neutron-deficient nuclei in the $A = 80$ region was performed at the National Superconducting Cyclotron Laboratory (NSCL) at Michigan State University (MSU) [81] in April 2017. It was the first to utilise the ^{92}Mo primary beam (developed in December 2016) at an energy of ∼140 MeV/nucleon. This was subsequently fragmented on a thick 802 mg/cm^2 ^{9}Be target into secondary beams which are dispersed via the A1900 separator [82] into a cocktail consisting predominantly of ^{81}Zr, ^{80}Y, ^{79}Sr, ^{78}Rb, ^{77}Kr and ^{76}Br (see Fig. 3.1 and Table 3.1 for more details). The cocktail beam was then dispersed by the four dipole magnets in the A1900 separator. Adjustable slits and a degrader wedge are then utilised to block and disperse the array of secondary beams, respectively, before impinging on the 188 mg/cm^2 ^{9}Be reaction target at the A1900 focal plane.

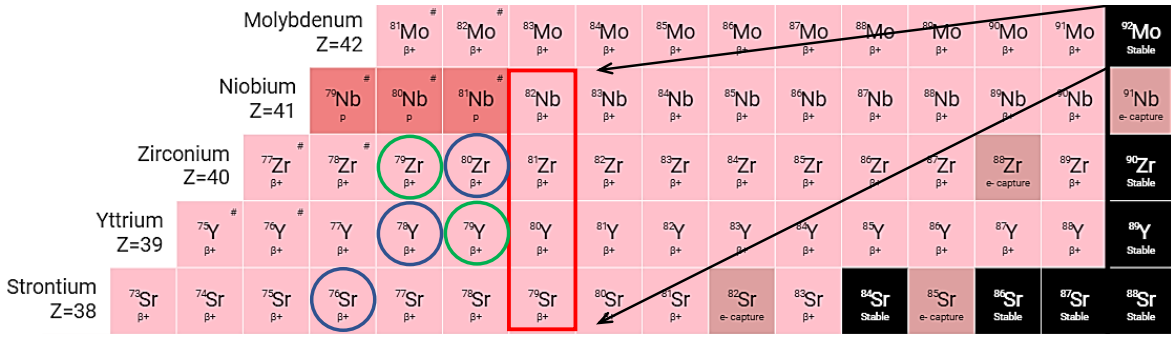

Figure 3.1: The ^{92}Mo primary beam (top right) is fragmented into the cocktail beam outlined in red at the entrance to the A1900 separator. The $N = Z$ nuclei of interest (circled in blue) and the $A = 79$ mirror pair (circled in green) are then populated from the cocktail beam via nucleon-knockout reactions from the ^{81}Zr and ^{80}Y components of the cocktail beam. Adapted from [83].

The main nuclei of interest: ^{80}Zr, ^{79}Zr, ^{79}Y, ^{78}Y, ^{78}Sr and ^{76}Sr were populated through nucleon-knockout reactions from the ^{81}Zr, ^{79}Sr and ^{80}Y secondary beams. The deexcitation γ rays from the reaction products at the 188 mg/cm^2-thick secondary target position were detected with the HPGe detector array GRETINA [84]. Following reactions within the target, the resulting particles then traverse the S800 spectrograph [85] which is utilised to resolve and identify reaction products through energy loss and time of flight measurements. The S800 spectrograph also provides invaluable information about recoil angles and momentum distributions of the reaction products, providing the capability of precise event-by-event γ-ray Doppler corrections. The lifetimes of the 2^+ states of the $N = Z$ being investigated are of the order of a few hundred picoseconds, corresponding to a position a few centimeters downstream of the target position at the time of decay. As a consequence of this, low-energy tails arise through the γ-ray Doppler correction process due to the assumption of the nucleus decaying at the target position. These low-energy tails can be simulated through a GEANT4 [86] simulation incorporating the GRETINA and S800 geometries [87], where the lifetimes of the decaying states are varied, providing an accurate probe of their lifetimes through comparison with experimental spectra. Throughout the duration of the experiment ~130 hours of data were obtained separated into 212 runs.

This chapter will describe in further detail the constituents of the experimental setup at NSCL and detail step-by-step how the measurements were taken from beam production through to γ-ray detection and identification of reaction products.

3.2 SuSI and K500/K1200 Cyclotrons

The Superconducting Source for Ions (SuSI) is a Electron Cyclotron Resonance (ECR) source at NSCL that has been used to produce primary beams ranging from ^{16}O to ^{209}Bi [88, 89] and in this instance was used to produce the ^{92}Mo primary beam. The ECR source is connected to the Coupled Cyclotron Facility consisting of two cyclotrons: K500 and subsequently the K1200 [90], the K500 being the world's first superconducting cyclotron. The source produces a beam of positive ions which is then injected into the K500 cyclotron, accelerating the beam to typical energies of 8−12 MeV/u. The beam is then transported through an rf bunching system, used to control the bunch length between the two cyclotrons, and is injected radially into the K1200 cyclotron where the beam is further accelerated up to an energy of ∼140 MeV/u (see Fig. 3.2). Here the beam is stripped with a carbon foil, with ∼85% of ions being in the fully-stripped $Q = Z$ state. The beam is then shaped through the use of several quadrupole and sextupole magnets prior to impinging upon the 802 mg/cm^2 ^{9}Be production target located at the entrance to the A1900 separator. Here the ^{92}Mo primary beam is fragmented into a vast cocktail of lighter secondary beams. A large fraction of these are removed in the separation process in the A1900 separator, resulting in final transmitted cocktail beam consisting of ^{81}Zr, ^{80}Y, ^{79}Sr etc. which are detailed in Table 3.1.

3.3 A1900 Separator

The purpose of the A1900 separator [82] is to disperse the variety of secondary beams and any unreacted ^{92}Mo primary beam produced following fragmentation of the primary beam at the ^{9}Be production target. This allows the level of undesired contaminants to be reduced through the use of wedges and slits before shaping the beam prior to impinging the secondary 188 mg/cm^2-thick ^{9}Be reaction target located at the entrance to the S800 spectrograph. The separator itself consists of a series of four 45° steering dipole magnets, 24 focusing quadrupole magnets in addition to other sextupole and octupole magnets in order to correct for higher order abberations. The dipole magnets are used to disperse the beams within a given plane while the quadrupole magnets are used to focus the beam radially when traversing the length of the spectrometer. Initial separation of the cocktail beam produced at the production target is achieved though varying the magnetic rigidity, Bρ, of the first two dipole magnets of the

separator, where B is the strength of the magnetic field and ρ is the bending radius of the dipole magnets. This disperses the initial beam in accordance with:

$$B\rho = \frac{Mv}{Q}\gamma = \frac{Am_u c}{Ze}\beta\gamma, \tag{3.1}$$

where M is the mass of the particle, v is its velocity and Q is its charge, $\gamma = 1/\sqrt{1-\beta^2}$, m_u is the unified atomic mass unit, e is the elementary charge and A and Z are the mass and atomic numbers of the particle, respectively. Therefore, this corresponds to dispersion proportional to the A/Q ratio of the beams, including $N = Z$ nuclei. This allows the Bρ of the dipole magnets to be specifically tuned to allow the maximum amount of the desired beams to enter the separator, whilst simultaneously removing large portions of contaminants/unreacted beam before further separation takes place.

This initial separation is proceeded by a set of slits located at image 2 (see Fig. 3.2) which can be varied in width, allowing one to further block any undesired beams following dispersion and to adjust the momentum acceptance of the cocktail beam, which in this experiment was set to 0.5%. Isotopic selection is then further improved by passing the ion beam through an achromatic 1050 mg/cm^2-thick Al wedge. Particles with the same Bρ but a different Z will emerge from the wedge with different momenta [82]. Following this, the emerging, now-filtered beam, is passed through the remaining two dipole magnets and a final slit where further selection takes place prior to the desired cocktail beam impinging on the secondary 188 mg/cm^2-thick ^{9}Be reaction target at the S800 target position.

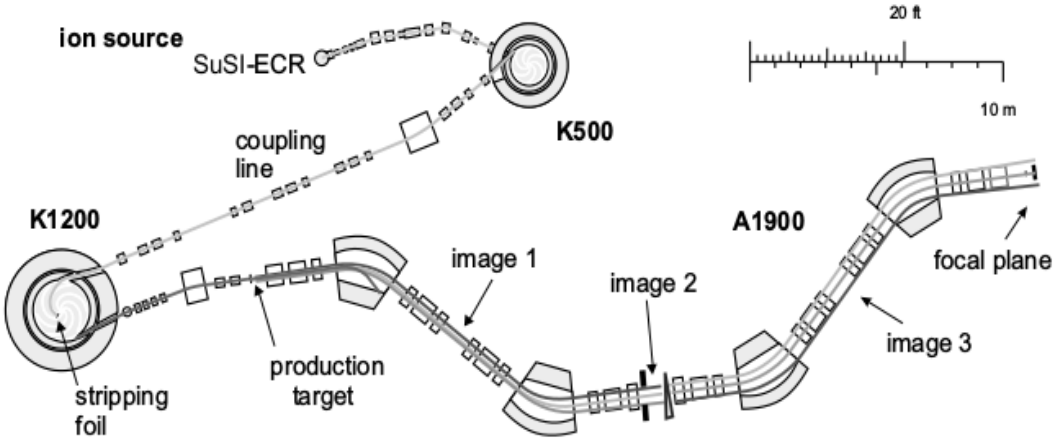

Figure 3.2: SuSI, the K500/K1200 cyclotrons and the A1900 separator at NSCL, MSU. After the primary ^{92}Mo beam is produced at SuSI it is then accelerated through the K500 and K1200 cyclotrons, finally reaching an energy of ∼140MeV/u before being focused by a quadrupole magnet prior to fragmentation on the thick ^{9}Be production target. A series of four dipole magnets, focusing quadrupoles, wedges and slits then disperse and block certain secondary beams allowing for the number of contaminants to be reduced before reacting with the secondary 188 mg/cm^2 ^{9}Be target located at the end of the separator. Taken from [82].

3.3.1 Time of Flight Scintillators

The extended focal plane (XFP) and object (OBJ) scintillators are located near the end of the A1900 separator (separated by ∼30 m). These are located upstream of the secondary ^{9}Be reaction target position, which is surrounded by the GRETINA detector array (see Fig. 3.4). These scintillators are ideal for time of flight (ToF) measurements given their excellent timing resolutions due to the fast decays of the light pulses created upon a particle interacting with the scintillators. Timing signals with a FWHM of the order of 100 ps have been achieved

Table 3.1: The constituents of the cocktail beam reaching the focal plane of the A1900 separator produced through fragmentation of the ∼ 140 MeV/u ^{92}Mo primary beam on the thick 802 mg/cm^2 production target at the entrance to the A1900.

Secondary Beam	Z	**Fraction of Secondary Cocktail Beam (%)**
^{81}Zr	40	0.87
^{80}Y	39	8.47
^{79}Sr	38	26.78
^{78}Rb	37	43.28
^{77}Kr	36	18.91
^{76}Br	35	1.36

[91] with both scintillators capable of withstanding rates up to 1 MHz [92]. The ToF of particles between the XFP/OBJ scintillators and the E1 scintillator located at the end of the focal plane in the S800 spectrograph can be used to identify different incoming beams from the A1900 separator allowing one to subsequently gate on a selected incoming beam in order to examine the corresponding reaction products in the S800 spectrograph (see Fig. 3.3). Furthermore, the OBJ to E1 scintillator ToF information is used in conjunction with the energy loss measurements from the ionisation chamber (corresponding to the A/Q of the particle; see Chapter 3.5.3) within the S800 spectrograph to resolve reaction products produced from a specific incoming beam. Three different electronic sources of ToF information are available for each of the scintillators, where the Mesytec MTDC was used in this case.

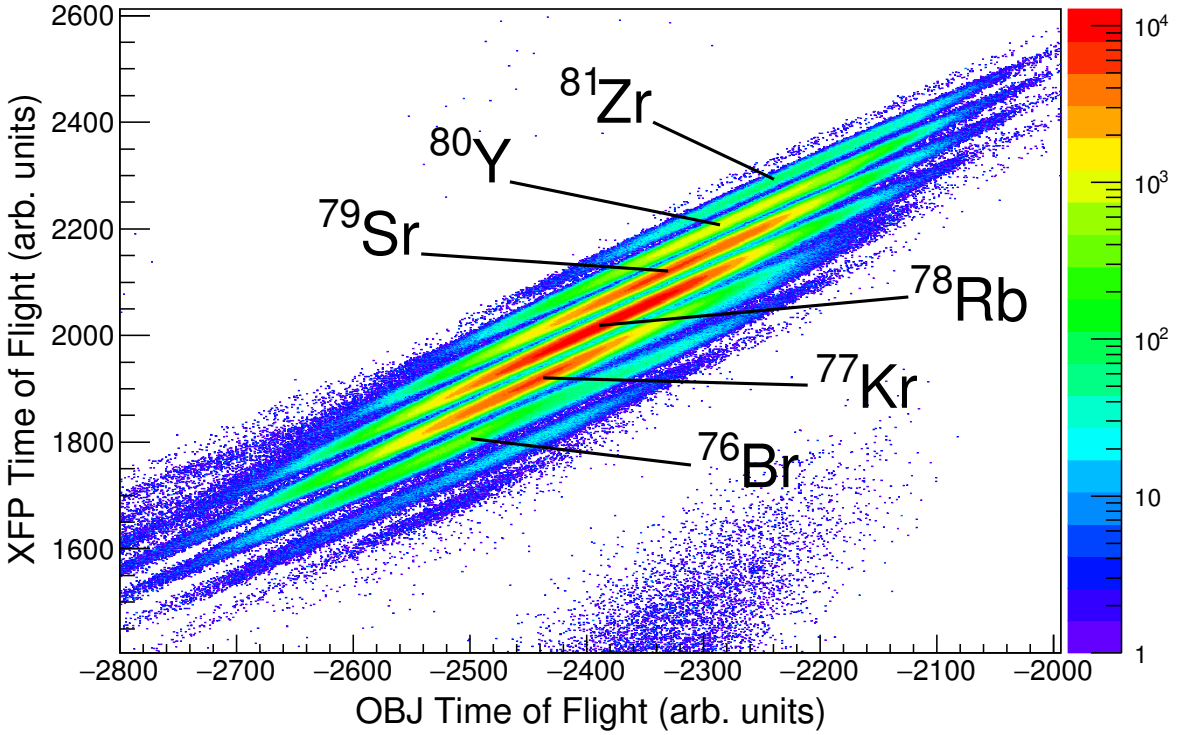

Figure 3.3: The incoming beams impinging upon the 188 mg/cm^2-thick ^{9}Be reaction target can be identified through the extended focal plane (XFP − E1) and object (OBJ − E1) scintillator time of flights relative to the E1 scintillator in the S800 spectrograph focal plane. An additional gate of requiring a γ-ray event in GRETINA is applied to eliminate any unreacted beam events from the plot. The ToF values have arbitrary units as positional and angular corrections have been applied to resolve the different secondary beams.

3.4 GRETINA

The Gamma-Ray Energy Tracking In-beam Nuclear Array (GRETINA) is a High-Purity Germanium (HPGe) detector array, typically ranging from seven to ten module configurations. This experiment used a ten module configuration with four mounted at 58° and six mounted at 90° relative to the beam line, covering laboratory angles ranging from 37° to 116°. The array currently covers a solid angle of $\sim 1\pi$, with plans to eventually increase this to a full 4π array named Gamma Ray Energy Tracking Array (GRETA), consisting of 30 modules [93]. This 1π coverage at the forward angles is the optimum ten module configuration in the case of fast ($\beta = \frac{v}{c} \approx 0.3$) isotope beams due to the forward focusing effect of emitted γ rays as a consequence of the Lorentz boost. In this experiment GRETINA was used to detect deexcitation γ rays emitted from reaction products following the incoming secondary cocktail beam reacting within the ^{9}Be reaction target (see Fig. 3.4). GRETINA has several attractive features for this kind of analysis such as the capability to perform γ-ray addback and tracking. As discussed in further detail in Chapters 3.4.1 and 3.4.2, for this work cluster addback was implemented to the dataset and γ-ray tracking was not used as its effects were negligible.

Figure 3.4: The ten HPGe detector modules of the GRETINA array directed at the secondary 188 mg/cm^2 ^{9}Be target located within the six inch diameter beam line. The distance between the endcap of each detector and the target position is around 18 cm.

Each detector module of GRETINA consists of four crystals, each divided into 36 segments allowing for the spatial coordinates of each γ-ray interaction along with the deposited energy to be recorded [94]. This allows the scattering paths of each γ-ray to be tracked through the tracking algorithms in accordance with the expected scattering angle from Compton scattering. This tracking results in peak-to-total performances comparable to that of Compton-shielded HPGe detector systems [84, 95]. Likewise, this tracking is capable of resolving the first point of γ-ray interaction to a level of $\sim$2 mm [84] enabling precise Doppler corrections, vital for lifetime measurements deduced through the lineshape methodology. By determining the point of first interaction of each γ-ray and calculating the corresponding point of decay and applying this to Doppler corrections (see Eq. 4.5), resolutions of 1.1% have been achieved with GRETINA at a beam velocity of $\beta = 0.3722$ [84].

3.4.1 γ-ray Tracking

One of the main features of GRETINA which makes it attractive for lifetime measurements is γ-ray tracking. GRETINA and the Advanced GAmma-ray Tracking Array (AGATA) [96] are the first HPGe γ-ray detectors to utilise γ-ray tracking [84]. γ-ray tracking is a procedure whereby the paths of Compton-scattered γ rays can be tracked within detector module crystals and neighbouring crystals through the use of an algorithm, allowing the paths of Compton-scattered γ rays to be reconstructed.

Each GRETINA HPGe crystal is segmented into 6 slices, varying in thickness from 8, 14, 16, 18, 20 and 14 mm from the front of the crystal to the back. Each slice is then further segmented radially into six segments, resulting in a total of 36 segments per crystal (see Fig. 3.5). Each detector module consists of 37 channels, one for each segment and an additional channel corresponding to the module core. Liquid nitrogen is used to cool the germanium crystals to limit the effects of thermal excitations due to the small band gap of germanium of just 0.67 eV [97]. Through the use of signal decomposition at a sampling rate of 10 ns [84], subsegment position resolutions can be achieved with GRETINA with first-interaction point position resolutions of 2 mm being measured [94]. This is accomplished through comparison of the detector response signals with a set of simulated response signals known as a basis. These basis responses are simulated throughout the crystal, with an average spacing of 1 mm. The generated response signals in a segment and neighbouring segments

for a given γ-ray interaction are then compared with to set of basis signals to determine the most probable position of the event with subsegment precision.

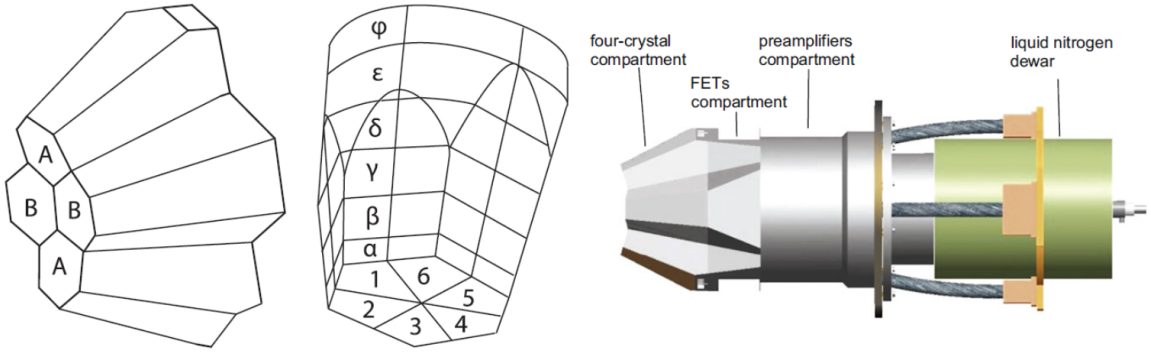

Figure 3.5: Each GRETINA HPGe module consists of four crystals, each segmented radially into six slices and then segmented into six slices along the length of the crystal, creating 36 segments in total. Each module has a corresponding preamplifier to amplify and extract signals from the detector and a liquid nitrogen dewar to limit the effects of thermal excitations within the crystals. Adapted from [94].

This subsegment interaction position precision allows for a value known as Figure-of-Merit (FoM) to be assigned to measure the agreement between the position of a series of scattering events within the GRETINA crystals in accordance with the Compton-scattering equation:

$$E'_{\gamma} = \frac{0.511}{1 + \frac{0.511}{E_{\gamma}} - \cos(\theta_c)}, \tag{3.2}$$

where E'_{γ} and E_{γ} denote the scattered and unscattered γ-ray energies in MeV, respectively, and θ_c corresponds to the angle of the scattering event. Likewise, the differential cross section ($d\sigma$) of a γ-ray Compton scattering to within a given solid angle ($d\Omega$) is given by the Klein-Nishina formula [98]:

$$\frac{d\sigma}{d\Omega} = Zr_e^2 \left[\frac{1}{1 + (h\nu/m_e c^2)(1 - \cos\theta_c)} \right] \times \left[1 + \frac{(h\nu/m_e c^2)^2 (1 - \cos\theta_c)^2}{(1 + \cos^2\theta_c)[1 + (h\nu/m_e c^2)(1 - \cos\theta_c)]} \right], \tag{3.3}$$

where r_e and m_e are the radius and mass of the electron, respectively. A tracking algorithm [99] is employed to determine the likelihood of a collection of recorded γ-ray energies being a genuine Compton-scattering sequence or uncorrelated events. For all possible Compton-

scattered interaction sequences a FoM value is assigned from [84]:

$$\text{FoM} = \sum \frac{(\cos\theta^i_{en} - \cos\theta^i_{vec})^2}{w_i}, \tag{3.4}$$

where θ_{vec} denotes the geometric angle that uses the coordinates for the interaction points for a given event i, θ_{en} is the same angle but calculated using Eq. 3.2 while using the measured energy depositions and w_i is a weighting factor, usually taken as the total number of scattering interactions in a sequence. Therefore, when there is good agreement between the measured scattering angles for a sequence of events and the theoretical angles from the Compton-scattering equation then $(\cos\theta^i_{en} - \cos\theta^i_{vec})$ will be small, resulting in a low FoM. After all possible scattering permutations have been considered, the sequence that produces the lowest FoM is considered the most probable scattering sequence and is used for Doppler corrections, where the derived first γ-ray interaction point is used to calculate θ in Eq. 4.5. A FoM of >1 is assumed to correspond to incorrect clustering, whereas photoelectric effect events with one interaction yield a FoM of 0.

The effects of assuming the first interaction point is the point of the highest energy deposition rather than using the interaction point determined through the γ-ray tracking FoM decomposition process with GRETINA were compared in Ref. [84]. Here it was concluded that for γ-ray energies ranging from 275 keV (^{19}Ne) up to 6.1 MeV (^{16}O) using the highest energy deposition point for Doppler reconstruction yielded improved peaks shapes and smaller full-width half-maximum values, with this effect being more prevalent at higher energies. For this reason in this analysis the interaction point with the highest detected energy by GRETINA was assumed to be the first interaction point in regards to any γ-ray Doppler corrections performed. Since this investigation was predominantly concerned with low-energy (typically $<$ 1 MeV) deexcitation γ rays from low-spin states in $N = Z$ nuclei, such as $2^+ \rightarrow 0^+$ and $4^+ \rightarrow 2^+$ decays, with a maximum multiplicity of 2, the advantages of the tracking feature of GRETINA were negligible when compared to simply using the highest energy event as the initial γ-ray interaction position.

3.4.2 Add-back of γ rays

GRETINA also possesses the capability to perform add-back, a procedure whereby algorithms are employed to distinguish Compton-scattered events across different detector crystals, which

are then subsequently summed to give the initial energy of the γ ray prior to Compton scattering, vastly reducing the Compton background. There are different add-back methods that can be utilised with GRETINA:

1. **Cluster Add-back**

   γ-ray events are only considered as potential candidates for the add-back summing procedure if they occur with a given cluster defined by an opening angle (usually between $10-20^{\circ}$).

2. **Calorimeter Add-back**

   All γ-ray events across the whole detector array within a time window are summed.

The effects of each add-back method are compared for a stationary ^{60}Co calibration source below in Fig. 3.6. As discussed above in regards to the γ-ray tracking algorithms, a vast majority of the γ-ray deexcitation transitions investigated in this analysis are of low multiplicity (typically E2 transitions) and low energy (< 1 MeV) given the nature of nucleon-knockout reactions to populate low-spin states. Therefore, the effects of add-back are not as paramount when compared to analysis of higher energy transitions, where the lower energy counts of γ-ray spectra are typically dominated by Compton-scattered events. For this reason the cluster add-back method was implemented for the data set. Although the calorimeter method produces comparatively improved signal-to-noise ratios, this also results in a large number of incorrectly summed events. Given the low statistics obtained for some of the nuclei of interest, in particular ^{78}Y, ^{76}Sr and ^{79}Zr, it was decided that conserving sufficient statistics for the peaks of interest was of greater importance than the reduced Compton background. Therefore the cluster add-back algorithm was implemented for any analysis.

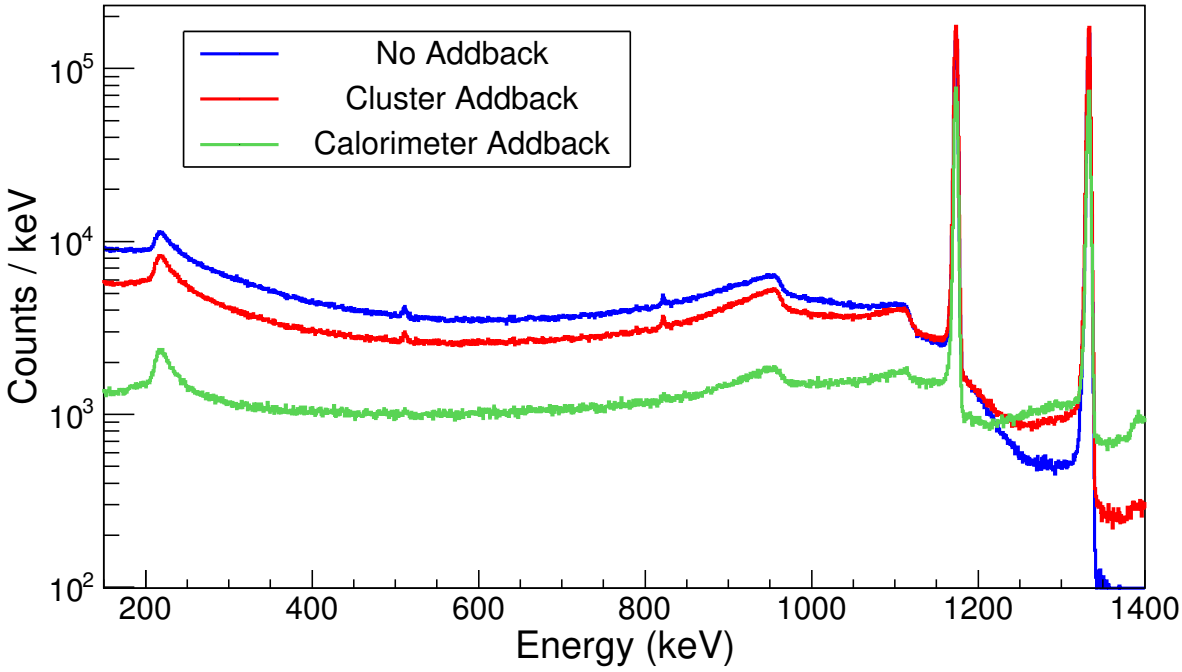

Figure 3.6: A comparison of the cluster (red) and calorimeter (green) add-back methods of GRETINA with no add-back (blue) implemented for the same ^{60}Co calibration source γ-ray run taken at the start of the experiment.

3.4.3 Absolute Efficiency Measurements

Absolute efficiencies of 6.08(4)%, 5.49(5)% and 5.07(5)% have been achieved by GRETINA for 898, 1173 and 1332 keV γ rays, respectively, whilst consisting of eight HPGe modules [84]. With the current ten module configuration this is further increased to efficiencies shown in Fig. 3.7. The absolute efficiency, ϵ_{abs}, was calculated using the recorded singles γ-ray spectra from ^{152}Eu, ^{133}Ba and ^{60}Co calibration sources and well documented decay intensities [100] through:

$$\epsilon_{abs} = \frac{N}{A \times t_{live} \times B}, \tag{3.5}$$

where N is the number of counts detected for a given decay, A is the source activity at the time of the measurement, t_{live} is the live time of the run (raw time minus the dead time) and B is the branching ratio of the decay. The dead time was accurately determined through the scaler data taken throughout the course of the experiment. The source activities at the time of the measurements were calculated from the known activities at the time of the source

production, A_0, and the known mean lifetime of the source, τ:

$$A = A_0 \exp(-\lambda t) = A_0 \exp\left(-\frac{t}{\tau}\right), \tag{3.6}$$

where $\lambda = \ln 2/t_{1/2}$ and t represents the time elapsed between the production of the source and the moment the measurement was taken. The uncertainty of ϵ_{abs} for each decay was derived by combining the uncertainties of N, A and B in quadrature:

$$\Delta\epsilon_{abs} = \epsilon_{abs}\sqrt{\left(\frac{\Delta A}{A}\right)^2 + \left(\frac{\Delta N}{N}\right)^2 + \left(\frac{\Delta B}{B}\right)^2}. \tag{3.7}$$

The uncertainty of t_{live} is assumed to be negligible given the high precision of the scaler data.

The absolute efficiency curves without add-back and with cluster add-back implemented are shown below in Fig. 3.7. The efficiency is enhanced with cluster add-back at all γ-ray energies $\gtrsim$ 256 keV. This value is a result of the most likely energy a fully back-scattered ($\theta = 180°$) γ ray will have, which can be derived from Eq. 3.2 as $E_\gamma \to \infty$, resulting in $\frac{m_e c^2}{2}$ which is equal to 256 keV. Therefore γ rays in the $\sim$ 256-keV energy region are the most likely to be part of a scattering sequence and are therefore summed through the add-back algorithm to the higher, unscattered γ-ray energy. This yields lower efficiencies $\sim$ 256 keV when add-back is implemented.

The relativistic recoil velocities observed in this experiment of $\beta \approx 0.3$ mean that the implications of the Lorentz boost effect on measured in-beam efficiencies can not be neglected. At these velocities the positions in space of the detector modules change in the reference frame of the nucleus, resulting in the spatial coordinates of modules moving in front of the travelling particle. This effect is known as the *'headlight effect'* as from the particle's reference frame it appears as if the γ rays are focused forwards, similar to a headlight. The measured absolute efficiencies in Fig. 3.7 were adjusted to account for this effect through simulating decays across and energy range of $0-2$ MeV for both a stationary and in-beam γ-ray source with GRETINA in the GEANT4 simulation package [86]. The ratios of the efficiencies whilst stationary and travelling in beam at $\beta = 0.3$ (see Fig. 3.8) were then used to adjust the efficiencies to their Lorentz-boost corrected values.

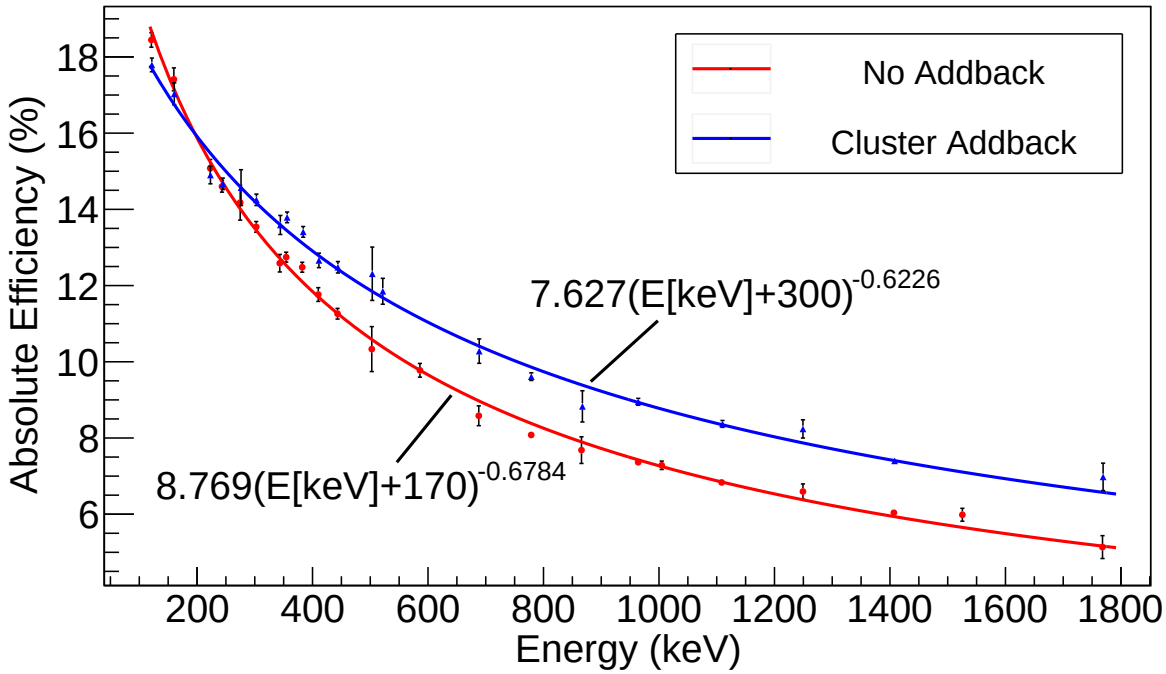

Figure 3.7: The fits of the singles absolute efficiency of GRETINA in the ten module configuration without add-back (red) and with cluster add-back implemented (blue).

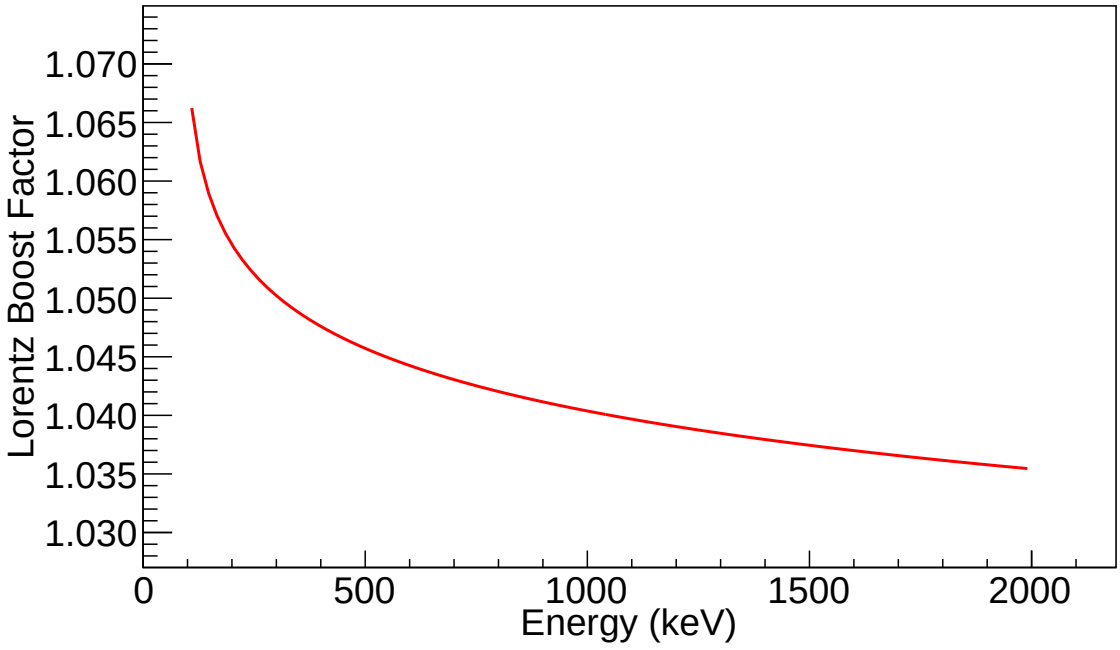

Figure 3.8: The factor by which the efficiency is increased by due to the Lorentz boost at $\beta = 0.3$ with GRETINA in the ten module configuration. This was achieved through simulating both a stationary and in-beam source and examining the difference in the peak-count ratios.

3.5 S800 Spectrograph

The S800 spectrograph [85] is a large acceptance, 3-storey, 250 ton, vertical spectrograph located downstream of the secondary 188 mg/cm^2-thick ^{9}Be reaction target position, the latter of which is surrounded by the HPGe array GRETINA. The S800 is installed in the S3 vault and is capable of rotating from 0° to 60° in the horizontal plane, covering a solid angle of 20 msr and with a maximum momentum acceptance of 5% [85]. The spectrograph itself consists of a quadrupole doublet located at the end of the target chamber which focuses outgoing reaction products in both the dispersive (x) and non-dispersive (y) planes before traversing two dipole magnets. Each of these dipole magnets can reach a maximum magnetic rigidity, Bρ, of 5 Tm [92], corresponding to 800 MeV protons, but were typically at B$\rho \approx$ 2 Tm throughout this experiment. This is then followed by two Cathode Readout Drift Chambers (CRDCs), an ionisation chamber and a series of three scintillators E1, 2, and 3 (see Fig. 3.9). The purpose of the spectrograph is to distinguish the different reaction products produced at the reaction target and to associate the different reaction products produced with the γ rays detected by GRETINA as well as provide information about the reacted beams to further optimise γ-ray Doppler corrections. Particle identification is achieved by tracking the ToF of each particle from the OBJ scintillator with respect to the E1 scintillator at the S800 focal plane (see Fig. 3.9) in conjunction with energy loss measurements from the ionisation chamber. The positional information from the CRDCs used to calculate the dispersive and non-dispersive beam angles and positions at the S800 focal plane can also be used to extrapolate the path of reacted nuclei back to the target position through the use of an inverse map (see Chapter 3.5.2). This provides valuable information such as the recoil angles and positions relative to the centre of the reaction target, enabling more precise event-by-event Doppler corrections. The E1 scintillator located at the end of the spectrograph is also used as the main trigger for the data acquisition (DAQ) system and to deduce the non-dispersive position of the recoiling beams in each CRDC.

The S800 analysis line is capable of running in two different modes: focused mode and dispersion-matching mode. The most common mode: focused mode, which was used in this experiment, utilises an achromatic beam i.e. the beam is focused upon the target and the focal plane displays the intrinsic momentum width of the beam folded with the resulting momentum change from reacting within the target. Therefore, the momentum resolution

of the S800 through this method corresponds to the momentum acceptance of the A1900 separator. The method typically allows larger momentum acceptances of ±2% [85] and is usually used in experiments where a precise momentum resolution is not vital as the energy resolution is limited to ∼0.1%. In dispersion-matching mode the beam is also achromatic, where the beam this time is momentum-dispersed at the reaction target position with a dispersion of ∼10 cm/%. This limits the momentum acceptance to a more restrictive ± 0.5%, but enhances the momentum resolution to 0.02% for a 1 mm beam spot [85].

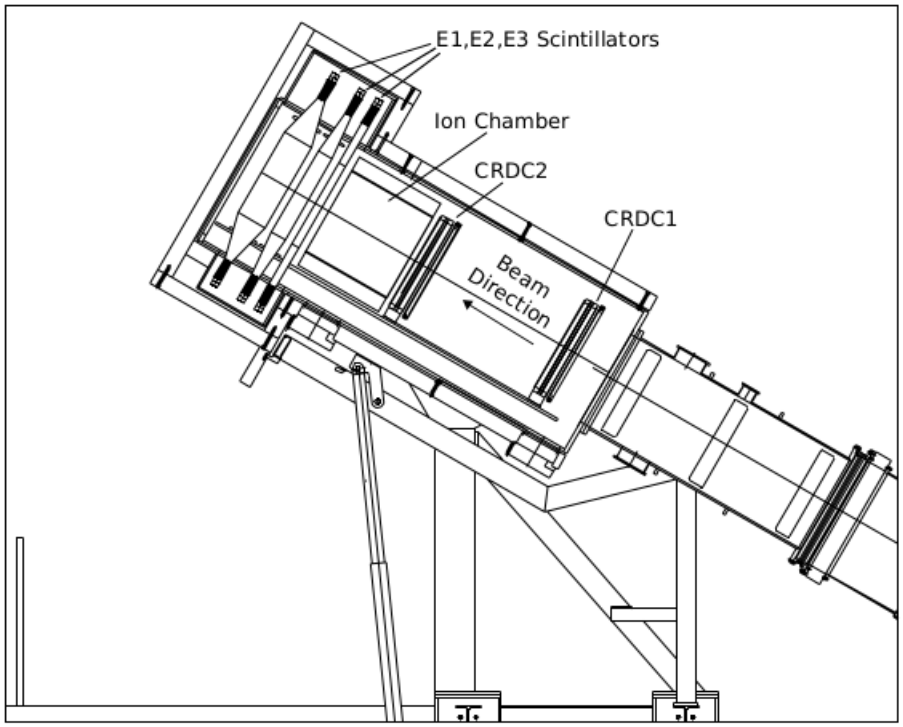

Figure 3.9: Schematic of the focal plane of the S800 spectrograph downstream of the two dipole magnets, containing both CRDCs, the ionisation chamber then followed by the E1, 2 and 3 scintillators. Taken from [91].

3.5.1 Cathode Readout Drift Chambers

The S800 spectrograph's focal plane includes two Cathode Readout Drift Chambers (CRDCs), used to map the trajectory of reaction products following dispersion by the two dipole magnets. The two CRDCs are positioned approximately 1073 mm apart, both having a depth of 1.5 cm and an active area of 26 cm by 56 cm in the non-dispersive (y-plane) and dispersive planes (x-plane), respectively. They are filled with a gas mixture consisting of 80% CF_4 and

20% C_4H_{10} which has a typical pressure of 40 Torr. This particular gas mixture is chosen due to its low ageing characteristics and low avalanche spread due to photon mediation [91]. The nuclei passing through the CRDCs ionise the gas resulting in free electrons that drift towards an anode wire whilst under the influence of an induced electric field. This charge is collected at the anode which subsequently induces a positive charge across a series of 2.54 mm wide cathode pads. The position of the ionisation in the dispersive plane (x-plane) is deduced by fitting a Gaussian function to the charge distribution across the cathode pads (see Fig. 3.10). The y-position can be deduced by recording the drift time of the electrons (typically $0-20$ μs) to the anode wire with respect the the trigger signal at the E1 scintillator. Both CRDCs have a spatial resolution of less than 0.5 mm and a maximum rate of 5,000 counts per second before efficiency losses can be expected [92]. The dispersive angle at the S800 focal plane (a_{fp}) is calculated through the dispersive (x) positions in each of the CRDCs:

$$a_{fp} = \tan^{-1}\left(\frac{x_2 - x_1}{d}\right), \tag{3.8}$$

where x_2 and x_1 are the recorded x positions at the second and first CRDC, respectively while d corresponds to the separation between the CRDCs of 1073 mm.

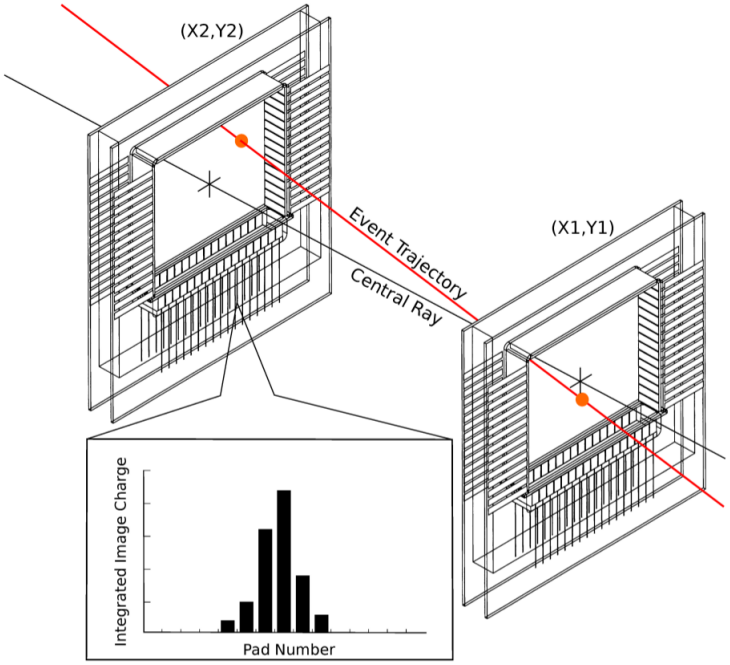

Figure 3.10: Schematic of the CRDCs located downstream of the second dipole magnet in the S800 spectrograph. Gas particles are ionised whilst passing through each CRDC, resulting in free electrons which drift towards the anode wire. This subsequently induces a positive charge across the cathode pads, from which a Gaussian function is fitted to determine the x-position of the particle. The y-position is determined from the electron drift time to the anode wire, relative to the trigger at the E1 scintillator located at the end of the S800 focal plane. Positional information from the CRDCs is used to correct for path length differences through the ionisation chamber as well as to calculate angles at the S800 focal plane used to determine recoil angles of the ions at the secondary target position through the use of the inverse map, allowing for more precise Doppler corrections. Taken from [101].

3.5.2 Particle Trajectory Reconstruction

A particle's trajectory through the spectrograph from the reaction target to the E1 scintillator can be accurately reconstructed using the COSY INFINITY code [102] which generates a transfer map $\mathbf{S}$, converting reacted beam information at the S800 focal plane to corresponding parameters at the reaction target position [103]. The inverse map is generated using the recorded x and y positions at each CRDC and the corresponding angular/positional information recorded at the S800 focal plane in conjunction with the precisely measured Bρ of the two dipole magnets at the entrance to the spectrograph. The inverse of this map $\mathbf{S}^{-1}$ can then be used to convert the beam data recorded at the S800 focal plane to beam properties

at the target position on an event-by-event basis:

$$\begin{pmatrix} a_{ta} \\ y_{ta} \\ b_{ta} \\ d_{ta} \end{pmatrix} = \mathbf{S^{-1}} \begin{pmatrix} x_{fp} \\ a_{fp} \\ y_{fp} \\ b_{fp} \end{pmatrix}, \tag{3.9}$$

where a and b denote the dispersive and non-dispersive angles, respectively, y denotes the y-position of the particle and d denotes the energy of the beam at the target position. The subscript ta and fp are used to distinguish between these values at the target position and S800 focal plane, respectively. The x-position at the the target (x_{ta}) is assumed to be 0 in order to reduce the number of parameters used to extrapolate the particle's trajectory, whereby the uncertainty of this parameter is included within the energy resolution of the S800 spectrograph.

Inverse maps can be produced via the MSU inverse map server [104] where the corresponding inverse map is calculated from the provided mass and charge of the particle of interest and recorded currents supplied to the dipole and quadrupole doublet magnets at the time the data were taken. This inverse map is then included in the sorting process for each run of the experiment to accurately reconstruct recoil angles and positions event-by-event, providing the capability of precise event-by-event Doppler corrections. The inverse map is calculated to order five since this corresponds to a positional precision comparable to 0.5 mm [85]. Since the path of a given nucleus traversing the two dipole magnets is dependent upon the particle's mass and charge, a different inverse map is required for each nucleus. Likewise, if there is an adjustment of the Bρ of the dipole magnets during the experiment then a new inverse map is required.

Each of the deduced recoiling beam parameters are incorporated into the Doppler-correcting procedure, providing a significantly enhanced resolution when compared to Doppler-corrected spectra when assuming the recoiling particles to all have an identical β and to have all recoiled down the central beam axis. The effects of including the additional information provided by the inverse map are displayed below in Fig 3.11. The incorporation of these parameters in the Doppler-correction procedure is discussed in further detail in Chapter 4.4.2.

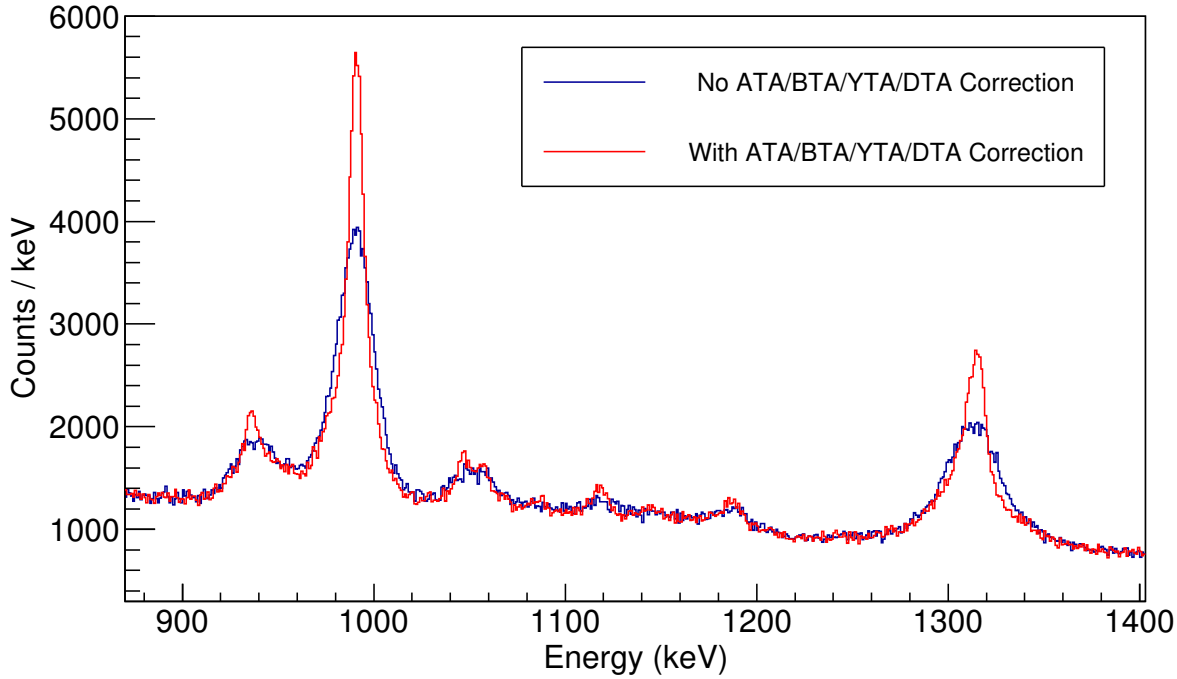

Figure 3.11: A comparison of the Doppler corrected γ-ray spectrum for ^{64}Zn, populated from the ^{78}Rb secondary beam, with (red) and without (blue) the inclusion of the additional data calculated through the inverse map (a_{ta}, b_{ta}, y_{ta} and d_{ta}) in the Doppler-correction process.

3.5.3 Ionisation Chamber

The ionisation chamber is located downstream of the second CRDC in the S800 focal plane (see Fig. 3.9). The purpose of the ionisation chamber is to identify the Z of the reacted beams from the secondary ^{9}Be target through energy-loss measurements. This can be used in conjunction with the ToF information from the OBJ to the E1 scintillator to produce a particle identification (PID) plot, allowing a specific reacted product to be selected from a given secondary beam reacting with the reaction target. The chamber itself it filled with P10 gas which consists of 90% argon and 10% methane, typically at a pressure of 300 Torr [91]. The chamber is divided into 16 segments, each with a narrow anode-cathode gap perpendicular to the direction of the beam. Upon the beam ionising the contained gas, the created electron/positive ion pair will drift to the nearest cathode and anode, respectively. The resulting signals from each of the 16 segments are then summed to give the total energy loss for that particular particle traversing the chamber. The average energy loss per unit length of the chamber $\langle dE/dx \rangle$ is deduced from the Bethe-Bloch equation (Eq. 3.10), which is proportional

to Z^2 of the particle:

$$-\left\langle \frac{dE}{dx} \right\rangle = \frac{4\pi n Z^2}{m_e c^2 \beta^2} \left(\frac{e^2}{4\pi\epsilon_0} \right)^2 \left[\ln\left(\frac{2m_e c^2 \beta^2}{I(1-\beta^2)} \right) - \beta^2 \right], \tag{3.10}$$

where Z is the atomic number of the nuclei, n is the electron density of the material, m_e is the mass of an electron, c is the speed of light, $\beta = \frac{v}{c}$, e is the charge of an electron, ϵ_0 is the permittivity of a vacuum and I is the average excitation energy of the material. The S800 spectrograph is capable of resolving nuclei up to $Z = 50$ [101]. Furthermore, the energy loss of a particle traversing the chamber is affected by the path length through the chamber. This is a consequence of particles with different A/Q values and different momenta have different trajectories through the spectrograph due to dispersion by the two dipole magnets at the entrance to the spectrograph. These changes in path length are accounted for with additional corrections to the ionisation chamber energy loss in relation to the ToF information between the OBJ and E1 scintillator (see Chapter 4.1 for more details).

3.6 Data Acquisition System

The data acquisition (DAQ) system of GRETINA and the S800 spectrograph is based on an event-by-event readout system. With GRETINA, each digitiser channel triggers and converts events individually whilst assigning a time stamp with a 10 ns granularity [84]. These triggers are then passed to the GRETINA Trigger Timing and Control logic where, if a certain global trigger condition is met, the locally-stored events are delivered to a global trigger via time-stamp comparison in a process called *'event validation'*. Each raw event from a detector crystal consists of digitised signals at a 100 MHz sampling rate including energies measured by the central contact and the 36 crystal segments. This information is fed to the GRETINA computing farm where the signal decomposition process takes place, allowing for subsegment position and energy deposition information (see chapter 3.4.1). GRETINA's computing resources are capable of processing 30,000 γ rays per second [84].

Event readout from the S800 spectrograph is initiated with a signal from the master trigger, signalling the conversion of all detector signals in the analogue to digital converters (ADC). This whole readout process takes around $120-200$ μs. At the start of data taking the timers for both GRETINA and the S800 are set to 0, allowing coincidence correlations between GRETINA and S800 data to be achieved through time-stamp comparison. Events

recorded by the S800 DAQ are transferred to the GRETINA event builder where events and merged and stored for analysis.

Chapter 4

Calibration and Corrections of Data

The unpacking of the raw data taken during the experiment and the calibration processes that follow were performed with the GrROOT [105] software package, built upon the ROOT framework [106]. GrROOT was used to unpack the raw data recorded at NSCL into ROOT format objects, which separates the data into ROOT *'trees'*, allowing one to inspect the correlated recorded values event-by-event.

This chapter will discuss the calibration procedures that were employed to ensure that any measurements taken by components of the A1900 separator, GRETINA and S800 spectrograph were reliable. The calibration parameters deduced in this chapter were applied to the experimental data through the use of a settings file which is included run-by-run in the unpacking stage of the raw data performed by GrROOT.

4.1 Scintillator Corrections

Additional corrections are necessary for the ToF data from the OBJ, XFP and E1 scintillators such that the ToF is constant over the dispersive angle (a_{fp}) and x-position (x_{fp}). This ToF correction is applied to the raw ToF data through Eq. 4.1:

$$\mathrm{ToF}_{corr} = \mathrm{ToF} + (A \times a_{fp}) + (B \times x_{fp}), \tag{4.1}$$

where ToF_{corr} denotes the corrected ToF and the parameters A and B are the correction values applied to the a_{fp} and x_{fp} data, respectively. These correction values, which essentially act

as *'tilting'* parameters, are adjusted until the ToF dependence on a_{fp}/x_{fp} is removed. The effects of these corrections can be seen in Fig. 4.1.

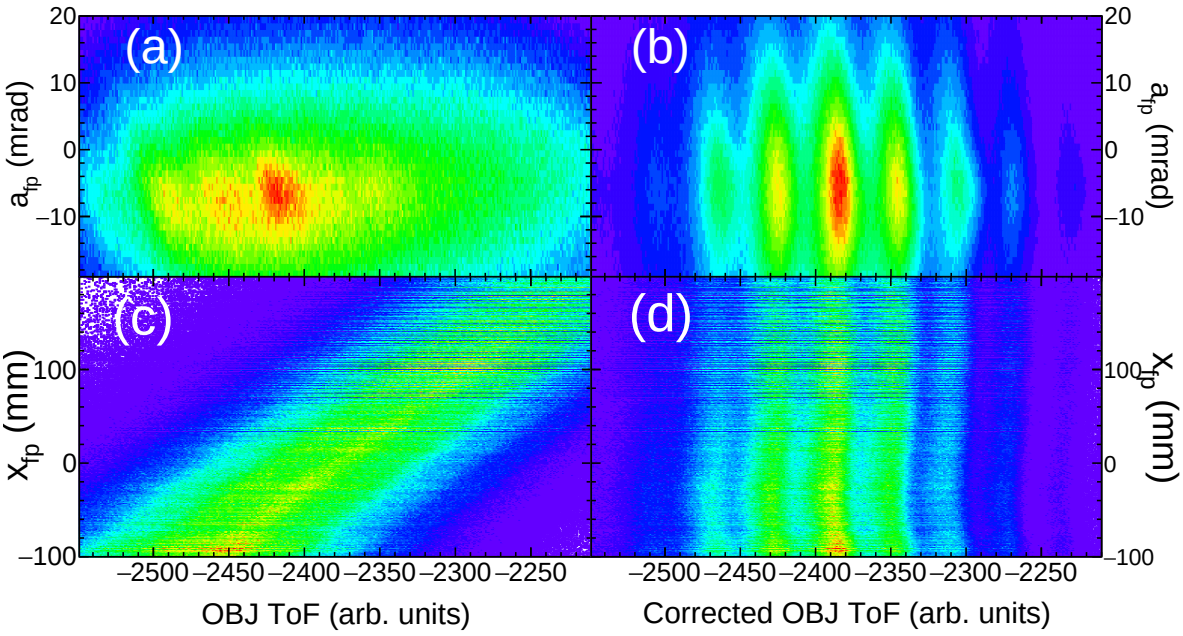

Figure 4.1: The effects of applying ToF corrections to the OBJ ToF relative to the x position (x_{fp}) and dispersive angle (a_{fp}) at the S800 focal plane. (a) and (c) display the correlations prior to the corrections being applied whilst (b) and (d) show the effects of applying the ToF corrections.

4.2 CRDC Calibrations

As discussed in Chapter 3.5.1, the CRDCs record the event-by-event x and y position of particles traversing the S800 spectrograph through detecting charges induced from the particles ionising the gas contained within the CRDC. The positional information from the CRDCs is crucial in providing precise recoil angles of reaction products to improve γ-ray Doppler corrections. For this reason a series of calibrations are necessary for the CRDCs to provide accurate measurements for use in the trajectory reconstruction procedure, which was discussed in Chapter 3.5.2.

4.2.1 CRDC Pad Gain Matching

As seen in Fig. 3.10, the x position of a particle traversing a CRDC is deduced through fitting a Gaussian function to the charge induced across the 224 cathode pads, which run either side of an anode wire on both sides of the x plane of the CRDC. The signal responses from pad to pad can vary greatly, meaning that a calibration was required to ensure that the signals are consistent across one another. This is achieved through an iterative gain-matching procedure. A particular incoming beam was selected and from there around five different reaction products were chosen, preferably those with the most statistics to reduce any statistical errors associated with the gain-matching procedure. Pad 64 was then chosen as the pad to which the other pads will be matched. For a given pad, Gaussian distributions are fitted to the pad amplitude signal measured for each of the given reaction products used for the calibration procedure. By then plotting the centroids of the Gaussian distributions obtained for each reaction product against the same centroids measured from pad 64, a gain and offset were extracted for each pad which, when applied, produced pad amplitudes consistent with pad 64. This was an iterative procedure, typically requiring two to three iterations before consistent pad amplitudes can be achieved. The effects of this calibration can be seen in Fig. 4.2 following two iterations.

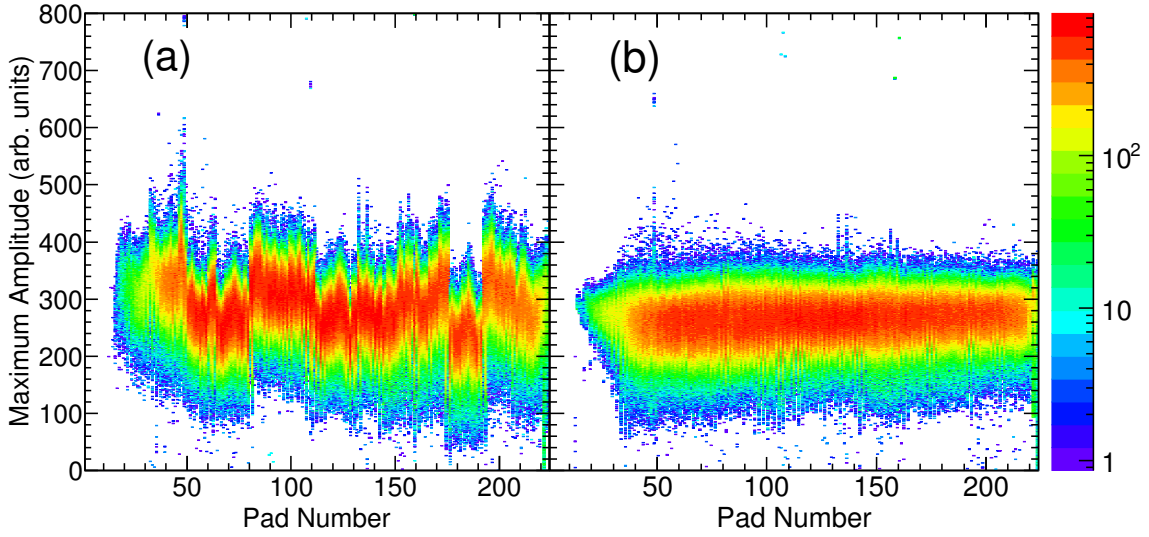

Figure 4.2: The 224 pads of the second CRDC against the pad maximum amplitude while gated on ^{64}Zn recoils. (a) is prior to calibration and (b) is after calibration, with each pad gain-matched to pad 64.

4.2.2 Mask Calibration

Following the calibration of the 224 pads of each CRDC, the next step was to calibrate the recorded dispersive (x) and non-dispersive (y) positions of the CRDCs. The measured CRDC x and y positions have to be calibrated to known values such that the arbitrarily measured positions of particles in the CRDCs will correspond to their true positions in space. These can then be used in the particle trajectory mapping process (see Chapter 3.5.2). This is achieved by mapping the recorded positions of a distinct pattern (see Fig. 4.3) to the known values through applying separate gains and offsets to the recorded x and y values of each CRDC.

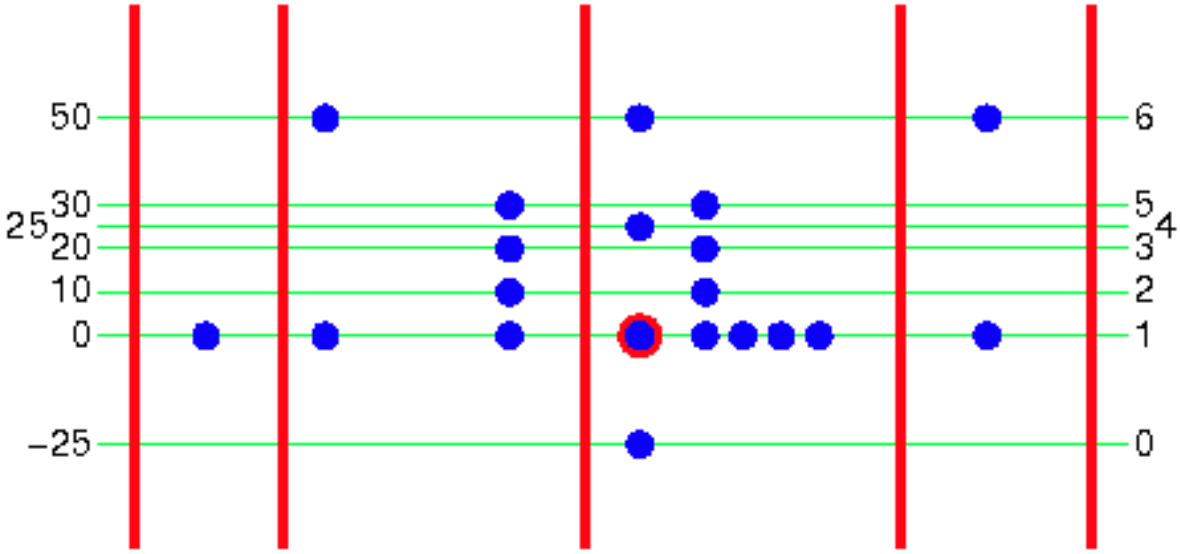

Figure 4.3: The distinct CRDC mask pattern used for the mask calibrations. The blue circles and the red lines correspond to holes and slits in the mask, respectively, through which particles are permitted to pass through. The point circled in red is used as a reference point at (0, 0). The values on the left-hand side correspond to the y position of the points on the mask in mm whilst the numbers on the right are used to label the rows of blue points.

These corrections are deduced through placing a tungsten mask with a series of holes and slits in front of each CRDC so that only particles passing through these holes/slits are detected. Once this distinct pattern has been observed these can be corrected to the known values, corresponding to the physical locations of the mask features, through applying gains and offsets to the recorded positions to translate them to the true physical positions. In the x-plane this gain is fixed as 2.54 as this corresponds to the pitch of the CRDC pads. Likewise, the x-plane offset is fixed at -281.94 mm. In the y-plane the gain is deduced by plotting the

recorded y-positions of the points observed on the mask against the physical positions seen in Fig. 4.3, from which a gradient can be extracted corresponding to the CRDC y-position gain. The y-plane offset is obtained by applying the deduced mask gain factor and a y-plane offset of 0 mm to the first experimental run following the mask run. By then gating on a particular reaction product and examining the y-position recorded at each CRDC, a y offset is deduced from the shift required to centre this recorded y position at 0 mm. Therefore, the CRDC y-position offsets vary on a nucleus-by-nucleus basis whilst the CRDC y-position gains remain constant regardless of the chosen reaction product. The effects of calibrating a mask run with these gains and offsets are seen below in Fig. 4.4.

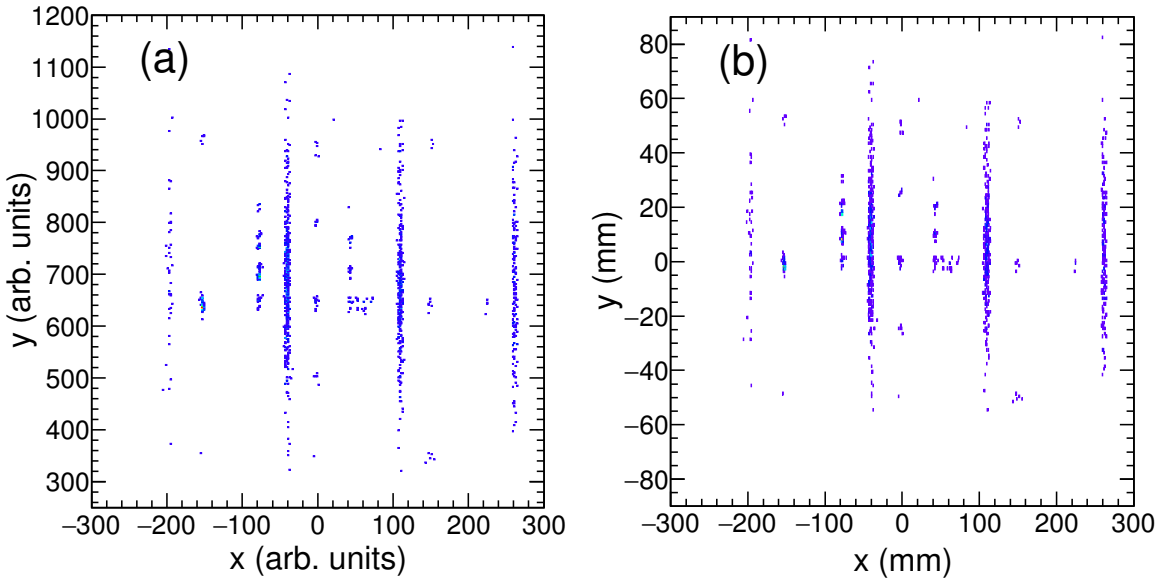

Figure 4.4: (a) displays the first mask run of the experiment for the first CRDC prior to calibration. (b) shows the same mask run after a gain and offset calibration has been applied, matching the recorded positions of each spot on the pattern to the values seen in Fig. 4.3.

Throughout the duration of the experiment there were ten different mask runs in total for each CRDC. Regularly performing CRDC mask runs provides a consistent reference point throughout the entire experiment to which the CRDC positions can be corrected to. The 212 runs of the experiment were divided into ten approximately equal groups such that each group of runs had a mask run in the centre. That particular group of runs was then calibrated with the gains and offsets, deduced through the procedure described above, from its corresponding mask run. The mask runs used for each experimental run are summarised below in Table 4.1.

Table 4.1: A summary of the CRDC mask run used for CRDC position calibrations for each experimental run. Note that experimental runs before run 18 were γ-ray source calibration and test runs.

Mask Run	Mask Run Numbers	First Run	Last Run
1	35/36	18	40
2	46/47	41	54
3	63/64	55	67
4	72/73	68	82
5	92/93	89	97
6	103/104	98	114
7	126/127	115	136
8	154/155	137	172
9	184/185	173	199
10	210/211	200	212

If these mask corrections are not performed then accurate positional information from the CRDCs can not be provided when generating an inverse map (see Chapter 3.5.2). This has the effect of yielding a poorer resolution in any Doppler-corrected γ-ray spectra due to the lack of additional positional information in the Doppler-correction process (see Fig. 3.11).

4.2.3 CRDC Drift Correction

As the temperature of the experimental hall can fluctuate throughout the course of the experiment this can result in changing pressures of the gas contained within the CRDCs that are responsible for particle position detection, thus affecting the electron drift time which is used to deduce the non-dispersive (y) position of the particle. This time-dependent effect is corrected through ensuring that the CRDC y-position drift is corrected on a run-by-run basis by applying a minor correction to the CRDC gain. This correction is deduced through adjusting the mask gain factor such that the y position remains centred at 0 mm in between mask runs and therefore throughout the entirety of the experiment. This CRDC drift-correction factor, m, is calculated through:

$$m = -\frac{c}{y}, \tag{4.2}$$

where c is the CRDC y offset determined through the mask calibration procedure described above and y is the measured CRDC y position seen for the chosen reaction product for a selected experimental run, without the offset c applied to the CRDC data. Using this equation,

the gain determined through the mask calibrations is multiplied by the drift correction factor m. This new gain and the original offset from the mask calibrations will produce a CRDC y position of 0 mm for that particular run. The effects of this drift correction are seen below in Fig. 4.5. These CRDC drift-correction factors were calculated run-by-run and optimised for each nucleus investigated separately. These correction factors are typically $0.98-1.02$, corresponding to a minor adjustment to the gain run-by-run.

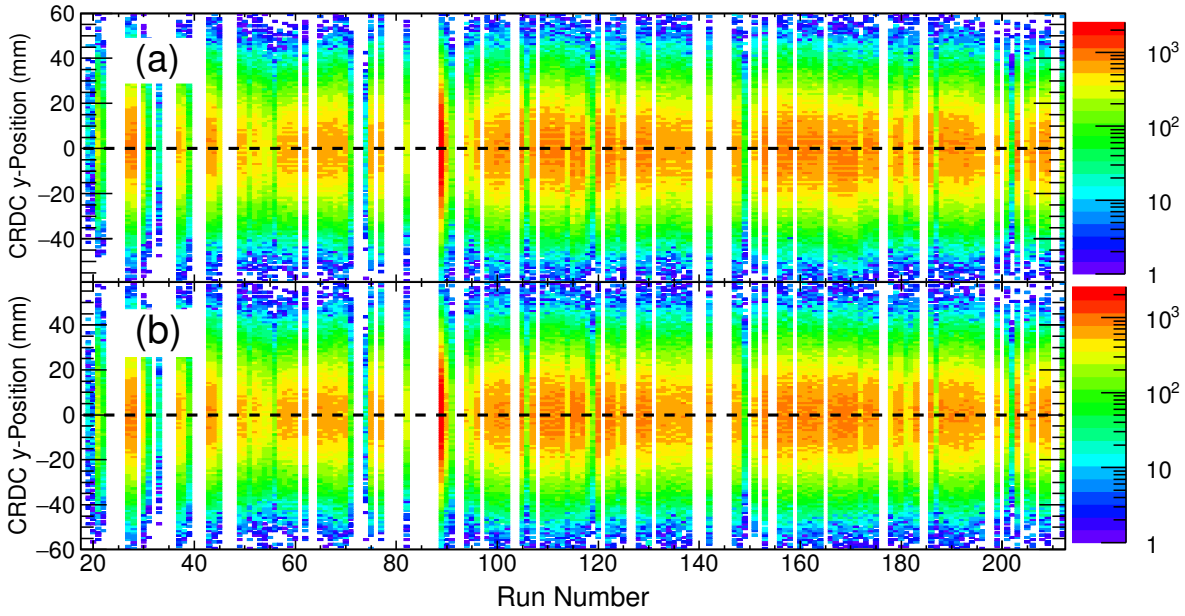

Figure 4.5: The recorded CRDC y-positions for the first CRDC while gated on ^{64}Zn populated through the ^{78}Rb secondary beam. (a) shows the y-position run-by-run before the CRDC drift correction whilst (b) is the same plot after the correction. The dotted black line indicates a y-position of 0 mm, to which each run was shifted to by applying the drift correction.

4.3 Ionisation Chamber Calibrations

4.3.1 Segment Gain Matching

Similarly to the pad calibrations required for the 224 pads of the CRDCs, a gain-matching calibration procedure is employed for the 16 segments of the ionisation chamber. As discussed in further detail in Chapter 3.5.3, energy-loss information taken from the ionisation chamber located within the S800 spectrograph is used to provide A/Q separation of reaction products and is used in conjunction with ToF information for identification of reaction products. For a

given particle, the energy loss in each of the 16 segments of the ionisation chamber is averaged to provide the average energy loss, dE, which is used to resolve nuclei with a different A/Q ratio. Therefore it is essential to ensure that the amplitude of the signals recorded within the segments are consistent. This is achieved through applying a gain and offset to the measured energy loss segment-by-segment.

In identical fashion to the CRDC pad calibration, a segment was chosen as the segment to which the rest will be matched. An incoming beam was then selected, preferably with high statistics to decrease any statistical uncertainties. Around five reaction products from that particular incoming beam were then selected to be utilised with the procedure. The recorded energy-loss amplitudes for each reaction product were plotted segment-by-segment against the measured values for the same reaction products in the segment that has been selected as the segment to which the others will be matched. This then produced a linear plot from which a gain and offset were extracted. As before this was an iterative procedure, typically requiring 2−3 iterations to produce consistent energy losses across all segments. The effects of this calibration are illustrated in Fig. 4.6.

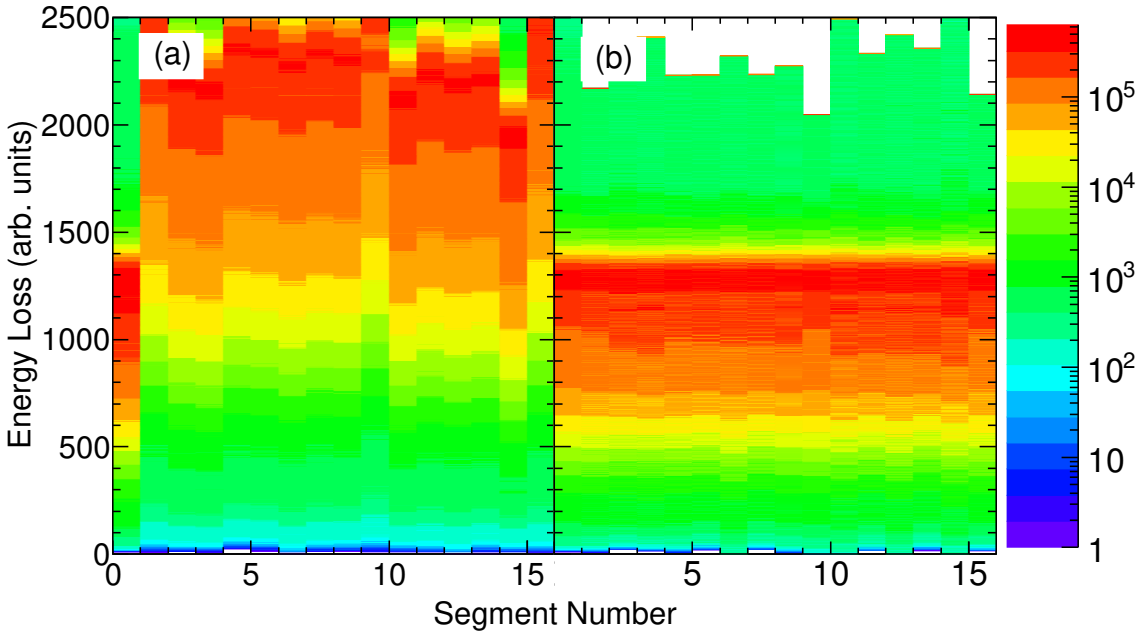

Figure 4.6: The effects of applying the gain and offset calibrations segment-by-segment until consistent values across all segments of the ionisation chamber are obtained. (a) displays the energy loss of each segment prior to calibrations whilst (b) is the same plot post calibration.

4.3.2 Positional Corrections

Additional corrections are required for the ionisation chamber energy-loss measurements to account for the longer/shorter path lengths through the chamber depending upon the trajectory of the particle. This is corrected by adjusting the recorded energy loss with three parameters to remove the dependence on the x and y positions of a particle through the CRDCs and at the S800 focal plane. This is applied through Eq. 4.3:

$$E_{corr} = E \times A \times y_{fp} \times \exp[B\ (C - x_{fp})] \tag{4.3}$$

where E_{corr} is the corrected energy loss of a particle traversing the ionisation chamber, E is the uncorrected energy loss, A and B are correction parameters related to the energy-loss gain relative to the y and x planes of the ionisation chamber, respectively. y_{fp} is the detected y position of a particle at the S800 focal plane and C is a gain factor associated with the x position of a particle at the focal plane (x_{fp}). The parameters A, B and C are optimised individually by examining the dependence of the energy loss of a chosen reaction product against x_{fp} and y_{fp} until any dependence is eliminated. As x_{fp} and y_{fp} are both closely related to the x and y positions recorded at each CRDC, the dependence can also be explored through the CRDC positions. An example of eliminating the first CRDC's x-position dependence of the energy loss through optimising A, B and C when gating on ^{64}Zn (populated through the ^{78}Rb secondary beam) can be seen in Fig. 4.7. If this correction is not performed then a consistent recorded energy loss is not obtained for a given reaction product. This can result in contamination during the particle identification procedure as reaction products are separated by their A/Q ratio through energy-loss measurements.

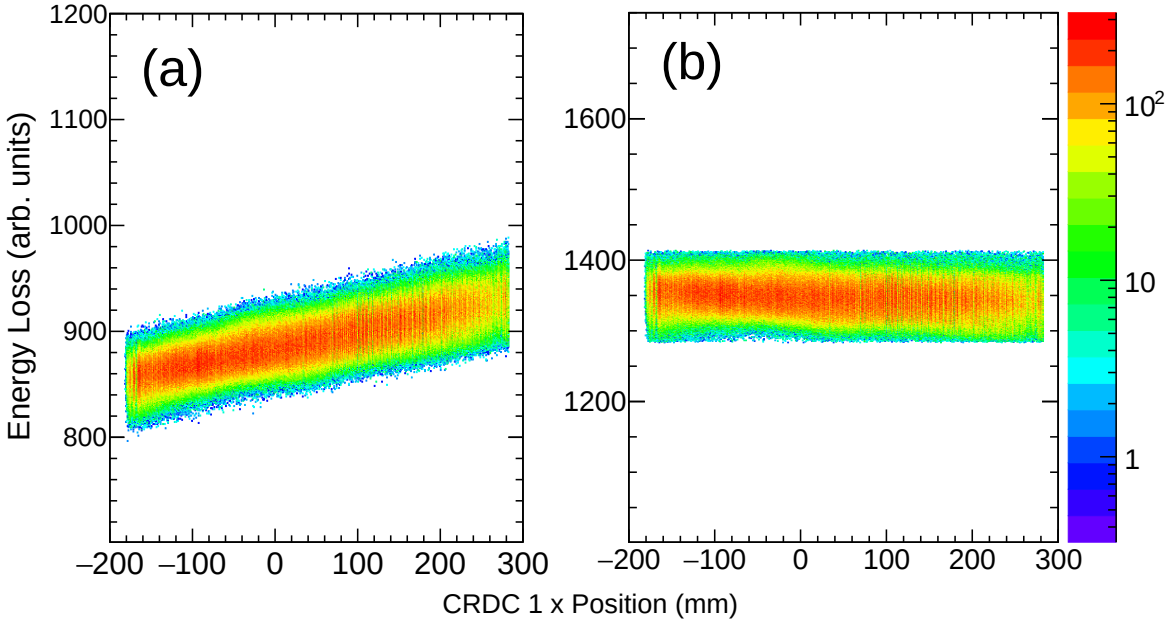

Figure 4.7: Ionisation chamber energy loss against the recorded x position of the first CRDC before (a) and after (b) the positional corrections whilst gating on ^{64}Zn recoils (populated through the ^{78}Rb secondary beam).

4.4 GRETINA

4.4.1 Energy Calibrations

Prior to the analysis of γ-rays detected by GRETINA it was necessary to ensure that the γ-ray energies recorded by each of the detector crystal were calibrated to known energies of calibration sources. A predetermined energy calibration is automatically applied during the signal decomposition process of GRETINA, resulting in raw data files with calibrated GRETINA energies. Several spectra from a variety of sources (^{152}Eu, ^{133}Ba, ^{56}Co and ^{60}Co) were recorded prior to the start of the experiment to ensure the reliability of the preliminary energy calibration. Likewise, a γ-ray energy spectrum from ^{152}Eu source was obtained at the end of the experiment to confirm that the recorded energies had not changed throughout the duration of the experiment.

Examining the source spectra crystal-by-crystal revealed clear, random deviations from the known energies from literature [107]. These deviations were typically < 0.5 keV but were as much as ~ 1 keV at certain energies in a small number of crystals. This effect is illustrated in Fig. 4.8 where there is no visible systematic behaviour to the discrepancies from the known

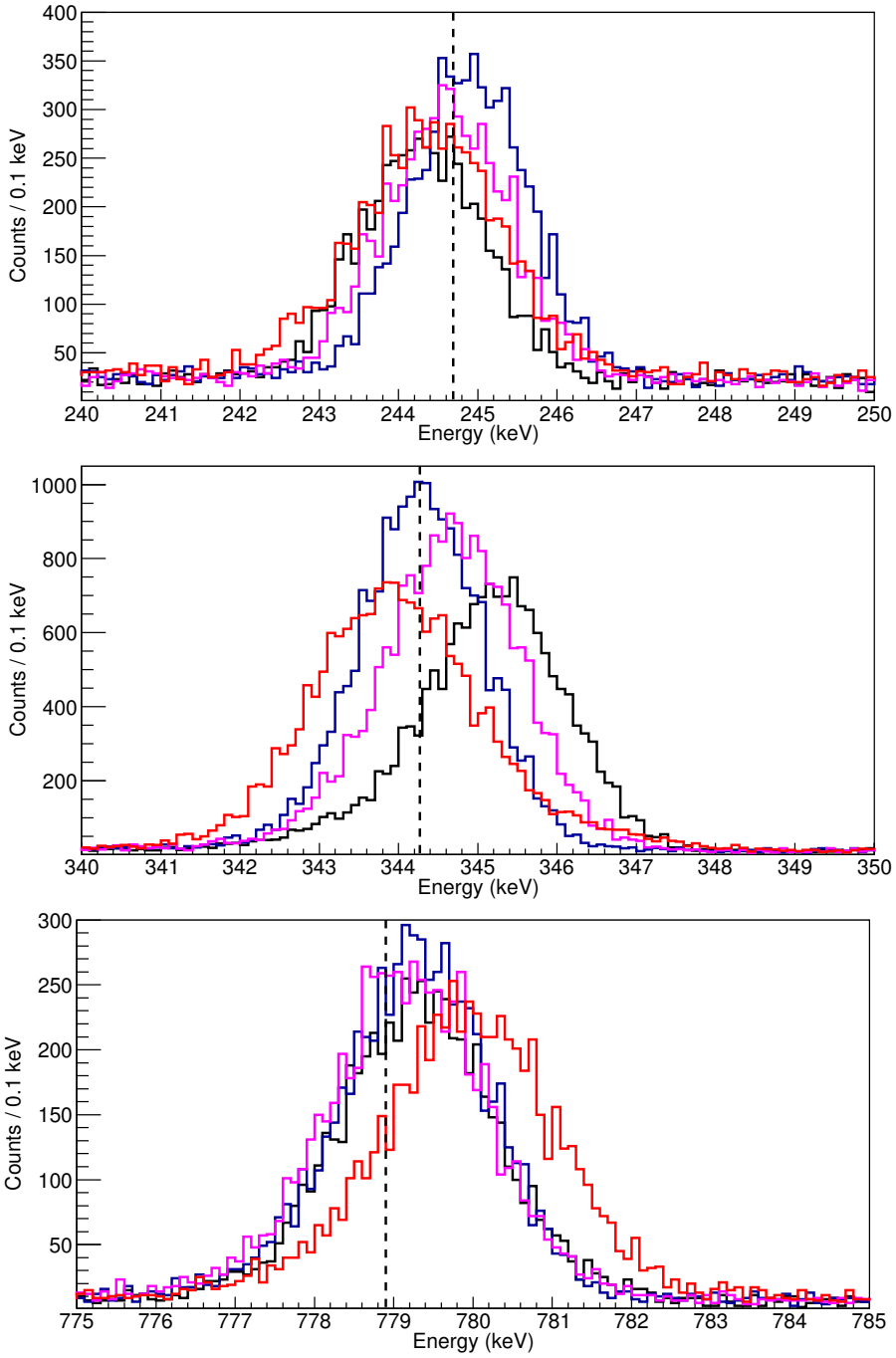

Figure 4.8: Energy spectra of four different crystals of the same detector module of GRETINA at 244.7, 344.3 and 778.9-keV peaks from a ^{152}Eu calibration source. The dashed black lines indicate the known energies from literature. The rate-dependent non-linearity of the ADC of the GRETINA signal decomposition is visible given the seemingly random shifts in energy of each crystal at different energies.

energies. This is best demonstrated by the crystal denoted with the black line, which is slightly too low for the 244.7-keV peak, $\sim$ 1 keV too high for the 344.3-keV peak and slightly too high for the 778.9-keV peak. This issue was addressed by attempting to perform linear and second-order polynomial recalibrations to each detector crystal. However it proved impossible to apply a function to the recorded energies to correct all peaks to the known literature values. This was confirmed to be a known issue with GRETINA associated with the differential non-linearity (DNL) of the ADC [94], which is a count-rate dependent effect, for which there is no simple fix [108]. Given that the beams appropriate to this experiment were at typical velocities of $0.29-0.30c$ the effects of this sub-keV energy discrepancy become negligible in comparison to uncertainties associated with any Doppler corrections performed, such as uncertainties in beam velocity, recoil angles and any intrinsic uncertainties of the S800 spectrograph. As all γ-ray spectra relevant to this experiment are Doppler corrected, the effects of this ADC DNL are essentially cancelled out given that prior to Doppler correction the 90° detector GRETINA ring will record energies lower than the true energy, and vice versa for the 58° detector ring. A Doppler correction corrects both detector rings to the correct energy, thus diminishing the effects of the DNL of the ADC. Furthermore, when the combined spectrum for all crystals is examined the deviation from known energies is negligible, meaning that the DNL of the ADCs contributes to a poorer energy resolution rather than incorrect energies. The recorded energies extracted from ^{152}Eu, ^{133}Ba, ^{56}Co and ^{60}Co γ-ray source spectra for all GRETINA crystals are compared with values from literature in Fig. 4.9 demonstrating the consistency of the calibrated data with known energies. The inset of Fig. 4.9 displays the energy range of 225$-$400 keV, the range at which the $E(2^+)$ of all of the $N = Z$ nuclei measured in this experiment are found, where there is clear agreement between the calibrated and known energies.

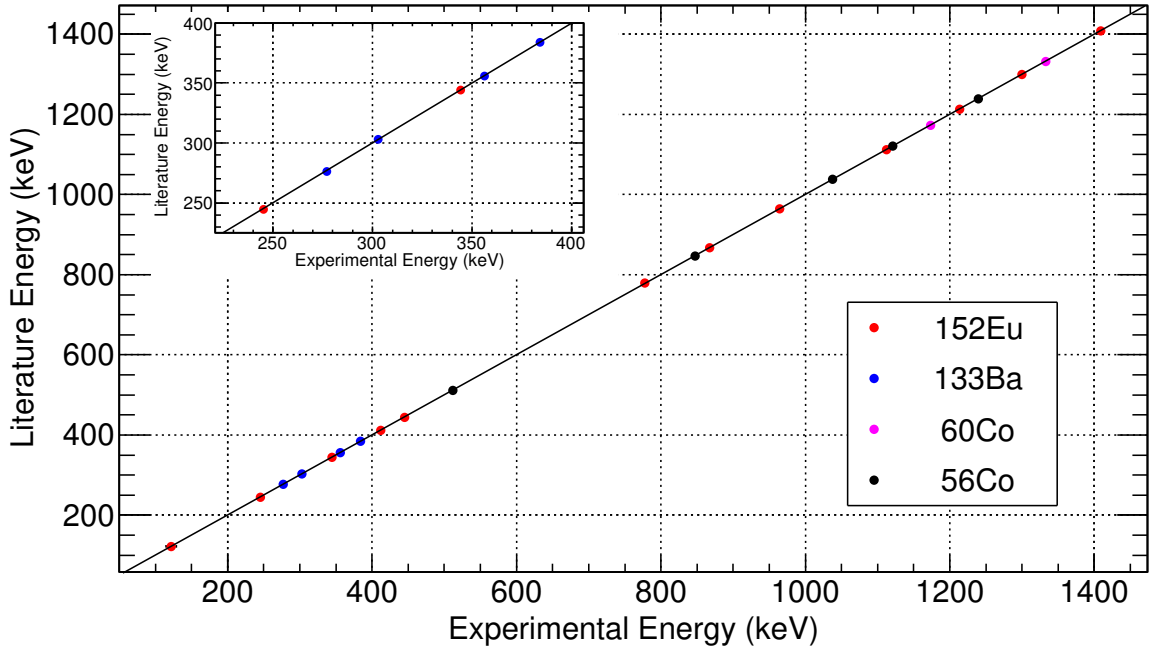

Figure 4.9: The calibrated experimental γ-ray energies from all detector crystals of GRETINA compared to the energies from literature. The inset displays the same plot in the energy range where the energies of the 2^+ states of the $N = Z$ nuclei investigated lie. The black line is to guide the eye and corresponds to where the calibrated energy is equal to the energy literature.

4.4.2 γ-ray Doppler Corrections

Since this experiment utilised relativistic reacted beams with typical velocities ranging from $0.29-0.3c$ the deexcitation γ rays detected by GRETINA have a considerable Doppler shift given by the Eq. 4.4 [84]:

$$E_{rest} = E_{lab}\frac{1-\beta\cos(\theta)}{\sqrt{1-\beta^2}}, \tag{4.4}$$

where E_{rest} is γ-ray energy in the frame of the nucleus moving at velocity v, E_{lab} is the γ-ray energy observed, $\beta = \frac{v}{c}$ and θ is the observation angle in the laboratory frame of the first γ-ray interaction point of GRETINA relative to the direction of the beam, $\vec{v}$. This will be taken into consideration by using a sophisticated event-by-event Doppler-correction process for any detected γ rays using a specified value for β. The β value is slightly adjusted on an event-by-event basis using the d_{ta} value calculated by the inverse map through Eq. 4.5 [84]:

$$\frac{d\beta}{\beta} = \frac{1}{\gamma(\gamma+1)}\frac{dT}{T}, \tag{4.5}$$

where T is the kinetic energy of the particle, d_{ta} calculated through the inverse map (see Chapter 3.5.2) corresponds to dT/T and $\gamma = 1/\sqrt{1-\beta^2}$. The recoiling nucleus is first assumed to have decayed at the target position at the mid-point in the target, which is initially assumed to be at the exact centre of GRETINA. From here an additional event-by-event shift in the y direction relative to the centre of the target is applied, corresponding to the y_{ta} value, again calculated from the inverse map. The calculated recoil angles a_{ta} and b_{ta} from the inverse map are incorporated into the Doppler-reconstruction process whereby the vector of the recoiling nucleus $\vec{v}$ is slightly adjusted from the central beam axis (corresponding to $a_{ta}/b_{ta} = 0$ mrad) to the values determined through the inverse map. This translates to a small (typically ≤ 15 mrad), but significant event-by-event correction to the calculated angle of emission, θ, used for the correction process.

As discussed in further detail in Chapter 5.2.2, the effective target x, y and z positions of the centre of the reaction target used for the γ-ray Doppler-correction process can be varied manually within the settings file included whilst sorting the raw data with GrROOT. Likewise, offsets to a_{ta} and b_{ta} can be manually adjusted within the settings file while calibrating a run of the experiment. The a_{ta} and b_{ta} distributions were shifted to centre each at 0 mrad on a run-by-run basis.

Chapter 5

Analysis Techniques

This chapter will discuss the different methods used in the analysis to optimise the γ-ray spectra produced from the data prior to the analysis of the γ-ray lineshapes. This will consist firstly of the particle identification (PID) methods used to distinguish reaction products following on to the procedures performed in regards to the optimisation of the γ-ray Doppler corrections. The final section will discuss additional methods that were employed in the process of obtaining the final results presented in Chapter 6.

5.1 Particle Identification

As previously discussed in Chapter 3.3.1, incoming secondary beams produced from the fragmentation of the ^{92}Mo primary beam on the 802 mg/cm^2 target at the entrance to the A1900 separator are identified through the use of ToF measurements from the XFP/OBJ to the E1 scintillator. By examining the XFP-E1 ToF against OBJ-E1 ToF the separate incoming beams can be clearly distinguished, although there is a clear contaminant line through the centre of the plot, as seen in Fig. 5.1(a). The contaminant was identified as secondary beams that traverse the reaction target without reacting before entering the S800 spectrograph. Since these contaminants pass directly through the centre of the incoming beams of interest, it is vital to remove these unreacted particles as much as possible to prevent contamination during the identification of reaction products produced at the reaction target. A condition of a particle requiring a GRETINA event in coincidence was applied to ensure that the particle had reacted within the reaction target. Additionally, a γ-ray energy gate of > 150 keV to this

detected GRETINA energy was applied to reduce the effects of any random coincidences with Bremmstrahlung radiation. Applying these conditions resulted in greatly reduced contaminant beams, as displayed in Fig 5.1. If these contaminants are not removed this can result in asymmetric a_{ta}, b_{ta}, y_{ta} and CRDC position distributions. Since these distributions are adjusted to perfect the Doppler-correction process the contaminants can have adverse affects on the final Doppler-corrected γ-ray spectra, resulting in a poorer resolution.

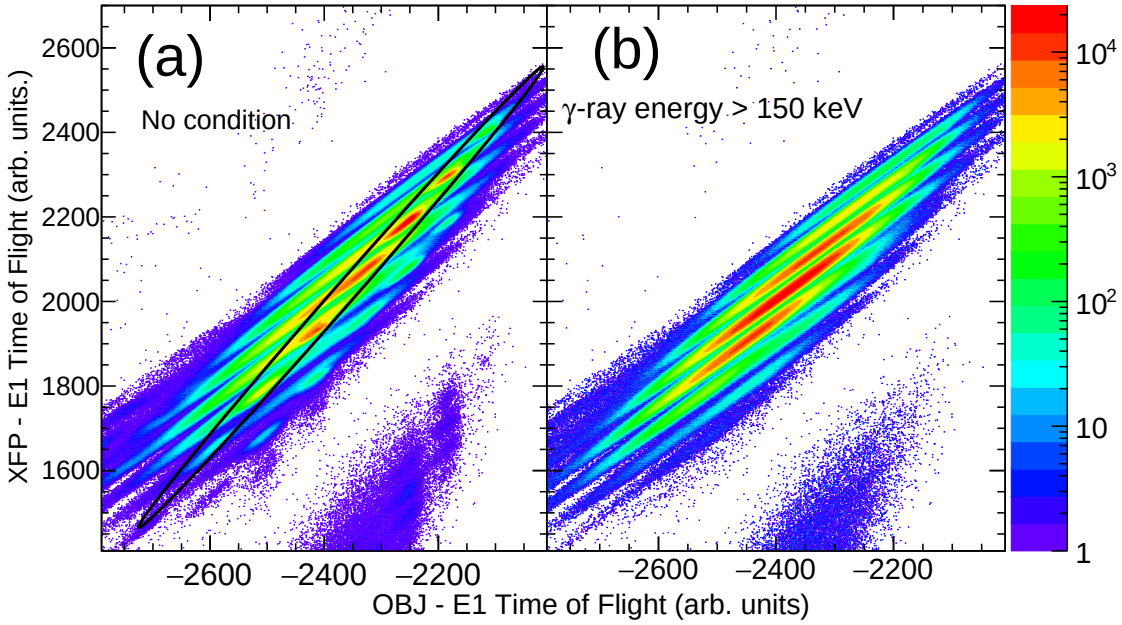

Figure 5.1: Comparison of incoming beam plot from ToF information from the OBJ/XFP to the E1 scintillator without (a) and with (b) the additional condition of requiring a γ-ray with an energy > 150 keV. This has the effect of greatly reducing any unreacted secondary beams, which are highlighted in black in (a), which can skew distributions such as a_{ta}, b_{ta} etc.

Reaction products at the secondary target for a given secondary beam are identified through energy loss (dE) information from the ionisation chamber and corrected ToF information from the OBJ scintillator located at the A1900 focal plane and E1 scintillator at the end of the S800 spectrograph. An incoming secondary beam can be selected using the ToF plot described above. From there a reaction product produced at the reaction target from the selected secondary beam can then be identified from S800 data. The y-axis of the plot used for PID corresponds to the mass-to-charge ratio (A/Q) of the reaction products. The vertical lines of reaction products (such as in Fig. 5.2) correspond to a specific total isospin projection T_z, with the straight vertical line of reaction products corresponding to $N = Z$

($T_z = 0$) nuclei. The PIDs used to identify any of the nuclei investigated are shown below.

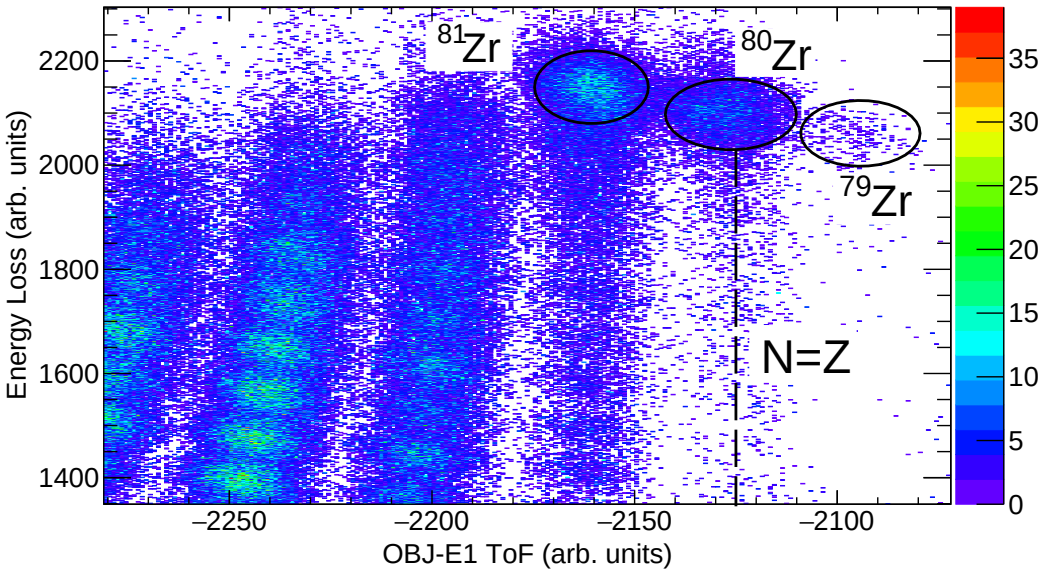

Figure 5.2: PID plot of energy loss in the ionisation chamber against the corrected OBJ - E1 scintillator ToF for the incoming ^{81}Zr beam. The ^{81}Zr beam as well as ^{80}Zr and ^{79}Zr, populated through one and two-neutron knockout, respectively, are labelled. The dashed black line indicates the column of the $N = Z$ reaction products.

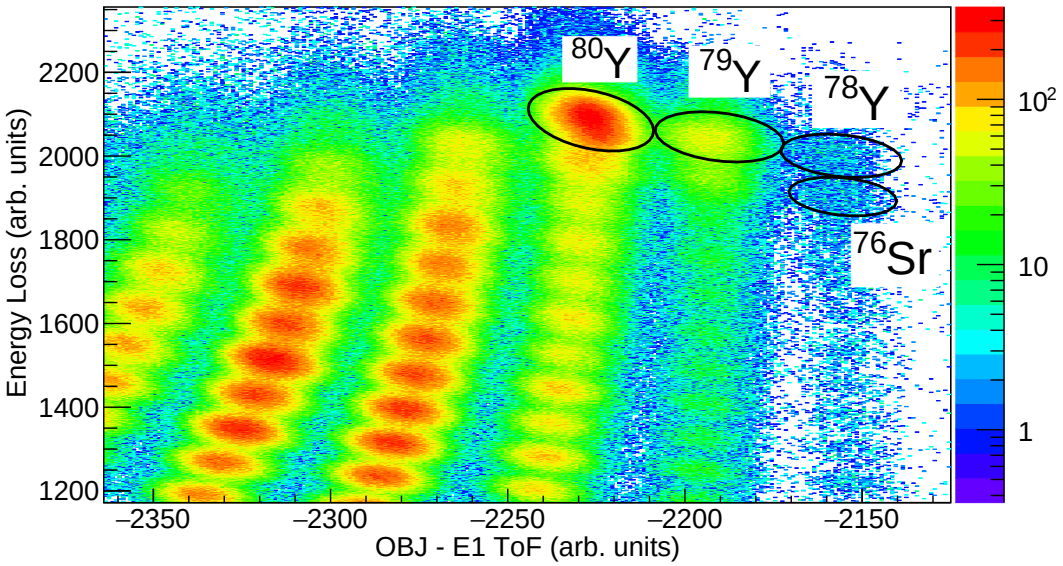

Figure 5.3: PID plot of energy loss in the ionisation chamber against the corrected OBJ - E1 scintillator ToF for the incoming ^{80}Y beam. The one and two-neutron knockout reactions to ^{79}Y and ^{78}Y, respectively, are labelled. The $N = Z$ ^{76}Sr, populated from three-neutron, one-proton removal is also labelled.

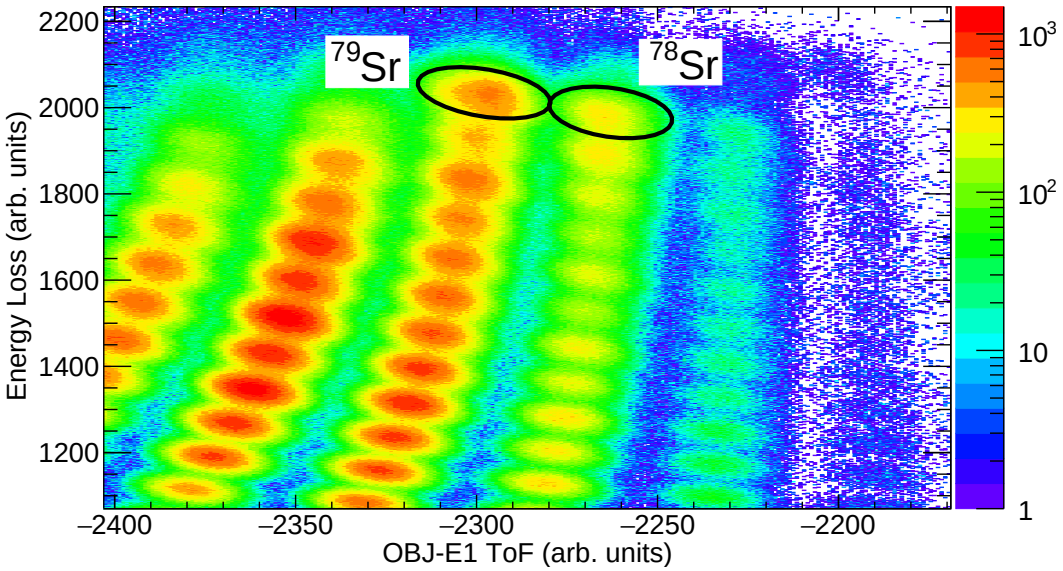

Figure 5.4: PID plot of energy loss in the ionisation chamber against the corrected OBJ - E1 scintillator ToF for the incoming ^{79}Sr beam. The one-neutron knockout reaction to ^{78}Sr is labelled.

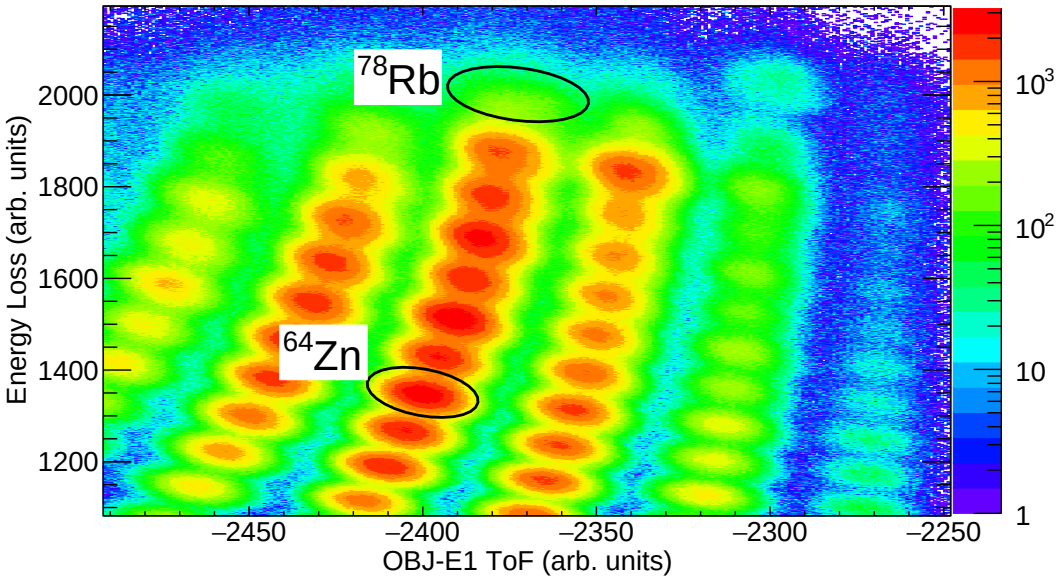

Figure 5.5: PID plot of energy loss in the ionisation chamber against the corrected OBJ - E1 scintillator ToF for the incoming ^{78}Rb beam. ^{64}Zn is labelled as it was used at several stages of the calibration process.

There was an issue which arose throughout the course of the experiment whereby both the XFP and OBJ ToF would sometimes be systematically shifted by $\sim$ 1000 arb. units when a new run was started. This affected approximately 15% of the total experimental runs. These affected runs were noted and treated separately to the non-shifted runs, since these runs would require separate cuts for the calibration processes given the shifted incoming beam and PID plots. All calibrations were calculated and applied in the same manner for both the shifted and non-shifted runs. Post calibration the resulting Doppler-corrected γ-ray spectra from both the shifted and non-shifted runs were summed to produce a single spectrum which was used for any further analysis.

5.2 Optimising γ-ray Spectra

5.2.1 Determining β

The optimum β values used for the γ-ray Doppler-correction processes were deduced by separately extracting the two recorded energies of a given transition from the 58° and 90° GRETINA detector rings. From Eq. 4.5 it can be seen that if β is correct then this will result in the Doppler-corrected γ-ray energy being constant over all θ angles of the GRETINA array,

assuming that θ and $\vec{v}$ are being calculated correctly. For two given measured energies of E_1 and E_2 for a given transition from the Doppler-corrected spectra of the forward and back angle detectors respectively, corrected with a given β value, the β value required to correct these two spectra to the same energy, denoted β_{new}, is given by Eq. 5.1 [105]:

$$\beta_{new} = \beta + \frac{E_1 - E_2}{-\beta^2\gamma^3(\cos\theta_1 + \cos\theta_2) + \gamma(\cos\theta_1 - \cos\theta_2)}, \tag{5.1}$$

where $\gamma = 1/\sqrt{1-\beta^2}$ and θ_1 and θ_2 are the average detector angles from the forward and back angle detector rings of 58° and 90° respectively. Different reaction products have different masses and charges and are produced through different reaction mechanisms from the range of secondary beams. Therefore, the optimum β value will vary nucleon-to-nucleon, in this case typically from 0.28 to 0.3.

The effects of optimising β through matching the Doppler-corrected γ-ray energy for the 58° and 90° detector rings can be seen in Fig. 5.6, where there is a visible divergence between the two detector rings at incorrect β values. In this example ^{64}Zn (populated from the ^{78}Rb incoming beam; see Fig. 5.5) is used due to the abundant statistics. The effects of eliminating the θ dependence through varying β is also shown in Fig. 5.7, where a much narrower peak is observed when β is optimised at $\beta = 0.2835$.

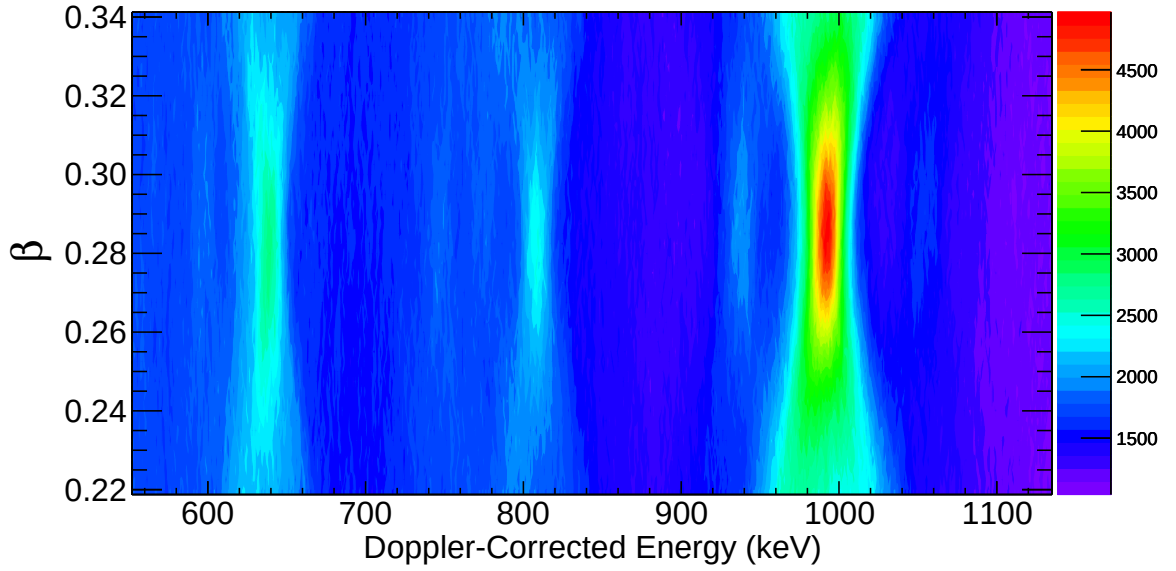

Figure 5.6: β Doppler-corrected γ-ray energy for ^{64}Zn. At incorrect β values there is a clear divergence between the forward and backward detector rings of GRETINA. Likewise, both detector rings converge at the same energy at the correct β value for a given decay. Different β values for different decays result from lifetime effects i.e. the decays occurring at different points within the reaction target.

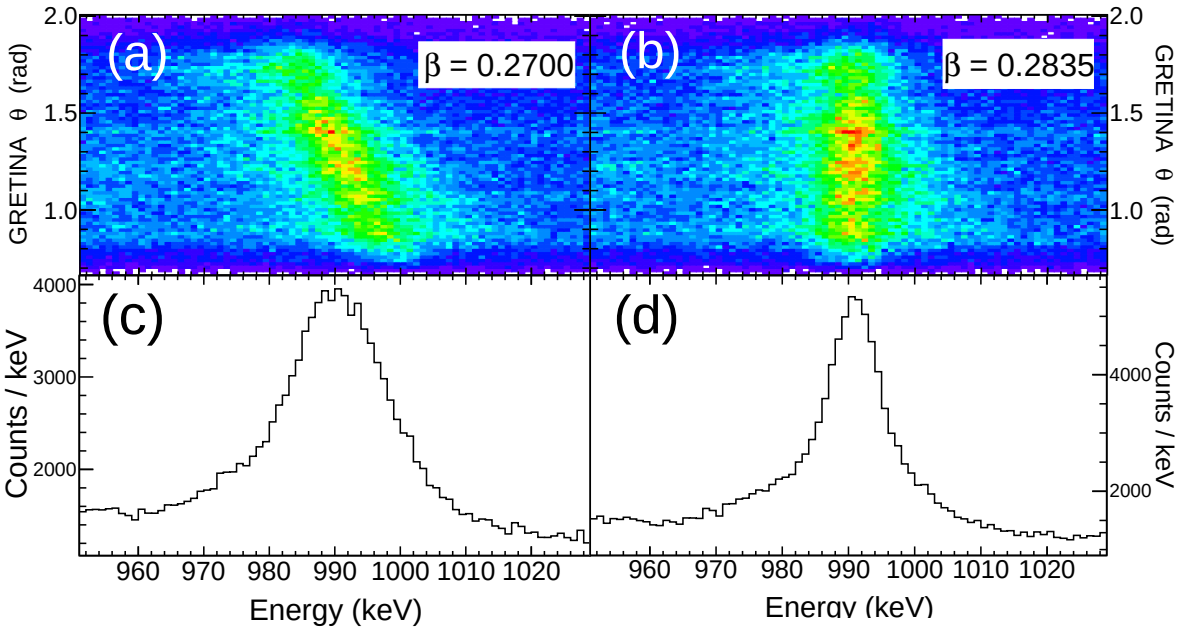

Figure 5.7: The effects of optimising the β value used for Doppler corrections for the 991.6-keV, $2^+ \rightarrow 0^+$ transition of ^{64}Zn. (a) and (c) show the dependence of the Doppler-corrected energy with the GRETINA θ angle and the corresponding γ-ray spectrum, respectively, corrected with $\beta = 0.270$. (b) and (d) shows the same plots Doppler corrected with the optimised value of $\beta = 0.2835$, eliminating any dependence on the GRETINA θ angle.

Furthermore, decays with a short lifetime (typically less than a few picoseconds) will occur within the target, resulting in a higher β value as the particle has not slowed down as much as a fully-attenuated particle that has traversed the entire length of the target and decayed downstream. This results in each nucleus having a separate optimum β for mid and after-target decays, denoted β_{mid} and β_{aft}, respectively. Despite a correct β_{mid} value of 0.2835 being chosen for Doppler corrections in Fig. 5.7(d), there are still small, low and high-energy tails visible on either side of the peak centroid. These tails are a consequence of the short 2.8 ps mean lifetime of the 2^+ state of ^{64}Zn [109]. The bulk of the decays occur mid target, which corresponds to the proportion of the peak that had been straightened by adjusting β in Fig. 5.7. However, there will be a small fraction of the particles that will react and decay earlier within the target, therefore resulting in a higher β at the time of decay due to a lower attenuation through traversing the target, resulting in an incorrect Doppler correction. This effect is displayed in further detail below in Fig. 5.8 where the labelled diagonal stripe is visible through the plot, an indication of a Doppler correction with a β that is too low. Since the S800 spectrograph does not currently provide any positional information in the z-axis in regards to the decay position, this effect cannot be further corrected for. Therefore, the effect of these tails for fast transitions is minimised by optimising β for the bulk of the counts, which comprise mostly of mid-target decays.

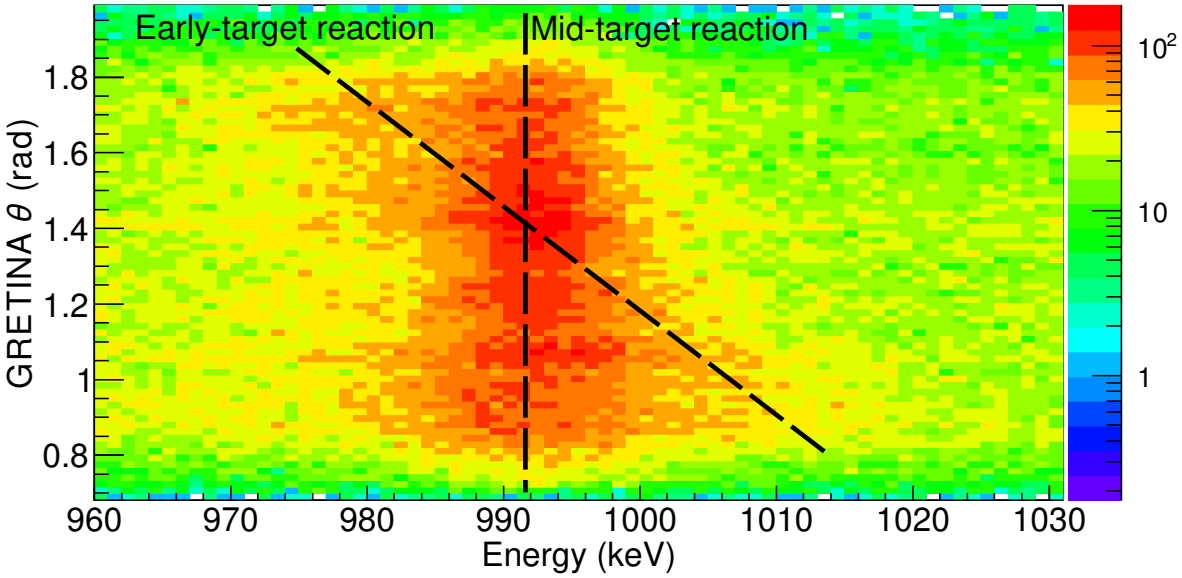

Figure 5.8: The dependence of the Doppler-corrected energy of the 991.6-keV, $2^+ \rightarrow 0^+$ decay of ^{64}Zn with the θ angle of the detection position of GRETINA, relative to the beam axis. The bulk of the counts have been corrected with a β_{mid} of 0.2835, corresponding to the labelled mid-target reactions. The diagonal line seen through the plot corresponds to particles reacting and subsequently decaying earlier or later in the target relative to the midpoint, thus having a different β at the time of decay.

The uncertainty in a decaying particle's β ($\Delta\beta$) has a significant contribution towards to total energy resolution (ΔE_γ^{cm}) of a Doppler-corrected γ-ray spectrum. The effects of $\Delta\beta$ in addition to the angle uncertainty subtended from the pulse-shape analysis within a detector crystal ($\Delta\theta$) and the intrinsic energy resolution of the detector ($\Delta E_\gamma^{lab}/E_\gamma^{lab}$) are explored in Ref. [110] and culminated in Eq. 5.2:

$$\left(\frac{\Delta E_\gamma^{cm}}{E_\gamma^{cm}}\right)^2 = \left(\frac{\beta \sin\theta}{1-\beta\cos\theta}\right)^2 (\Delta\theta)^2 + \left(\frac{\beta - \cos\theta}{(1-\beta^2)(1-\beta\cos\theta)}\right)^2 (\Delta\beta)^2 + \left(\frac{\Delta E_\gamma^{lab}}{E_\gamma^{lab}}\right)^2. \quad (5.2)$$

There is a θ angle $\sim$ 1.4 rad (75°) at which the Doppler broadening due to β variations is minimal, which can be seen by the area of highest concentration of counts in Fig. 5.8. The detector angle uncertainty ($\Delta\theta$) can be improved by increasing the distance of the detector from the γ-ray source, decreasing the solid angle of the detected γ-ray interaction position. However, this comes at the expense of decreasing the absolute efficiency of the detector. For this reason the GRETINA array in the ten module configuration was positioned approximately 18 cm from the reaction target position.

5.2.2 Determining the Effective Target Position

The effective target z position (where the beam is travelling in the positive z direction) used for the event-by-event γ-ray Doppler correction process can be varied manually within the settings file when calibrating an experimental run. At recoil velocities appropriate to this experiment of $\beta \sim 0.3$ a particle will travel ∼9 mm per 100 ps. For this lifetime analysis, since the lifetimes of the 2^+ states are typically of the order of a few hundred picoseconds, the effective z position used for these corrections was set to the end of the target as β would no longer change after this point. This z position is therefore defined by Eq. 5.3:

$$z_{corr} = z_{mid} + \frac{t}{2}. \tag{5.3}$$

Here z_{corr} is the specified z position used for the corrections, z_{mid} is the z position of the mid-point of the target and t is the target thickness (1 mm, corresponding to 188 mg/cm^2 of ^{9}Be). The z position of the mid-point of the target was deduced through measuring the energy of a decay from a short lifetime (<5 ps) state while varying the z_{corr} value after optimising the mid-target β until the measured energy matched that in literature. The very short lifetime of this state means that the resulting nucleus will decay near instantaneously following reacting within the target. Assuming an average reaction occurring mid target, this is an excellent probe of the precise location of the mid-point of the target relative to GRETINA. The nucleus used for this measurement was ^{64}Zn, populated through 7n, 7p removal from the ^{78}Rb secondary beam. This was ideal for determining the mid-point of the target due to the high $2^+ \rightarrow 0^+$ energy of 991.6 keV, making it very sensitive to Doppler corrections as well as its short 2^+ state mean lifetime of just 2.8 ps [109]. The ^{78}Rb beam was also the most abundant secondary beam meaning that high statistics were available for ^{64}Zn, therefore reducing any statistical uncertainties associated with the Doppler-corrected energies. Through this method the mid-target z position was determined to be −0.93 mm, corresponding to an after-target z position of −0.43 mm relative to the centre of GRETINA. This small adjustment to the z position of the target arises from inaccuracies in the placement of the target in the beamline at the centre of GRETINA. It can be seen from this analysis that the adjustment is usually small (< 1 mm). The effects of implementing this mid-target z position in the Doppler-correction process for a γ-ray decay are illustrated in Fig. 5.9.

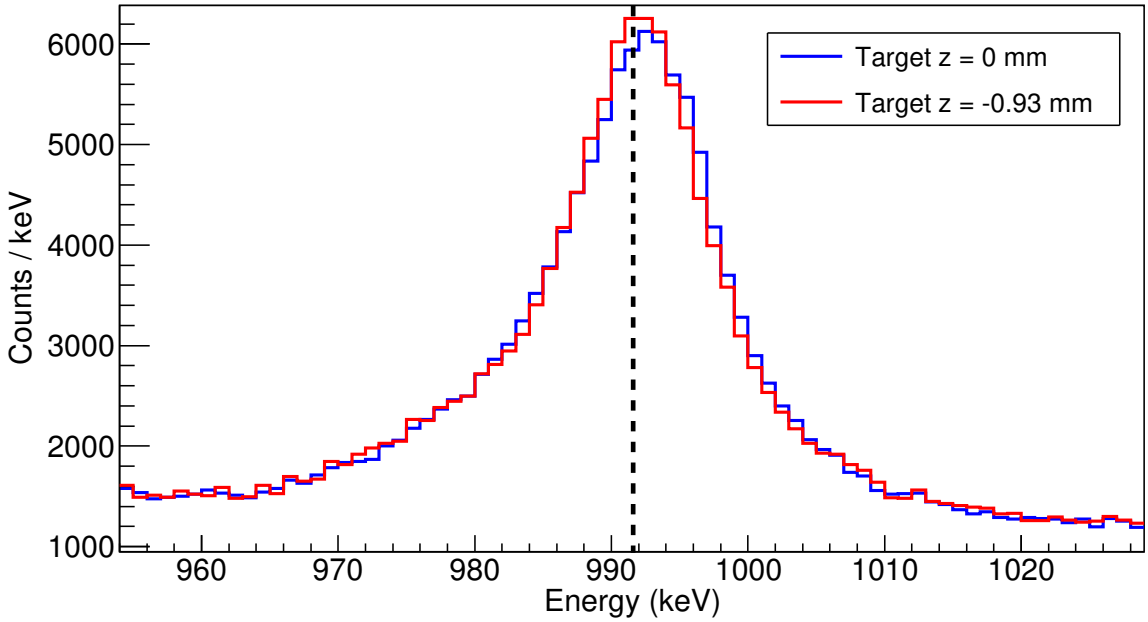

Figure 5.9: A comparison of the Doppler-corrected γ-ray spectra whilst using a target z position of -0.93 mm (red) and no target z-position offset (blue). The black dashed line indicates 991.6 keV, to which a target offset of -0.93 mm was need to centre the mean of the distribution to this energy. Both spectra are Doppler corrected with $\beta_{mid} = 0.2835$.

Given the inclusion of the target z-position whilst performing Doppler corrections of γ rays, the effects of the effective target x and y positions cannot be neglected. These effective target x and y positions are used to account for small inaccuracies in the inverse map calculations and therefore correct beam spot position determined through the inverse map to the centre of GRETINA. Therefore, these do not necessarily correspond to the physical x and y positions of the centre of the target, hence the reason for these being named as '*effective*' target positions. These effective target positions, as with the target z-position, can be varied manually within the settings file included during the process of applying calibrations to each run of the experiment. The optimum values for these parameters were probed through the dependence of the Doppler-corrected γ-ray energy relative to the azimuthal ϕ angle of the deduced first-interaction point of GRETINA. This dependence was investigated for the 58° and 90° detector rings separately, as seen in Fig. 5.10. Through exploring the effects of adjustments to the effective target x and y-positions, it was observed that the initially slanted dependence of the 58° detector ring was strongly dependent on the y-position of the target. This value was adjusted until the dependence was removed as much as possible at a target

y position of 2.2 mm. The spectrum from the 58° detector ring was slightly bowed at first, which was reduced through adjusting the x position to 1 mm. The dependence of the 90° detector ring was far less dependent upon the x and y position of the target, with minimal changes seen by adjusting the target y position. A slight bowing was observed with the 90° detector ring which, as with the 58° detector ring, was reduced slightly with the the inclusion of an x-offset to the target position of 1 mm. However, this bowing could not be further corrected for without the consequence of increasing the ϕ dependence of the 58° detector ring (see Fig. 5.10).

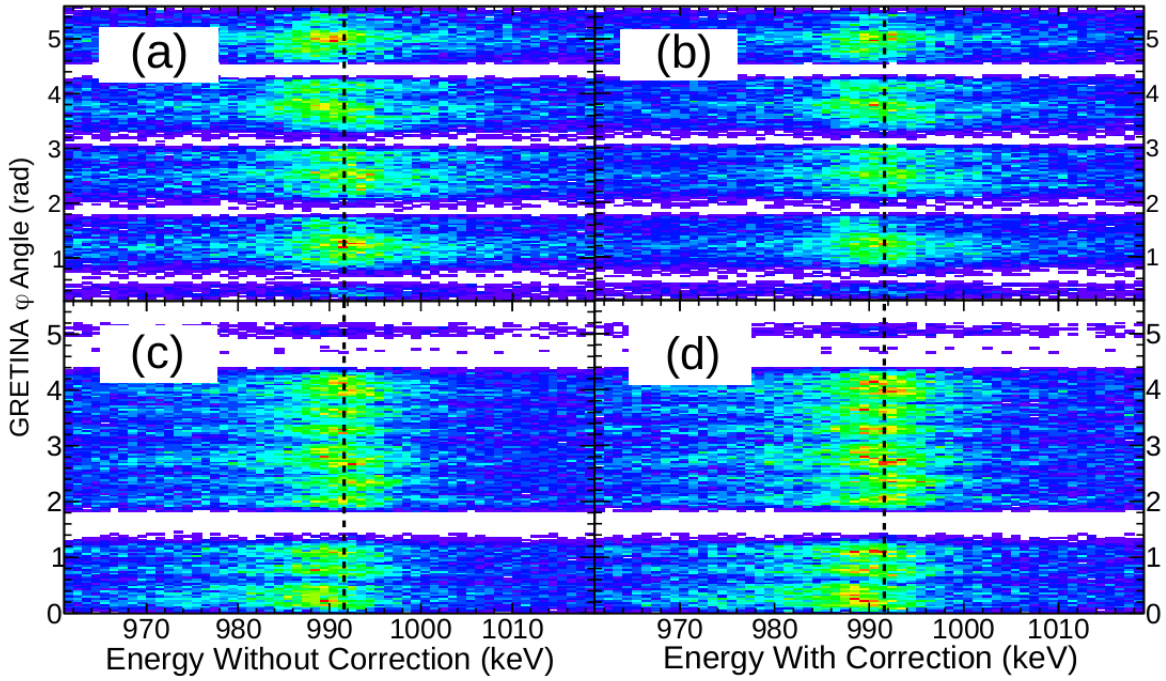

Figure 5.10: A comparison of the Doppler-corrected γ-ray spectra whilst adjusting the effective target x and y positions used in the Doppler-correction process. (a) and (c) display the forward and backward angle detector rings, respectively, before adjusting the positions. (b) and (d) correspond to the same plots after the correction. The black dashed lines indicate the literature energy of the 991.6-keV, $2^+ \rightarrow 0^+$ decay of ^{64}Zn.

5.2.3 Timing Gate

Given that all of the reacted beams in this experiment have typical beam velocities from $0.28 - 0.30c$, there is a signature time difference between the GRETINA trigger from a detected γ-ray event and the E1 scintillator trigger from the corresponding implanted particle

at S800 focal plane. This time difference is usually ∼70 ns, allowing one to gate on a narrow timing window to eliminate contributions to the γ-ray spectrum arising from background radiation and Bremmstrahlung radiation from particles stopping within the GRETINA detector frame. In this instance, a timing window of −70 to −55 ns was applied, as displayed in Fig. 5.11. Here the second streak of counts ∼ −140 ns corresponds to random coincidences with events from the previous cyclotron beam pulse, which have signature time differences of ∼ 77 ns. The horizontal lines at 511 and ∼700 keV seen above −70 ns are γ-ray decays occurring post reaction from electron-positron annihilation and neutron activation of germanium, respectively.

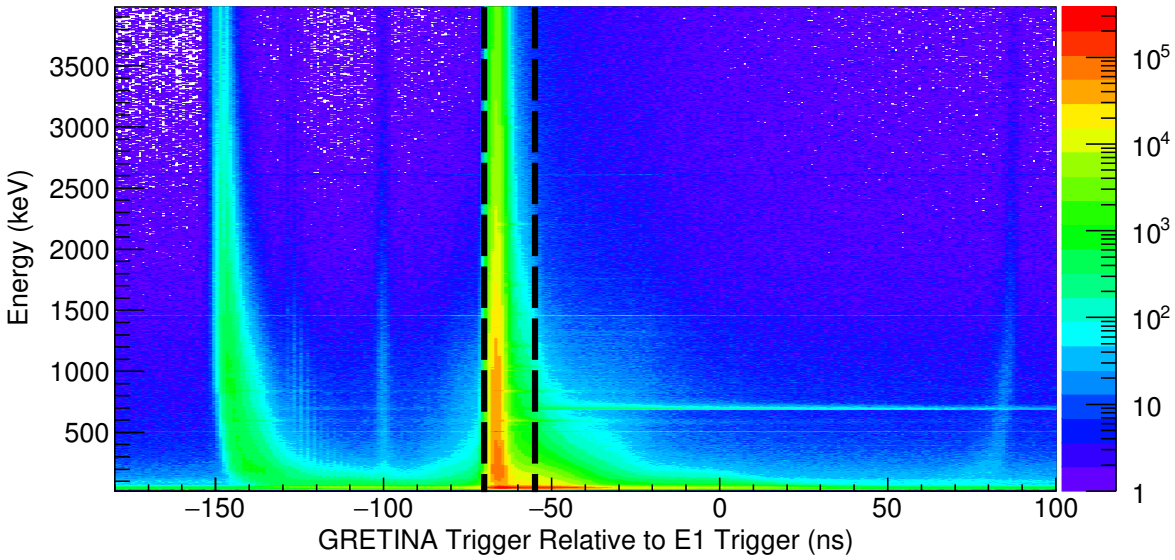

Figure 5.11: Detected γ-ray energy relative to the time difference between the GRETINA and E1 scintillator triggers. The black dashed lines indicate the timing gate of -70 to -55 ns which was applied.

Applying this timing condition is of particular importance when examining low-energy decays (< 300 keV) with low intensities as these can often get engulfed by Bremmstrahlung and background γ rays. The effects of the timing condition on the Doppler corrected γ-ray spectrum for ^{64}Zn is shown in Fig. 5.12, where there is a clear reduction in background counts < 200 keV. The signal-to-noise ratios at different energies with and without this timing condition are compared in Table 5.1 where there is an observed improvement across the whole energy range.

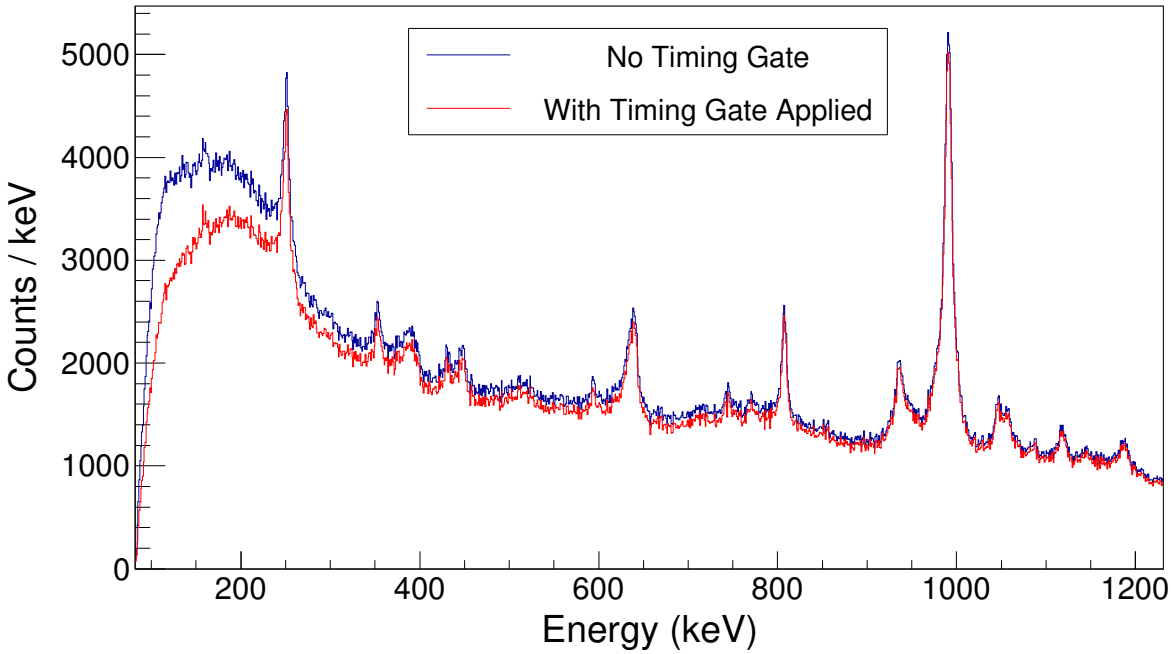

Figure 5.12: Comparison of ^{64}Zn γ-ray spectrum with (red) and without (blue) timing condition applied. There is a clear reduction in background counts < 200 keV.

Table 5.1: Comparison of signal-to-noise ratios across the energy range of $0-1$ MeV of the Doppler corrected γ-ray spectrum for ^{64}Zn in Fig. 5.12 with and without the timing gate applied.

Energy (keV)	**No Timing Gate**	**With Timing Gate**
160	1.47	1.53
250	1.22	1.24
350	1.07	1.08
449	1.23	1.25
808	1.66	1.69
991	3.63	3.69

5.2.4 Additional Corrections

As discussed in Ref. [84], sometimes additional corrections to the orientation of the beam axis relative to GRETINA are necessary to produce Doppler-corrected γ-ray energies that are constant over the polar angle, θ, and the azimuthal angle, ϕ, of GRETINA. This is achieved through applying offsets to the θ and ϕ of the beam, denoted θ_{beam} and ϕ_{beam}, respectively, typically of the order of a few mrad. Following optimisation of the target x, y, z-positions and β, the effects of the offset ϕ_{beam} were investigated through examining the dependence of the Doppler-corrected γ-ray energies with respect to the difference between polar angle ϕ of the point of first interaction of GRETINA and the polar angle of the beam, denoted $d\phi$. The $d\phi$ dependence of the 991.6-keV, $2^+ \rightarrow 0^+$ decay of ^{64}Zn is displayed in Fig. 5.13. Since there is no visible $d\phi$ dependence which was described in Ref. [84] no additional correction to θ_{beam} was applied.

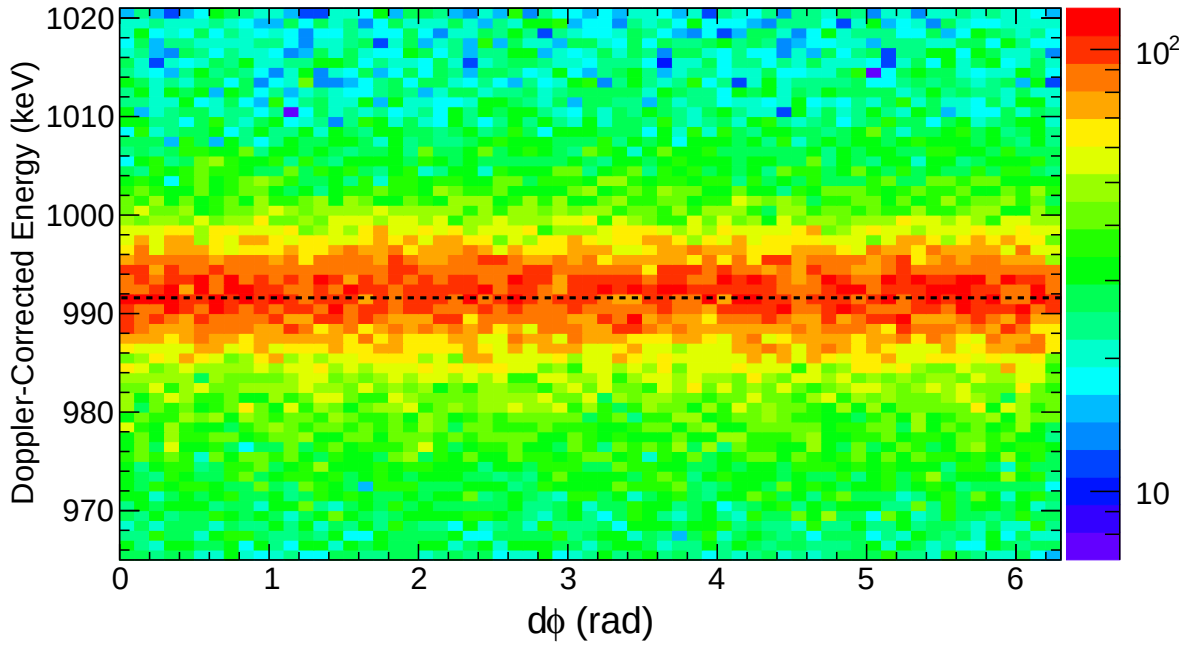

Figure 5.13: The dependence of the Doppler-corrected energy of the 991.6-keV, $2^+ \rightarrow 0^+$ decay of ^{64}Zn with the difference between the the azimuthal angle of the beam and the γ-ray detection azimuthal angle, denoted as $d\phi$. There is no apparent $d\phi$ dependence meaning that no correction to θ_{beam} was necessary.

5.3 $\gamma - \gamma$ Coincidence Analysis

$\gamma - \gamma$ coincidence events can be utilised to determine the series of γ-ray decays within a given cascade, allowing one to deduce a decay scheme for a given nucleus. A 2D $\gamma - \gamma$ matrix can be constructed by plotting the measured γ-ray energies with a multiplicity >1 within a given time window, which is then symmetrised along the diagonal such as in Fig. 5.14. Decays occurring within the same cascade will feed into one another, resulting in the series of decays occurring within a short time period. One can gate on a given energy through examining the projection onto either axis at the desired energy. This spectrum will then exhibit enhanced intensities at the energies of decays that occur within coincidence, or within the same cascade.

In some circumstances a background-subtraction procedure is required when examining gated $\gamma - \gamma$ coincidence data to distinguish which events exhibited a greater intensity than background. This is particularly important when gating at low energies (< 500 keV) where there is a greater background contribution. This was performed by taking a background sample, typically consisting of a gated spectrum averaged over gates just above and below the transition of interest, which is then scaled to correspond to the same width as the desired energy gate. This is then subtracted from the primary energy gate to remove any background events, leaving only genuine coincidence events.

In this case this method was of particular importance when determining transitions which feed into the $2^+ \rightarrow 0^+$ decay since these have to be included within the simulations given their impact of the measured lifetime of the $2^+ \rightarrow 0^+$ decay through the γ-ray lineshape method. This method was also employed to identify previously unobserved γ-ray transitions in ^{80}Zr and ^{79}Y, allowing for expansion upon the previously published decay schemes.

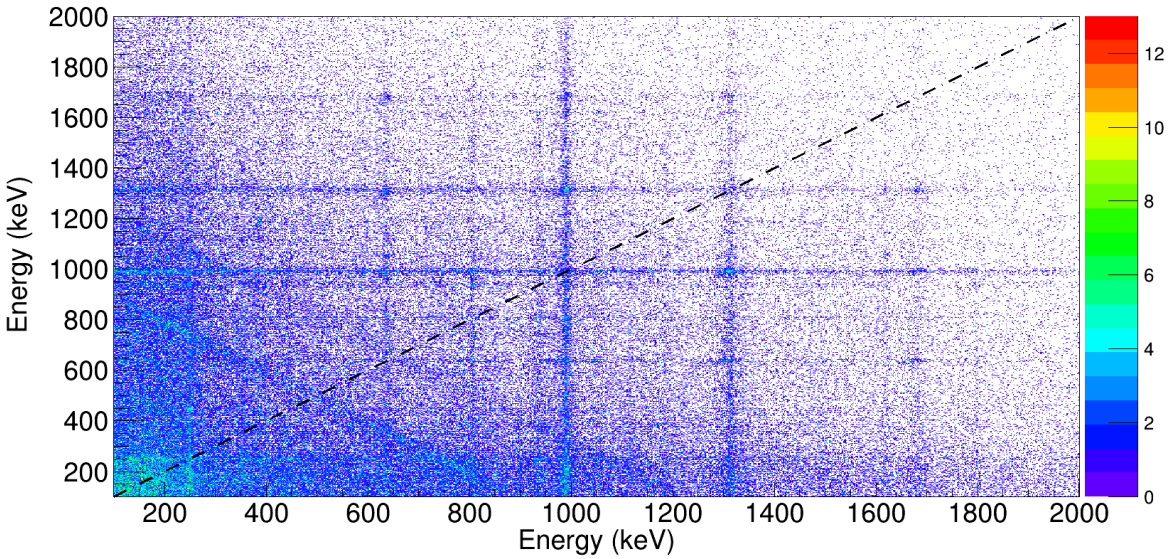

Figure 5.14: 2D $\gamma - \gamma$ matrix for ^{64}Zn. The dashed black line indicates where the matrix is symmetrised. A concentration of counts correlates to the two decays being in coincidence with one another, allowing a decay scheme to be deduced.

5.4 Extracting Relative Intensities

Decay intensities of γ-rays relative to the strongest decay can be calculated through measuring the integral under a given peak and correcting for the absolute efficiency of GRETINA at that given energy (see Fig. 3.7). This value can then be expressed as a percentage of the strongest decay, known as a relative intensity. In most cases the integral of a peak was calculated with a simple Gaussian function with a linear background. However in some cases, such as where two peaks are in close proximity to one another, a more sophisticated function had to be employed. In this case, a function with two overlapping Gaussian distributions and a linear background was used, allowing the integrals of each Gaussian peak to be extracted separately (see Fig. 5.15). When a peak possessed a low-energy tail a Crystal Ball function [111] was used, which is essentially a exponential term stitched to a Gaussian core such that the function and its first derivative are continuous.

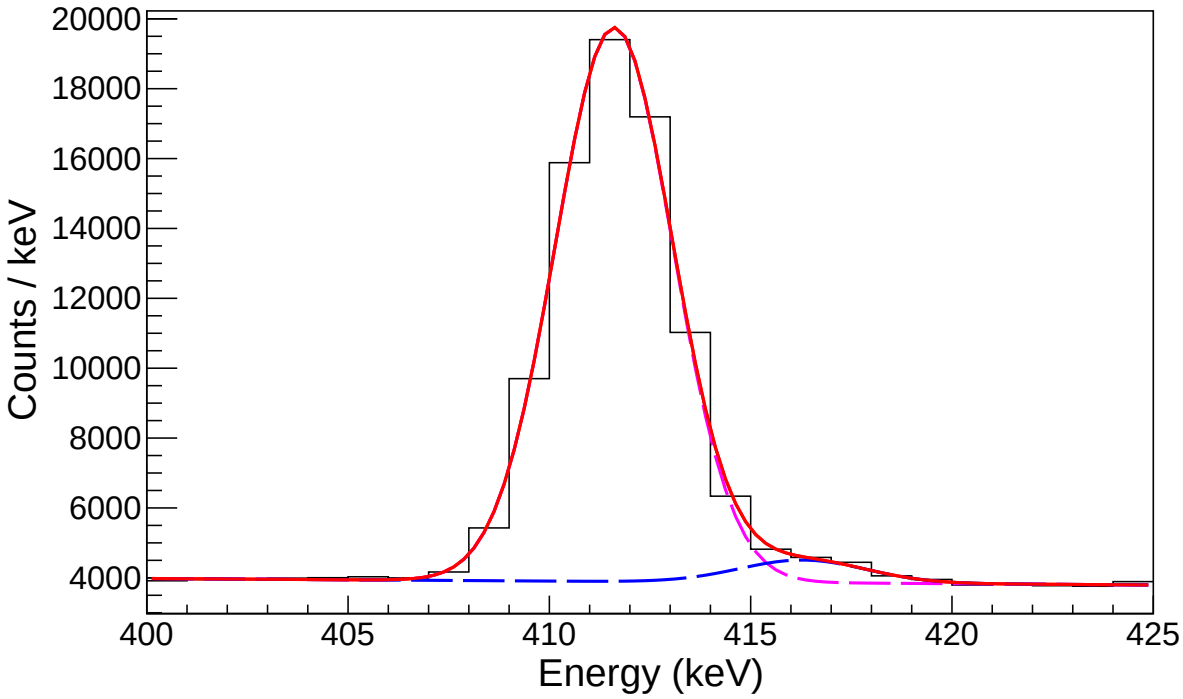

Figure 5.15: Two Gaussian functions with a linear background used to fit the 411-keV (dashed pink line) and 416-keV (dashed blue line) decays of the ^{152}Eu calibration source. The red line represents the sum of both of these fits. Decomposing the total fit into the Gaussian components allows the intensities of the overlapping peaks to be extracted separately.

As discussed in Chapter 5.2.1, the distribution of β values arising from nuclei reacting and decaying at different points within the target results in high and low-energy tails on peaks (see Fig. 5.8). The percentage of total counts within these tails was measured from the 991-keV peak in ^{64}Zn to be $\sim$3%. As all peaks will possess similar tails this percentage can be assumed to be consistent throughout all spectra. This therefore corresponds to a universal systematic discrepancy to the integrated counts of all peaks. As the intensities being measured are relative intensities, this therefore means that the ratios of counts of peaks relative to the strongest decay are unaffected by these tails.

5.5 Lifetime Simulations

Here the process of extracting the lifetimes and energies of the 2^+ states of the $N = Z$ nuclei of interest through the use of a simulation package simulating the geometry and physical properties of GRETINA, the reaction target and the S800 spectrograph will be detailed. This

will start by detailing the preliminary procedure of optimising properties of the simulation to accurate replicate experimentally-observed values. This will then lead to the procedure of measuring the lifetimes and energies of the decays through systematically varying parameters within the simulation until the experimental spectra are replicated.

5.5.1 γ-ray Lineshapes

The primary aim of this experiment was to extract the lifetimes of the $N = Z$ nuclei in question through the established γ-ray lineshape method [112, 113]. This method relies on the principle of states of nuclei with a long lifetime (>100 ps) decaying downstream of the target following the measured state being populated through a knockout reaction from the secondary beam within the ^{9}Be reaction target. At typical beam velocities of this experiment of $\sim 0.3c$, this corresponds to the reaction products travelling 9 mm downstream of the target per 100 ps. As discussed in Chapter 4.4.2, the γ-ray Doppler corrections are performed event-by-event and rely upon the γ-ray emission angle, θ, being accurately determined between the recoiling beam direction and first interaction point within GRETINA (see Eq. 4.4). As Doppler corrections are performed assuming the nucleus to have decayed at an effective target z-position, typically the end of the target in this case, this results in a low-energy shift in the Doppler-corrected γ rays emitted from nuclei decaying downstream of the target resulting in low-energy tails. The further downstream from the target the nuclei is at the time of deexcitation, the greater the magnitude of the low-energy Doppler shift. This results in a longer low-energy tail accompanied by proportional low-energy shift of the centroid of the peak with increasing lifetime (see Figs. 5.16 and 5.17). This method is only possible with HPGe arrays with high interaction position resolution such as GRETINA [84], SeGA [114] and AGATA [96] (all with a position resolutions <5 mm) since precisely determining the γ-ray emission angle, θ, is essential for the Doppler-correction process to provide an position resolution capable of resolving γ-ray lineshapes.

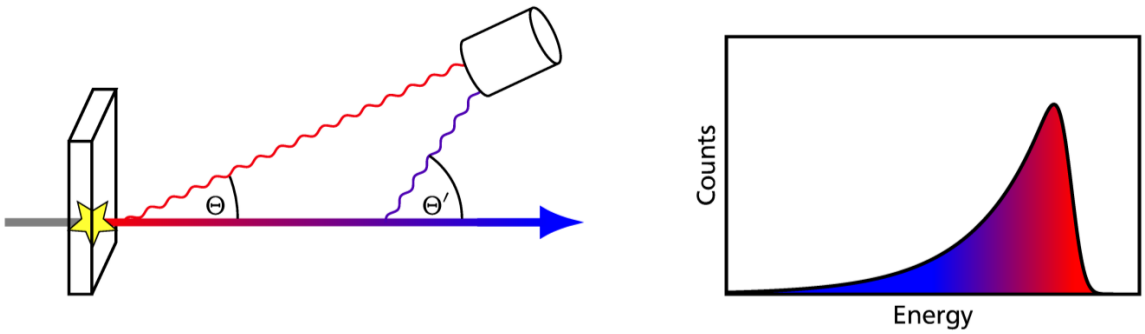

Figure 5.16: The effects on the γ-ray lineshape of a nucleus decaying downstream of the target as a consequence of a long lifetime. The longer the lifetime of the decay, the further downstream the average decay position. The further downstream the nucleus is at the time of decay, greater the magnitude of the low-energy shift and longer lineshape when Doppler corrected. Taken from [115].

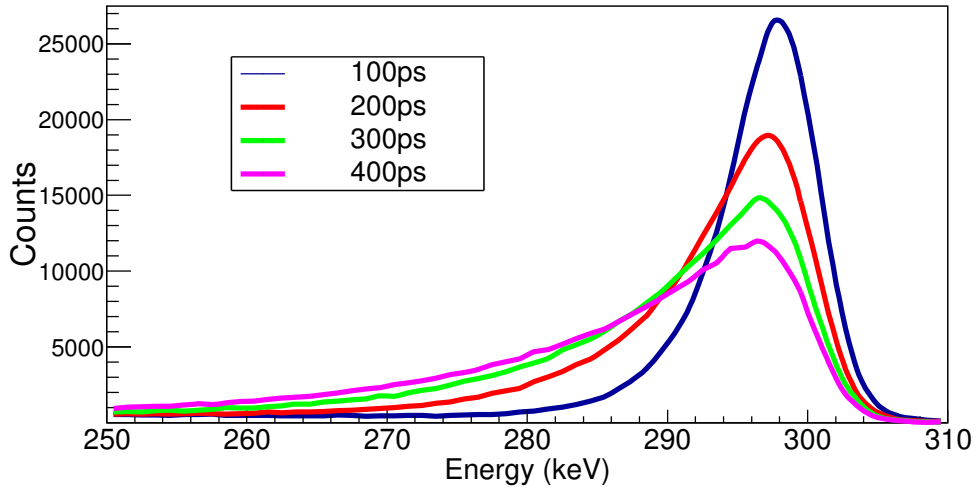

Figure 5.17: The simulated GRETINA lineshape spectra of a 300-keV γ ray decaying from a state with mean lifetimes varying from 100 to 400 ps at a beam velocity of $0.3c$. All simulations have the same intensity. Note that in addition to the longer low-energy tails the position of the peak is also lower in energy with increasing mean lifetime.

5.5.2 G4Lifetime Package

The lifetime analysis to measure the lifetime of the 2^+ states was performed through the use of the GEANT4 simulation framework [86]. The G4Lifetime package [87] for GEANT4, which has been developed at NSCL, was updated to incorporate the current ten module configuration of GRETINA geometry, including properties of the beamline, the ^{9}Be reaction target and

the detector frame (see Fig. 5.18). GEANT4 has the capability of accurately replicating the interactions of particle beams and the γ rays with matter, such as the interaction of the secondary beams with the ^{9}Be reaction target, the resulting interactions of the γ rays within the GRETINA detector modules and frame and the measurements taken in the S800 spectrometer. Properties of the GRETINA detector modules such as the first-interaction point position resolution and energy resolution can also be specified within the simulation package to produce values consistent with experimental data. The resulting simulated spectra are then available to view in the standard ROOT format (as with the experimental data) allowing for direct comparison.

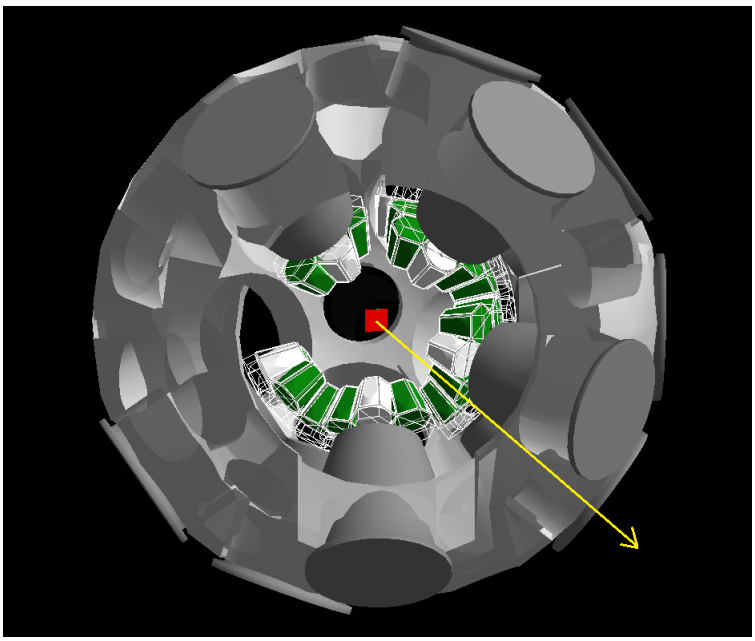

Figure 5.18: The geometry of the ten GRETINA modules (green and white) along with the ^{9}Be reaction target (red) and the detector frame (grey) simulated within the G4Lifetime GEANT4 package. Note that the viewing angle is slightly off centre to give the best perspective of each component of the simulation.

Throughout the lifetime simulation analysis it was vital that several experimental spectra were replicated in the GEANT4 simulation to ensure that the properties both the incoming and outgoing beams, in addition to the reaction target, are being accurately reproduced. This ascertains that processes such as the energy loss of the beam within the target and energy losses associated with the knockout reactions are consistent with the experiment. Optimising these simulation parameters results in outgoing beam energies that are an accurate

representation of the experimentally-observed outgoing beam, which is vital given that the lineshape that will be replicated is highly dependent on the β and momentum distribution of the decaying particles. The experimental spectra that have to be replicated to prior to exploring the effects of varying the lifetime and energy of decaying transitions include:

1. The dispersive and non-dispersive recoil angles at the target position (a_{ta} and b_{ta}). This is replicated by simply adjusting the centroid and widths of the a_{ta} and b_{ta} distributions within the simulation until the experimental spectra are replicated.

2. The non-dispersive position of the beam on the target (y_{ta}). As with a_{ta} and b_{ta} spectra, this is simply a case of adjusting the centroid and width of the y_{ta} distribution to match the experiment.

3. The kinetic energy (T) spread of the outgoing reacted particles, d_{ta}, given by dT/T. This was adjusted by varying the beam energy and momentum acceptance of the A1900 separator as well as the incoming and outgoing beam energies. When the reaction target is in place, d_{ta} is also dependent upon the scale density (accounting for discrepancies between stopping table data), thickness of the target and properties of the reaction mechanism within the simulation.

4. The β spectrum, which is very closely related to the d_{ta} spectrum. In most cases when the d_{ta} properties of the beam have been replicated within the simulation only minor adjustments to the beam energy are necessary to replicate the experimentally measured β.

The optimum simulation parameters are determined through comparison with experimental spectra and is achieved through the use of a χ^2-minimisation procedure, where χ^2 is given in [116]:

$$\chi^2 = \sum_{i=1}^{N} \frac{(x_i - y_i)^2}{\sigma_i^2}. \tag{5.4}$$

N is the total number of data points, x_i and y_i correspond to the experimental or the simulated data point, respectively and σ_i corresponds to the error on the experimental data point. When the simulation is accurately replicating the experimental data $(x_i - y_i)^2$ for a given data point will be small, resulting in a low total χ^2. Therefore, the total χ^2 is a good measure of

the agreement between the simulation and experimental spectra. Examples of optimising simulated parameters to match experimental spectra can be seen in Fig. 5.19.

The first preliminary stage of the lifetime analysis was to replicate the d_{ta} spectrum through simulation for the data where no reaction target was in place, therefore meaning that the full cocktail beam passes into the S800 spectrograph. In this case, the Bρ of the dipole magnets of the S800 spectrograph were tuned to 2.6037 Tm to allow maximum amount of the main secondary beam of interest (^{81}Zr) to reach the S800 focal plane. The d_{ta} spectrum produced for the incoming secondary beam through the use of the inverse map (see Chapter 3.5.2) can then be replicated through simulation by varying the incoming beam energy (KEU$_{in}$) and momentum acceptance (dp) within the simulation until consistency with experiment in accordance with Eq. 5.4 is achieved. The G4Lifetime package at the time of this analysis did not allow for the option of having no secondary reaction target, so the target thickness and scale density were both set to the lowest accepted values to replicate the absence of the target of 10^{-6} mm. Once the incoming beam and momentum acceptance values in the simulation have been optimised these remain constant throughout any further lifetime analysis utilising that specific secondary beam.

The next step was to optimise the target scale density of the ^{9}Be reaction target within the simulation to ensure the energy loss of the secondary beam within the target, both prior and post reaction, is accurately replicated within the simulation. This scale density factor is to account for any discrepancies between the LISE++ [117] and GEANT4 stopping tables and is therefore very close to 1, typically between 0.95 and 1.05. Optimisation of the properties of the target is vital given the strong dependence of the lineshape on β, which is closely related to the energy of outgoing reaction products produced at the target position. The scale density parameter is optimised through comparison with an experimental run where the S800 dipole magnets' Bρ were tuned to ensure that the ^{81}Zr beam is centred at the S800 focal plane, with the exception that this time there is a 188 mg/cm^2 ^{9}Be target in place. This therefore means that the secondary beam has been attenuated within the target prior to entering the spectrograph. As before, the d_{ta} spectrum is replicated, however, in this case this requires varying the scale density of the target and the energy of the outgoing beam (KEU$_{out}$). Once the target scale density has been determined it was kept constant throughout any further analysis with that given secondary beam.

The final stage was then to incorporate a nucleon-knockout reaction mechanism within the simulation to replicate the energy transfer occurring within the reaction target. This was achieved through varying the dp_{frac}, dp and dp_{FWHM} parameters, corresponding to the parallel momentum shift and transverse momentum shift and width, respectively. dp_{frac} and dp are incorporated into the final simulated momentum distribution of the particle following reaction within the target through Eq. 5.5 [118]:

$$p_{out} = p_{in} \times dp \times dp_{frac} \times \frac{A_{out}}{A_{in}}, \tag{5.5}$$

where $p_{in/out}$ corresponds to the momentum of a particle before and after the reaction, respectively, and A_{out}/A_{in} is the mass ratio of the reaction product and the incoming unreacted beam. dp_{FWHM} dictates the width of the momentum shift. Following the prescription of optimising earlier beam parameters, the optimum values were deduced through minimising the χ^2 when comparing the d_{ta} spectrum to the experimental spectrum of a reacted run with the ^{9}Be target in place [see Fig. 5.19(b)].

Once all of the properties of the incoming and outgoing beams have been replicated within the simulation, the known decay scheme of a specific nucleus can be specified within a GEANT4 macro, allowing a γ-ray spectrum to be produced while being Doppler corrected event-by-event with the simulated recoil velocities and angles. The current G4Lifetime code allows for the energies, lifetimes and intensities of different decays within a cascade to be specified, meaning that the effects of feeding from any higher spin transitions can be incorporated when simulating the γ-ray spectrum of any specified decay sequence. An *'effective'* GRETINA position resolution also has to be specified within the simulation. This is typically much larger than the true position resolution of 2 mm as the G4Lifetime package includes the x position of the recoil (i.e. x_{ta}) is included within the Doppler-correction process. As this information is not included with the experimental data the effective position resolution is increased to compensate for this. In this case an effective position resolution of 4.6 mm was found to produce the lowest χ^2.

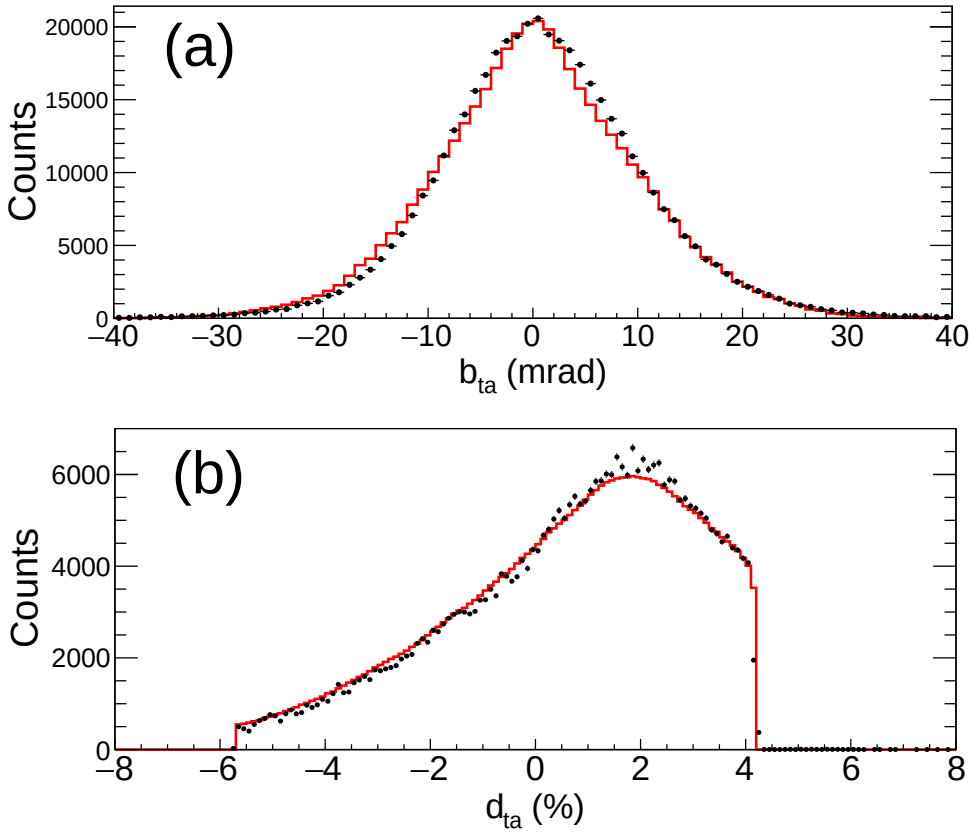

Figure 5.19: Examples of simulated spectra being optimised to accurately represent experimental data for ^{78}Sr. (a) shows the experimental b_{ta} spectrum (black data points) is compared with the simulated spectrum (solid red line). (b) shows the same with the d_{ta} spectrum with the reaction target in place. In both plots the y axis is the number of counts, where the simulated spectrum has been scaled down to match the experimental spectrum.

5.5.2.1 χ^2-Minimisation Procedure

Following the optimisation of the simulation, energies and lifetimes of the $2^+ \rightarrow 0^+$ states of the nuclei of interest were extracted from the experimental γ-ray spectra through systematically varying both within the G4Lifetime code. The optimum total χ^2 was then measured for each energy and lifetime combination when compared with the experimental γ-ray spectrum. For each combination of energy and lifetime of the 2^+ state of each nucleus a high-statistics simulation was produced with the G4Lifetime package. The scale of the simulated spectrum was then allowed to vary as a free parameter until the total χ^2 when compared to the experimental spectrum was minimised (see Eq. 5.4). An exponential background contribution (in the form $y = Ae^{-Bx}$) was added to each simulation to replicate background radiation

observed in the the experimental spectrum. Both of the terms A and B were allowed to vary as free parameters, resulting in a 3D χ^2-minimisation procedure for each simulated energy and lifetime combination. An example of this 3D χ^2-minimisation can be seen in Fig. 5.20, where a 2D slice of a the 3D plot showing the χ^2 distribution when varying the scale of the simulation and the gain of the exponential background (A) is displayed.

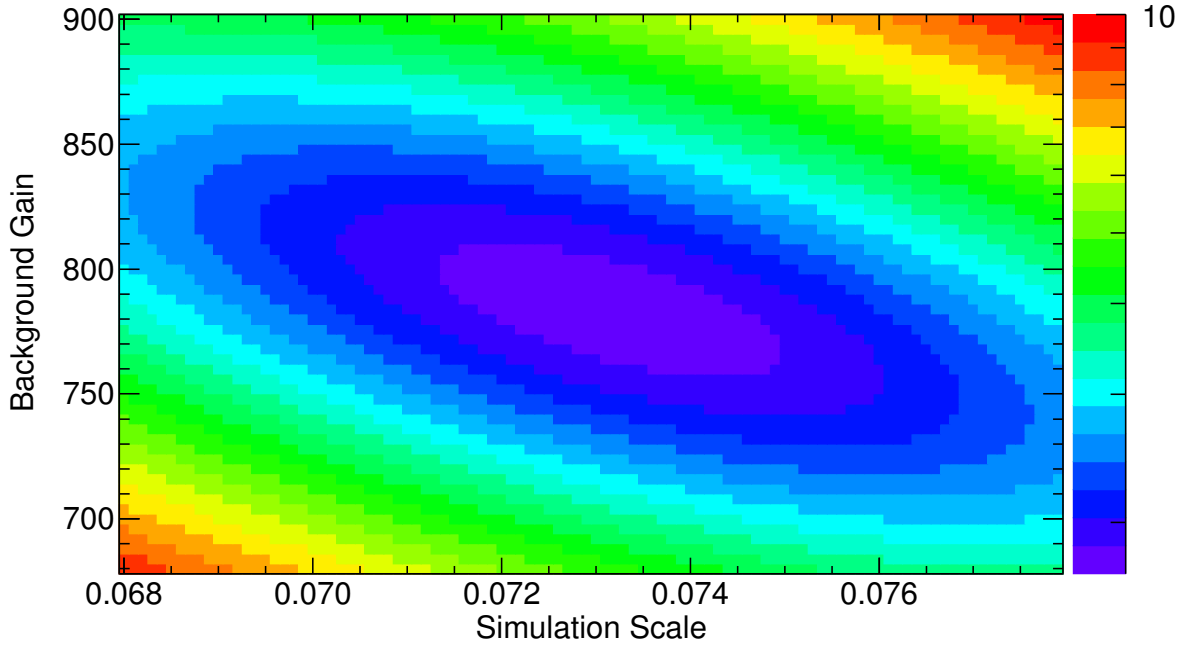

Figure 5.20: 2D χ^2 per degree of freedom (NDF) of the simulated spectrum compared to the experimental spectrum for ^{78}Sr whilst varying the scale of the simulated γ-ray spectrum (x axis) and the gain of the exponential background (A) added to the simulation (y axis). Note that this is a 2D slice of a 3D plot, with the third free parameter being the slope factor of the exponential background (B). The values at the minimum χ^2/NDF of this plot are used to determine the lowest χ^2/NDF for a given simulation with a specific $E(2^+)$ and lifetime.

The optimum χ^2 per degree of freedom (NDF), or reduced χ^2, for a given simulated energy and lifetime following the optimising of the simulation scale and exponential background contribution can then be plotted as a 2D histogram of lifetime vs energy. From this an energy and lifetime can be extracted from the minimum of the distribution, replicating the χ^2-minimisation procedure in Ref. [119]. Allowing the energy to vary in addition to the lifetime allows for uncertainties in energy associated with the z-position of the secondary target and other geometrical effects to be minimised, ensuring that the optimum value for the lifetime is deduced. This also eliminates factors arising from uncertainties of literature values

of the $2^+ \rightarrow 0^+$ decays. χ^2/NDF is a reliable measure of the consistency of the simulation with experiment, given that a χ^2/NDF ~ 1 is an indication that the simulation matches the experiment in accordance with the error variance [116].

5.5.2.2 Determining Uncertainties

The χ^2/NDF distributions as a function of lifetime for a given energy are typically parabolic. The statistical uncertainties of the measured lifetime at the optimised $E(2^+)$ energy can then be derived by determining the χ^2 value 1σ away from χ^2_{min}, corresponding to Eq. 5.6 [116]:

$$\Delta\chi^2_{min} = \chi^2_{min} + 1. \tag{5.6}$$

This statistical uncertainty can then be combined in quadrature with systematic uncertainties associated with a variety of factors to culminate in a total uncertainty on the measured lifetimes. The systematic uncertainties taken into account in the present work include:

1. The optimum outgoing beam velocity (β) for Doppler corrections.
2. The exponential background added to the simulated files to replicate the background radiation observed in the experimental spectrum.
3. The simulated position resolution of GRETINA.
4. Any factors associated with contaminant peaks within the lineshape, including the peak's lifetime and energy.
5. Effects of higher-energy states feeding into the $2^+ \rightarrow 0^+$ transition, including errors of the intensities of any feeding decays.
6. γ-ray anisotropy effects.
7. Geometrical uncertainties.

The systematic error associated with the uncertainty of the optimum β value used for Doppler corrections is determined by producing a Doppler-corrected γ-ray spectrum with a higher β value, approaching the upper/lower limit of an acceptable recoil velocity. The simulation parameters within the G4Lifetime code are then slightly adjusted to account for this change in the β value of the outgoing beam. The difference of the measured lifetime deduced

through the χ^2-minimisation procedure is then compared with the value measured with the optimised-β γ-ray spectrum to determine the associated systematic error. Likewise, the systematic error associated with the exponential background is simply derived through repeating the χ^2-minimisation procedure whilst varying the background range for the χ^2-minimisation procedure, therefore increasing the background contribution. Uncertainties arising from the simulated GRETINA position were determined by adjusting the simulated effective position resolution from 4.6 mm to the lowest previously used value of 3.5 mm [120] (where the typically used range is 4−5 mm) and repeating the procedure. The effects of feeding transitions were evaluated by removing any feeding transitions from the simulation and reevaluating the lifetime of the $2^+ \rightarrow 0^+$ state. Values for the uncertainties associated with γ-ray anisotropy effects and geometrical uncertainties are taken from Ref. [21] as 1.5% and 3%, respectively. Given that in this case the experimental γ-ray spectrum for ^{78}Sr has significantly more statistics than the other measured nuclei, ^{78}Sr was used a benchmark from which the systematic uncertainties associated with the GRETINA position resolution and the exponential background contribution were evaluated and the same percentage error was applied to the measured lifetimes of the other nuclei. This is described in further detail in Chapter 6.1.1.

In a similar fashion, the statistical uncertainty on the $2^+ \rightarrow 0^+$ energy was measured through projecting the 2D χ^2 plot onto the energy axis and extracting errors corresponding to $\chi^2_{min} + 1$. The systematic uncertainties which were added in quadrature with these to produce final $E(2^+)$ values include:

1. The optimum outgoing recoiling beam velocity (β) for γ-ray Doppler corrections.
2. The effective target z position used for γ-ray Doppler corrections.
3. The simulated position resolution of GRETINA.
4. Effects of the granularity of the 2D χ^2/NDF plot.

In the case of the recoil velocity and simulated GRETINA position resolution errors these were measured in the same manner as discussed above for the lifetimes.

The effects of any inaccuracies while deducing the effective target z position for the Doppler-correction process were accounted for through removing any offsets applied to the

reaction target z-position and repeating the χ^2-minimisation procedure. This is therefore assuming the target to be perfectly positioned in the centre of GRETINA. The 2D granularity error arises from the fact that the χ^2/NDF vs energy distribution used to measure $E(2^+)$ is produced by projecting the 2D χ^2/NDF plot onto the energy axis at the measured mean lifetime. Since this is projected at the measured lifetime from the fitted minimum of the χ^2/NDF distribution this can sometimes lie inbetween two data points on the lifetime axis. This means that the energy measured after projecting onto the energy axis may vary slightly depending on which row of bins is projected. Therefore, this systematic error is deduced by projecting onto the energy axis from the next bin along on the lifetime axis and remeasuring the energy. As before, the systematic uncertainties of $E(2^+)$ associated with the simulated GRETINA position resolution and the effective target z position are evaluated once for ^{78}Sr and the same percentage error was applied to the other measured nuclei. The remainder of the systematic errors were evaluated nucleus-by-nucleus. The 2D granularity factor was not evaluated for the lifetime uncertainty as comparatively the χ^2 is far less sensitive to a change in lifetime relative to a change in energy. This is because the measured energy is highly dependent upon the high-energy side of the γ-ray peak, meaning that a small shift in the simulated energy of the decay will drastically affect the χ^2. By comparison, the effects of varying the lifetime by $\pm$5 ps has a much smaller influence on the χ^2 as this will only slightly affect the γ-ray lineshape.

Chapter 6

Results

This chapter will detail the results obtained from both the lifetime and MED analysis. This will start by detailing the process of measuring the mean lifetime and energies of the 2^+ states of ^{80}Zr, ^{78}Y, ^{78}Sr and ^{76}Sr and extracting the systematic and statistical uncertainties of the final values. This will then proceed onto the stages that were involved in measuring the MED of ^{79}Zr/^{79}Y, including the elimination of any contamination and the optimising of the γ-ray spectra prior to extracting energies.

6.1 Lifetime Measurements

6.1.1 ^{78}Sr

The lifetime of the 2^+ state of ^{78}Sr was the first to be investigated as this would act as a test of the veracity of any further results given that there has been a previous, high precision measurement of the lifetime through the same method at NSCL of τ = 276(39) ps [21]. Furthermore, since ^{79}Sr was the second most abundant secondary beam and the one-neutron knockout reaction mechanism employed to populate ^{78}Sr has a large cross section a high number of counts were obtained during the experiment, allowing a value for the lifetime to be extracted with a small statistical uncertainty.

Through the method displayed in Fig. 5.7 an after-target recoil velocity of $\beta_{aft} = 0.294$ was deduced for the $2^+ \rightarrow 0^+$ decay and a mid-target recoil velocity of $\beta_{mid} = 0.296$ for the faster $4^+ \rightarrow 2^+$ decay. The γ-ray spectrum Doppler-corrected with β_{mid} and an average mid-target decay position to enhance faster transitions is shown in Fig. 6.1. The 278, 503

and 712-keV transitions correspond to the known $2^+ \rightarrow 0^+$, $4^+ \rightarrow 2^+$ and $6^+ \rightarrow 4^+$ decays [121], respectively. Although the 6^+ state can not be directly populated through one-neutron knockout (see Table 2.2), it is likely that the weak $6^+ \rightarrow 4^+$ decay is present due to the 6^- state being populated through one-knockout from the $g_{9/2}$ orbital which feeds into the 6^+ state [121]. This known $(6^-) \rightarrow (6^+)$ 1646-keV transition [121] has been tentatively labelled as 1645 keV in Fig. 6.1 due to the low statistics. There is also a clear low-energy 151-keV peak which is unassigned. Several low-intensity peaks seen between $0.8-2$ MeV are displayed in the inset of Fig. 6.1. The only higher energy decays of these which are known (other than the 1645-keV decay) are the 894-keV decay which is consistent with the known $8^+ \rightarrow 6^+$ energy and 1756-keV decay which corresponds to a known $(4^-) \rightarrow 4^+$ transition between two previously identified bands [121]. The decays seen for ^{78}Sr populated through the one-neutron knockout reaction mechanism from ^{79}Sr are summarised in Table 6.1 along with their relative intensities.

Upon inspection of the γ-ray lineshape there is a clear peak at 254 keV (see Fig. 6.1 and Fig. 6.5 for an expanded view), which was identified the known $5^- \rightarrow 4^-$ decay [121]. Through $\gamma - \gamma$ coincidence data this was found to be a feeding transition to the 2^+ state, although the exact γ-ray sequence could not be confirmed. It is likely that one of the unidentified high-energy decays from $1 - 2$ MeV seen in the inset of Fig. 6.1 form part of the $4^- \rightarrow 2^+$ decay sequence. This 254-keV decay was therefore included as a feeding transition within the simulation. Given that the lifetime of this state is unknown, one can assume a pure single-particle transition and estimate the lifetime through the Weisskopf estimate (see Eq. 2.26) to be of the order of a picosecond. Therefore, this 254-keV transition was included as a feeding transition with a lifetime of 1 ps in the γ-ray lineshape simulation, where its intensity was allowed to vary freely. The 503-keV, $4^+ \rightarrow 2^+$ decay was also included within the simulation with its known lifetime of 7.4 ps [122].

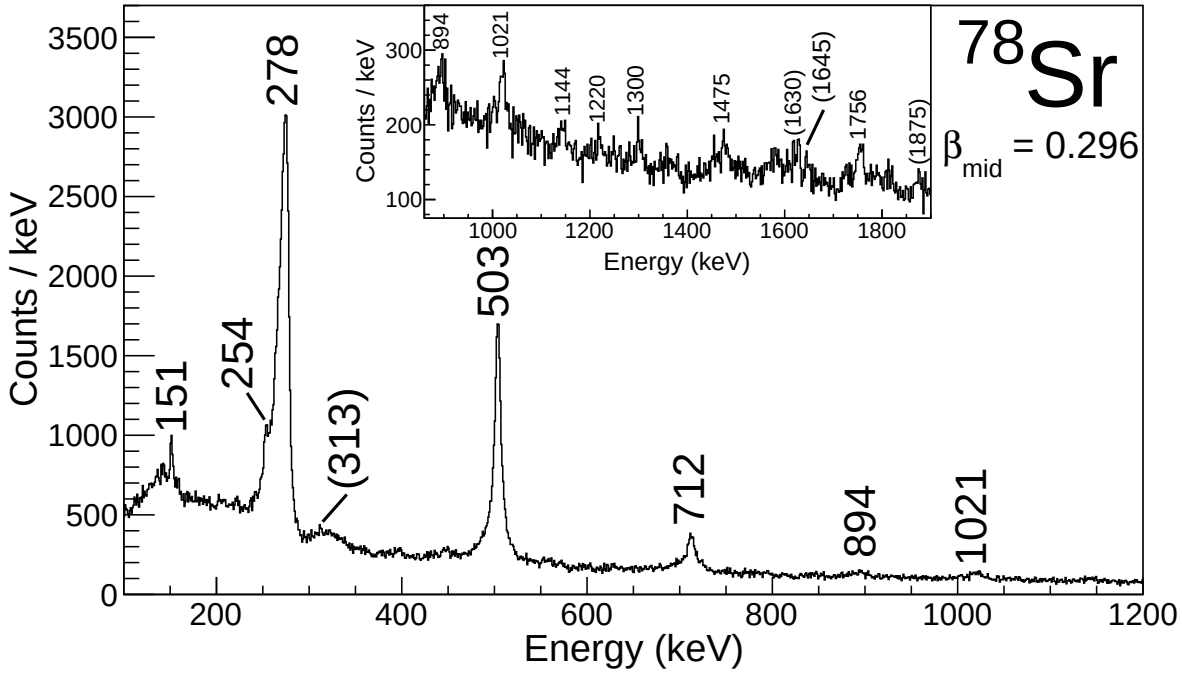

Figure 6.1: The Doppler-corrected γ-ray spectrum for ^{78}Sr corrected with a recoil velocity of $\beta_{mid} = 0.296$ and a mid-target average decay position to enhance faster transitions. The known 278-keV $2^+ \rightarrow 0^+$, 503-keV $4^+ \rightarrow 2^+$ and 712-keV $6^+ \rightarrow 4^+$ transitions are labelled, as well as the known 254-keV $5^- \rightarrow 4^-$ decay in the lineshape of the 278-keV peak.

Table 6.1: Efficiency-corrected relative intensities of decays of ^{78}Sr (populated from one-neutron knockout from ^{79}Sr) when Doppler-corrected with a mid-target average decay position and $\beta_{mid} = 0.296$. The measured energies are compared with earlier values from Ref. [121].

Transition	**Energy (keV)**	**Lit. Energy (keV)**	**Relative Intensity (%)**
	151.4(2)		2.3(5)
$(5^-) \rightarrow (4^-)$	253.8(3)	254.0(2)	1.3(3)
$2^+ \rightarrow 0^+$	278.1(3)	277.6(1)	100
$(6^-) \rightarrow (5^-)$	313.2(3)	313.0(4)	1.2(5)
$4^+ \rightarrow 2^+$	503.4(1)	503.2(1)	40.4(7)
$6^+ \rightarrow 4^+$	712.4(2)	712.4(2)	7.9(5)
$8^+ \rightarrow 6^+$	894.4(15)	895.2(2)	1.2(4)
	1020.8(6)		2.1(6)
	1143.8(19)		0.8(3)
	1219.8(18)		0.6(4)
	1300.2(12)		0.8(5)
	1476.8(13)		1.2(5)
	1626.6(20)		0.8(3)
$(6^-) \rightarrow 6^+$	1645.3(16)	1646.0(10)	0.6(3)
$(4^-) \rightarrow 4^+$	1755.0(12)	1756.0(10)	1.6(4)
	1874.8(15)		0.8(5)

Upon closer inspection of the $2^+ \rightarrow 0^+$ 278.1-keV decay [122] in Fig. 6.5 there is a high-energy tail around 280−290 keV. It was found that to replicate this high-energy tail it was necessary to increase the effective GRETINA position resolution within the simulation to $\sigma \sim 6.4$ mm, far exceeding the typically used values of 4−5 mm [120]. This was later judged to be a consequence of the incorrect reconstruction of a small number of a events by GRETINA and there is no simple way of including this effect within the simulations [120]. To account for this the region of 280−290 keV was excluded from the χ^2-minimisation procedure for ^{78}Sr. This was found to significantly lower the optimum χ^2/NDF but had no effect on the measured lifetime and energy. Furthermore, following the exclusion of this high-energy tail the utilised simulated GRETINA position resolution of 4.6 mm was found to produce the lowest χ^2, which was in the accepted range of 4−5 mm.

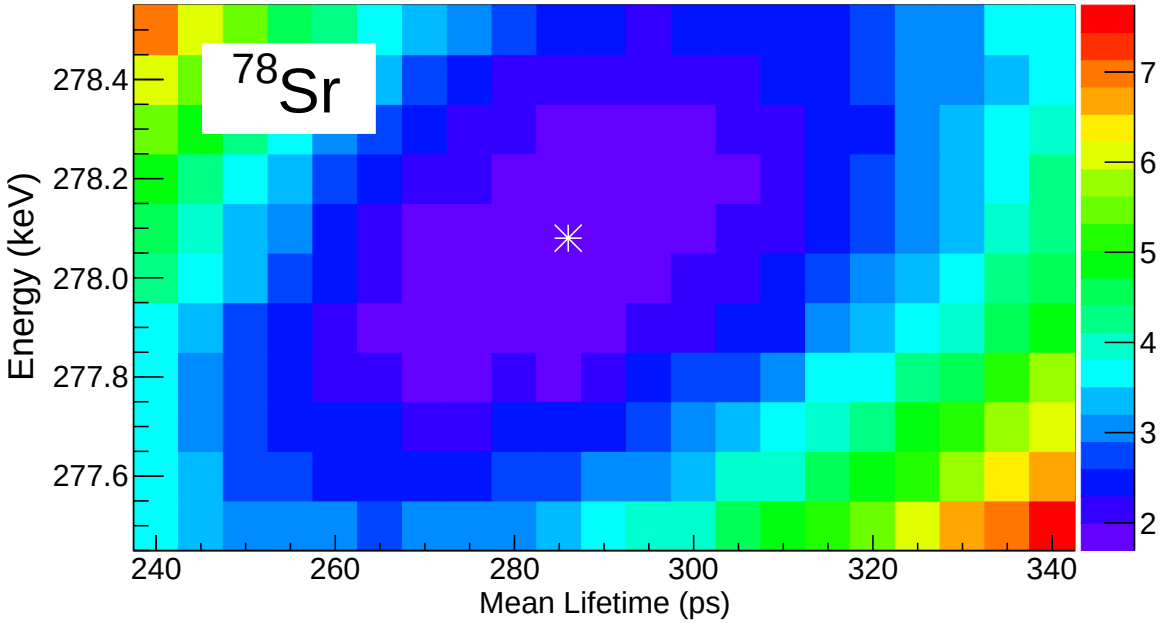

Figure 6.2: 2D χ^2 per degree of freedom (NDF) plot of mean lifetime and energy of the 2^+ state of ^{78}Sr of the experimental spectrum when compared with simulation. The white star indicates the location of the fitted minimum χ^2/NDF.

The 2D energy/lifetime χ^2/NDF plot for the ^{78}Sr $2^+ \rightarrow 0^+$ lineshape displayed in Fig. 6.2 was found to be minimised at $E(2^+) = 278.1$ keV and $\tau = 286$ ps. As discussed in further detail in Chapter 5.5.2.2, the discrepancy between the extracted lifetimes through varying the effective position resolution of GRETINA within the G4Lifetime simulation package from 4.6 to 3.5 mm for the 2^+ state in ^{78}Sr was used as a benchmark from which an uncertainty

of 6.2% was determined and applied to the measured lifetimes of the remaining nuclei. Likewise, repeating the χ^2-minimisation procedure with a background range of 220−380 keV rather than 190−350 keV was also used as a reference for the systematic error associated with the background energy range. To indicate this both of these systematic uncertainties are highlighted in bold in Table 6.2, which are listed with the remainder of the systematic uncertainties arising from the factors discussed in Chapter 5.5.2.2. Likewise, the systematic uncertainties in regards to the extracted $E(2^+)$ energy are detailed in Table 6.3, where again the values from ^{78}Sr used as references for the other nuclei investigated are in bold.

The 1D projections onto each axis of Fig. 6.2 are displayed along with the statistical uncertainties derived from $\chi^2_{min}+1$ from the χ^2-minimisation procedure in Figs. 6.3 and 6.4. When these statistical uncertainties of $\pm$0.04 keV and $\pm$3 ps are combined in quadrature with the systematic uncertainties detailed in Tables 6.2 and 6.3 values of $E(2^+)$= 278.1(3) keV and τ = 286(20) ps are obtained, making this the most precise measurement of the lifetime of the 2^+ state of ^{78}Sr to date. This shows agreement with the previous measurement of τ = 276(39) ps [21] and is consistent with the other measurement of τ = 224(27) ps [122] to just over 1σ. The weighted average of these values yields τ = 266(15) ps corresponding to B(E2$\downarrow$)= 1840(100) e^2fm^4. The experimental spectrum is presented with the optimised simulation at $E(2^+)$= 278.1 keV and τ = 286 ps in Fig. 6.5.

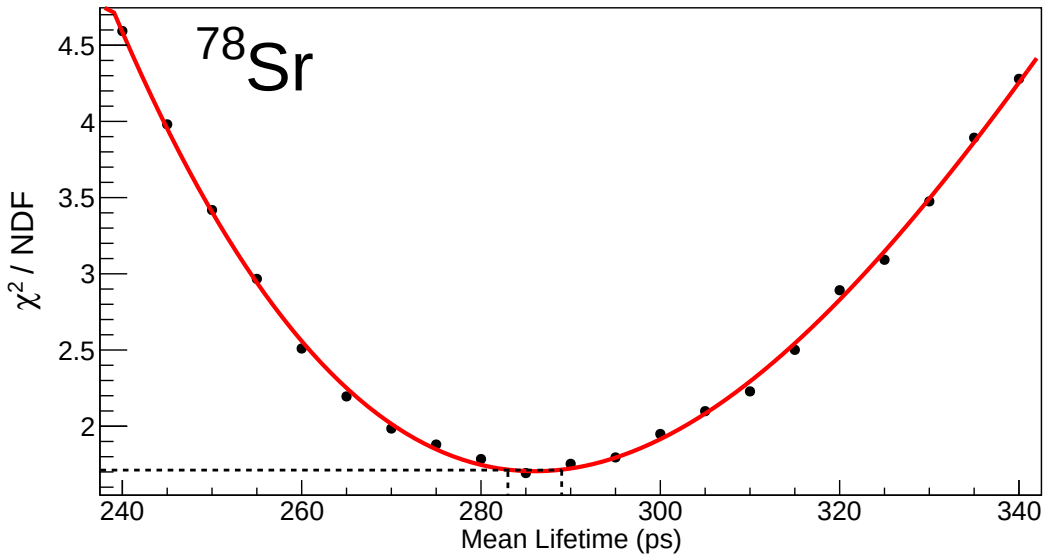

Figure 6.3: The χ^2 per degree of freedom (NDF) distribution of the simulated γ-ray spectrum when compared to the experimental spectrum of the mean lifetime of 2^+ state ^{78}Sr at the optimised energy of 278.1 keV. The red line is a third-order polynomial fit of the distribution. The dashed black line corresponds to the $\chi^2_{min} + 1/\text{NDF}$ from which the statistical uncertainties of ± 3 ps are deduced by projecting onto the lifetime axis.

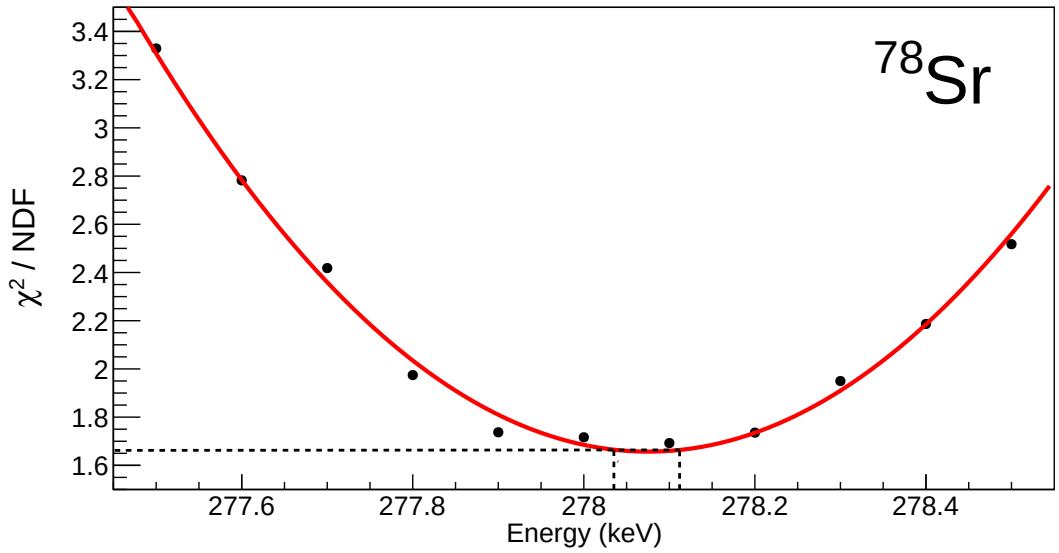

Figure 6.4: The χ^2 per degree of freedom distribution of the energy of 2^+ state ^{78}Sr at the optimised lifetime of 286 ps. The red line is a third-order polynomial fit of the distribution. The dashed black line corresponds to the $\chi^2_{min} + 1$ from which the statistical uncertainties are deduced by projecting onto the x axis.

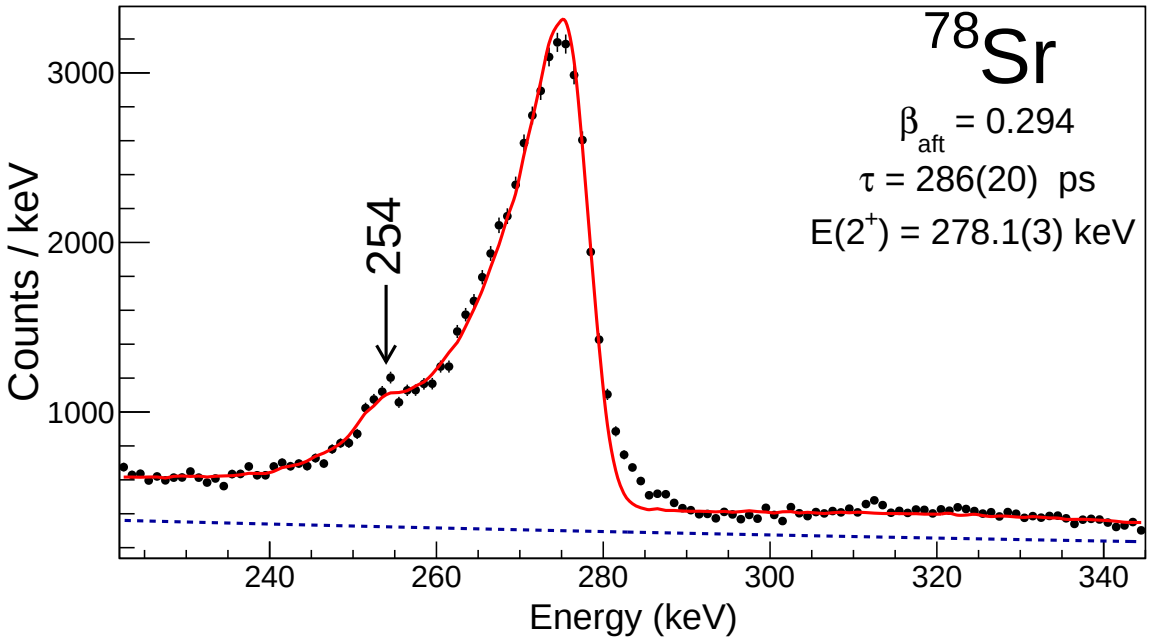

Figure 6.5: The optimised lineshape simulation (red) for ^{78}Sr at $E(2^+) = 278.1$ keV and $\tau = 286$ ps compared with the experimental γ-ray spectrum (black). The low-intensity 254-keV, $5^- \rightarrow 4^-$ transition is included as a feeding transition to the 2^+ state with a short lifetime of 1 ps. The simulation has an additional background contribution, indicated by the dashed blue line. The high-energy tail region from 280−290 keV was determined to be a consequence of incorrect GRETINA event reconstruction and was therefore excluded from the χ^2-minimisation procedure.

Table 6.2: Contributions to the total systematic error for the extracted lifetimes from the χ^2-minimisation procedure for ^{78}Sr. The values highlighted in bold were used as a reference values and applied to any other nuclei investigated.

Contribution	**Lifetime (ps)**	**Sys. Error (ps)**	**Sys. Error (%)**
Optimised	286.0		
No feeding	284.7	-1.3	0.4
$\beta = 0.290$	288.9	$+2.9$	1.0
3.5 mm position resolution	303.8	$+17.8$	**6.2**
Increased background	285.7	-0.3	**0.1**
Anisotropy effects		± 4.3	1.5
Geometrical uncertainties		± 8.6	3.0
Total		± 20.4	7.1

Table 6.3: Contributions to the total systematic error for the extracted 2^+ state energy from the χ^2-minimisation procedure for ^{78}Sr. The values highlighted in bold were used as a reference values and applied to any other nuclei investigated.

Contribution	$\boldsymbol{E(2^+)}$ **(keV)**	**Sys. Error (keV)**	**Sys. Error (%)**
Optimised	278.08		
No target offset	278.25	$+0.17$	**0.06**
$\beta = 0.290$	278.10	$+0.02$	0.01
2D granularity	278.13	$+0.05$	0.02
3.5 mm position resolution	278.25	$+0.17$	**0.06**
Total		± 0.25	0.09

6.1.2 ^{76}Sr

As with ^{78}Sr, a previous measurement of the lifetime of the 2^+ state of ^{76}Sr of $\tau = 296(36)$ ps [21] (also taken at NSCL through the γ-ray lineshape method) provides a good reference to test the reliability of any results obtained in this investigation through the same method. Since ^{76}Sr is an $N = Z$ nucleus it is also of particular interest in terms of $B(\text{E2}\downarrow)$ evolution along the $N = Z$ line meaning a repeated measurement and a reduction in uncertainty is highly desirable.

^{76}Sr was populated through a more complicated reaction mechanism than the other nuclei investigated, being three-neutron, one-proton removal from the ^{80}Y secondary beam. As a result of this, relatively low statistics were acquired as a consequence of the low reaction cross section. Although statistics similar to that of ^{78}Y (for which there was difficulty determining the recoil velocity) were obtained for ^{76}Sr, the absence of any peaks near both the $2^+ \rightarrow 0^+$ and $4^+ \rightarrow 2^+$ decays meant that the traditional method of eliminating the θ dependence of the Doppler-corrected γ-ray energy could still be employed to determine β. This resulted in an after-target recoil velocity of $\beta_{aft} = 0.298$ and $\beta_{mid} = 0.305$ for the faster 484-keV, $4^+ \rightarrow 2^+$ decay.

Previous spectroscopy of ^{76}Sr has been performed through the ^{40}Ca(^{40}Ca, 2p2n)^{76}Sr [9] and ^{24}Mg(^{54}Fe, 2n)^{76}Sr [123] fusion-evaporation reactions where states up to $J = 16^+$ were identified. The γ-ray spectrum from this work, Doppler-corrected with $\beta_{mid} = 0.305$ to enhance any faster decays, is shown in Fig. 6.6. The known 262-keV $2^+ \rightarrow 0^+$ and 484-keV $4^+ \rightarrow 2^+$ decays [9, 123] are both very pronounced. The peak tentatively labelled at 700 keV is assumed to correspond to the $6^+ \rightarrow 4^+$ decay given its consistency with the known energy [9, 123]. There is also another peak around four times above background which is assigned tentatively at 903 keV due to its width of just one 2-keV channel, whereas a *'true'* peak would possess a FWHM of several channels. Due to their low statistics, the uncertainty of the 700 and 903-keV decay energies are given as the one channel width of 2 keV. These and the other two visible peaks are summarised with their corresponding efficiency-corrected relative intensities in Table 6.4. The measured decay energies are compared to the literature values from Refs. [9, 123] where weighted averages have been taken. Due to low statistics it was not possible to perform any $\gamma - \gamma$ coincidence analysis to explore these unidentified transitions any further.

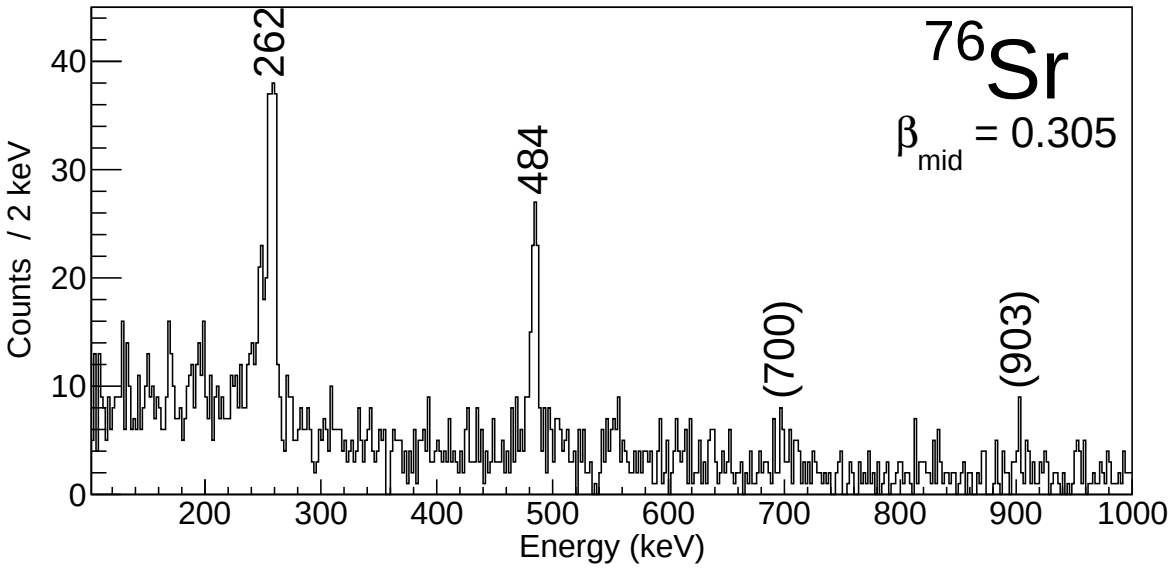

Figure 6.6: Doppler-corrected γ-ray spectrum for ^{76}Sr Doppler corrected with a mid-target recoil velocity of $\beta_{mid} = 0.305$ to enhance any faster decays. The only clear transitions are the known $2^+ \rightarrow 0^+$ and $4^+ \rightarrow 2^+$ decays at 262 and 484 keV, respectively. There is a tentatively labelled peak at 700 keV which is assumed to be the $6^+ \rightarrow 4^+$ decay given the consistency with the known energy.

Table 6.4: Efficiency-corrected relative intensities of decays of ^{76}Sr populated from three-neutron, one-proton removal from ^{80}Y. The uncertainties on the 700 and 903-keV energies are quoted as the one-channel width of 2 keV given the low statistics. Where available, the energies are compared with weighted average values from Refs. [9, 123].

Transition	**Energy (keV)**	**Lit. Energy (keV)**	**Relative Intensity (%)**
$2^+ \rightarrow 0^+$	261.6(5)	261.8(2)	100
$4^+ \rightarrow 2^+$	484.4(4)	483.7(2)	50(12)
$6^+ \rightarrow 4^+$	700.0(20)	698.4(2)	23(8)
	902.5(20)		9(7)

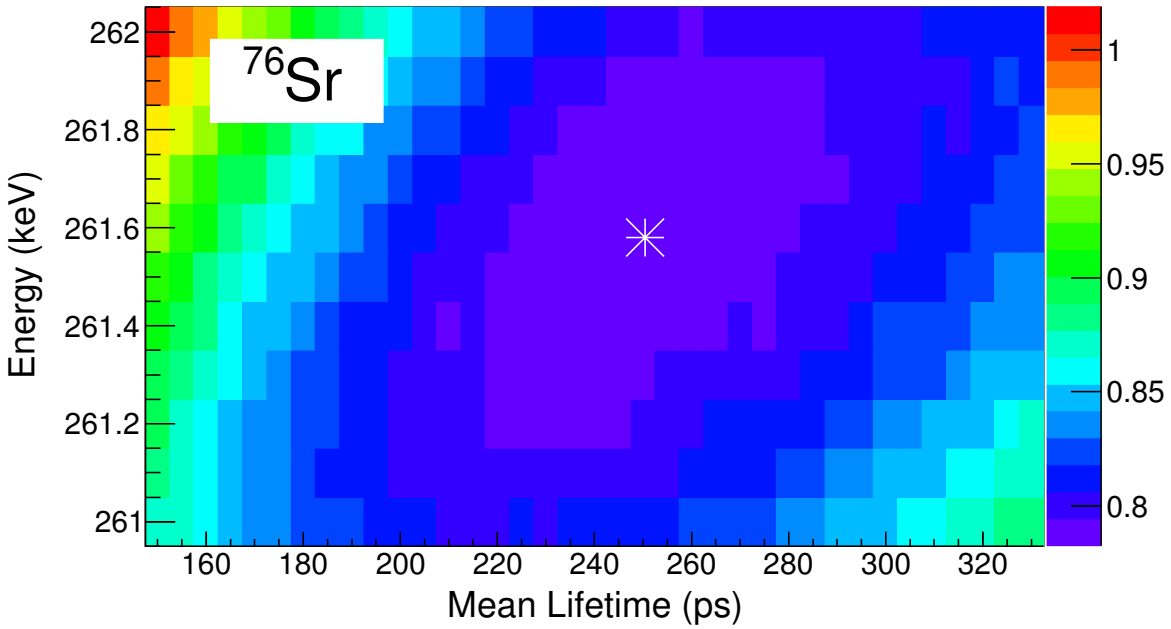

Figure 6.7: 2D χ^2 per degree of freedom plot of the simulated $2^+ \rightarrow 0^+$ transition of ^{76}Sr against the experimental spectrum whilst varying the energy and the mean lifetime of the state. The white star indicates the minimum of the distribution.

The 2D energy/lifetime χ^2/NDF distribution of the simulated spectra when compared to the experimental spectrum for the $2^+ \rightarrow 0^+$ decay of ^{76}Sr is shown in Fig. 6.7. The $4^+ \rightarrow 2^+$ decay was included as a feeding transition within the simulation, which if assuming a similar $B(\text{E2}\downarrow)$ to that of ^{78}Sr and scaling by a factor of $1/E_\gamma^5$ (see Eq. 2.20) yields a mean lifetime of 7 ps. The projections onto the lifetime and energy axis are displayed in Figs. 6.8 and 6.9, respectively, where values and statistical errors of $\tau = 250(35)$ ps and $E(2^+)= 261.6(4)$ keV are extracted from the $\chi^2_{min} + 1/\text{NDF}$ values of each distribution. The systematic factors of the uncertainty are detailed for the measured lifetime and energy in Tables 6.5 and 6.6, respectively. Incorporating both statistical and systematic uncertainties in quadrature yields values of $\tau = 250(44)$ ps and $E(2^+)= 261.6(5)$ keV, producing a $B(\text{E2}\downarrow)= 2660(470)$ $e^2\text{fm}^4$, by far the largest measured $B(\text{E2}\downarrow)$ of the $N = Z$ nuclei in this region. The measured mean lifetime is consistent with the previous measurement of $\tau = 296(36)$ ps [21]. The measured $E(2^+)$ of 261.6(5) keV also agrees with the weighted average of the measurements of Refs. [9, 123] of $E(2^+)= 261.8(2)$ keV. Taking a weighted average of these two measurements yields a mean lifetime of $\tau = 278(28)$ ps, corresponding to a $B(\text{E2}\downarrow)= 2390(240)$ $e^2\text{fm}^4$. This still exceeds the measured $B(\text{E2}\downarrow)$ of ^{80}Zr of 1910(170) $e^2\text{fm}^4$, making ^{76}Sr the location of the

maximum of collectivity, just before the mid-shell ^{78}Y which is found to show a significant reduction in collectivity.

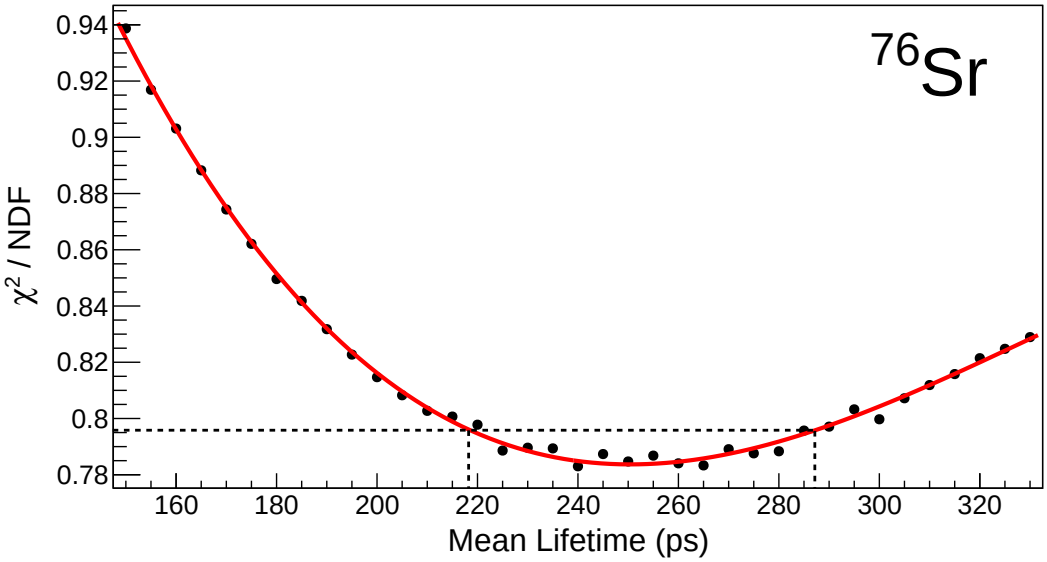

Figure 6.8: The χ^2 per degree of freedom distribution of the mean lifetime of 2^+ state ^{76}Sr at the optimised energy of 261.6 keV. The red line is a third-order polynomial fit of the distribution. The dashed black line corresponds to the $\chi^2_{min} + 1$ from which the statistical uncertainties are deduced by projecting onto the x axis.

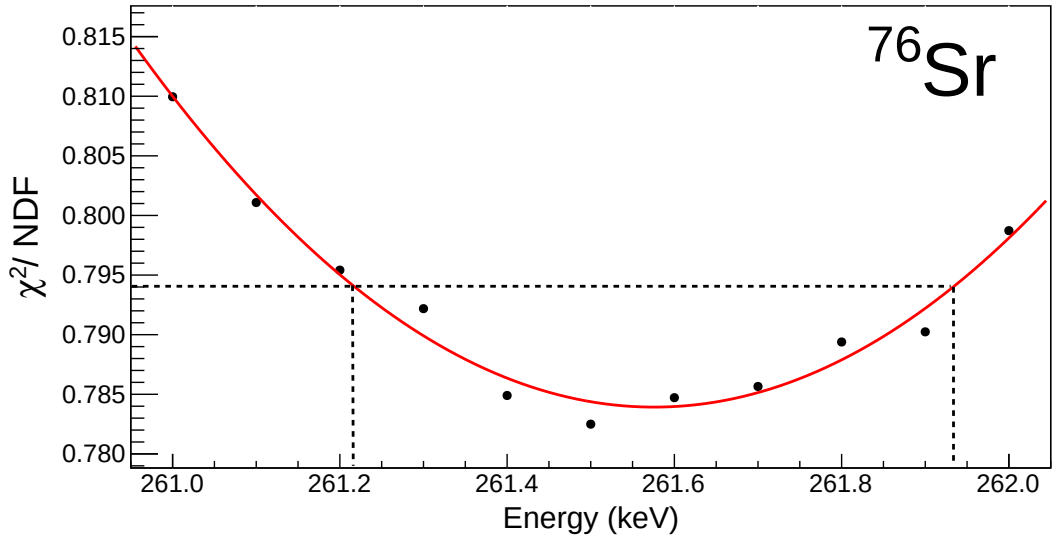

Figure 6.9: The χ^2 per degree of freedom distribution of the energy of 2^+ state ^{76}Sr at the optimised mean lifetime of 250 ps. The red line is a third-order polynomial fit of the distribution. The dashed black line corresponds to the $\chi^2_{min} + 1$ from which the statistical uncertainties are deduced by projecting onto the x axis.

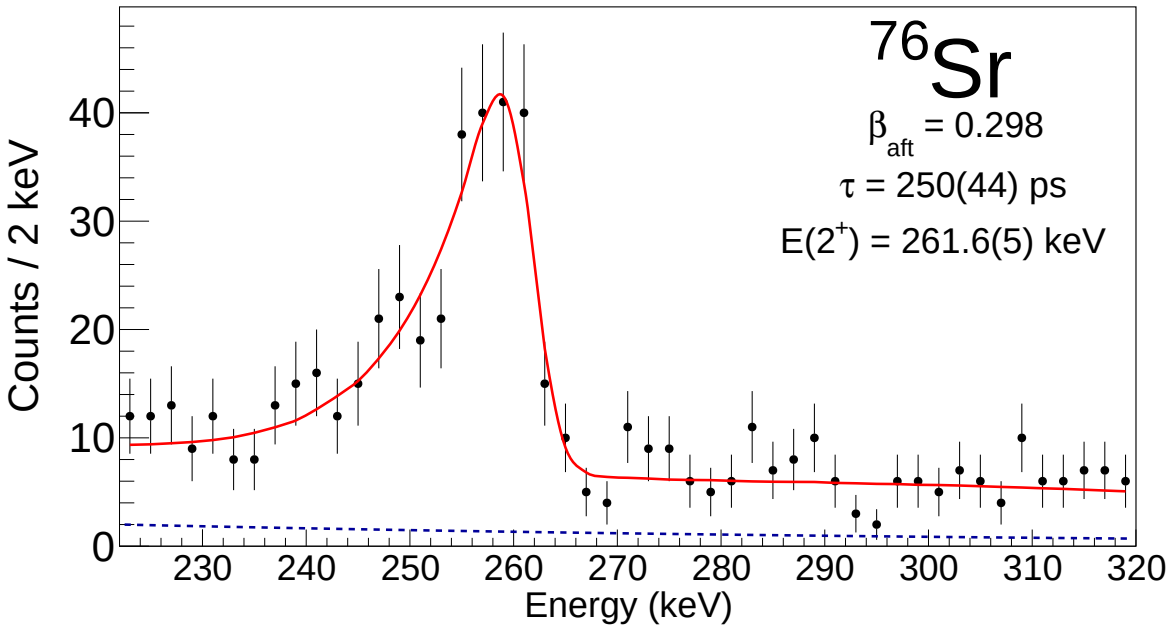

Figure 6.10: The optimised simulated γ-ray spectrum (red) with τ = 250 ps at $E(2^+)$= 261.6 keV compared with experiment (black) Doppler corrected with β_{aft} = 0.298. The dashed blue line is the additional exponential background contribution.

Table 6.5: Summary of systematic errors associated with the mean lifetime for the 2^+ state of ^{76}Sr. The errors are combined in quadrature at the bottom of the table.

Contribution	**Lifetime (ps)**	**Sys. Error (ps)**	**Sys. Error (%)**
With feeding	250.4		
No feeding	250.2	-0.2	0.1
$\beta = 0.296$	270.6	$+20.2$	8.1
3.5 mm position resolution		$+15.5$	6.2
Increased background		± 0.3	0.1
Anisotropy effects		± 3.8	1.5
Geometrical uncertainties		± 7.5	3.0
Total		± 26.8	10.7

Table 6.6: Contributions to the total systematic error for the extracted 2^+ state energy from the χ^2-minimisation procedure for ^{76}Sr. The values for the no target offset and 3.5 mm simulated position resolution systematic errors were taken from the percentage error of 0.06% measured from ^{78}Sr.

Contribution	$\boldsymbol{E(2^+)}$ **(keV)**	**Sys. Error (keV)**	**Sys. Error (%)**
Optimised	261.59		
No target offset	261.75	$+0.16$	0.06
$\beta = 0.296$	261.80	$+0.21$	0.08
2D granularity	261.53	-0.06	0.02
3.5 mm position resolution	261.75	$+0.16$	0.06
Total		± 0.31	0.12

6.1.3 ^{80}Zr

Prior to any lifetime analysis of the $2_1^+ \rightarrow 0_1^+$ peak lineshape of ^{80}Zr the possibility of any feeding transitions had to be assessed. The after-target recoil velocity in this case was well known since throughout the experiment the Bρ of the S800 spectrograph had been tuned for the optimum amount of ^{80}Zr to reach the focal plane. This Bρ of 1.95175 Tm corresponds to $\beta_{aft} = 0.299$ which indeed was found to be the optimum velocity at which the polar angle of GRETINA dependence of the Doppler-corrected γ-ray energy was eliminated. The recoil velocity of the faster transitions was found to be $\beta_{mid} = 0.304$ which was deduced through removing the dependence for the known 539-keV $4_1^+ \rightarrow 2_1^+$ transition [11, 123]. When corrected with this recoil velocity and assuming a mid-target decay position (see Fig. 6.11) there are several previously unidentified transitions, namely those at 464, 891, 950 and 1416 keV.

The expected state population from one-neutron knockout from ^{81}Zr detailed in Table 2.2 is consistent with the spectrum in Fig. 6.11. Decays from the 2^+ and 4^+ states are observed but as expected there is no visible 779-keV $6^+ \rightarrow 4^+$ decay as there are no orbitals in ^{81}Zr from which a neutron can be removed to directly populate the 6^+ state in ^{80}Zr. The unknown decays discussed above are likely negative parity states populated from 1n knockout from the $g_{9/2}$ and $d_{5/2}$ orbitals. ^{80}Zr was previously produced through a ^{24}Mg(^{58}Ni, 2n)^{80}Zr fusion-evaporation reaction in the work presented in Ref. [123] where states up to 10^+ were populated. The 891-keV transition was previously alluded to in Ref. [123], but was not identified as a part of a γ-ray decay sequence, where the authors hypothesised it may be a member of the γ band. None of the other unidentified decays are seen in the ^{80}Zr spectrum in Ref. [123]. The only other ^{80}Zr γ-ray spectrum was measured in Ref. [11] (produced through the same fusion-evaporation reaction) where only the $2^+ \rightarrow 0^+$ and $4^+ \rightarrow 2^+$ decays were observed. The measured transition energies from Refs. [11] and [123] are compared with the values measured in this work in Table 6.7, where weighted averages have been used where possible. The $E(2^+)$ deduced through the χ^2-minimisation procedure is slightly higher than the previous measurements. However, the $2^+ \rightarrow 0^+$ is labelled as 290 keV in the γ-ray spectrum in Ref. [11], which agrees with the new measurement of 290.4(4) keV.

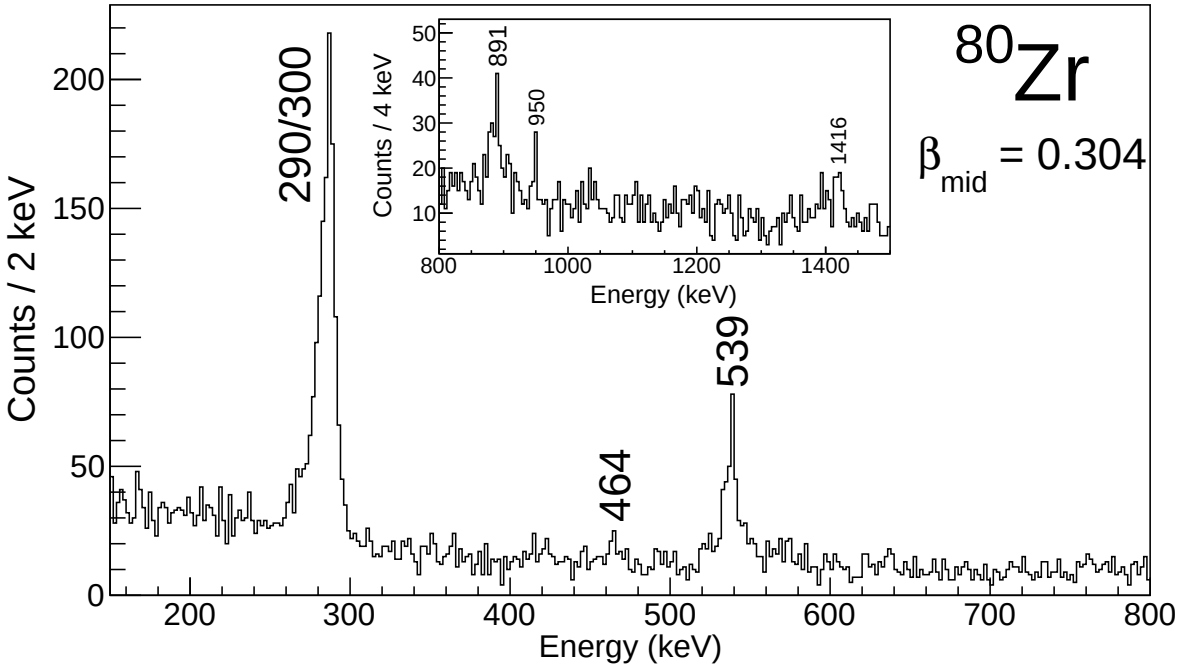

Figure 6.11: The Doppler-corrected γ-ray spectrum for ^{80}Zr, populated from one-neutron knockout from ^{81}Zr, Doppler corrected with a mid-target recoil velocity of $\beta_{mid} = 0.304$ and an average decay position at the centre of the target. The $2^+ \rightarrow 0^+$ decay is labelled as 290/300 keV as $\gamma - \gamma$ analysis suggests the presence of a weak 300-keV decay engulfed by the high intensity 290-keV decay (see text and Fig. 6.13).

Through examining $\gamma - \gamma$ coincidence data and gating on the 290-keV transition the known 539-keV $4_1^+ \rightarrow 2_1^+$ peak and the previously unidentified peak at 950 keV are visible as a feeding transitions [see Fig. 6.12(a)]. There is also a visible peak $\sim$ 625 keV when gating on 290 keV, but this is not clear on the ungated spectrum in Fig. 6.11. The 950-keV peak disappears when gating on 539 keV [see Fig. 6.12(b)], an indication of the 950-keV decay feeding directly into the 2_1^+ state. Gating on the 950-keV peak only shows a peak at 290 keV [see Fig. 6.12(c)], cementing the 950-keV decay as a feeding transition to the 2_1^+ state. Likewise, this was also the case when gating on the 464-keV transition [see Fig. 6.12(d)]. Interestingly, a peak at 300 keV is visible when gating on the unknown 891-keV transition [see Fig. 6.12(e)], which is not clear in the ungated spectrum (Fig. 6.11) since it is enveloped by the high intensity 290-keV peak. This is displayed with an expanded view in Fig. 6.13, where there is an evident discrepancy between the peaks at 290 and 300 keV when gating on 539 and 891 keV, respectively. It is therefore probable that the 300-keV peak corresponds to a $4_2^+ \rightarrow 2_2^+$ decay of a previously unseen rotational band, with the 891-keV peak corresponding

to the decay from the 2_2^+ of this new band to the 0_1^+ ground state. Several rotational bands like this all below 2.5 MeV were predicted through beyond mean-field methods by Rodríguez in Ref. [29]. If the hypothesis of Ref. [123] is true then this 891-keV decay may be a transition from one of these bands to the 0_1 ground state. There were no clear transitions in coincidence when gating on the 1416-keV peak which was therefore tentatively assigned as a decay straight to the 0_1^+ ground state.

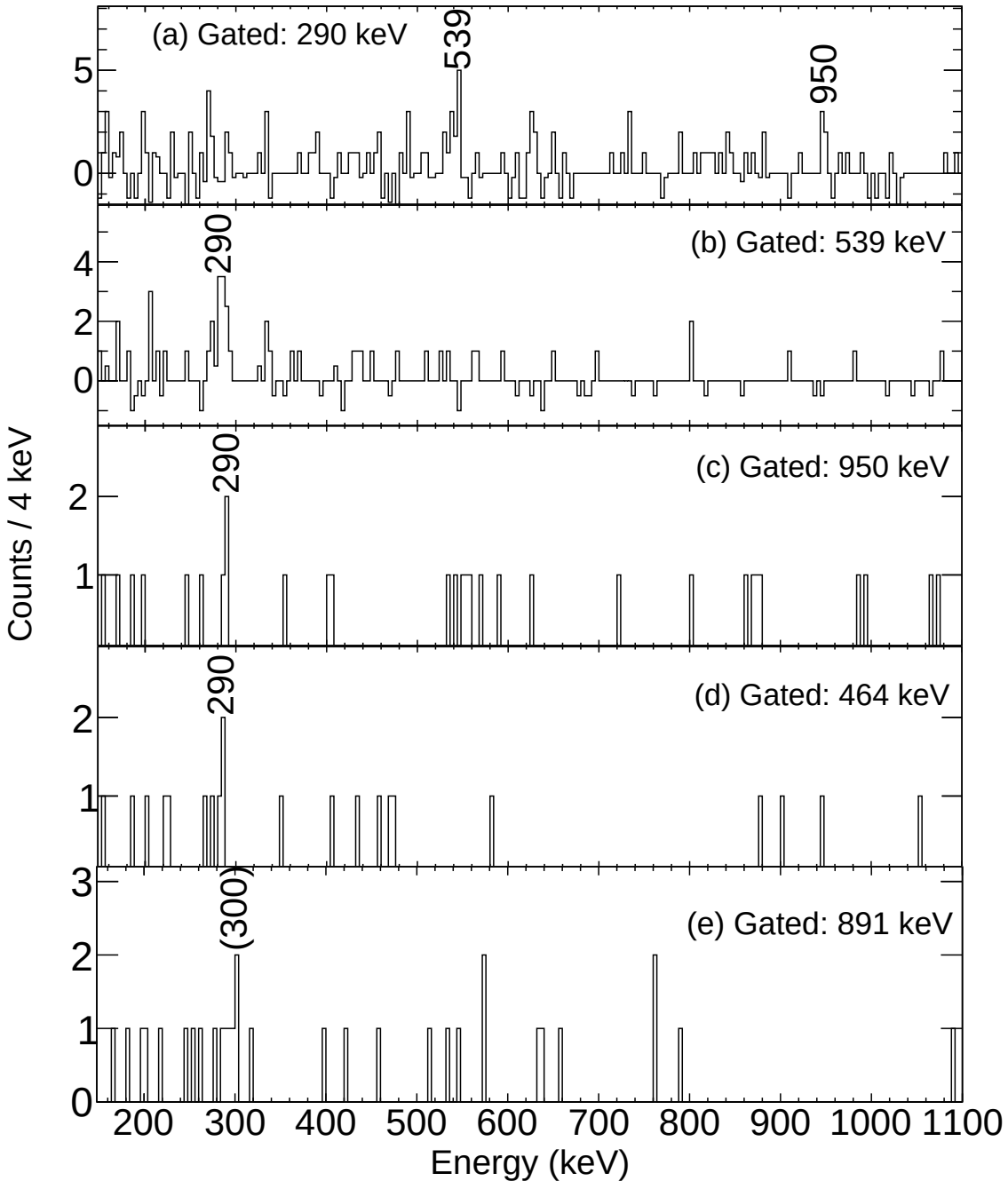

Figure 6.12: $\gamma - \gamma$ coincidence spectra of ^{80}Zr when gating on 290 (a), 539 (b), 950 (c), 464 (d) and 891 keV (e). The 290 and 539-keV gated spectra are background subtracted. The 539, 950 and 464-keV transitions are shown to feed into the 290-keV $2^+ \rightarrow 0^+$ decay. The 891-keV gated spectrum is shown to be in coincidence with a 300-keV transition, which are postulated to reside in a separate band.

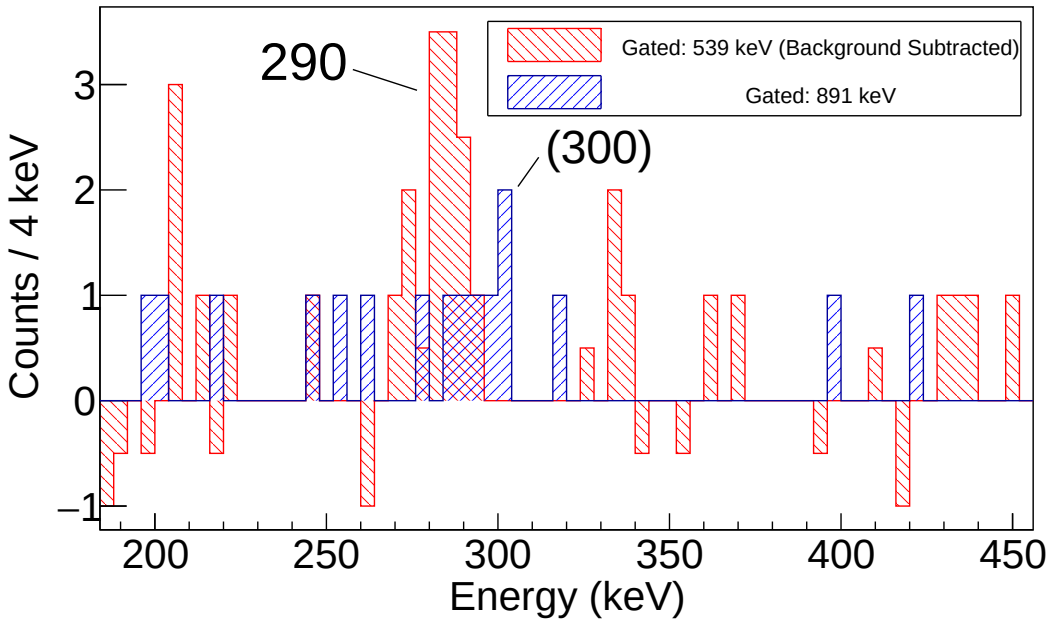

Figure 6.13: Comparison between γ-ray spectra when gating on the known 539-keV $4_1^+ \rightarrow 2_1^+$ transition (red) of ^{80}Zr and the unknown 891-keV transition (blue). There is a clear difference between the observed $2_1^+ \rightarrow 0_1^+$ 290-keV peak and the one seen at 300 keV. The 300 and 891-keV transitions were then assigned to a separate γ-ray sequence.

The deduced decay scheme from this $\gamma - \gamma$ coincidence data is shown in Fig. 6.14, where the 300 and 891-keV transitions are tentatively assigned to a new rotational band. The 464-keV transition is also assigned tentatively as a feeding transition to the 2_1^+ state as a peak at 290 keV is visible when gating on 464 keV, but the 464-keV peak is not visible whilst gating on the $2_1^+ \rightarrow 0_1^+$ 290-keV transition. The 950-keV decay is firmly labelled as a feeding transition to the 2_1^+ state as both transitions are visible when gating on one another. The relative intensities for the populated states of ^{80}Zr from the one-neutron knockout reaction from ^{81}Zr are also detailed in Table 6.7. As it was not possible to extract an uncertainty or intensity for the 300-keV decay given its close proximity to the high-intensity 290-keV peak its intensity is quoted to be the same as the 891-keV decay in Fig. 6.14.

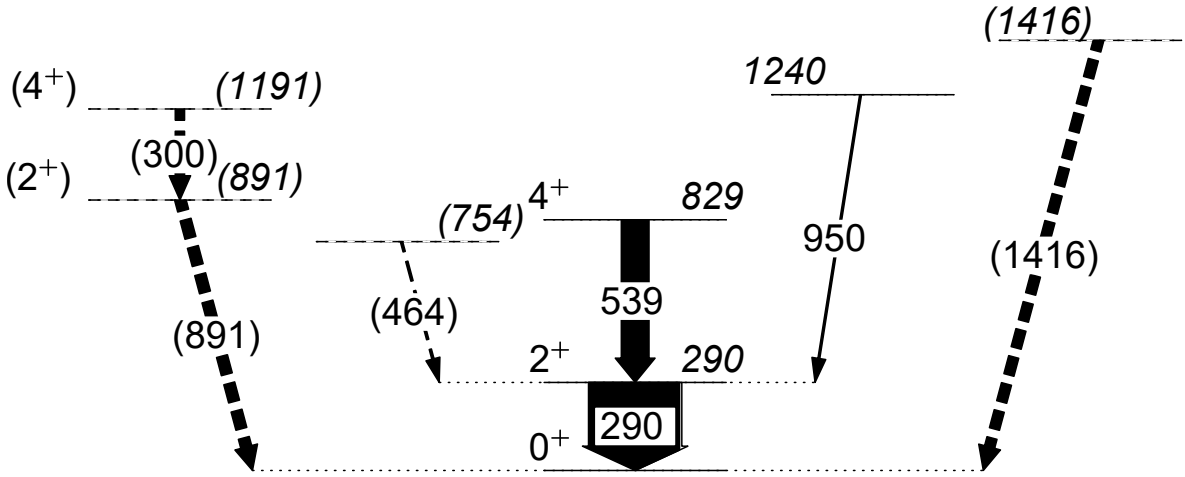

Figure 6.14: The deduced energy level scheme of ^{80}Zr showing the states populated through the one-neutron knockout reaction from ^{81}Zr. The 891 and 300-keV transitions are tentatively assigned to a new band. The thickness of the arrows correspond to the relative intensities of the decays.

Table 6.7: Efficiency-corrected relative intensities of decays of ^{80}Zr populated from one-neutron knockout from ^{81}Zr. Energies of known transitions are compared with weighted averages of previous measurements [11, 123]. Note that although the energy of the $2^+ \rightarrow 0^+$ decay is given as 289.9 keV in Ref. [11], the peak is labelled as 290 keV in the γ-ray spectrum. Given the close proximity of the proposed 300-keV decay to the 290-keV peak it was not possible to extract a relative intensity.

Transition	**Energy (keV)**	**Lit. Energy (keV)**	**Relative Intensity (%)**
$2_1^+ \rightarrow 0_1^+$	290.4(4)	289.5(2)	100
	300		
	463.6(3)		2(1)
$4_1^+ \rightarrow 2_1^+$	538.5(5)	537.5(2)	28(3)
$(2_2^+) \rightarrow (0_1^+)$	890.7(16)		11(2)
	949.7(5)		2(1)
	1415.9(26)		9(2)

As with ^{78}Sr, there was a visible high-energy tail from 295−300 keV in the γ-ray spectrum Doppler-corrected with an after-target recoil velocity of $\beta_{aft} = 0.299$ (see Fig. 6.18). Repeating the prescription of ^{78}Sr this was excluded from the χ^2-minimisation procedure, which again was found to lower the optimum χ^2/NDF but had no effect on the measured energy and lifetime. Following the usual procedure, the 539-keV $4_1^+ \rightarrow 2_1^+$ decay was included within the simulation as a feeding transition where its intensity was adjusted manually until it produced the lowest χ^2 when compared with the experimental spectrum. The lifetime of the 4^+ state was set to 5 ps (scaled from the factor of $1/E_\gamma^5$). As the 464 and 950-keV decays were also identified as transitions feeding into the 2_1^+ state, these were included within the simulations with lifetimes of 1 ps. Although the lifetimes of these states are unknown and there was not sufficient statistics acquired to determine whether an indication of a longer lifetime (e.g. a low-energy tail) was apparent, the intensity of these states are comparatively much lower than that of the 539-keV $4_1^+ \rightarrow 2_1^+$ decay meaning that the effects of these feeding states on the measured lifetime of the $2_1^+ \rightarrow 0_1^+$ decay are negligible.

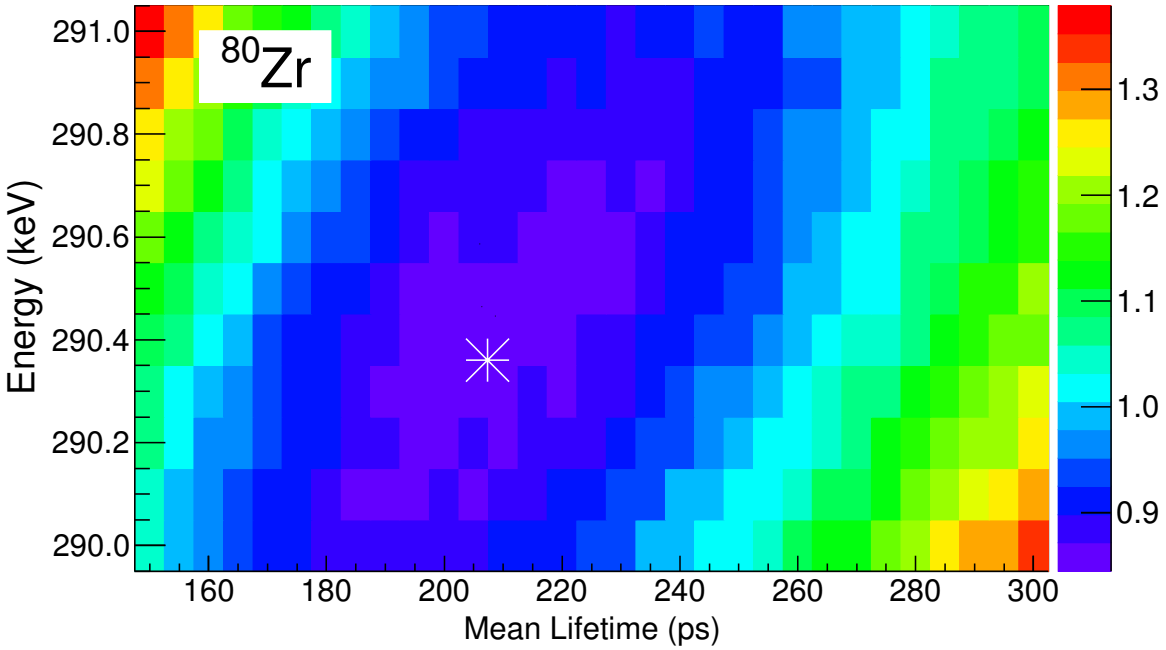

Figure 6.15: 2D χ^2 per degree of freedom plot of the simulated $2_1^+ \rightarrow 0_1^+$ transition of ^{80}Zr against the experimental spectrum whilst varying the energy and the mean lifetime of the state. The white star indicates the minimum of the distribution.

The 2D energy/lifetime χ^2/NDF distribution for the $2_1^+ \rightarrow 0_1^+$ peak of ^{80}Zr is displayed in

Fig. 6.15. By fitting a third-order polynomial to the projections of the distribution onto each axis (see Figs. 6.16 and 6.17), values and the corresponding statistical errors uncertainties of τ = 207(10) ps and $E(2^+)$= 290.4(2) keV are extracted. Combined in quadrature with the factors of systematic uncertainties detailed in Chapter 5.5.2.2, which are summarised in Tables 6.8 and 6.9, produces values of τ = 207(19) ps and $E(2^+)$= 290.4(4) keV, corresponding to $B(\mathrm{E2}\downarrow)$= 1910(180) $e^2\mathrm{fm}^4$. Although this $2^+ \rightarrow 0^+$ energy is not quite consistent with the previously published value of Ref. [123] of 289.2(2) keV, it is consistent to the older measurement of Ref. [11] of 289.9(3) keV which is labelled as 290 keV in Fig. 2 of the paper. The optimum simulation with τ = 207 ps and $E(2^+)$ = 290.4 keV is shown with the experimental spectrum below in Fig. 6.18.

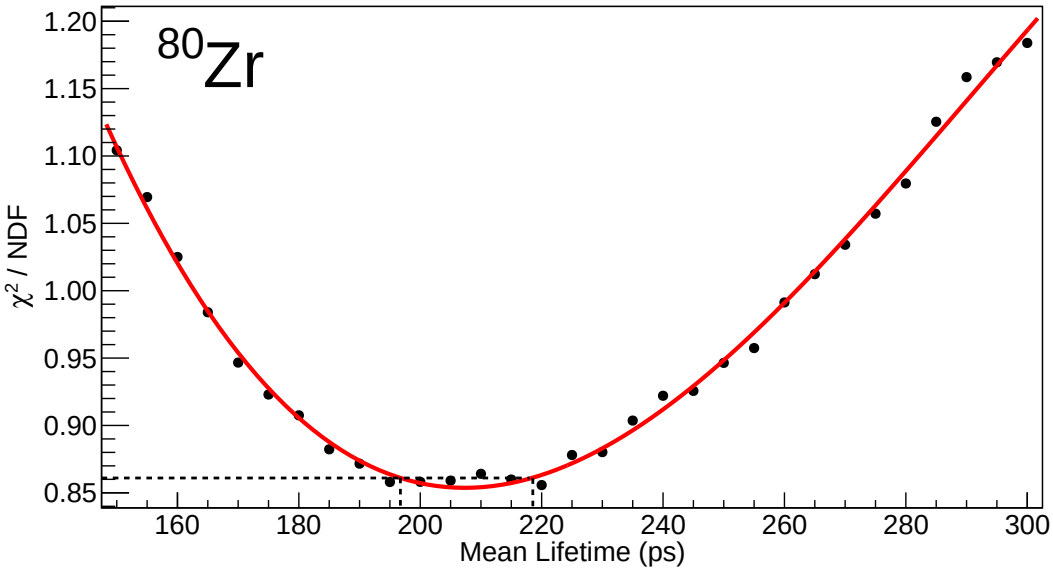

Figure 6.16: The χ^2 per degree of freedom distribution of the mean lifetime of 2^+ state ^{80}Zr at the optimised energy of 290.4 keV. The red line is a third-order polynomial fit of the distribution. The dashed black line corresponds to the $\chi^2_{min} + 1$ from which the statistical uncertainties are deduced by projecting onto the x axis.

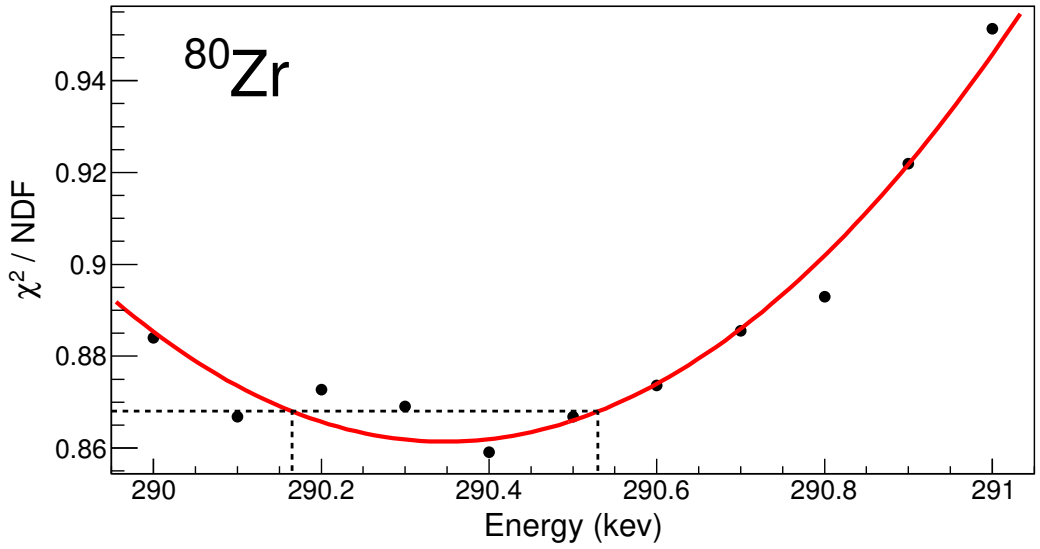

Figure 6.17: The χ^2 per degree of freedom distribution of the $E(2^+)$ energy, projected at the optimum $\tau = 207$ ps. The dashed lines indicates $\chi^2_{min} + 1/\text{NDF}$ from which the statistical uncertainties of ± 0.2 keV are extracted.

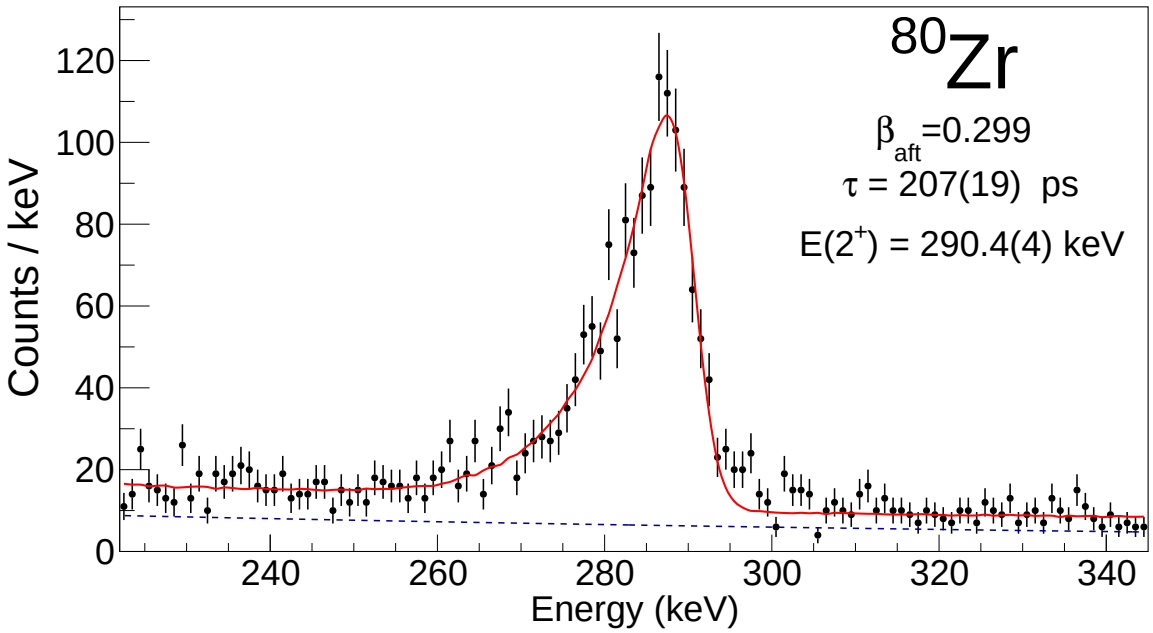

Figure 6.18: The experimental spectrum (black) for ^{80}Zr Doppler corrected with β_{aft}=0.299 compared with the simulated spectrum (red) with the optimum $\tau = 207$ ps and $E(2^+)$= 290.4 keV, deduced through the χ^2-minimisation procedure. The dashed blue line indicates the exponential background term added to the simulation.

Table 6.8: A summary of the systematic errors contributing to the total systematic error of the measured lifetime of the 2^+ state of ^{80}Zr.

Contribution	**Lifetime (ps)**	**Sys. Error (ps)**	**Sys. Error (%)**
With feeding	207.3		
No feeding	202.2	-5.1	2.5
$\beta = 0.304$	203.2	-4.1	2.0
3.5 mm position resolution		± 12.9	6.2
Increased background		± 0.2	0.1
Anisotropy effects		± 3.1	1.5
Geometrical uncertainties		± 6.2	3.0
Total		± 16.0	7.7

Table 6.9: Contributions to the total systematic error for the extracted 2^+ state energy from the χ^2-minimisation procedure for ^{80}Zr. The values for the no target offset and 3.5 mm simulated position resolution systematic errors were taken from the percentage error of 0.06% measured from ^{78}Sr.

Contribution	$\boldsymbol{E(2^+)}$ **(keV)**	**Sys. Error (keV)**	**Sys. Error (%)**
Optimised	290.36		
No target offset	290.54	$+0.18$	0.06
$\beta = 0.304$	290.42	$+0.06$	0.02
2D granularity	290.52	-0.16	0.06
3.5 mm position resolution	290.54	$+0.18$	0.06
Total		± 0.31	0.11

6.1.4 ^{78}Y

The limited statistics acquired for ^{78}Y due to the two-neutron knockout reaction mechanism from ^{80}Y meant that is was not possible to employ the traditional method of eliminating the GRETINA θ angle dependence to determine the optimum β as the dependence was not clearly visible. This was also hindered by the presence of a neighbouring 252-keV contaminant peak in the near proximity to the known 284-keV $2^+ \rightarrow 0^+$ peak [10] (see Fig. 6.19). Assuming a similar β_{aft} of the other investigated nuclei it can be assumed that the recoil velocity is approximately $0.29 - 0.30c$. Through experimenting with β_{aft} values in this range it was found that both $\beta_{aft} = 0.290$ and 0.300 produced a clean Doppler-corrected γ-ray lineshape. Since it was difficult to distinguish between the two of these, an average β_{aft} of 0.295 was taken as the final after-target recoil velocity to be used for the analysis. Given that the β_{aft} of ^{76}Sr (populated from the same ^{80}Y secondary beam) was measured to be $\beta_{aft} = 0.298$ the recoil velocity for ^{78}Y should be similar, meaning that a value of 0.295 is approximately what would be expected. Given that a mid-target recoil velocity is typically $\sim 0.005c$ faster than the after-target velocity (e.g. $\beta_{aft} = 0.299$ and $\beta_{mid} = 0.304$ for ^{80}Zr) the mid-target recoil velocity was taken as $\beta_{mid} = 0.300$ for ^{78}Y.

The γ-ray spectrum Doppler corrected with this recoil velocity and assuming an average decay position at the centre of the target is seen in Fig. 6.19. The $2^+ \rightarrow 0^+$ and $4^+ \rightarrow 2^+$ decays are immediately apparently at 284 and 506 keV [10], respectively, along with the unidentified 252-keV contaminant peak. In terms of unidentified transitions, there is also a visible peak at 559 keV and one at 217 keV, which is tentatively labelled due to its width of just one 2-keV channel. The observed decays and their relative intensities are listed in Table 6.10. The only other previous γ-ray spectrum for ^{78}Y is seen in Fig. 1(a) of Ref. [10] where the $2^+ \rightarrow 0^+$ and $4^+ \rightarrow 2^+$ were measured to be 281 and 506 keV, respectively. A 615-keV peak is also present. However, this spectrum has very low statistics and the energies are quoted with no error. Furthermore, unique particle identification was not achievable in Ref. [10] meaning that contaminant peaks identified as those from ^{74}Rb, ^{76}Kr and ^{77}Rb are also present in the spectrum. Therefore the possibility of the ^{78}Y decays being contaminated can not be excluded.

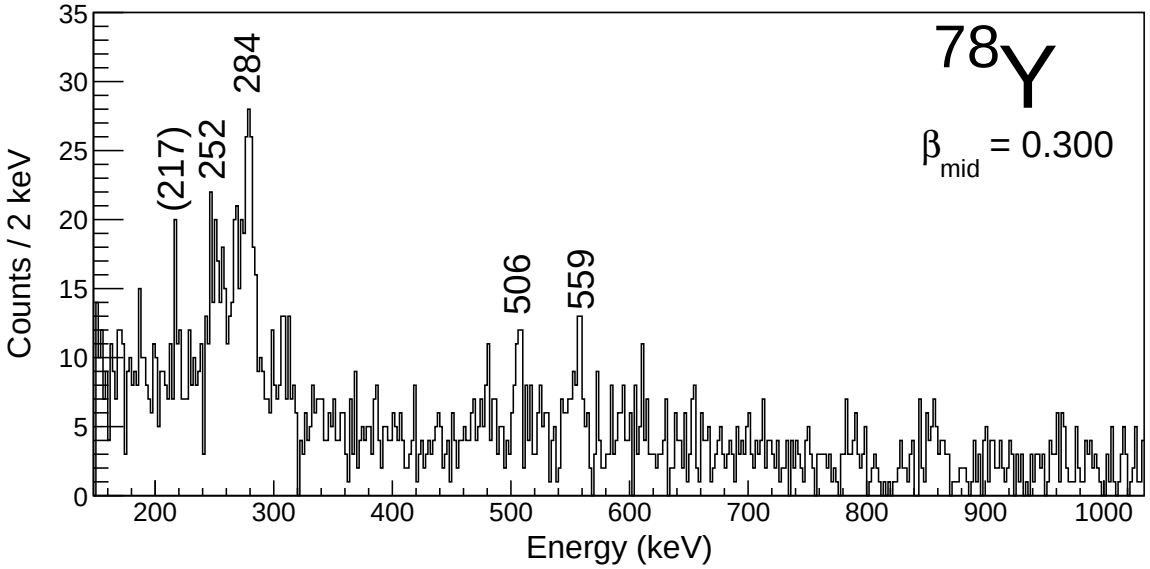

Figure 6.19: The Doppler-corrected γ-ray for ^{78}Y, corrected with a mid-target recoil velocity of β_{mid} and assuming a mid-target average decay position to enhance any faster decays. The peak at 284 keV is the $2^+ \rightarrow 0^+$ decay, which was previous measured with low statistics in Ref. [10] as 281 keV but quoted with no error. The 506-keV peak is the $4^+ \rightarrow 2^+$ decay whilst the remaining peaks are unidentified transitions.

Table 6.10: Efficiency-corrected relative intensities of decays of ^{78}Y populated from two-neutron knockout from ^{80}Y. Energies are compared with the only other previous measurement from Ref. [10], which are given with no error. The uncertainties of the 217-keV decay energy is given as the one-channel width of 2 keV given the low statistics.

Transition	**Energy (keV)**	**Lit. Energy (keV)**	**Relative Intensity (%)**
	217.0(20)		8(2)
	252.0(6)		40(5)
$2^+ \rightarrow 0^+$	283.6(8)	281	100
$4^+ \rightarrow 2^+$	505.7(8)	506	11(7)
	558.6(16)		29(5)

Before probing the lifetime of the 2^+ state it had to be ascertained that the unidentified 252-keV contaminant was a genuine decay from ^{78}Y and not a consequence of contamination of a neighbouring nucleus on the PID plot. This is of particular importance in this case as the contaminant is observed directly in the lineshape, the area of the spectrum that the measured lifetime is sensitive to. The effects of decreasing the the size of the PID cut to eliminate any residual contamination from ^{76}Sr (below ^{78}Y in the PID) are seen in Fig. 6.20(b), where it is compared to the full PID cut [Fig. 6.20(a)]. It can be seen in Fig. 6.20(a) and (b) that the relative intensities of the 284 and 252-keV peaks remain unchanged with the implementation of the smaller, more restrictive cut. Additionally, when gating solely on ^{80}Zr (above ^{78}Y in the PID) in Fig. 6.20(c) there is no 252-keV peak observed. This evidence therefore concludes that the 252-keV peak is a genuine decay of ^{78}Y.

Due to the low statistics acquired for ^{78}Y it was not possible to determine whether this 252-keV transition, or any other unidentified decays, were feeding transitions to the $2^+ \rightarrow 0^+$ decay through $\gamma - \gamma$ coincidence data. Therefore the 252-keV decay was assumed to not be a feeding state in the lifetime simulations when measuring the lifetime of the 2^+ state. The only feeding state including in the simulation was the $4^+ \rightarrow 2^+$ transition, which as before possessed a lifetime scaled by a factor of $1/E_\gamma^5$, corresponding to 7 ps. The intensity of the 252-keV peak was allowed to vary freely in the χ^2-minimisation procedure to minimise the χ^2 when comparing the simulation with the experimental spectrum. It should be noted that although this 252-keV contaminant lies within the γ-ray lineshape (the part of the spectrum that the measured lifetime is sensitive to), when using a compression of 2 keV per channel there are nine data points within the lineshape outside of the contaminant peak. This means that are nine data points which are highly sensitive to the lifetime from which a measurement can be extracted.

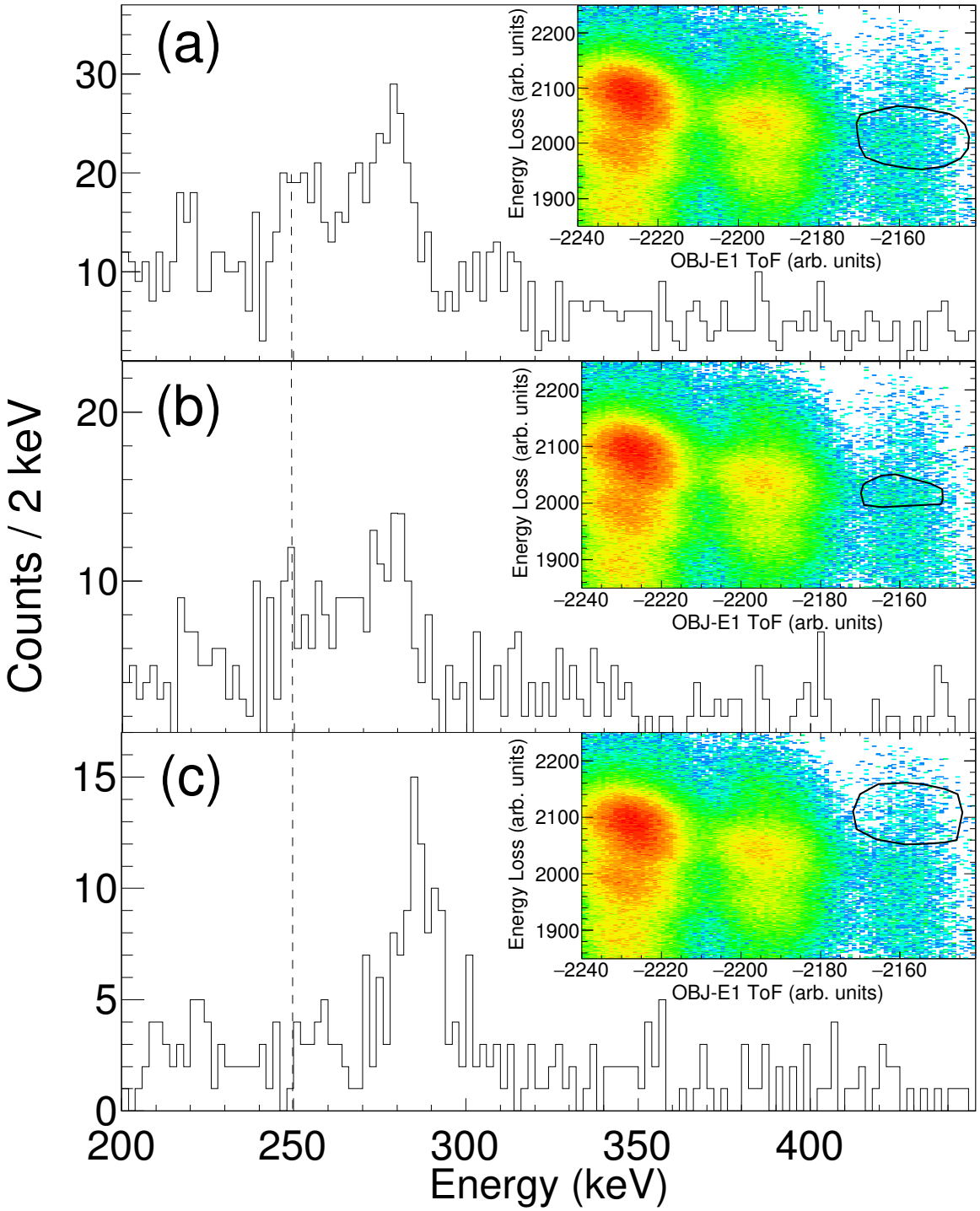

Figure 6.20: The Doppler-corrected γ-ray spectra for ^{78}Y (a), ^{78}Y with a small, limited cut (b) and ^{80}Zr (c), all populated through the ^{80}Y secondary beam and all corrected with the same β_{aft} (0.295). The inset plots display the corresponding cut made on the PID to produce the spectrum. The contaminant peak ~250 keV in the lineshape of ^{78}Y (indicated with the dashed black line) is still visible with a limited cut (b) and not visible in (c). Furthermore, this peak is not visible the spectrum of ^{76}Sr or ^{79}Y, eliminating all possibilities other than this peak corresponding to a genuine ^{78}Y decay.

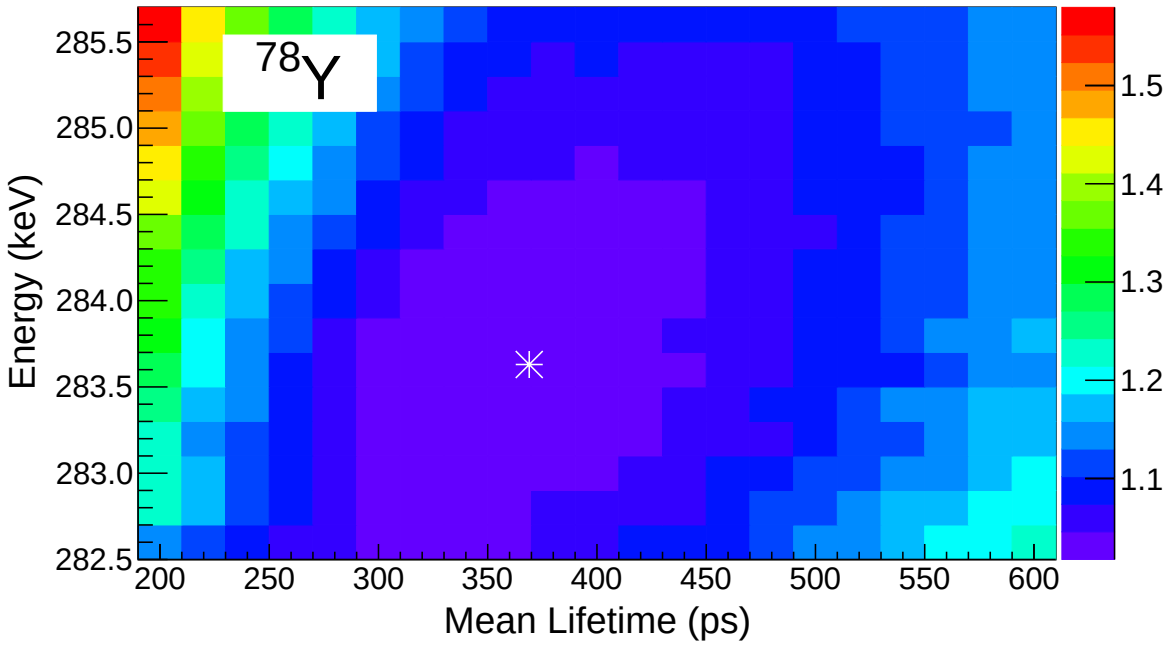

Figure 6.21: 2D χ^2 per degree of freedom (NDF) plot of mean lifetime and energy of the 2^+ state of ^{78}Y of the experimental spectrum when compared with simulation. The white star indicates the location of the fitted minimum χ^2/NDF.

The 2D energy/lifetime χ^2/NDF plot of the $2^+ \rightarrow 0^+$ decay is displayed in Fig. 6.21. The projections onto both axes are shown in Fig. 6.22 and 6.23, where the distributions are fitted with a third-order polynomial to extract the final lifetime and $E(2^+)$ energy. The location of the fitted minimum of the 2D χ^2/NDF distribution at $\tau = 369$ ps and $E(2^+)= 283.6$ keV is indicated with the white star in Fig. 6.21. The 252-keV peak in the lineshape results in an asymmetric χ^2/NDF distribution when projected onto the lifetime axis, yielding a statistical error of $^{+49}_{-44}$ ps (see Fig. 6.22). This is not the case when projecting onto the energy axis as the energy of the γ-ray lineshape is strongly dependent upon the high-energy side of the peak and is therefore unaffected by the contaminant peak within the lineshape. Therefore, the statistical error for the measured $E(2^+)$ energy is symmetric and was measured to be ± 0.7 keV (see Fig. 6.23).

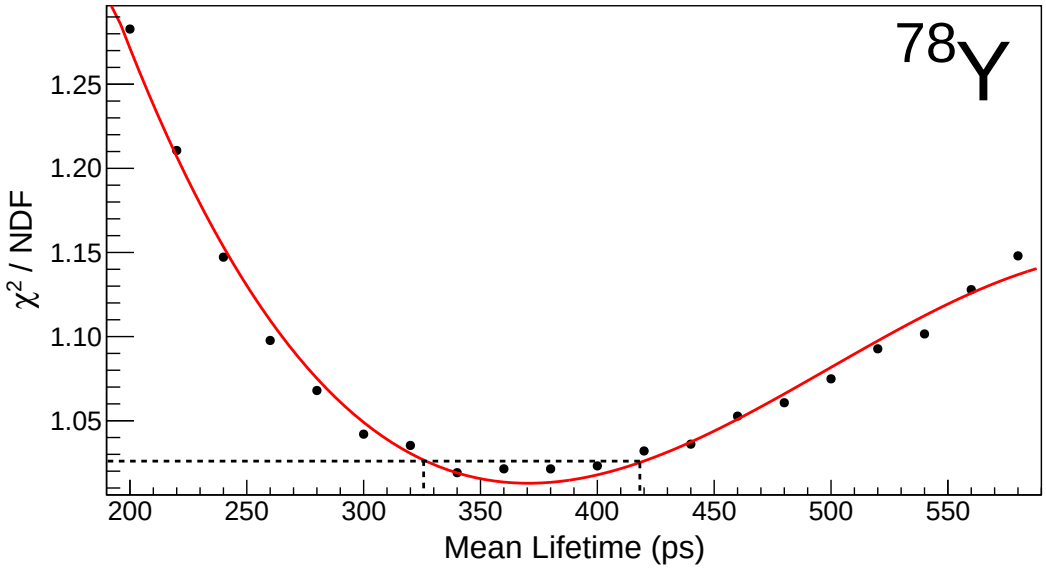

Figure 6.22: 1D projection of the 2D energy/lifetime χ^2/NDF plot onto the lifetime axis for ^{78}Y at the optimised $E(2^+)$= 283.6 keV. The dashed lines indicates $\chi^2_{min}+1$/NDF from which the statistical uncertainties of $^{+49}_{-44}$ ps are extracted.

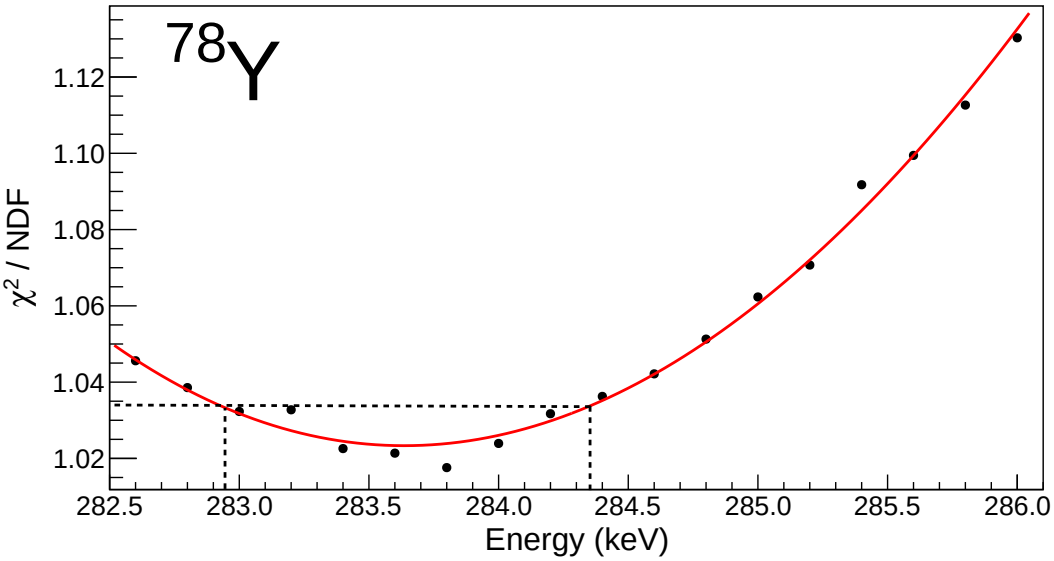

Figure 6.23: 1D projection onto the energy axis for ^{78}Y at the optimised lifetime of 369 ps. The dashed lines indicates $\chi^2_{min}+1$/NDF from a third-order polynomial fit (red) of the distribution from which the statistical uncertainties of $\pm$0.7 keV are extracted.

Since this 252-keV peak is an unknown transition, two additional systematic errors were introduced to compensate for the unknown energy and lifetime of this decay. The error associated with the unknown lifetime was derived by increasing the lifetime of the 252-keV

state in the simulation from 1 to 100 ps and repeating the χ^2-minimisation procedure, which resulted in a measured mean lifetime of $\tau = 412$ ps. The error arising from the contaminant's unknown energy was deduced through repeating the procedure by adjusting its energy by ± 1 keV, yielding $\tau = 381$ and $\tau = 410$ ps for 251 and 253 keV, respectively, corresponding to an average of $\tau = 396$ ps. Since both of these additional systematic uncertainties yield a longer lifetime these factors were taken only as a positive error on the measured lifetime, further extending upon the larger positive statistical error. These are summarised with the other systematic errors in Table 6.11 and 6.12. Combining statistical errors of $^{+49}_{-44}$ ps and ± 0.7 keV in quadrature with the systematic errors listed in Tables 6.11 and 6.12, final values of $\tau = 369^{+77}_{-54}$ ps and $E(2^+)$= 283.6(8) keV are obtained, yielding $B(\mathrm{E2}\downarrow)$= 1200^{+180}_{-250} $e^2\mathrm{fm}^4$. Including the 252-keV decay as a feeding transition with a lifetime of 100 ps yielded $\tau = 398^{+61}_{-53}$ ps, which proves to be consistent with the final value. Likewise, repeating the procedure while using 4 keV per channel produced a mean lifetime of 421^{+64}_{-50} ps, again consistent with the final value. The optimised simulated spectrum is presented with the experimental γ-ray spectrum Doppler-corrected with $\beta_{aft} = 0.295$ in Fig. 6.24. The measured $E(2^+)$= 283.6(8) keV slightly differs from the only other measurement of Ref. [10] of 281 keV, however this was a very low statistic measurement and the energy is given with no error. There is also no evidence of a 252-keV peak in Ref. [10].

The optimum simulation is shown with the experimental spectrum in Fig. 6.24. This result makes the ^{78}Y the lowest measured $B(\mathrm{E2}\downarrow)$ of the three $N = Z$ nuclei and shows a drastic reduction in collectivity from ^{76}Sr, with a reduction in $B(\mathrm{E2}\downarrow)$ by almost a factor of two, surprising given that ^{78}Y is located at the mid-shell point at $N = Z = 39$.

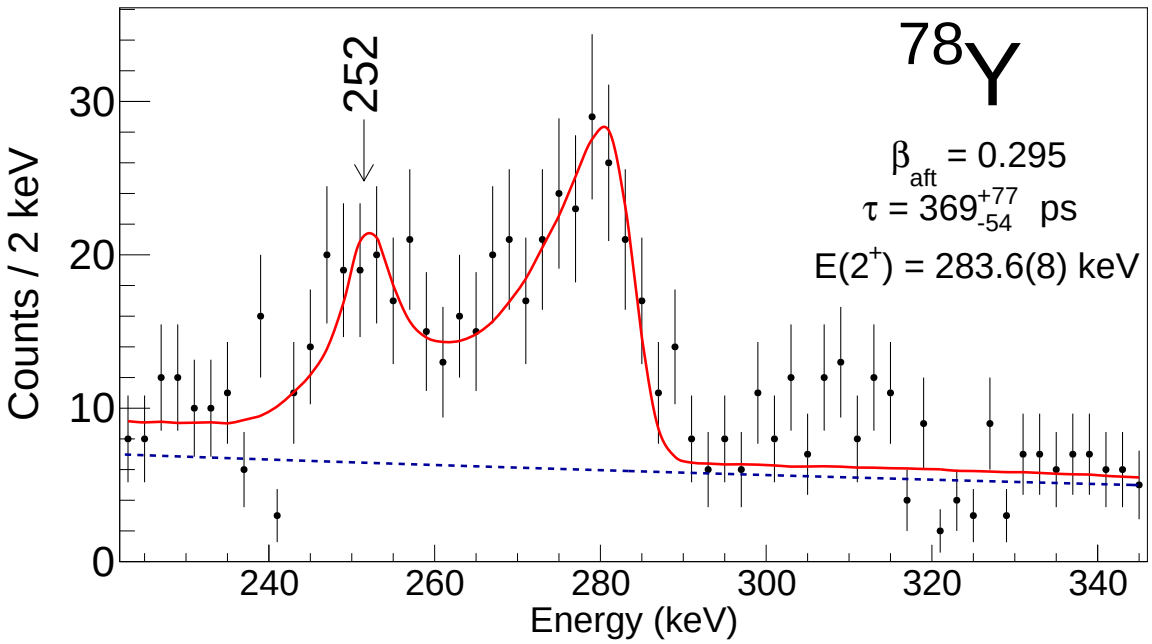

Figure 6.24: The optimised simulated spectrum (red) with $\tau = 369$ ps at $E(2^+)$= 283.6 keV with an additional exponential background contribution (dashed blue line) compared with experiment (black) Doppler-corrected with $\beta_{aft} = 0.295$. The contaminant peak at 252 keV within the lineshape is labelled, where its intensity was allowed to vary freely.

Table 6.11: A summary of the systematic errors of the measured mean lifetime of the 2^+ state of ^{78}Y. Due to the contaminant peak at 252 keV additional systematic errors are introduced to compensate for the unknown energy and lifetime of this decay. Both factors were found to increase the measured lifetime when varied, resulting in an asymmetric total systematic error. Values for the position resolution and background errors were taken from the references values measured for ^{78}Sr.

Contribution	**Lifetime (ps)**	**Sys. Error (ps)**	**Sys. Error (%)**
With feeding	369.0		
No feeding	371.5	+2.5	0.7
$\beta = 0.290/0.300$	384.8	+15.8	4.3
3.5 mm position resolution		±23.0	6.2
Increased background		±0.4	0.1
Anisotropy effects		±5.5	1.5
Geometrical uncertainties		±11.1	3.0
Contaminant energy ±1 keV	395.7	+26.7	7.2
Contaminant lifetime = 100 ps	411.7	+42.7	11.6
Total		−30.6, +59.0	+16.0, −8.3

Table 6.12: Contributions to the total systematic error for the extracted 2^+ state energy from the χ^2-minimisation procedure for ^{78}Y. The values for the no target offset and 3.5 mm simulated position resolution systematic errors were taken from the percentage error of 0.06% measured from ^{78}Sr.

Contribution	$E(2^+)$ **(keV)**	**Sys. Error (keV)**	**Sys. Error (%)**
Optimised	283.63		
No target offset	283.80	+0.17	0.06
$\beta = 0.295/0.300$	283.66	+0.03	0.01
2D granularity	283.90	−0.27	0.10
3.5 mm position resolution	283.80	+0.17	0.06
Total		±0.37	0.13

6.1.5 Summary

The extracted lifetimes of the 2^+ states of ^{80}Zr, ^{78}Y, ^{78}Sr and ^{76}Sr and the corresponding $B(\mathrm{E2}\downarrow)$ values are summarised below in Table 6.13. The measured mean lifetimes are listed with the statistical and systematic uncertainties and any previous measurements where possible. Weighted averages of the mean lifetimes are then used with the measured $E(2^+)$ energies measured in this work to calculate $B(\mathrm{E2}\downarrow)$. $B(\mathrm{E2}\downarrow)$ values are converted into Weisskopf units per nucleon in accordance with the values in Table 2.1. Here the uncertainty of $B(\mathrm{E2}\downarrow)$ in terms of Weisskopf units was derived from:

$$\Delta B(\mathrm{E2}\downarrow)(\mathrm{W.\ u.}) = \frac{B(\mathrm{E2}\downarrow)}{B(\mathrm{E2}\downarrow)_{sp}}\sqrt{\left(\frac{\Delta B(\mathrm{E2}\downarrow)}{B(\mathrm{E2}\downarrow)}\right)^2 + \left(\frac{\Delta B(\mathrm{E2}\downarrow)_{sp}}{B(\mathrm{E2}\downarrow)_{sp}}\right)^2}, \tag{6.1}$$

where

$$\Delta B(\mathrm{E2}\downarrow)_{sp} = 7.3 \times 10^7 A^{4/3} \Delta E_\gamma^5. \tag{6.2}$$

Here $B(\mathrm{E2}\downarrow)$ and $B(\mathrm{E2}\downarrow)_{sp}$ denote the measured $B(\mathrm{E2}\downarrow)$ value and the corresponding single-particle estimate from the values shown in Table 2.1, respectively. The quadrupole deformation (β_2) is calculated from Eq. 2.29 where its error is determined from Eq. 6.3:

$$\Delta\beta_2 = \frac{2\pi}{3ZR_0^2}\ \frac{\Delta B(\mathrm{E2}\uparrow)}{\sqrt{B(\mathrm{E2}\uparrow)}}. \tag{6.3}$$

Table 6.13: Optimum $E(2^+)$ energies in keV and mean lifetimes τ in ps extracted from the χ^2-minimization procedure. $E(2^+)$ errors are calculated from systematic uncertainties in the target position, beam velocity, simulated GRETINA position resolution and the 2D χ^2-minimization procedure, combined with statistical uncertainties. The measured mean lifetimes are compared with previously measured values (τ_{prev}) where possible. Weighted averages for the mean lifetimes (τ_{avg}) are then used to calculate B(E2$\downarrow$) values in e^2fm^4. β_2 is calculated from Eq. 2.29 assuming an axial deformation.

	$E(2^+)$	τ	Stat.	Sys.	Total	$\tau_{prev,1}$	$\tau_{prev,2}$	τ_{avg}	B(E2$\downarrow$)	B(E2$\downarrow$)/A (W. u.)	β_2
^{80}Zr	290.4(4)	207	10	16	19				1910(180)	1.16(11)	0.38(2)
^{78}Y	283.6(8)	369	$^{+49}_{-44}$	$^{+59}_{-31}$	$^{+77}_{-54}$				1200^{+180}_{-250}	$0.78^{+0.12}_{-0.16}$	$0.32^{+0.02}_{-0.03}$
^{78}Sr	278.1(3)	286	3	20	20	276(39) [21]	224(27) [122]	266(15)	1840(100)	1.19(8)	0.40(1)
^{76}Sr	261.6(5)	250	35	27	44	296(36) [21]		278(28)	2390(240)	1.64(17)	0.47(2)

6.2 Mirror Energy Differences of ^{79}Zr/^{79}Y

This section will discuss the process of the extracting the excitation energies of the $A = 79$ mirror pair. There had not been any γ-ray spectroscopy of ^{79}Zr prior to this work. Yrast states of ^{79}Y were previously identified in Ref. [124] through the ^{54}Fe(^{28}Si, 1p2n)^{79}Y fusion-evaporation reaction which identified states up to $J = (\frac{13}{2}^{+})$.

The first stage of examining γ-ray spectra from both ^{79}Zr and ^{79}Y was to ensure that any contamination from neighbouring nuclei on the PID plot was eliminated. With ^{79}Zr this was not an issue as there is clear separation between the ^{79}Zr (-2n) and the neighbouring ^{80}Zr (-1n) from the ^{81}Zr secondary beam (see Fig. 5.3). Furthermore, due to the low cross sections the population of ^{81}Nb and ^{77}Y (above and below ^{79}Zr on the PID, respectively) from the ^{81}Zr secondary beam are negligible.

This was not as trivial with ^{79}Y as it was adjacent to the abundant ^{80}Y secondary beam on the PID plot (see Fig. 5.3), meaning that extra care was necessary when making a cut on the plot to limit contamination. Likewise, ^{81}Zr and ^{77}Sr are neighbouring ^{79}Y with sufficient statistics to contaminate the ^{79}Y spectrum if the cut on the PID is too large. To confirm that any contamination from ^{81}Zr and/or ^{77}Sr was absent from the final ^{79}Y cut several other cuts were made to inspect the effects to the Doppler-corrected γ-ray spectrum. It can be seen in Fig. 6.25 (a) and (b) that greatly reducing the size of the cut around ^{79}Y reduced the number of counts but the relative intensities of the visible peaks remained unchanged, an indication that all of the peaks are genuine ^{79}Y decays. Interestingly, several of the peaks seen in both Fig. 6.25 (a) and (b) are at near identical energies to that of the [301]3/2 band of ^{81}Zr built upon the $(\frac{5}{2}^{+})$ ground state [79], e.g. those at 167 and 238 keV. This phenomenon of identical normal deformed bands has been noted before in this mass region [125, 126].

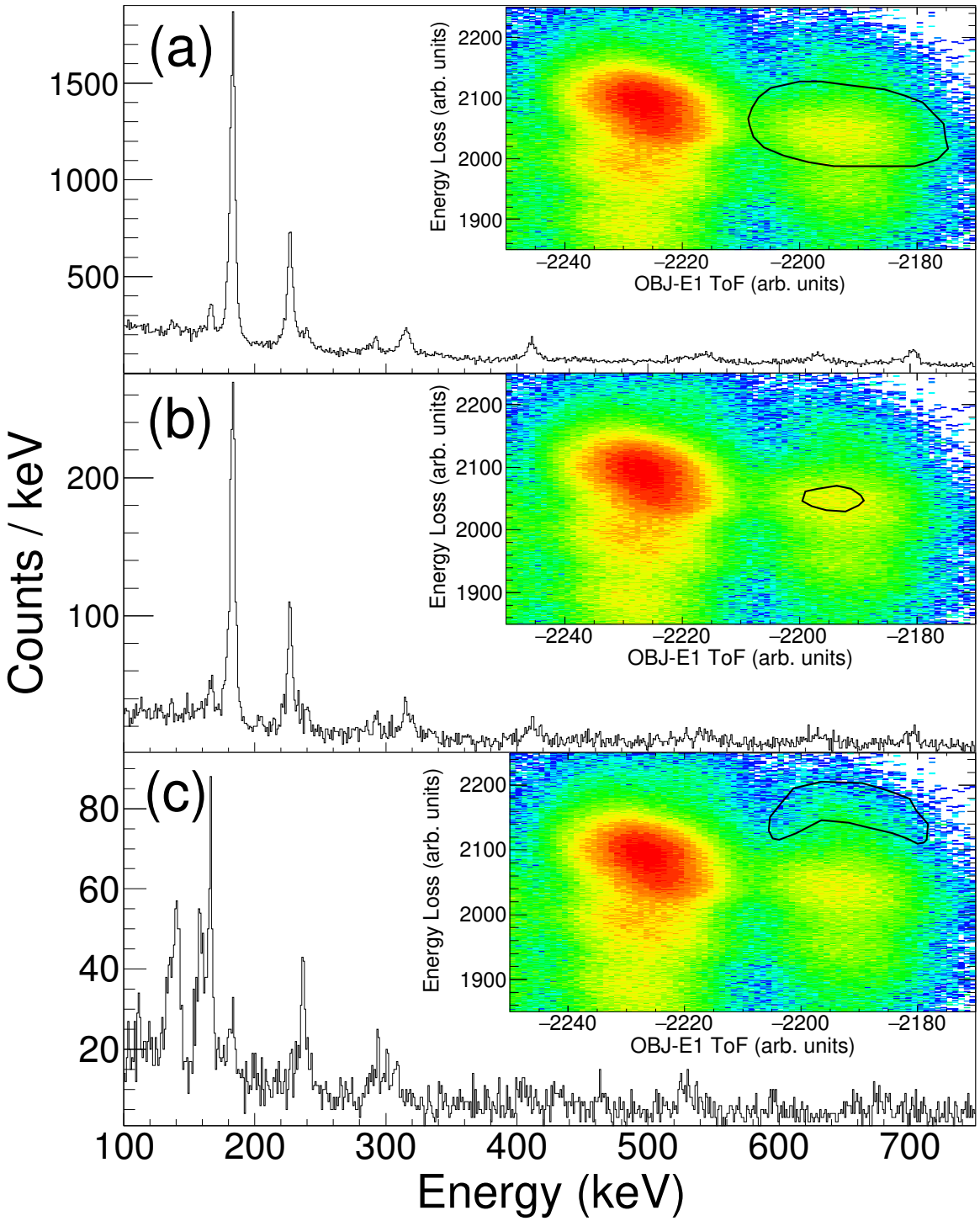

Figure 6.25: The Doppler-corrected γ-ray spectra for ^{79}Y [(a) and (b)] and ^{81}Zr (c), all populated through the ^{80}Y secondary beam and all Doppler corrected with the same β (0.294). The inset plots display the corresponding cuts on the PID plot. It is clear that even with a small, limited cut around ^{79}Y on the PID plot seen in (b) the relative intensities of each peak remain unchanged from a larger cut in (a). Therefore, it is apparent that all of the peaks in (a) are genuine transitions from ^{79}Y and not ^{81}Zr (c).

Following confirmation that no contaminants were being introduced to the ^{79}Y γ-ray spectrum, it was necessary to determine the optimum recoil velocity to use in the γ-ray energy Doppler-correction process. The known 184.0(5)-keV $(\frac{7}{2}^+) \rightarrow (\frac{5}{2}^+)$ decay [124] was optimised at $\beta_{aft} = 0.294$ [see Fig. 6.26(a)]. Upon closer inspection there is a visible low-energy tail on this peak [see inset of Fig. 6.27(b)], a consequence of an incorrect Doppler correction due to the $(\frac{7}{2}^+)$ state having a sufficiently long lifetime to decay at a position downstream of the reaction target. Hence, the β to optimise this peak is denoted as β_{aft}. Provided with this evidence of a longer lifetime state, the effective target z position used for the Doppler-correction procedure was set to the end of the target position, repeating the procedure used for the lifetime analysis of ^{80}Zr, ^{78}Y, ^{78}Sr and ^{76}Sr. With this recoil velocity and target position an energy of 183(1) keV was extracted. This energy is slightly lower than (although still consistent) the value from Ref. [124] of 184.0(5) keV but this is to be expected since the peak of a decay with a lifetime < 100 ps with a recoil velocity of $\beta \sim 0.3$ will exhibit a small low-energy shift (see Fig. 5.17). For the case of extracting MED, the errors on peak centroids were taken as the one channel width of 1 keV for ^{79}Y. For ^{79}Zr the centroids of each peak were deduced with an integral fit performed with the Radware software package [127]. The range of the fit and the offset applied to the energy calibration were then systematically varied. The maximum variation of the measured centroid for each peak was then taken as the uncertainty of the peak energy.

The fastest of the decays, such as the 315/316-keV peak, were found have a mid-target velocity, β_{mid}, of 0.304 [see Fig. 6.26(b)]. Given the fast velocity necessary to correct these decays, corresponding to very short lifetimes, these states were Doppler-corrected assuming an average decay position around 75% through the target. For the 227-keV $(\frac{9}{2}^+) \rightarrow (\frac{7}{2}^+)$ and 411-keV $(\frac{9}{2}^+) \rightarrow (\frac{5}{2}^+)$ transitions a slightly faster recoil velocity of $\beta = 0.296$ was measured, therefore corresponding to a decay occurring with an average position near the end of the target. Using LISE++ [117] to extrapolate the after-target energy of a nucleus back into the target this was found to correspond to an average decay position of 0.03 mm from the end of the target. The z position for the Doppler-correction process was therefore slightly adjusted to this position to extract the energies.

The energies of the remainder of the peaks were extracted with β_{mid} and all of the known transitions were measured to have energies that are consistent with Ref. [124] (see Table

6.14). In the case of the 315/316-keV peak labelled in Fig. 6.27, both the 315 and 316-keV peaks are assumed to be present given the observation of the 631-keV $(\frac{13}{2}^+) \rightarrow (\frac{9}{2}^+)$ decay, meaning that 315-keV $(\frac{13}{2}^+) \rightarrow (\frac{11}{2}^+)$ and 316-keV $(\frac{11}{2}^+) \rightarrow (\frac{9}{2}^+)$ transitions will also occur. The relative intensity listed in Table 6.14 is therefore the sum of these as they can not be distinguished.

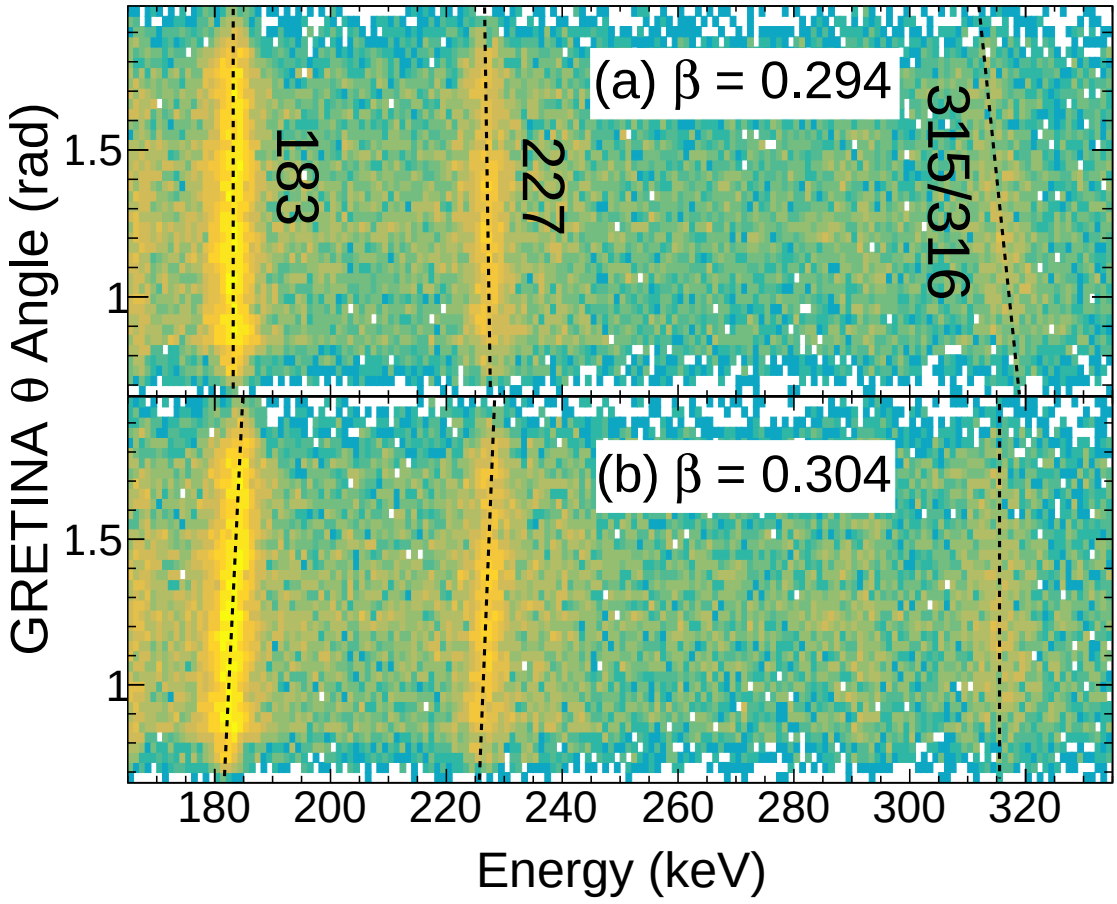

Figure 6.26: Doppler-corrected γ-ray spectra for ^{79}Y corrected with recoil velocities of $\beta = 0.294$ (a) and 0.304 (b). The 184-keV decay is optimised at the slower $\beta = 0.294$, an indication of an after-target decay. The 227-keV decay is optimised at a slightly faster $\beta = 0.296$, corresponding to a decay near the end of the target (see text). The 315/316-keV transition requires a far faster β of 0.304 which is likely a fast decay occurring at an average position which is closer to the centre of the target.

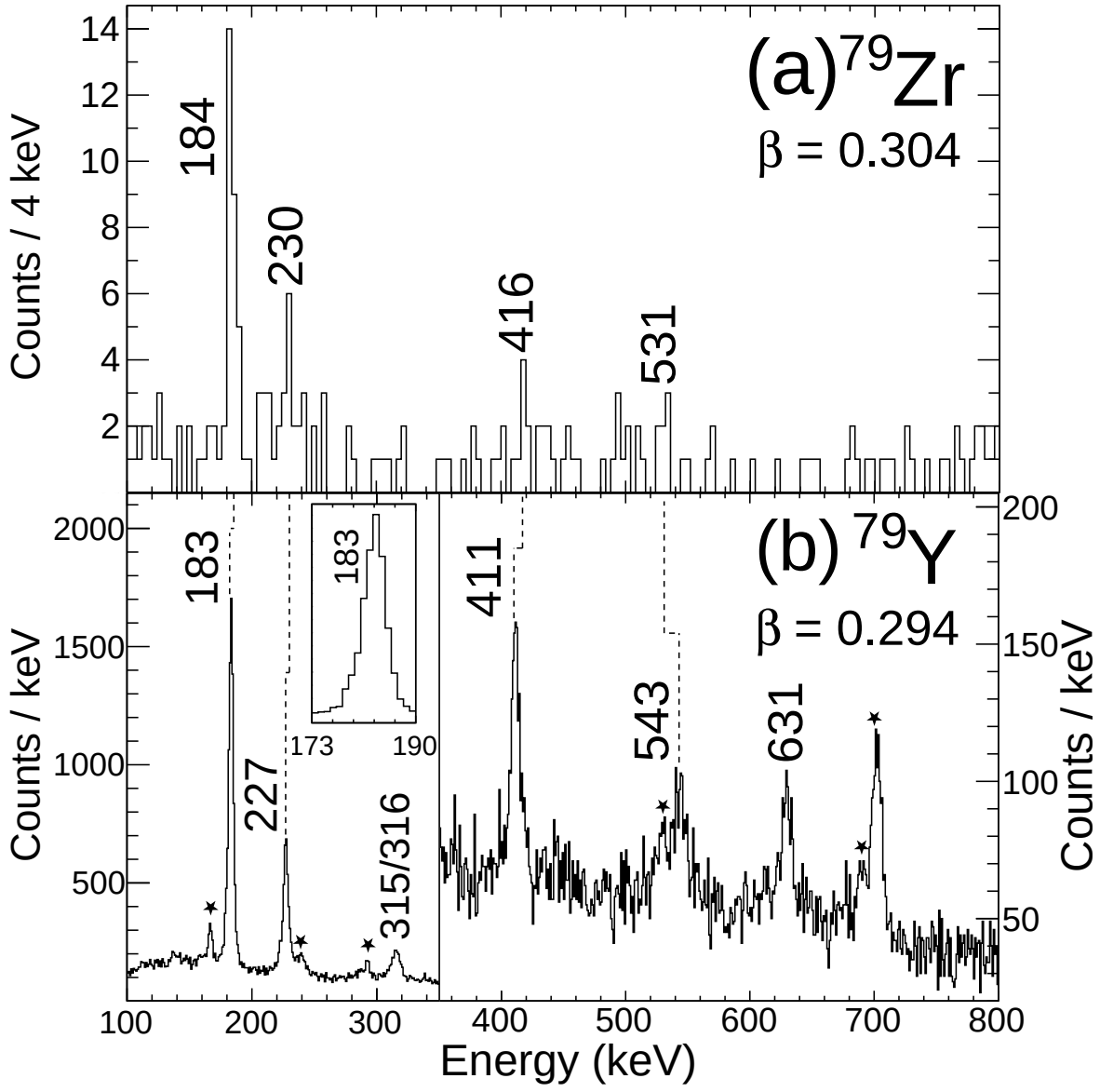

Figure 6.27: The Doppler-corrected γ-ray spectra for (a) ^{79}Zr and (b) ^{79}Y, corrected with the labelled recoil velocities. The inset of (b) displays an expanded view of the 183-keV transition of ^{79}Y, where there is a visible low-energy tail, where $\beta_{aft} = 0.294$ has been chosen to emphasise the tail. Black stars indicate previously unidentified transitions.

For the ^{79}Zr spectrum seen in Fig. 6.27, isospin symmetry arguments dictate that the proposed $(\frac{7}{2}^+) \rightarrow (\frac{5}{2}^+)$ decay's lifetime can be assumed to be of the same order of that of mirror ^{79}Y. Given the very low statistics acquired for ^{79}Zr [see Fig. 6.27(a)] is was not possible to deduce β_{aft} in the usual manner. Therefore, β_{aft} was derived from energy per nucleon of the known β_{aft} of ^{80}Zr of 0.2999 using LISE++, which for ^{79}Zr yielded a β_{aft} of 0.2980. When

Doppler corrected with this velocity and an back of target decay position the $(\frac{7}{2}^+) \rightarrow (\frac{5}{2}^+)$ energy was measured to be 184(2) keV. Taking the recoil velocity range of $\beta = 0.294-0.304$ for the slow and fast decays of ^{79}Y and applying the same distribution of β to ^{79}Zr corresponds to $0.298 - 0.308$. The recoil velocity was then systematically varied within these limits until the faster decays were found to be optimised at $\beta = 0.304$, as shown in Fig. 6.27(a). Three peaks other than the $(\frac{7}{2}^+) \rightarrow (\frac{5}{2}^+)$ decay are visible when corrected with this velocity and a mid-target decay position. These are taken as the $(\frac{9}{2}^+) \rightarrow (\frac{7}{2}^+)$, $(\frac{9}{2}^+) \rightarrow (\frac{5}{2}^+)$ and $(\frac{11}{2}^+) \rightarrow (\frac{7}{2}^+)$ decays and were measured to be 230(2), 416(2) and 531(4) keV, respectively. The measured FWHM of 9 keV for the 411-keV peak of ^{79}Y is consistent with the mirror decay in ^{79}Zr, suggesting that the peaks are real and not statistical fluctuations. All of the decays for ^{79}Zr and ^{79}Y are listed with the recorded energies and relative intensities in Table 6.14. The MED resulting from these measured energies are small (all $< \pm 12$ keV), much lower than MED seen in the fp shell which can typically reach values of $\pm$100-250keV (see Chapter 2.5). The measured states are summarised in Table 6.15 where the $(\frac{5}{2}^+)$ state is taken as the ground state in ^{79}Zr assuming it is the same as ^{79}Y [124].

Through examining $\gamma-\gamma$ coincidence data for ^{79}Y the unidentified 167-keV decay is found to be in coincidence with 238 and 700-keV decays [see Fig. 6.28(b)]. When gating on 700 keV [Fig. 6.28(e)] the 167-keV peak is clear, providing further evidence of these being a part of the same cascade. There is no 700-keV peak visible when gating on 238 keV [Fig. 6.28(c)] leading to the conclusion that the 700-transition feeds into the 167-keV state. The deduced decay schemes of ^{79}Zr and ^{79}Y are shown in Fig. 6.29 where the widths of the arrows correspond to the relative intensities of the decays.

This decay scheme is as one would expect when assuming a rotational band identical to the [301]3/2 band of ^{81}Zr [79]. Following the consistency of the deduced decay scheme of ^{79}Y with ^{81}Zr, the unidentified 293-keV transition (see peak labelled with star in Fig. 7.4(b)) should feed into the 239-keV decay. However, when gating on 293 keV [Fig. 6.28(d)] there are no discernible peaks. Therefore it was not possible to assign to 293-keV peak to a particular transition. If indeed this band is identical to that of ^{81}Zr then the 167 and 238-keV decays would correspond to $(\frac{5}{2}^-) \rightarrow (\frac{3}{2}^-)$ and $(\frac{7}{2}^-) \rightarrow (\frac{2}{2}^-)$ transitions, respectively. However, the acquired statistics are not sufficient to confirm this.

Table 6.14: Measured γ-ray energies (in keV) and relative intensities of decays in the ^{79}Zr and ^{79}Y mirror pair. For ^{79}Y the measured γ-ray energies are compared with that of Ref. [124]. The recoil velocities ($\beta = \frac{v}{c}$) used in the Doppler-correction process to extract the energies are also detailed.

$J_i \rightarrow J_f$	^{79}Zr (^{81}Zr -2n)			^{79}Y (^{80}Y -1n)			
	E_γ	β	Rel. Int.	E_γ	Lit.	β	Rel. Int.
				167(1)		0.304	7(1)
$(\frac{7}{2}^+) \rightarrow (\frac{5}{2}^+)$	184(1)	0.298	100	183(1)	184.0(5)	0.294	100
$(\frac{9}{2}^+) \rightarrow (\frac{7}{2}^+)$	230(2)	0.304	22(10)	227(1)	227.0(5)	0.296	35(1)
				238(1)		0.304	10(1)
				293(1)		0.304	9(1)
$(\frac{11}{2}^+) \rightarrow (\frac{9}{2}^+)$				316(1)	316.1(5)	0.304	15(1)†
$(\frac{13}{2}^+) \rightarrow (\frac{11}{2}^+)$				315(1)*	315.0(5)		
$(\frac{9}{2}^+) \rightarrow (\frac{5}{2}^+)$	416(2)	0.304	15(10)	411(1)	411.3(5)	0.296	14(2)
				529(1)		0.304	5(2)
$(\frac{11}{2}^+) \rightarrow (\frac{7}{2}^+)$	531(4)	0.304	18(11)	543(1)	543.1(5)	0.304	10(2)
$(\frac{13}{2}^+) \rightarrow (\frac{9}{2}^+)$				631(1)	631.1(5)	0.304	8(1)
				690(1)		0.304	4(1)
				700(1)		0.304	15(1)

* Assumed given observation of 631-keV decay.
† Combined intensity of 315 and 316-keV decays.

Table 6.15: Spins/parities, excitation energies in keV and MED in keV of the isobaric analogue states in ^{79}Zr/^{79}Y. The $(\frac{5}{2}^+)$ states are assumed to be the ground states in both nuclei.

J^π	^{79}Zr	^{79}Y	MED
$(\frac{5}{2}^+)$	0	0	0
$(\frac{7}{2}^+)$	184(1)	183(1)	1(1)
$(\frac{9}{2}^+)$	416(2)	411(1)	5(2)
$(\frac{11}{2}^+)$	715(4)	726(1)	-11(4)

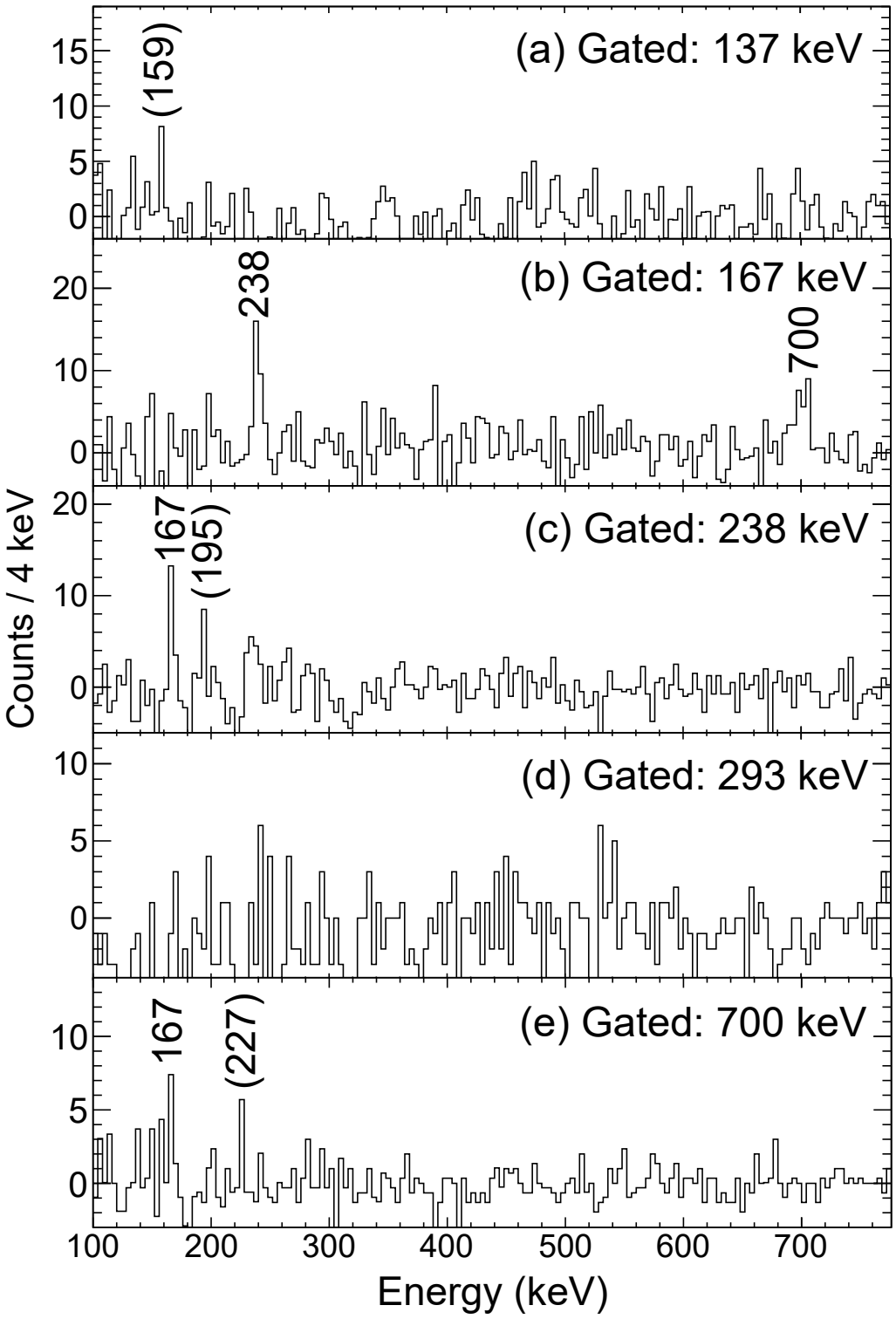

Figure 6.28: 137 (a), 167 (b), 238 (c), 293 (d) and 700-keV (e) gated spectra for ^{79}Y. From this data the unidentified 167 and 700-keV transitions can be seen to be within the same cascade. The 167 and 239-keV transitions are also within the same cascade, producing a structure identical to that of ^{81}Zr.

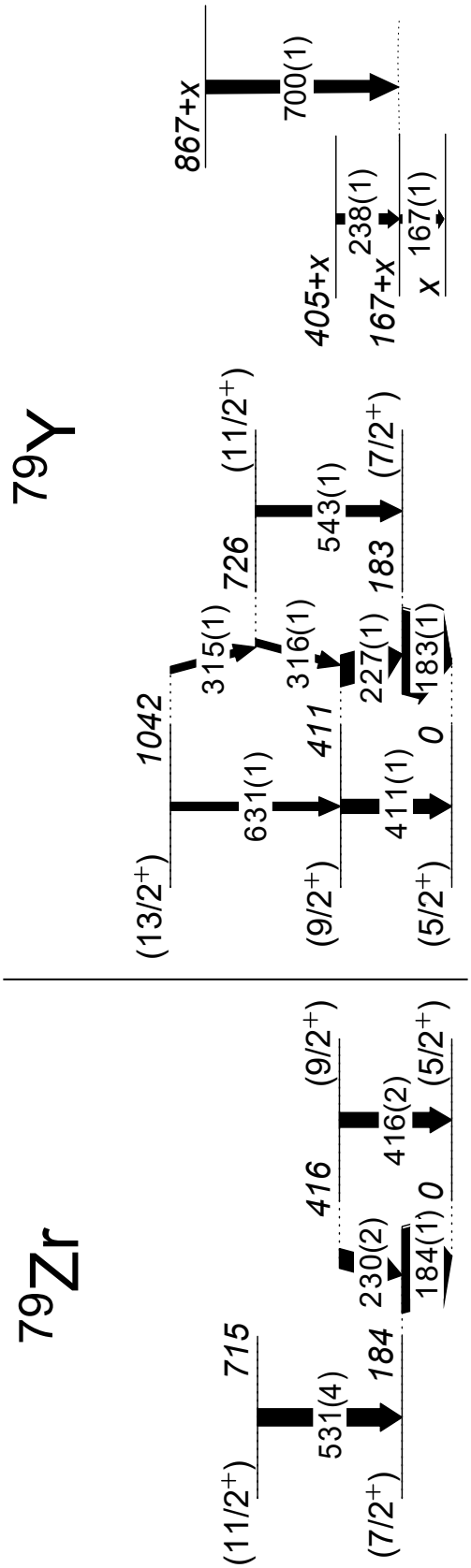

Figure 6.29: Deduced γ-ray decay schemes of ^{79}Zr (^{80}Zr -2n) and ^{79}Y (^{80}Y -1n). Note that there is a slight discrepancy between the sum of γ-ray energies and energy levels of states arise from lifetime effects of the $(\frac{7}{2}^+) \rightarrow (\frac{5}{2}^+)$ decays and uncertainties on γ-ray energies. The newly identified decay sequence of ^{79}Y is shown on the right-hand side.

Chapter 7

Discussion

7.1 B(E2↓) Systematics

The newly measured values for the B(E2↓) for ^{78}Y and ^{80}Zr expand the picture of the evolution of collectivity to and beyond the $N = Z = 39$ mid shell point. The measurement of the B(E2↓) of ^{80}Zr is a notable achievement as it is the heaviest $N = Z$ nucleus where a B(E2↓) measurement has been made to date in one of the most deformed and hard to access regions of the whole nuclear chart. This is a result that has eluded nuclear physicists since the first decay scheme was deduced in 1987 [11], a time when ^{80}Zr was initially thought to be spherical [28]. Measuring the B(E2↓) has only recently become possible with modern developments in radioactive ion-beam production using fragmentation techniques, exploitation of knockout reactions and γ-ray tracking arrays such as GRETINA.

These new measurements are labelled with red squares in Fig. 7.1, where the red triangle is used to indicate the weighted average of the B(E2↓) value for ^{76}Sr with the result from this experiment and the value obtained in Ref. [21]. The values for the remaining previously measured $N = Z$ nuclei are taken from [15, 16, 17, 18, 19, 20] where weighted averages have been used where possible. The sharp increase in collectivity beyond $A = 70$ can be attributed to the increasing dominance of the role of the $g_{9/2}$ orbital. The occupation of neutrons and protons in the $g_{9/2}$ orbital is predicted to increase from two to three from ^{72}Kr to ^{76}Sr [23]. The steepness of the downwards sloping low Ω $g_{9/2}$ orbital projections in the Nilsson level scheme (see Fig. 2.5) results in its intrusion towards the Fermi level at the deformations seen in this mass region of $\beta_2 \sim 0.4$. This provides stability to more collective, deformed nuclear

shapes.

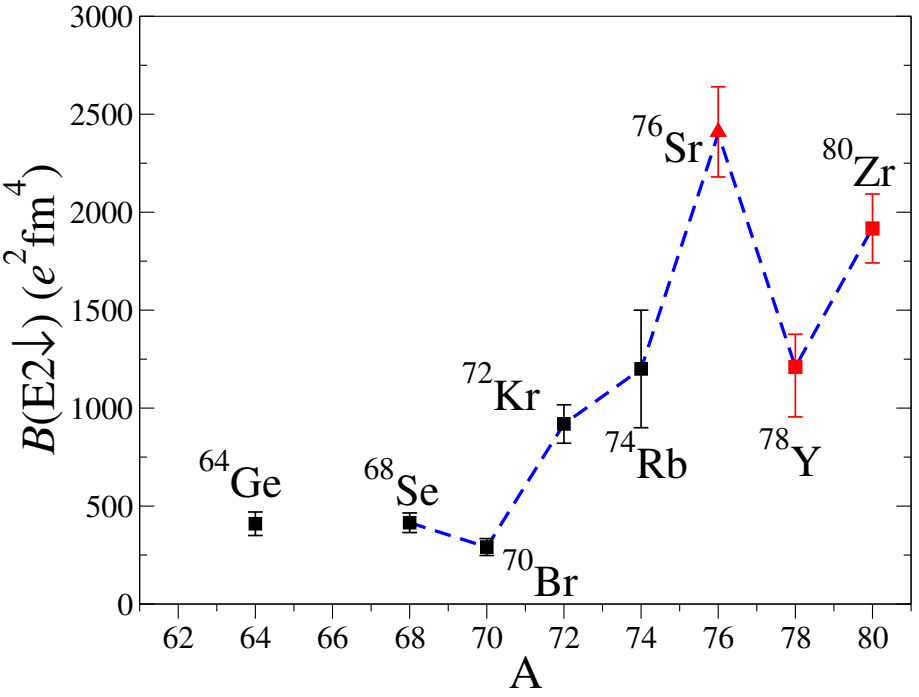

Figure 7.1: Schematics of $B(\mathrm{E2}\downarrow)$ values for the $N = Z$ nuclei from $A = 64 - 80$, where the newly obtained values are indicated in red. Data were taken from Refs. [15, 16, 17, 18, 19, 20] where weighted averages are used where possible. For ^{76}Sr (red triangle) is the value is a weighted average of the newly measured value and that from Ref. [21]. There is a clear odd-odd, even-even $B(\mathrm{E2}\downarrow)$ staggering effect observed above ^{68}Se. The dashed blue line is to guide the eye.

From Fig. 7.1 it can be seen that the maximum collectivity along the $N = Z$ line is now firmly established to occur at ^{76}Sr. Despite the fact the number of neutrons in the deformation-driving $g_{9/2}$ orbital is predicted to increase from ^{76}Sr to ^{78}Sr [23], ^{78}Sr is found to possess a $B(\mathrm{E2}\downarrow)$ ~30% lower than ^{76}Sr. This therefore suggests that the occupation of the $g_{9/2}$ orbital is saturated at $N = Z = 38$. Indeed, this theory is consistent with the lower $B(\mathrm{E2}\downarrow)$ measured in ^{80}Zr beyond ^{76}Sr.

7.1.1 B(E2↓) Staggering

One of the most intriguing features of these $B(\mathrm{E2}\downarrow)$ systematics approaching the $A = 80$ region is a continuation of an odd-odd, even-even staggering effect, which was first noticed with ^{70}Br [17]. However, approaching the mid-shell point at ^{78}Y, where one would naturally expect the peak of collectivity, this staggering is very clear with a reduction by a factor of

around two from that of ^{76}Sr. Exploring lighter $N = Z$ nuclei there is no evidence of a similar staggering around the $A = 48$ $f_{7/2}$ region. From Fig. 7.2 it can be seen that there is a steady increase in collectivity up to the even-even mid-shell ^{48}Cr followed by a steady decrease. The B(E2↓) staggering phenomenon is therefore not universal across all mass regions.

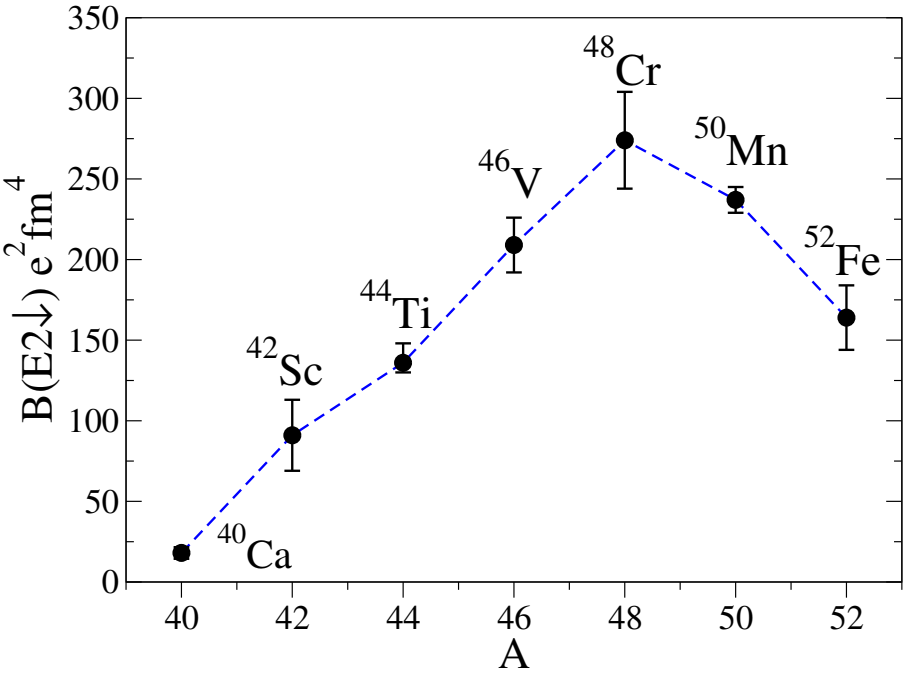

Figure 7.2: B(E2↓) values for $N = Z$ nuclei in the $f_{7/2}$ region. Data were taken from the ENSDF database [107] and Refs. [128, 129, 130]. Note that the value for ^{50}Mn from Ref. [129] may have uncertainties associated with branching ratios that are not taken into consideration. The dashed blue line is to guide the eye.

7.1.2 B(E2↓) vs $R_{4/2}$

As an increase in the deformation of a nucleus corresponds to a larger B(E2↓) and a larger ratio of the energies of the 4^+ and 2^+ states ($R_{4/2}$), one would expect these two values to be directly correlated. When normalising B(E2↓) by a nucleus' mass [B(E2↓)/A] and converting into Weisskopf units (W. u.) an overall trend between these properties is observed, although the correlation is weak. A deviation from the global behaviour of B(E2↓)/A vs. $R_{4/2}$ of the yrast band has been suggested as a possible signature of shape coexistence [21, 131]. When a nucleus possesses multiple coexisting shapes at low excitation energies, a mixing amongst these results in a reduced $R_{4/2}$ as the coexisting shapes lower 0^+ states more than others

[131]. This results in an increased $2^+ \rightarrow 0^+$ energy, yielding a reduced $R_{4/2}$ ratio.

Data for the even-even $N = Z$ nuclei ranging from $A = 16 - 80$ is shown in Fig. 7.3. The data were taken from Ref. [21] and references therein, along with the present work where weighted averages have been used where possible. From this figure it can be seen that there are two distinct linear tracks - those which follow the overall trend (indicated with the black line) and those which follow a similar trend but possess a significantly reduced $R_{4/2}$ relative to $B(\mathrm{E2}\downarrow)$. The $N = Z$ nuclei which are believed to exhibit shape coexistence [19, 21] are labelled in green, whereas ^{20}Ne is believed to have a ground state consisting of a cluster configuration (e.g. $^{16}\mathrm{O} + \alpha$ [132]) and is labelled in red. The anomaly in this plot is ^{68}Se which despite being believed to possess coexisting nuclear shapes [16] is found to show good agreement with the lower trend. A possible explanation of this observation may lie with the nature of the shape coexistence. ^{72}Kr is believed to have a ground state with 50/50 mixing of oblate and prolate shapes [19] whereas calculations for ^{80}Zr predict as many as five different low-energy ground states [29]. This therefore points to the possibility of shape mixing in the ground state being responsible for nuclei being found higher up the plot, with ^{68}Se being found to follow the usual trend due to mixing in excited states [16].

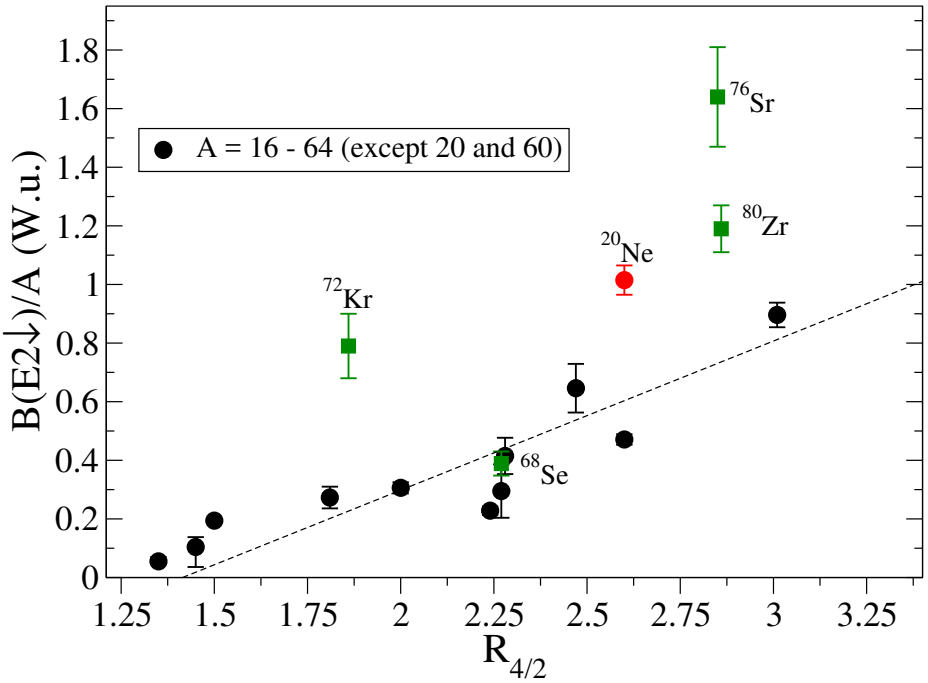

Figure 7.3: $B(\mathrm{E2}\downarrow)/A$ values in Weisskopf units (W. u.) plotted against the energies ratios of the 4^+ and 2^+ states $R_{4/2}$ for even-even $N = Z$ nuclei. The green data points are nuclei which are believed to exhibit shape coexistence while the red data point represents ^{20}Ne which is believed to have a ground state consisting of cluster configurations. The dashed black line signifies the trend of the lower data points. Data are taken from the present work and the ENSDF database [107].

For systematic comparison this picture is expanded beyond $N = Z$ nuclei in Fig. 7.4 where data for several isotopic chains from Kr to Pb are shown. As before the nuclei that are believed to possess coexisting shapes are represented with colour symbols and are individually labelled. Isotopes not known to exhibit shape coexistence are indicated with black solid symbols, where the corresponding elements are detailed in the key in the inset of the figure. Values were taken from the ENSDF database [107] and the present work. As with Fig. 7.3, the lower trend between the vibrational $R_{4/2} \approx 2$ and rotational $R_{4/2} \approx 3.3$ is shown with the dashed black line. In contrast to Fig. 7.3 there is a far greater deviation from the trend line when the picture is expanded across the nuclear chart. However, the overall behaviour is the same - all of the nuclei found higher up the plot are believed to exhibit shape coexistence. It is possible that the cluster seen around $R_{4/2} \approx 2.25$ are rotational nuclei or nuclei with single-particle excitations, hence the low $B(\mathrm{E2}\downarrow)$. Addressing the reason as to why certain nuclei are found higher on the plot has the additional complication of where exactly the lower

trend line is located. Ref. [131] speculated that there may in fact be two distinct tracks - the trend that is plotted and an additional lower curved track that starts lower at $R_{4/2} \approx 2$ and curves sharply upwards at $R_{4/2} \approx 3.3$. This was proposed as a transition from γ-soft to symmetric rotor nuclei.

If the heaviest nuclei on this plot - ^{186}Pb, is indeed found above these trends then this agrees with the earlier hypothesis of ground-state shape mixing being responsible for the deviation from the global behaviour as ^{186}Pb has been suggested to possess three different 0^+ states [133]. This demonstrates that this behaviour may be consistent over an expansive range of the nuclear chart. However, this conclusion may be premature as the variance of the nuclei on this plot is large meaning that nuclei may be identified as following or deviating from the trend depending on where it is drawn. Another notable feature is that all Se isotopes are found lower on the plot and seemingly either follow the trend line or are found below it, whereas other nuclei around the same region are found to deviate from the trend. These systematics are particularly intriguing and as the origin of certain nuclei being found where they are remains uncertain this could be an topic of further research and discussion.

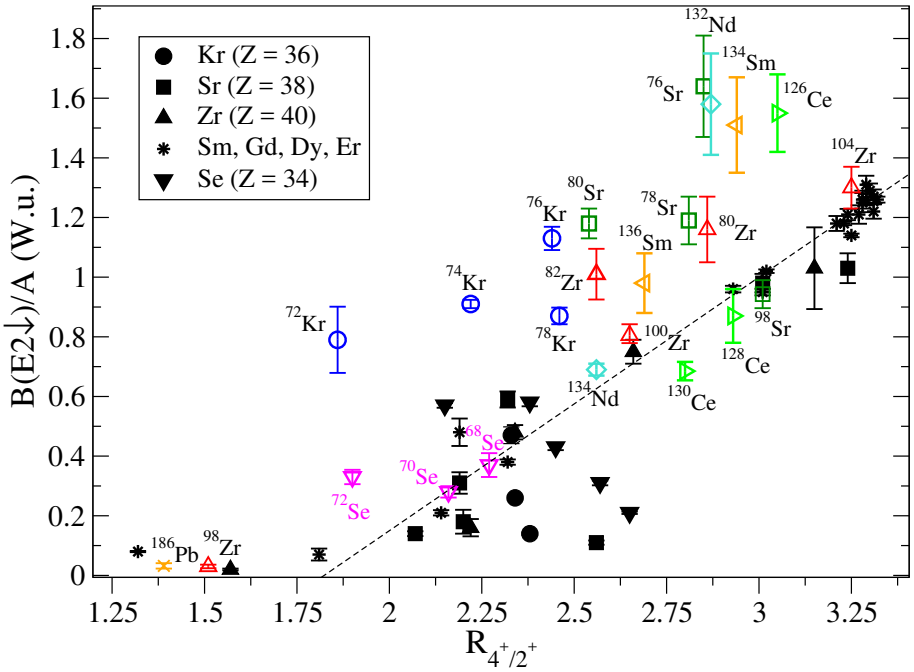

Figure 7.4: $B(\mathrm{E2}\downarrow)/A$ values in Weisskopf units (W. u.) plotted against the energies ratios of the 4^+ and 2^+ states $R_{4/2}$. The dashed black line represents the typical $B(\mathrm{E2}\downarrow)/R_{4/2}$ trend. The nuclei possessing an enhanced $B(\mathrm{E2}\downarrow)/R_{4/2}$ ratio (a signature of shape coexistence) are labelled in colour. Data are taken from the present work and the ENSDF database [107].

7.1.3 E2 Matrix Elements

From these new B(E2↓) measurements one can calculate the transition matrix elements from Eq. 2.25 and decompose these into isoscalar (M_0) and isovector (M_1) parts. The M_0 and M_1 terms against A are shown in Fig. 7.5 along with the new data extracted for $A = 78$ derived from the measured B(E2↓) values for ^{78}Y ($T_z = 0$) and ^{78}Sr ($T_z = +1$). The isoscalar terms are shown to show an increase beyond the *sd* shell, which is consistent with the observed increase in collectivity in this region. Interestingly, the M_1 terms are found to show no correlation with A until $A = 78$ where a deviation from 0 to ∼-40 $e$fm^2 is seen. This provides an indication of isoscalar-isovector configuration mixing occurring above $A = 70$, whereas before the matrix elements where dominated by their isoscalar parts. This deviation from the norm of both the M_0 and M_1 may be an indication that isospin is no longer conserved across the isobaric triplet at these heavier masses. If isospin is conserved then the B(E2↓) values should be be very similar, which is not the case with ^{78}Sr and ^{78}Y. The large M_0 $T = 1$ contribution at $A = 78$ also shows a continuation of the agreement with M_0 $T = 0$ values derived from even-even nuclei which are shown in Ref. [20].

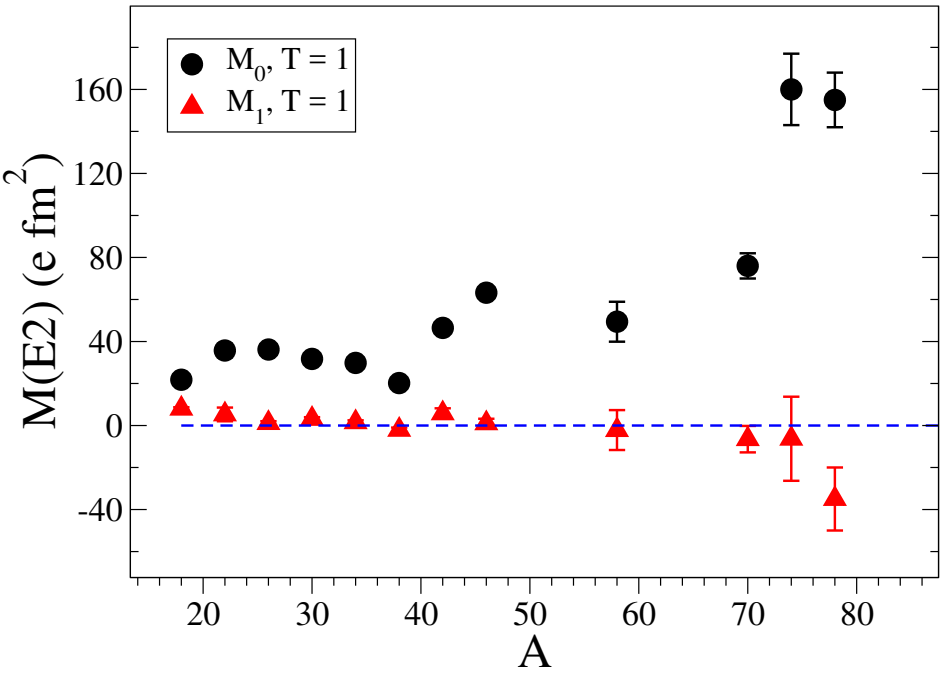

Figure 7.5: The E2 matrix transition elements split into isoscalar (black circles) and isovector (red triangles) components for the odd-odd ($T = 1$) nuclei. The isovector components remain relatively constant over the $T = 1$ triplets whilst the isoscalar components increase in dominance approaching $A = 78$. Data are taken from the present work and Ref. [20] and references therein.

7.2 Large-Scale Shell Model Calculations

When numerically feasible large-scale shell model (LSSM) calculations are an excellent theoretical tool to investigate nuclear structure. However, the results from these types of calculations in the $A \approx 80$ $N = Z$ are highly dependent upon the model spaces and quadrupole degrees of freedom. These arise due to the large gap between the $N = Z = 28$ and $N = Z = 50$ closed shells and therefore demand the inclusion of a large number of valence particles above the $N = Z = 28$ core. A series of LSSM calculations were performed in Ref [134] for even-even $N = Z$ nuclei ranging from ^{56}Ni to ^{96}Cd. The calculated B(E2$\downarrow$) values for ^{72}Kr, ^{76}Sr and ^{80}Zr are shown in Fig. 7.6 with a variety of model spaces for each. Here the notation used for the model spaces is $r_3^k(gds)^l$ where k is used to denote the number of particles occupying the r_3 space (or fp shells) whilst l is the number of particles in the gds orbitals. In the case of oblate nuclei (represented by the solid symbols), the model space is simplified to only include the $g_{9/2}$ orbital: $r_3^k g^l$. These variables along with the type of deformation are represented

in Fig. 7.6 as different colour, shaped and shaded symbols (see the inset key for more information). Fig. 7.6 clearly demonstrates the importance of the choice of model space and its drastic effect on the calculated $B(\mathrm{E2}\downarrow)$ values in this mass region.

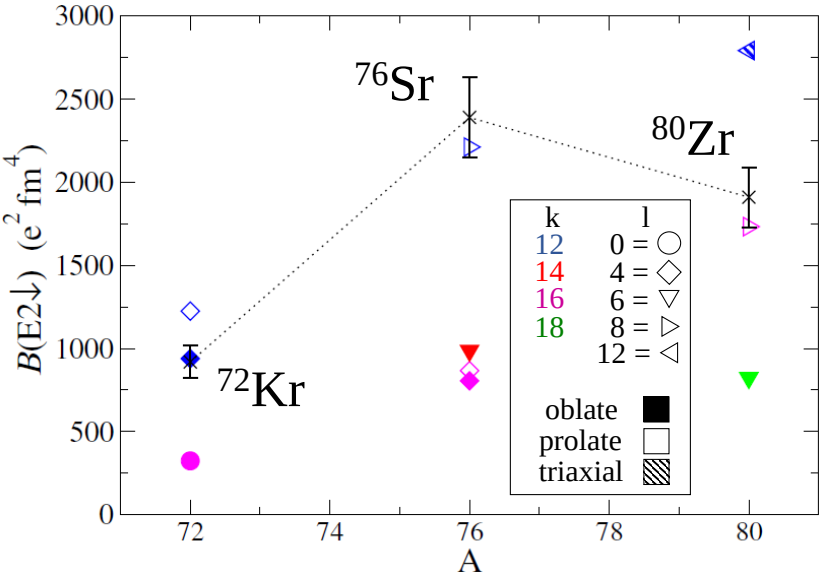

Figure 7.6: Comparison of the experimental $B(\mathrm{E2}\downarrow)$ values of even-even $N = Z$ nuclei (black data points) with LSSM calculations from Ref. [134]. The LSSM calculations explore the effects of different model spaces. For prolate and triaxial shapes, the $r_3^k(gds)^l$ model space is used whilst for oblate shapes $r_3^k g^l$ is used. Here k and l denote the number of particles in the r_3 space (fp shell) and the gds/g orbitals, respectively. The key on the inset of the plot indicates the k and l values used and the type of deformation. The black dashed line is to guide the eye.

Prolate solutions for ^{76}Sr and ^{80}Zr are found to be consistent with experiment with the $r_3^{12}(gds)^8$ and $r_3^{16}(gds)^8$ model spaces, respectively. This therefore equates to the addition of four nucleons into the fp shells onto ^{76}Sr to form ^{80}Zr. ^{72}Kr is found to show good agreement with an oblate solution with the $r_3^{12}g^4$ model space. However, it is noted in Ref. [19] that ^{72}Kr possesses a rapid oblate-prolate shape transition with increasing spin, where the measured $B(\mathrm{E2}\downarrow)$ was found to be too small to be prolate, whilst the $B(\mathrm{E2};\ 4^+ \rightarrow 2^+)$ was too large to be oblate. Therefore the effects of shape coexistence have to be implemented in this case. This was addressed in the calculations in Ref. [134] where the the $r_3^{16-t}(gd)^t$ model space was used with the JUN45 interaction [55] supplemented with matrix elements for the $d_{5/2}$ orbital. Incorporating these factors reduces the calculated $B(\mathrm{E2}\downarrow)$ from 939 to 740 $e^2\mathrm{fm}^4$, a decrease of 27%. This demonstrates that despite the difficulty of a shell-model approach in this mass

region calculations consistent with experiment can be achieved. However, there is a not a consistent treatment for the optimum model space to reproduce experimental data across the whole region, which is further complicated with the consideration of shape-coexistence effects.

7.3 Density Functional Theory Calculations

The discussion in Chapter 7.2 in regards to LSSM calculations in the neutron-deficient $N = Z$ $A \approx 80$ region concluded that the large deformations and the inclusion of shape-coexistence effects provide vast computational challenges arising from the large $fpgds$ model space required. In the case of attempting to replicate the collectivity in this region a severe truncation is required, which are greatly hampered by the treatment of valence spaces and interactions. Given the mean-field approach of DFT calculations, these do not suffer from the same issues associated with the limited valence spaces of shell-model calculations making DFT calculations in this mass region potentially more viable.

7.3.1 Constrained 5D Collective Quadrupole Hamiltonian HFB Calculations

The introduction of unpaired nucleons in odd-odd nuclei provides many computational challenges through both shell model and DFT approaches. This problem is greatly simplified with even-even nuclei, where nucleons paired with anti-aligned spins vastly decrease the number of free parameters. A comprehensive series of HFB calculations mapped to a constrained five-dimensional collective quadrupole Hamiltonian (CHFB + 5DCH) using the Gogny D1S interaction [135] were performed for even-even nuclei in Ref. [8], calculating $B(\text{E2}\downarrow)$ values from $A = 18 - 296$. These incorporate factors such as the mixing of shapes, including a triaxial degree of freedom. The calculations are compared with the measured $B(\text{E2}\downarrow)$ values (black data points) in Fig. 7.7 where the newly obtained values are shown in red. Weighted averages are used where possible, which in the case of ^{76}Sr (red triangle) is a weighted average of the new value and that of Ref. [21]. The blue data points correspond to the CHFB + 5DCH calculations, where the dotted blue line is to guide the eye.

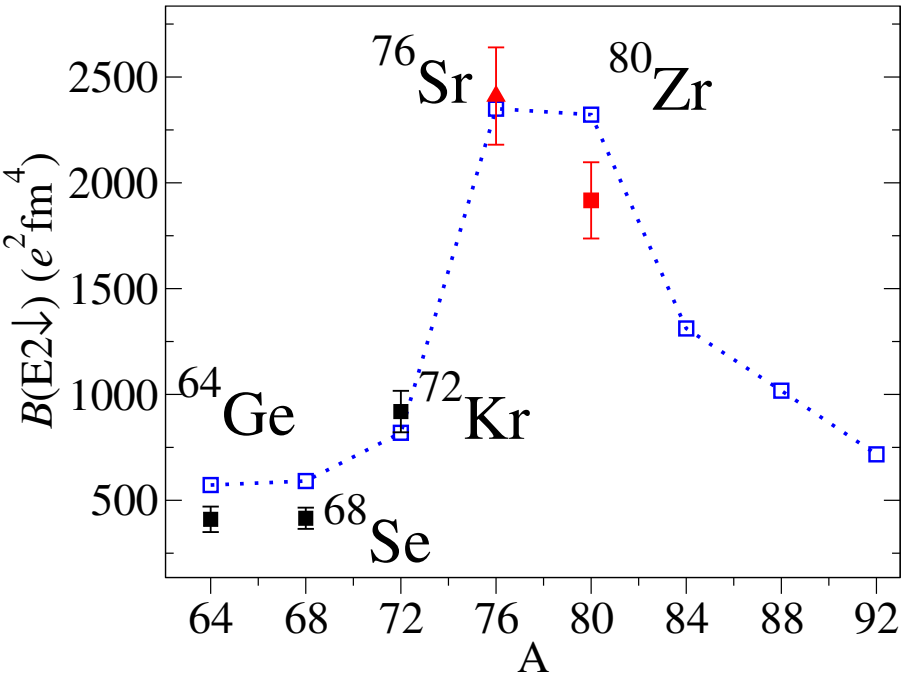

Figure 7.7: Comparison of the previously obtained experimental $B(\mathrm{E2}\downarrow)$ values of even-even $N = Z$ nuclei (black data points) and the new data (red data points) with constrained five-dimensional collective quadrupole Hamiltonian HFB calculations from Ref. [8] (dotted blue line). Weighted averages are used for values where possible.

From examining Fig. 7.7, it can be seen that the observed sharp increase in collectivity in the even-even $N = Z$ nuclei beyond $A = 68$ is replicated. These calculations also agree with the experimentally-observed maximum of collectivity at ^{76}Sr, which shows excellent agreement with the measured $B(\mathrm{E2}\downarrow)$.

7.3.2 HFB Calculations with Pair Blocking

The calculations in Ref. [8] discussed above demonstrate the capability of a DFT approach in modelling the trend in collectivity for the even-even $A = 64-80$ $N = Z$ nuclei. However, when addressing the odd-odd nuclei, where the unexplained staggering effect is seen, the unpaired nucleons make the calculations far more complex. The relatively steady $B(\mathrm{E2}\downarrow)$ across the even-even $N = Z$ ^{76}Sr and ^{80}Zr (see Fig. 7.7) provides a stringent test for DFT calculations in this region and provides a reliable stepping stone prior to exploring the implications of the odd number of neutrons and protons in ^{78}Y.

To investigate the origins of odd-odd/even-even $B(\mathrm{E2}\downarrow)$ staggering effect HFB DFT calcu-

lations were performed by Prof. Jacek Dobaczewski utilising the Skyrme UNEDF0 functional [136] for ^{76}Sr, ^{78}Y and ^{80}Zr. In these calculations the pairing strengths were increased by 20% to compensate for the fact that the Lipkin-Nogami approximation [137] was not used. These calculations show excellent agreement with the experimentally measured values for the even-even ^{76}Sr and ^{80}Zr (see right-hand panel of Fig. 7.8).

When addressing ^{78}Y, the calculated Nilsson model [422]5/2 and [301]3/2 quasiparticle levels were found to converge at the Fermi level (see left-hand panel of Fig. 7.8). This potentially provides an insight as to the origin of the sharp reduction of collectivity observed in ^{78}Y given that the downsloping [422]5/2 is a deformation-increasing orbital and the upsloping [301]3/2 orbital is deformation-decreasing. Without the inclusion of orbital blocking effects these two Nilsson orbitals were found to be degenerate and equally occupied. There is therefore a possibility of the B(E2$\downarrow$) staggering effect having local nuclear-structure based origin related to the roles of these deformation-driving/reducing orbitals.

As these quasiparticle levels are degenerate, the impact of pair blocking [68] on the B(E2$\downarrow$) can be explored (see Chapter 2.3.4 for more details). It was found that blocking a neutron or proton in either the [422] or [301] level significantly reduced the pairing correlations. Blocking the [422] level had the effect of increasing its occupation whilst simultaneously decreasing the occupation of the [301] level. This, coupled with the reduced pairing correlations, is a deformation-increasing effect and therefore yields a larger B(E2$\downarrow$), as shown by the purple data points in the right-hand panel of Fig. 7.8. When blocking the [301] level one would expect a reduction in B(E2$\downarrow$). However, this reduction in collectivity is cancelled out by the reduced pairing in the even-even core caused by pair blocking. Therefore, the sharp reduction in the B(E2$\downarrow$) seen experimentally with ^{78}Y can not be reproduced (see blue data points in right-hand panel of Fig. 7.8).

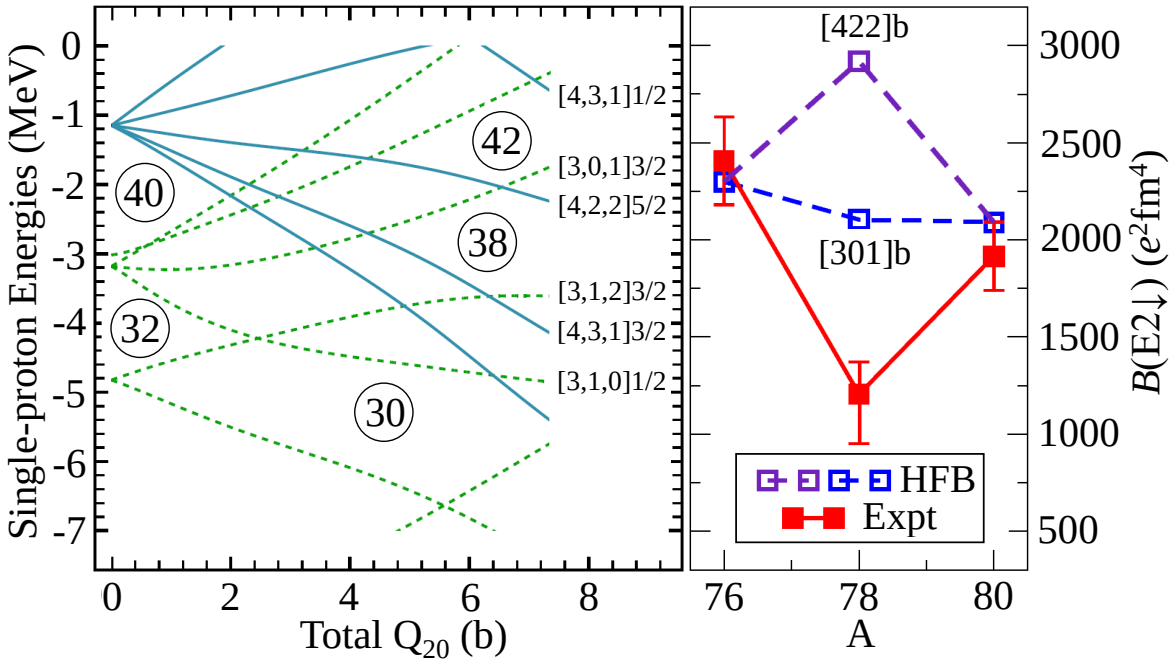

Figure 7.8: The left-hand panel displays the calculated single-particle Nilsson levels as a function of total quadrupole moment (Total Q_{20}). The Fermi level of the odd-odd ^{78}Y is found at the crossing point of the [422]5/2 and [301]3/2 quasiparticle levels. The right-hand panel displays the B(E2↓) values from HFB calculations compared with experimental values (red data points). Here the effects of blocking the the [422] and [301] levels on the B(E2↓) is explored for ^{78}Y (purple and blue data points).

As discussed in further detail in Chapter 2.3.4, these HFB calculations only include $T = 1$ np pairing. Although there have been previous HFB calculations performed incorporating $T = 0$ np pairing (see e.g. [12, 13, 38, 64]), these calculations make specific approximations. For example, they assume that particle-hole and neutron and proton fields are considered separate from one another. In a true self-consistent approach these mean fields would be mixed [65, 66, 67]. An inclusion of this in HFB calculations requires a major overhaul to current HFB codes and progress has already been made in pursuing fully self-consistent calculations with the inclusion of a mixed neutron-proton quasiparticle wave function [3]. Hence the possibility of the observed staggering effect being reproducible with the inclusion of $T = 0$ np pairing in HFB calculations can not be dismissed at the present time. Likewise, the possibility of a different functional possessing the capability of reproducing the results can not be excluded.

7.4 Mirror Energy Differences

The MED extracted for the $A = 79$ ^{79}Zr/^{79}Y mirror pair correspond to the heaviest nuclei where such measurements have been made to date. These MED are the first to probe the effects of the $g_{9/2}$ orbitals in one of the most deformed regions of the whole nuclear chart, following extensive studies in the upper-sd and lower-fp shells (see Ref. [32] and references therein for a review). The MED of the $A = 79$ mirror pair which are listed in Table 6.15 are remarkably small in comparison to previous MED studies in lighter nuclei. For example, MED of the order of 100 keV were measured in the fp shell [36]. This implies that the deformed $A = 79$ systems are likely to be based upon highly stable configurations.

As previously discussed in Chapter 7.2 there is great difficulty in interpreting these results through a shell-model approach due to the large model space required around the mid-fpg shell region, with the nuclei requiring valence spaces with orbitals originating above the ^{100}Sn core to account for their large deformations [134]. Therefore these results were analysed through a novel DFT approach through the no-core configuration-interaction (NCCI) model [138]. This methodology has been refined to allow the study of isospin-breaking and nuclear charge-symmetry breaking (CSB) effects.

The calculations to determine the angular-momentum projected states of ^{79}Zr/^{79}Y were performed by Prof. Wojciech Satuła. 40 low-lying Hartree-Fock configurations were established for each nucleus, which were then mixed through the Hamiltonian corresponding to the density-independent Skyrme force SV$_T$ [139]. After considering the mixing properties of all configurations it was determined that only ten have meaningful non-zero mixing coefficients with the ground state configuration. The calculations were therefore restricted to these ten configurations as it can be assumed that the calculations are converged with respect to a growing configuration space.

The details of these configurations are displayed in the table in Fig. 7.4 where hollow circles are used to represent broken pairs with the arrows indicating the spin of the unpaired nucleon. The configurations are categorised as either seniority $\nu = 1$ or 3 (denoting the number of unpaired nucleons), like-particle pair excitations (nn/pp) or neutron-proton pair excitations (np). Fig. 7.4(b) shows the step-by-step contribution of these to the calculated MED when these configurations are incrementally mixed with the ground state. Here the contributions are grouped into $\nu = 1$ (1), nn/pp and np excitations (2) and $\nu = 3$ (3) and are

represented by the different colour arrows. It is clear that $\nu = 3$ excitations have the great influence on the calculated values and significantly lower the MED and show an improved agreement with the experimental MED. In contrast pair configurations are found to have a minimal effect.

The final calculations with all ten configurations incorporated (blue triangles) are compared with the experimental MED data in Fig. 7.4(a), where the same calculations whilst only including Coulomb effects are plotted for comparison (blue diamonds). The calculations are consistent with the experimental data up to $J = (\frac{9}{2}^+)$. There is then a departure at $J = (\frac{11}{2}^+)$, the magnitude of which can not be explained with the current calculations. However, it must be remembered that here the MED are incredibly small and a discrepancy between theory and experiment of at most ~ 20 keV is still impressive. Moreover, it is impossible to accurately quantify the uncertainty of the values obtained through the NCCI calculations [140] so these are not taken into consideration. The implications of the $h_{11/2}$ [550]1/2 orbital were also explored to investigate whether this would have any effect the calculated $\frac{11}{2}^+$ MED. However, this was found to not have any meaningful contribution to the states included in the model. Additionally, due to the low statistics acquired for ^{79}Zr, therefore making it impossible to perform any $\gamma - \gamma$ coincidence analysis, there is the small possibility that the 531-keV decay may correspond to a decay from a state other than the $(\frac{11}{2}^+)$. However, given the similarity of the measured energy with the known $(\frac{11}{2}^+) \rightarrow (\frac{7}{2}^+)$ decay of ^{79}Y this is unlikely.

One of the main achievements of this MED analysis is the proof of concept that MED in a particularly difficult mass region can be reproduced with the NCCI model. MED analysis of the ^{79}Zr/^{79}Y mirror pair may not have been otherwise possible with the traditional shell-model approach. This work therefore opens a gateway to a new MED investigations in this highly deformed, mid-shell region that require large model spaces in shell model calculations that are not computationally viable at present. A comparison of MED calculations of several lighter nuclei through an NCCI approach is currently ongoing [141] and will provide a comprehensive test given that there are established shell-model benchmarks in these lighter regions. This may also provide some guidelines as to how to approach and refine these calculations in future work.

Group		1			2					3	
Config.	g.s.	ν=1			nn/pp			np		ν=3	
total Ω	+5/2	+3/2	+1/2	+7/2	+5/2	+5/2	+5/2	+5/2	+5/2	+3/2	+7/2
N,Z or Z,N	39 40	39 40	39 40	39 40	39 40	39 40	39 40	39 40	39 40	39 40	39 40
[413]7/2				↑	●			↑ ↓		↓	↑
[301]3/2						●	●		↑ ↓		
[422]5/2	↑ ●	● ●	● ●	●	↑	↑ ●	↑ ●	●	↑ ●	↑ ↓	↑ ↓
[303]7/2	● ●	● ●	● ●	● ●	● ●	●	●	● ●	↓ ●	● ●	● ●
[431]3/2	● ●	↑ ●	● ●	● ●	● ●	● ●	● ●	● ●	● ●	● ●	● ●
[440]1/2	● ●	● ●	↑ ●	● ●	● ●	● ●	● ●	● ●	● ●	● ●	● ●

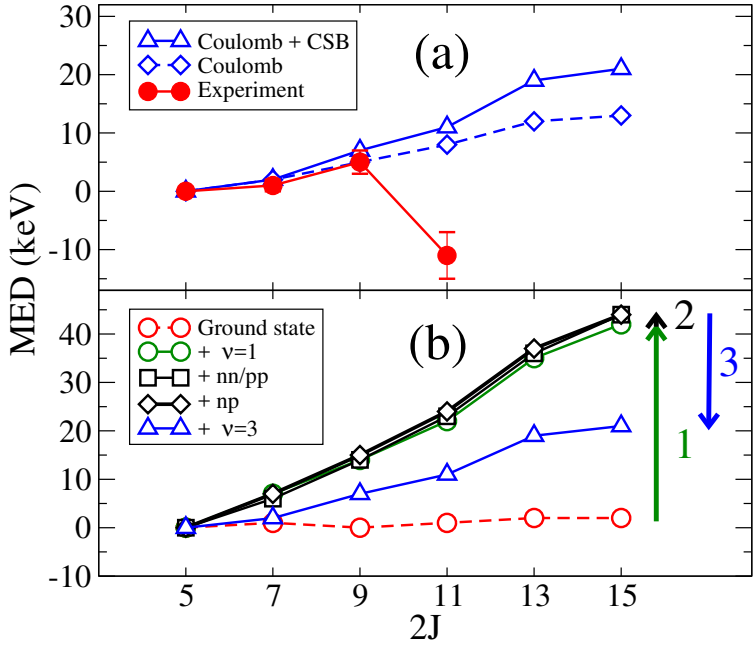

Figure 7.9: Configurations used in the NCCI calculations to obtain results shown in (a) and (b) are detailed in the table (see text for more information). Full dots denote deformed $[N\Lambda n_z]K$ orbitals occupied by pairs of nucleons in the 39 or 40 subsystems. Empty dots with up (down) arrows denote orbitals occupied by single nucleons with individual positive (negative) projections Ω of angular momentum on the axial-symmetry axis. (a) shows the calculated and experimental (red) mirror energy differences as a function of spin J for the tentatively assigned ground-state configuration of $[422]\frac{5}{2}^+$ in the ^{79}Zr/^{79}Y mirror pair with (blue triangle) and without charge-symmetry breaking (CSB) effects (blue diamond). The lower plot shows how the final calculations were constructed by incrementally incorporating different excited configurations shown in the table. These configurations are grouped into three categories (see table) and are represented with coloured arrows. Note that the blue triangles in (a) and (b) are the same calculations.

Chapter 8

Conclusion and Future Work

In conclusion, $B(\mathrm{E2}\downarrow)$ values have been extracted for the previously unmeasured $N = Z$ ^{78}Y and ^{80}Zr, along with repeat measurements for ^{76}Sr and ^{78}Sr, through the γ-ray lineshape method with GRETINA. These measurements extend the picture of the evolution of collectivity along the $N = Z$ line to and beyond the mid-shell point between the doubly closed-shell nuclei ^{56}Ni and ^{100}Sn.

Values measured for ^{78}Sr and ^{76}Sr were both consistent with the previous values measured through the same technique, confirming the veracity of the new results. These new values suggest a continuation of the odd-odd/even-even staggering in collectivity, which was first noticed in ^{70}Br [17]. The reduction in collectivity seen in the odd-odd ^{78}Y at the mid-shell point from the neighbouring even-even ^{76}Sr and ^{80}Zr is very pronounced, with a reduction by a factor of around two. The maximum collectivity along the $N = Z$ line is firmly established to be located at ^{76}Sr, just before the mid-shell point, which agrees with trend suggested by the CHFB+5DCH calculations in Ref. [8] for the even-even $N = Z$ nuclei.

The origin of the clear odd-odd/even-even staggering remains unclear. The HFB calculations shown in Fig. 7.8 demonstrate that current calculations including only standard $T = 1$ np pairing are incapable of replicating the experimentally observed sharp decrease in $B(\mathrm{E2}\downarrow)$ in ^{78}Y. However, these calculations with this pairing show excellent agreement with the even-even ^{76}Sr and ^{80}Zr. Given the recent progress towards fully self-consistent HFB calculations with the inclusion of mixed isoscalar and isovector np pairing [3], this $B(\mathrm{E2}\downarrow)$ staggering effect will provide a comprehensive test of future calculations and provide possible evidence as to whether this staggering effect is indeed a consequence of $T = 0$ np pairing correlations.

Experimentally the next logical step is to continue $B(\text{E2}\downarrow)$ measurements along with $N = Z$ line towards the doubly-magic ^{100}Sn to observe whether a continuation of this staggering is seen. Experiments have already been approved to measure 2^+ state lifetimes in the $N = Z$ ^{84}Mo [142], ^{86}Tc and ^{88}Ru [143]. The lifetime of the 2^+ state of ^{84}Mo is expected to be $\sim$10 times faster than the lifetimes measured in this work and will therefore require a plunger-target setup (see e.g. Ref. [20]).

The measurements presented in this thesis demonstrate the need for a repeat measurement of the $B(\text{E2}\downarrow)$ of the odd-odd ^{78}Y as this nucleus is where the staggering phenomenon is most prominent. The statistics acquired during this experiment for ^{78}Y were low and the two-neutron knockout reaction mechanism resulted in the 252-keV contaminant peak within the γ-ray lineshape. Although the staggering is still pronounced with both of these factors incorporated into the total uncertainty on the measured $B(\text{E2}\downarrow)$, a higher statistics measurement with a reduced error will firmly establish the extent of this reduction in collectivity. Furthermore, a different reaction mechanism (i.e. one-neutron knockout) may avert the state population responsible for the 252-keV decay which contaminated the lineshape. If this peak is still observed then higher statistics will allow the exact origin of this decay to be identified through $\gamma-\gamma$ coincidence data, eliminating the factors associated with the unknown nature of this decay which were addressed in this work. Likewise, ^{74}Rb currently has a large uncertainty on its $B(\text{E2}\downarrow)$ [20] (see Fig. 7.1), meaning that a repeated measurement is also desirable.

In regards to MEDs, the success of the modelling of the $A = 79$ MEDs with the NCCI model is an excellent achievement and is a big stepping stone towards further development of explaining MEDs through a DFT approach. This will provide access to reliable MED calculations in mass regions that may have otherwise been inaccessible through the traditional shell-model approach which is computationally limited. As with ^{78}Y, a higher statistics γ-ray spectrum of ^{79}Zr and confirmation of the energies of states up to and beyond $\frac{11}{2}^+$ is desirable and would confirm the validity of the present work. This may be achievable with the future development of a ^{80}Zr secondary beam to populate ^{79}Zr through a one-neutron knockout reaction or with a much higher intensity ^{81}Zr secondary beam. As with producing ^{78}Y through a one-neutron knockout reaction, this may be possible in the future with the opening of the Facility for Rare Isotope Beams (FRIB) at NSCL [81] which is due to be completed in 2021/2022.

List of Abbreviations

ADC - Analogue to Digital Converter

AGATA - Advanced Gamma-Ray Tracking Array

CRDC - Cathode Readout Drift Chamber

DAQ - Data Acquisition

DFT - Density Functional Theory

DNL - Differential Non-Linearity

FoM - Figure of Merit

GRETA - Gamma-Ray Energy Tracking Array

GRETINA - Gamma-Ray Energy Tracking In-beam Nuclear Array

HFB - Hartree-Fock-Bogoliubov

HPGe - High-Purity Germanium

LSSM - Large-Scale Shell Model

MED - Mirror Energy Difference

MSU - Michigan State University

NCCI - No-Core Configuration-Interaction

NDF - Number of Degrees of Freedom

NSCL - National Superconducting Cyclotron Laboratory

PID - Particle Identification

OBJ - Object Scintillator

SeGA - Segmented Germanium Array

ToF - Time of Flight

XFP - Extended Focal Plane Scintillator

Bibliography

[1] K. Kaneko, Y. Sun, and G. de Angelis, Nucl. Phys. A **957**, 144 (2017).

[2] B. Cederwall *et al.*, Nature **469** (2011).

[3] A. M. Romero, J. Dobaczewski, and A. Pastore, Phys. Lett. B **795**, 177 (2019).

[4] A. Bohr, B. R. Mottelson, and D. Pines, Phys. Rev. **110**, 936 (1958).

[5] P. Möller, A. Sierk, T. Ichikawa, and H. Sagawa, At. Data and Nucl. Data Tab. **109-110**, 1 (2016).

[6] J. Erler *et al.*, Nature **486**, 509 (2012).

[7] S. E. Agbemava, A. V. Afanasjev, D. Ray, and P. Ring, Phys. Rev. C **89**, 054320 (2014).

[8] J. P. Delaroche *et al.*, Phys. Rev. C **81**, 014303 (2010).

[9] P. J. Davies *et al.*, Phys. Rev. C **75**, 011302(R) (2007).

[10] B. S. Nara Singh *et al.*, Phys. Rev. C **75**, 061301(R) (2007).

[11] C. J. Lister *et al.*, Phys. Rev. Lett. **59**, 1270 (1987).

[12] A. L. Goodman, Phys. Rev. C **60**, 014311 (1999).

[13] A. L. Goodman, Phys. Rev. C **63**, 044325 (2001).

[14] S. Frauendorf and A. Macchiavelli, Prog. in Part. and Nucl. Phys. **78**, 24 (2014).

[15] K. Starosta *et al.*, Phys. Rev. Lett. **99**, 042503 (2007).

[16] A. Obertelli *et al.*, Phys. Rev. C **80**, 031304(R) (2009).

[17] A. J. Nichols *et al.*, Phys. Lett. B **733**, 52 (2014).

[18] A. Gade *et al.*, Phys. Rev. Lett. **95**, 022502 (2005).

[19] H. Iwasaki *et al.*, Phys. Rev. Lett. **112**, 142502 (2014).

[20] C. Morse *et al.*, Phys. Lett. B **787**, 198 (2018).

[21] A. Lemasson *et al.*, Phys. Rev. C **85**, 041303 (2012).

[22] M. Hasegawa, K. Kaneko, T. Mizusaki, and Y. Sun, Phys. Lett. B **656**, 51 (2007).

[23] K. Langanke, D. Dean, and W. Nazarewicz, Nucl. Phys. A **728**, 109 (2003).

[24] S. M. Fischer *et al.*, Phys. Rev. Lett. **84**, 4064 (2000).

[25] J. H. Hamilton *et al.*, Phys. Rev. Lett. **32**, 239 (1974).

[26] E. Clément *et al.*, Phys. Rev. C **75**, 054313 (2007).

[27] E. Bouchez *et al.*, Phys. Rev. Lett. **90**, 082502 (2003).

[28] K. Heyde, J. Moreau, and M. Waroquier, Phys. Rev. C **29**, 1859 (1984).

[29] T. R. Rodríguez and J. L. Egido, Phys. Lett. B **705**, 255 (2011).

[30] J. J. Ressler *et al.*, Phys. Rev. Lett. **84**, 2104 (2000).

[31] E. Wigner, Phys. Rev. **51**, 106 (1937).

[32] M. A. Bentley and S. M. Lenzi, Prog. in Part. and Nucl. Phys. **59**, 497 (2007).

[33] S. M. Lenzi *et al.*, Phys. Rev. Lett. **87**, 122501 (2001).

[34] Y. H. Lam, N. A. Smirnova, and E. Caurier, Phys. Rev. C **87**, 054304 (2013).

[35] M. A. Bentley *et al.*, Phys. Lett. B **437**, 243 (1998).

[36] D. M. Debenham *et al.*, Phys. Rev. C **94**, 054311 (2016).

[37] G. Martínez-Pinedo, K. Langanke, and P. Vogel, Nucl. Phys. A **651** (1999).

[38] W. Satuła and R. Wyss, Phys. Lett. B **393**, 1 (1997).

[39] J. Engel, S. Pittel, M. Stoitsov, P. Vogel, and J. Dukelsky, Phys. Rev. C **55**, 1781 (1997).

[40] L. N. Cooper, Phys. Rev. **104**, 1189 (1956).

[41] M. Cheoun, A. Faessler, F. Šimkovic, G. Teneva, and A. Bobyk, Nucl. Phys. A **587**, 301 (1995).

[42] G. Pantis, F. Šimkovic, J. D. Vergados, and A. Faessler, Phys. Rev. C **53**, 695 (1996).

[43] B. Cederwall *et al.*, Phys. Rev. Lett. **124**, 062501 (2020).

[44] P. J. Davies *et al.*, Phys. Rev. C **99**, 021302 (2019).

[45] K. Kaneko, Y. Sun, T. Mizusaki, and S. Tazaki, Phys. Rev. C **89**, 031302 (2014).

[46] P. Van Isacker, A. O. Macchiavelli, P. Fallon, and S. Zerguine, Phys. Rev. C **94**, 024324 (2016).

[47] J. Dobaczewski, Private communication (2019).

[48] R. Machleidt and I. Slaus, Journal of Phys. G: Nucl. and Part. Phys. **27**, R69 (2001).

[49] W. Heisenberg, Zeitschrift für Physik **77**, 1 (1932).

[50] D. Dean, S. Koonin, K. Langanke, and P. Radha, Phys. Lett. B **399**, 1 (1997).

[51] R. D. Woods and D. S. Saxon, Phys. Rev. **95**, 577 (1954).

[52] B. A. Brown, "Lecture notes in nuclear structure physics," (2005).

[53] R. F. Casten, *Nuclear Structure From a Simple Perspective* (Oxford University Press, 1990) pp. 327–333.

[54] J. Ekman, *Isospin Symmetry Breaking in the Mass A=35 and A=51 Mirror Nuclei*, Ph.D. thesis, Lund University (2004).

[55] M. Honma, T. Otsuka, T. Mizusaki, and M. Hjorth-Jensen, Phys. Rev. C **80**, 064323 (2009).

[56] K. Kaneko, T. Mizusaki, Y. Sun, and S. Tazaki, Phys. Rev. C **89**, 011302 (2014).

[57] A. P. Zuker, S. M. Lenzi, G. Martínez-Pinedo, and A. Poves, Phys. Rev. Lett. **89**, 142502 (2002).

[58] K. S. Krane, *Introductory Nuclear Physics* (John Wiley Sons, 1987) pp. 327–333.

[59] R. B. Firestone, *Table of Isotopes*, 8th ed. (Wiley-Interscience, 1999) p. 14163.

[60] P. Maris, Journal of Physics: Conference Series **402**, 012031 (2012).

[61] M. Bender, P.-H. Heenen, and P.-G. Reinhard, Rev. Mod. Phys. **75**, 121 (2003).

[62] C. Bertulani, *Nuclear Physics in a Nutshell* (Princeton University Press, 2007) pp. 160–175.

[63] H. Nam *et al.*, Journal of Physics: Conference Series **402**, 012033 (2012).

[64] A. L. Goodman, Adv. Nucl. Phys. **11**, 263 (1979).

[65] E. Perlińska, S. G. Rohoziński, J. Dobaczewski, and W. Nazarewicz, Phys. Rev. C **69**, 014316 (2004).

[66] J. A. Sheikh *et al.*, Phys. Rev. C **89**, 054317 (2014).

[67] K. Sato, J. Dobaczewski, T. Nakatsukasa, and W. Satuła, Phys. Rev. C **88**, 061301 (2013).

[68] P. Ring and P. Schuck, *The Nuclear Many-Body Problem* (Springer, 2000).

[69] P. Dirac, Proceedings of the Royal Society of London A: Mathematical, Physical and Engineering Sciences **114**, 243 (1927).

[70] J. Suhonen, "Electromagnetic multipole moments and transitions," in *From Nucleons to Nucleus: Concepts of Microscopic Nuclear Theory* (Springer Berlin Heidelberg, Berlin, Heidelberg, 2007) pp. 117–156.

[71] A. M. Bernstein, V. R. Brown, and V. A. Madsen, Phys. Rev. Lett. **42**, 425 (1979).

[72] V. F. Weisskopf, Phys. Rev. **83**, 1073 (1951).

[73] S. Raman and C. W. Nestor, in *Weak and Electromagnetic Interactions in Nuclei* (Springer Berlin Heidelberg, Berlin, Heidelberg, 1986) pp. 25–30.

[74] M. A. Bentley, S. M. Lenzi, S. A. Simpson, and C. A. Diget, Phys. Rev. C **92**, 024310 (2015).

[75] P. J. Davies *et al.*, Phys. Rev. Lett. **111**, 072501 (2013).

[76] P. Ruotsalainen *et al.*, Phys. Rev. C **88**, 041308 (2013).

[77] E. C. Simpson and J. A. Tostevin, Phys. Rev. C **79**, 024616 (2009).

[78] Z. Podolyák *et al.*, Phys. Lett. B **632**, 203 (2006).

[79] N. Mărginean *et al.*, Phys. Rev. C **69**, 054301 (2004).

[80] J. Heese *et al.*, Phys. Rev. C **41**, 603 (1990).

[81] A. Gade and B. M. Sherrill, Phys. Scr. **91**, 053003 (2016).

[82] D. J. Morrissey, B. Sherrill, M. Steiner, A. Stolz, and I. Wiedenhoever, Nucl. Instrum. Methods Phys. Res., Sec. B **204**, 90 (2003).

[83] "The Colourful Nuclide Chart," `https://people.physics.anu.edu.au/~ecs103/chart/`, [Online; accessed 5-November-2019].

[84] D. Weisshaar *et al.*, Nucl. Instrum. Methods Phys. Res., Sec. A **847**, 187 (2017).

[85] D. Bazin, J. Caggiano, B. Sherrill, J. Yurkon, and A. Zeller, Nucl. Instrum. Methods Phys. Res., Sec. B **204**, 629 (2003).

[86] S. Agostinelli *et al.*, Nucl. Instrum. Methods Phys. Res., Sec. A **506**, 250 (2003).

[87] P. Adrich *et al.*, Nucl. Instrum. Methods Phys. Res., Sec. A **598**, 454 (2009).

[88] P. A. Zavodszky *et al.*, Nucl. Instrum. Methods Phys. Res., Sec. B **241**, 959 (2005).

[89] P. A. Zavodszky *et al.*, Rev. Sci. Instrum. **77**, 03A334 (2006).

[90] D. J. Morrissey, Nucl. Phys. A **616**, 45 (1997).

[91] J. Yurkon *et al.*, Nucl. Instrum. Methods Phys. Res., Sec. A **422**, 291 (1999).

[92] D. Bazin, "S800 Spectograph Service Level Description," `https://www.nscl.msu.edu/users/s800_sld-Feb20171.pdf`, [Online; Accessed: 23-June-2020].

[93] I. Y. Lee, Journal of Physics: Conference Series **420**, 012156 (2013).

[94] S. Paschalis *et al.*, Nucl. Instrum. Methods Phys. Res., Sec. A **709**, 44 (2013).

[95] T. Lauritsen *et al.*, Nucl. Instrum. Methods Phys. Res., Sec. A **836**, 46 (2016).

[96] S. Akkoyun *et al.*, Nucl. Instrum. Methods Phys. Res., Sec. A **668**, 26 (2012).

[97] G. F. Knoll, *Radiation Detection and Measurement*, 4th ed. (John Wiley Sons, 2010) p. 1163.

[98] O. Klein and Y. Nishina, Zeitschrift für Physik **52**, 853 (1929).

[99] G. Schmid *et al.*, Nucl. Instrum. Methods Phys. Res., Sec. A **430**, 69 (1999).

[100] Y. Yoshizawa, Y. Iwata, and Y. Iinuma, Nucl. Instrum. and Meth. **174**, 133 (1980).

[101] "S800 Documentation," `https://wikihost.nscl.msu.edu/S800Doc/`, [Online; accessed 21-October-2019].

[102] K. Makino and M. Berz, Nucl. Instrum. Methods Phys. Res., Sec. A **427**, 338 (1999).

[103] M. Berz, K. Joh, J. A. Nolen, B. M. Sherrill, and A. F. Zeller, Phys. Rev. C **47**, 537 (1993).

[104] "MSU Inverse map server," `http://maps.nscl.msu.edu/~s800maps/`, [Online; accessed 19-October-2019].

[105] K. Wimmer, "GrROOT," `http://nucl.phys.s.u-tokyo.ac.jp/wimmer/software.php`, [Online; Accessed: 23-May-2019].

[106] R. Brun and F. Rademakers, Nucl. Instrum. Methods Phys. Res., Sec. A **389**, 81 (1997).

[107] J. K. Tuli, Nucl. Instrum. Methods Phys. Res., Sec. A. **369** (1996).

[108] D. Weisshaar, Private communication (2018).

[109] J. Jabbour, L. Rosier, B. Ramstein, R. Tamisier, and P. Avignon, Nucl. Phys. A **464**, 260 (1987).

[110] W. Mueller *et al.*, Nucl. Instrum. Methods Phys. Res., Sec. A **466**, 492 (2001).

[111] M. Oreglia, *A Study of the Reactions* $\psi' \to \gamma\gamma\psi$, Ph.D. thesis, SLAC (1980).

[112] J. R. Terry *et al.*, Phys. Rev. C **77**, 014316 (2008).

[113] P. Doornenbal *et al.*, Nucl. Instrum. Methods Phys. Res., Sec. A **613**, 218 (2010).

[114] W. Mueller *et al.*, Nucl. Instrum. Methods Phys. Res., Sec. A **466**, 492 (2001).

[115] S. Heil, *Electromagnetic Properties of* ^{21}O *and the Self-Calibration of Compton Tracking Arrays*, Ph.D. thesis, TU Darmstadt (2019).

[116] R. J. Barlow, *Statistics: A Guide to the Use of Statistical Methods in the Physical Sciences (Manchester Physics Series)*, reprint ed. (WileyBlackwell, 1989).

[117] O. Tarasov and D. Bazin, Nucl. Phys. A **746**, 411 (2004), Proceedings of the Sixth International Conference on Radioactive Nuclear Beams (RNB6).

[118] "NSCL Lifetime Wiki," `https://wikihost.nscl.msu.edu/lifetime/doku.php?id=g4lifetime:docs`, [Online; accessed 10-February-2020].

[119] S. A. Milne *et al.*, Phys. Rev. C **93**, 024318 (2016).

[120] H. Iwasaki, Private communication (2018).

[121] D. Rudolph *et al.*, Phys. Rev. C **56**, 98 (1997).

[122] C. J. Lister, B. J. Varley, H. G. Price, and J. W. Olness, Phys. Rev. Lett. **49**, 308 (1982).

[123] S. M. Fischer *et al.*, Phys. Rev. Lett. **87**, 132501 (2001).

[124] M. J. Leddy *et al.*, Phys. Rev. C **58**, 1438 (1998).

[125] C. J. Gross *et al.*, Phys. Rev. C **49**, R580 (1994).

[126] C. Baktash, B. Haas, and W. Nazarewicz, Annual Review of Nuclear and Particle Science **45**, 485 (1995).

[127] D. Radford, "Radware," `https://radware.phy.ornl.gov/`, [Online; Accessed: 24-June-2020].

[128] B. Pritychenko, M. Birch, and B. Singh, Nucl. Phys. A **962**, 73 (2017).

[129] M. M. Giles *et al.*, Phys. Rev. C **99**, 044317 (2019).

[130] A. Boso *et al.*, Phys. Lett. B **797**, 134835 (2019).

[131] R. F. Casten and N. V. Zamfir, Phys. Rev. Lett. **70**, 402 (1993).

[132] M. Freer, H. Horiuchi, Y. Kanada-En'yo, D. Lee, and U.-G. Meißner, Rev. Mod. Phys. **90**, 035004 (2018).

[133] A. Andreyev *et al.*, Nature **405**, 430 (2000).

[134] A. P. Zuker, A. Poves, F. Nowacki, and S. M. Lenzi, Phys. Rev. C **92**, 024320 (2015).

[135] J. Dechargé and D. Gogny, Phys. Rev. C **21**, 1568 (1980).

[136] M. Kortelainen *et al.*, Phys. Rev. C **82**, 024313 (2010).

[137] W. Y. Ng and B. Castel, Phys. Rev. C **10**, 2643 (1974).

[138] W. Satuła, P. Baczyk, J. Dobaczewski, and M. Konieczka, Phys. Rev. C **94**, 024306 (2016).

[139] W. Satuła and J. Dobaczewski, Phys. Rev. C **90**, 054303 (2014).

[140] W. Satuła, Private communication (2020).

[141] W. Satuła, (2020), et al., to be published.

[142] F. Recchia *et al.*, (2020), accepted proposal at NSCL.

[143] M. A. Bentley, R. Wadsworth, *et al.*, (2020), accepted proposal at RIKEN.